UNIVERSITY OF BIRMINGHAM

Design of Multinuclear Transition Metal and Lanthanide Complexes: Magnetic and Luminescent Properties

By

ZHILIN GUO

A thesis submitted to The University of Birmingham for the degree of DOCTOR OF PHILOSOPHY

The School of Chemistry
College of Engineering and Physical Sciences
The University of Birmingham
Department of Chemistry
Southern University of Science and Technology
July 2021

Abstract

The work presented in this thesis focuses on the syntheses and characterisation of a series of multi-nuclear transition metal and lanthanide-based coordination complexes. Their structures, magnetic and luminescent properties are investigated by various experimental techniques including single crystal X-ray diffraction, UV-vis, SQUID magnetometry and time-resolved luminescent spectroscopy.

Rational design of molecular clusters with intricate supramolecular architectures have received continuous attention in many interdisciplinary fields. In comparison with those closed-shell bridging ligands that suffer from weak magnetic coupling between the metal centres due to the large spanning distance, the use of free radical bridges can produce efficient spin exchange beyond distance limit and further enhances magnetic interaction with other spin centres arising from the direct orbital overlap.

Toward this end, two neutral bis-bidentate pyridazine ligands, pydz and pzdz, with the versatile azido bridge are used in ***Chapter 2*** and ***3*** to synthesise tetranuclear Co and Fe grid-like complexes $[M^{II}_4(pydz)_4(N_3)_4](BPh_4)_4 \cdot 4MeCN$ and $[M^{II}_4(pzdz)_4(N_3)_4](BPh_4)_4 \cdot$solvents. The Co complexes behave as typical field-induced SMMs with energy barriers of 36 and 56 K, respectively. The Fe complex with pydz ligand shows remarkable SCO behaviour ($T_{1/2}$ = 230 K) which is first observed in azide-bridged systems, while the pzdz analogue only shows overall antiferromagnetic interaction.

In ***Chapter 4***, tetrazine radical $bpztz^{\bullet-}$ is used to prepare tetranuclear complexes $[M^{II}_4(bpztz^{\bullet-})_4(N_3)_4]$ (M = Co and Zn). Strong antiferromagnetic metal-radical interactions with J = -65 cm^{-1} was obtained in Co complex. Meanwhile, an unexpected metamagnetic behaviour at low temperatures as well as significant enhancement of SMM behaviour compared to the neutral pyridazine bridge are observed.

Another tetrazine ligand bptz is introduced in ***Chapter 5*** making tetranuclear Co grids $[Co^{II}_4(bptz^{\bullet-})_4(N_3)_4] \cdot MeOH$ along with two mixed-valence components

$[Co^{2.5}_4(bptz^{\bullet-})_4(N_3)_4](ClO_4)_2 \cdot 5MeOH$ and $[Co^{II}_2Co^{III}_2(Hbptz)_4(N_3)_4](OTF)_2 \cdot$solvents. SMM behaviours are observed for the tetrazine radical based complexes with higher effective energy barriers compared to the pyridazine counterparts. However, the slow magnetic relaxation is switched off for the hydrogenated tetrazine-bridged one. The redox properties are also studied.

Lanthanide complexes with well-designed organic chromophores are considered as ideal candidates for luminescent materials for their intense emission, long lifetimes and high quantum yields. Polynuclear complexes, specially heterometallic complexes, are of particular interest when incorporating luminescence with magnetic properties that are able to provide additional functions.

Chapter 6 describes the homo- and hetero-dinuclear assemblies of lanthanide complexes using a bis-bidentate bistpOp ligand for shielding around the lanthanide ions. Characteristic emission for Eu^{3+}, Tb^{3+}, Dy^{3+}, Sm^{3+} and Yb^{3+} ions are obtained with long lifetimes for $[Eu_2(bistpOp)_3]$ and $[Tb_2(bistpOp)_3]$ complexes. The formation of heterodinuclear $[DyEu(bistpOp)_3]$ and $[EuYb(bistpOp)_3]$ complexes are investigated in solution via luminescence titration. Significant energy transfer is observed from the spectra with efficiency above 50%.

A novel DTPA-bisamide derivative with terpyridine arms is successfully synthesised and characterised in ***Chapter 7*** making lanthanide complexes. Photophysical studies prove that the ligand is a good antenna for sensitising visible lanthanide emissions of Tb^{3+} and Eu^{3+}. Moreover, the heterometallic 3d-4f assembly of a macrocyclic complex $\mathbf{Eu_2Fe_2}^{4+}$ is studied by UV-vis titration.

Declaration

This thesis is an original work of my research and contains no material which has been accepted for the award of any other degree or diploma at any university or equivalent institution.

This thesis is presented in an "Alternative format" where the work in ***Chapter 2, 3*** and ***4*** have been published in peer-reviewed journals. Co-authors are acknowledged and their contributions are identified in each chapter.

Acknowledgement

First of all, as a student of the Joint PhD Training Programme offered by the University of Birmingham (UoB) and Southern University of Science and Technology (SUSTech), I would like to express my heartfelt gratitude to my supervisors Prof. Zoe Pikramenou in UoB and Dr Yuan-Zhu Zhang in SUSTech, for their supervision as well as to UoB and SUSTech for their support for my studies in both universities.

I also would like to thank Prof. Mike Hannon, Dr Louise Male, Dr Cecile de Corla and Dr Chi Tsang in UoB, Dr Xiao-Yong Chang and Dr Yang Yu in SUSTech for the trainings and helpful discussions on characterisation and analysis of my complexes, sharing knowledges and good chats.

Being the first ever Chinese PhD student in the ZP group, I honestly could not have hoped to work as part of a more supportive team in UoB. I wish to thank Zoe for her trust in me to work independently, her continuous patience and suggestions, and particularly arranging online monthly meetings during the pandemic when I am in SUSTech. The past and present ZP group members, Andrew, Irene, Jamie, Luke, Menisha, Sajni, Sarah, Sunil, Tasha, you guys have given me an unforgettable and unique experience both on and off work. It is not always easy to live in a foreign country but working with the ZP family has been one of the most rewarding and exciting time of my life. I will never forget how I did my first ever column chromatography and when I had my first drink in the UK, the first Christmas dinner with Menisha's big family, as well as the first ever fantastic Chemball. Plus the interdisciplinary research the group performed also helps me develop different knowledges and expand my horizon in nature science.

Back in SUSTech I want to thank Yuanzhu for giving me the chances to present my work at global conferences and his willingness to submit the manuscripts. I also would like to thank all my colleagues from CF3M group in SUSTech, especially Dr Yi-Fei Deng for his assistance and tutorials

in the magnetic measurements, and Maolin You for sharing what he knew about crystallography, spectra and experiments in the lab. I am also grateful to my collaborators in SUSTech, Dr Peiyuan Yu and Dr Keith Man-Chong Wong, for theoretical investigations, and gaining access to different knowledge apart from magnetism.

There are also a few people I cannot wait to say thank you to, no matter how much they know about my projects or just offered their encouragement, especially during the unexpected COVID pandemic. Zeyu Jiang (Aaron) – you have made my time in Birmingham full of food, cats and fun. My one and only Yuan Kang (Kyle) – even though you are in Melbourne, we spend hours texting and calling, I could not imagine how my PhD would have gone without your support and understanding. Mingyang Yang (Samuel) – life outside of research and experiment would not have been be any fun without you in SUSTech. Baifu Huang – thank you for your company throughout the most difficult time preparing the thesis and viva. I also want to thank tennis hitting partners who helped me up my game.

Last but not least, I want to give all my gratitude to my parents for their greatest, the most selfless cares, support and love that is not limited by time or space.

Publications and Presentations

Manuscripts

1. **Zhilin Guo**, Maolin You, Yi-Fei Deng, Qiang Liu, Yin-Shan Meng, Zoe Pikramenou and Yuan-Zhu Zhang, An azido-bridged [Fe^{II}_4] grid-like molecule showing spin crossover behaviour, *Dalton Trans.*, 2021, **50**, 14303-14308. (*Chapter 3*)

2. **Zhilin Guo**, Yi-Fei Deng*, Zoe Pikramenou, Kim R. Dunbar* and Yuan-Zhu Zhang*, Strong Coupling and Slow Relaxation of the Magnetization for an Air-Stable [Co_4] Square with Both Tetrazine Radicals and Azido Bridges, *Inorg. Chem.*, 2021, **60**, 3651-3656. (*Chapter 4*)

3. **Zhilin Guo**, Yi-Fei Deng*, Yipei Zhang, Zoe Pikramenou and Yuan-Zhu Zhang*, Two azido-bridged [2×2] cobalt(II) grids featuring single-molecule magnet behaviour, *Dalton Trans.*, 2020, **49**, 9218. (*Chapter 2*)

4. Dita Davis, Andrew J. Carrod, **Zhilin Guo**, Benson M. Kariuki, Yuan-Zhu Zhang, and Zoe Pikramenou*, Imidodiphosphonate Ligands for Enhanced Sensitization and Shielding of Visible and Near-Infrared Lanthanides, *Inorg. Chem.*, 2019, **58**, 13268–13275.

Presentations

1. *Tuning Magnetic Properties in Azido-Bridged Molecular Grids*, 17th International Conference on Molecule Based Magnets (ICMM2021), Manchester (Online), UK, 14-18 June, 2021. (**Contributed Talk**)

2. *Imidodiphosphonate-Based Mononuclear and Binuclear Lanthanide Complexes*, The 23rd International Symposium on the Photochemistry and Photophysics of Coordination Compounds (ISPPCC 2019), Hong Kong, China, 15-19 July, 2019. **(Poster)**

3. *Manipulating Magnetic Properties in Azido-Bridged Co^{II} and Fe^{II} Squares*, 14th International Conference on Materials Chemistry (MC14), Birmingham, UK, 08-14 July, 2019. **(Poster, Funded by Royal Society of Chemistry Materials Chemistry Division)**

4. *Luminescent Homo and Heterometallic Lanthanide Complexes*, RSC Photophysics and Photochemistry Group Early Career Meeting 2018, Swansea, UK, 20-21 September, 2018. **(Poster)**

5. *Luminescent Homo and Heterometallic Dinuclear Lanthanide Probes*, 14th European Biological Inorganic Chemistry Conference (EuroBIC 14), Birmingham, UK, 26-30 August, 2018. **(Poster)**

List of Abbreviations and Symbols

AC	Alternating current
CV	Cyclic voltammetry
DC	Direct current
EPR	Electron paramagnetic resonance
FC	Field-cooled
LIESST	Light-induced excited spin-state trapping
MLCT	Metal-to-ligand charge transfer
PXRD	Powder X-ray diffraction
QTM	Quantum tunnelling of the magnetisation
SCXRD	Single crystal X-ray diffraction
SCO	Spin crossover
SMM	Single-molecule magnet
SQUID	Superconducting quantum interference device
ZFC	Zero-field cooled
ZFS	Zero-field splitting
pydz	3,6-di (pyridin-2-yl)pyridazine
pzdz	3,6-bis(3,5-dimethyl-1H-pyrazol-1-yl)pyridazine
bpztz	3,6-bis(3,5-dimethyl-pyrazolyl)-1,2,4,5-tetrazine
bptz	3,6-bispyridyl-1,2,4,5-tetrazine
HtpOp	Tetraphenyl imidodiphosphonate
H_2bistpOp	Pentaphenyl diimidotriphosphate
DTPA	Diethylentriaminepentaacetic acid

tpy / terpy	2,2';6',2"-terpyridine
D	Axial zero-field splitting parameter
H	Magnetic field
J	Magnetic exchange coupling constant
M	Field dependence magnetisation
S	Electronic spin state
θ	Weiss constant
g	Landé g-value
χ_M	Molecular magnetic susceptibility
χ'	In-phase magnetic susceptibility
χ''	Out-of-phase magnetic susceptibility
T	Temperature
T_B	Magnetic blocking temperature
Φ	Quantum yield
U_{eff}	Effective energy barrier
τ_L	Luminescence lifetime
τ	Magnetic relaxation time
τ_0	Pre-exponential factor
k_B	Boltzmann constant

Table of Contents

Chapter 1 Introduction

1.1 Overview of magnetism

When a material is placed under a magnetic field, the magnetic property is related to the electron configuration of the atoms and ions, which can be generally classified into diamagnetic or paramagnetic. A diamagnetic system originates from the all-paired electrons that leads to zero magnetic moment and negative magnetic susceptibility. In contrast, a paramagnetic substance consists of one or more unpaired electrons that display positive magnetic susceptibility under an external magnetic field. Magnetic materials have been widely investigated and applied in magnetomechanical equipment, acoustic devices, information storage and telecommunications devices, electrical motors/generators, magnetic shielding, and magnetic refrigeration. Three magnetic interactions that have been discovered thus far are (**Figure 1.1**):

(1) Ferromagnetic interaction: the magnetic moments are aligned parallel to the ordered positions.

(2) Antiferromagnetic interaction: the magnetic moments are arranged regularly with neighbouring spins in opposite directions.

(3) Ferrimagnetic interaction: spin arrangement is similar to an antiferromagnetic system, however the magnitude of the antiparallel interactions is non-equivalent.

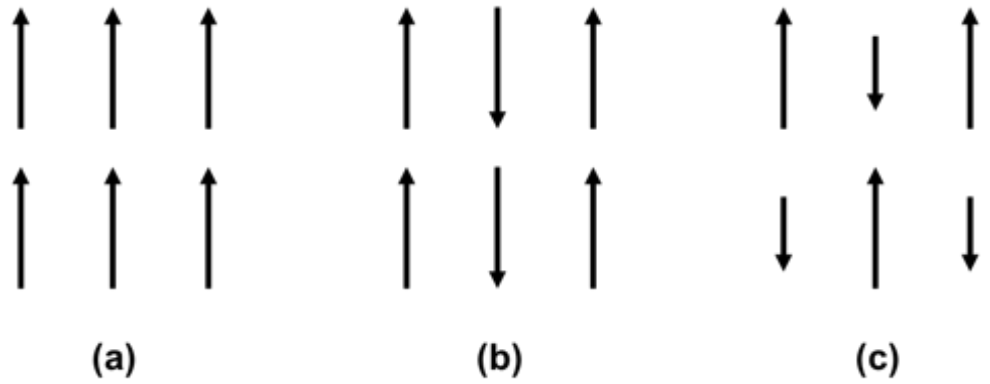

Figure 1.1. Neighbouring magnetic interactions of spins. Black arrows indicate the direction and magnitude of the spin, displaying ferromagnetic (a), antiferromagnetic (b) and ferrimagnetic (c).

1.1.1 Measurements of molecular magnetism

The growing interest in molecular-based magnetic materials has raised fundamental concerns in both scientific and technology circles. Organic molecules and specific coordination metal complexes synthesised by chemical reactions can be easily controlled and characterised, thus providing potentials for novel and multiple functions. A superconducting quantum interference device (SQUID) magnetometer or Physical Property Measurement System (PPMS) technique is often used to measure the direct current (DC) or alternating current (AC) magnetic susceptibilities of a sample.

DC magnetic susceptibility measurement is used to evaluate any changes of the magnetic moment on the sample under an applied DC static field. The data are generally plotted as molecular magnetic susceptibility (χT) vs temperature (T) and the field dependence magnetisation (M) vs magnetic field (H). Spin ground state (S) and the magnetic exchange interaction of the sample can be directly obtained from the plots. The magnetic interaction can be described by the fit to the Curie-Weiss law $\chi = C/(T - \theta)$ where C is the Curie constant, T is the temperature and θ is the Weiss constant. A positive θ indicates ferromagnetic interaction while a negative one suggests an antiferromagnetic interaction being present. Furthermore, quantitative information can be extracted from the χT vs. T

plot by fitting the curves with appropriate spin-Hamiltonians or Heisenberg-Dirac-Van Vleck (*vide infra*) equations via specific programmes.[1] This approach allows to obtain parameters for the magnetic exchange coupling constant (*J*) that describe the nature and strength of the spin magnetic interaction as well as the *g*-factor and the axial zero-field splitting parameters (*D*). The magnetisation *M*-*H* curves provide information about the internal response of the magnetic material with an increase in the DC field, including the saturation of magnetisation and magnetic hysteresis.

The AC magnetic susceptibility measurement is generally used to evaluate the magnetic relaxation behaviour of the sample by measuring the in-phase (or real, χ') and out-of-phase (or imaginary, χ'') magnetic susceptibility under zero or external DC fields, where the former is the slope of the *M*-*H* curve, and the latter suggests the dissipative process of the sample.

1.2 Magnetic Properties of Coordination Metal Complexes

1.2.1 Spin Crossover (SCO)

The history of spin crossover dates back to 1931 when the magnetic properties of a series tris(N,N-disubstituted dithiocarbamate) iron(III) derivatives were first discovered.[2] Then in the 1960s, the first Co(II) SCO complex bis-(2,6-pyridindialdihydrazone)-cobalt(II) iodide and Fe(II) SCO complex based on 1,10-phenanthroline were reported in succession (**Figure 1.2**).[3] It is generally believed that metal ions with d^n (n = 4, 5, 6, 7) electron configuration can possibly process SCO under different external stimuli, such as temperature, pressure and light, where d^6 Fe(II) complexes in an octahedral geometry account for the largest number of SCO and have been under thoroughly investigation between the paramagnetic high-spin state ($S = 2$) and diamagnetic low-spin state ($S = 0$). This property can be potentially applied in molecular switches, data storage and spintronic devices.

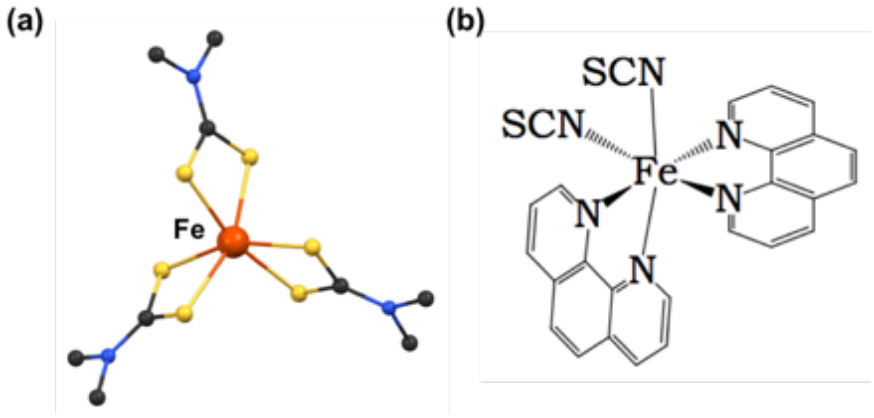

Figure 1.2. Structures of (a) tris(N,N-disubstituted dithiocarbamate) iron(III)[2] and (b) $[Fe^{II}(phen)_2(NCS)_2]$[3a] SCO compounds. Atom colours: C, black; N, blue; S, yellow.

Ligand field theory plays an important role in the research of SCO. In an octahedral geometry, the five *d* orbitals of a transition metal ion are split into two subsets, d_{xy}, d_{xz} and d_{yz} of t_{2g} and d_{z^2} and $d_{x^2-y^2}$ of e_g orbitals. The difference of energy between t_{2g} and e_g is defined as the ligand field splitting energy Δ. When Δ is larger than the spin pairing energy (*P*), the electrons have a tendency to occupy only the lower energy t_{2g} orbitals arranging in a low spin state (LS). If $\Delta < P$ instead, the electrons fill the d-orbitals by obeying Hund's first rule and the high spin state (HS) is adopted, maximising the spin multiplicity (**Figure 1.3**). Since the e_g orbitals have an anti-bonding characteristic, their population is associated with an increase in the metal-ligand bond length. Conversely, the opposite population change in t_{2g} influences the electron back-donation between the metal ion and the empty π* orbitals of the ligands. This provides significant evidence to evaluate the SCO complexes through single crystal X-ray diffraction analysis. For Fe(II) complexes in a six-N coordination environment, the high-spin bond length (2.12-2.18 Å) is generally 0.2 Å longer than the low-spin (1.95-2.00 Å).

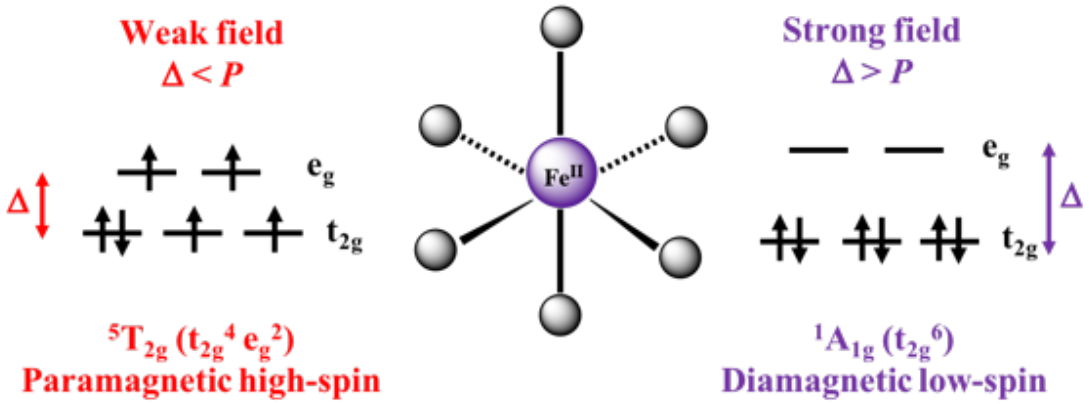

Figure 1.3. Electronic configurations of the two ground states for six-coordinated Fe(II) ion in an octahedral geometry.

The χT vs T plot from static magnetic susceptibility measurement is one of the most visualised methods to evaluate the spin crossover behaviour. Five main types of spin transition in SCO system that have been discovered are gradual, abrupt, hysteretic, multi-step and incomplete have been discovered, as shown in **Figure 1.4**.[4] Gradual transition is normally observed when weak intermolecular interaction is involved. In contrast, the abrupt transition relates to strong cooperativity. A hysteresis may occur when a particularly high cooperative interaction is present, indicating a bistable system and that exhibits memory effect. The multi-step transition involves additional intermediate stable states and is often observed in polymeric or high dimensional complexes. Incomplete SCO occurs when the compound still exists in a mixture of spin states due to kinetic effects, dislocations or defects in the lattice.

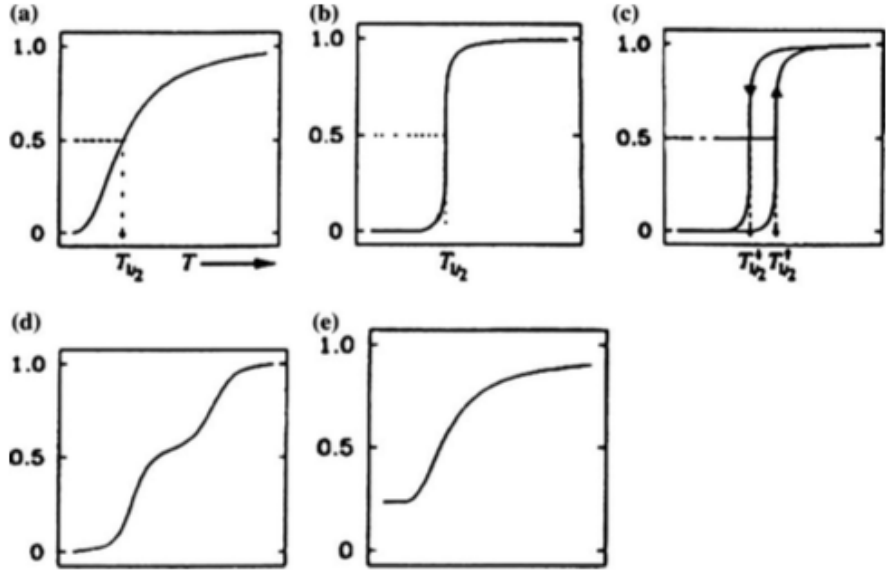

Figure 1.4. Five types of SCO: (a) gradual, (b) sharp, (c) hysteresis, (d) multi-step and (e) incomplete, with temperature as x axis and HS population on y axis.[4]

In 1980s, the spin state of a low-spin Fe compound was found to be able to switch to high-spin under irradiation at low temperatures.[5] This new type of photomagnetism, light-induced excited spin-state trapping (LIESST) effect, has then been widely explored mainly in various Fe(II)-SCO complexes in solid state and solution.[6] The mechanism can be explained as light pumping from the ground singlet state to excited singlet states, from which the system can eventually decay via two consecutive intersystem crossings to low lying quintet state due to the spin-orbital coupling (**Figure 1.5**).[7] T(LIESST) is used to evaluate the metastable high-spin of a complex, which is the derivation minimum of the photo-induced magnetic susceptibility data. To empirically characterise or predict the LIESST effect, Létard et al proposed an equation $T(\text{LIESST}) = T_0 - 0.3T_{1/2}$, where the parameter T_0 depends on the coordination environment (for Fe^{2+} complexes with bidentate ligands, $T_0 = 120$ K), $T_{1/2}$ is the transition temperature of thermal-induced SCO and 0.3 means the equation is suitable only when the heating rate is 0.3 K min^{-1}.[8] However, this equation still lacks fundamental theoretical background. Up to now, the highest observed T(LIESST) is 145 K in a mononuclear Fe complex

(**Figure 1.6** top).[9] This behaviour is found to be reversible in some complexes when using different irradiations in some recent research (**Figure 1.6** bottom).[10]

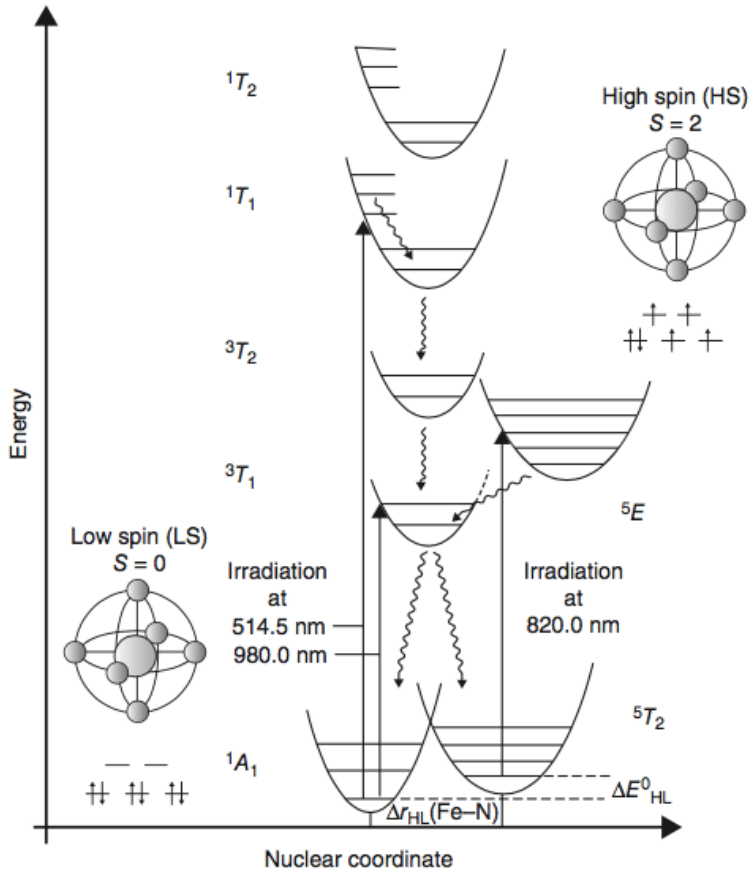

Figure 1.5. Mechanism of LIESST.[7]

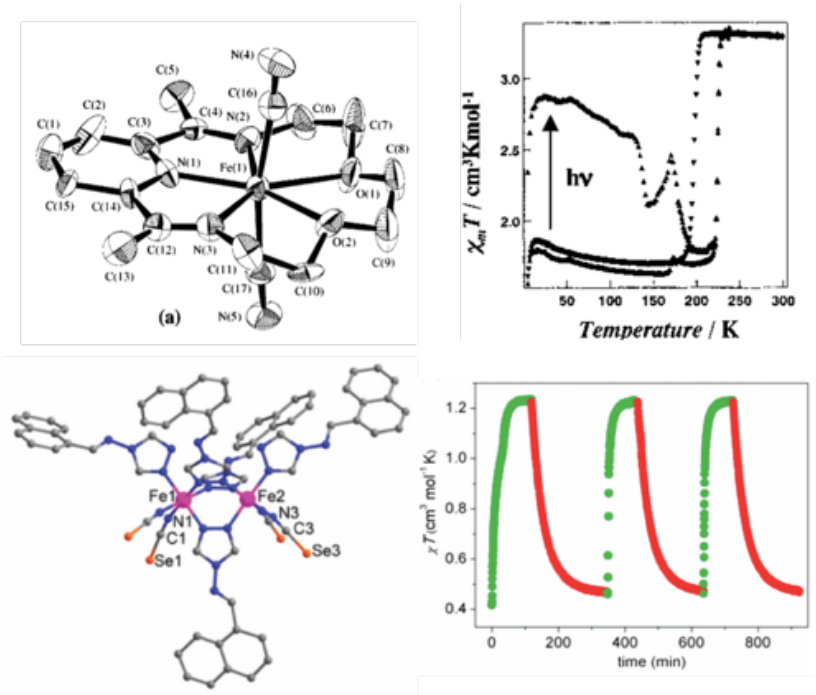

Figure 1.6. Top: A Fe(II) complex based on a Schiff-base ligand showing LIESST effects with high *T*(LIESST).[9] Bottom: An asymmetric dinuclear $[Fe_2L_2(\mu\text{-}L)_3(NCSe)_4]\cdot 2DMF\cdot 2H_2O$ (L = 1-naphthylimino-1,2,4-triazole) showing reversible LIESST effect under successive irradiation at 532 nm (green) and 808 nm (red) at 10 K.[10]

1.2.2 Electron transfer and valence tautomeric

Electron transfer (ET) and valence tautomeric (VT) are also spin-state transition related magnetic behaviours, where reversible changes in the oxidation state of a metal ion are observed. ET was first observed in Prussian blue analogues in a complicate polymeric system and it is now prevalent among the structurally characterised coordination complexes especially the most studied Co-Fe system. The electron can transfer between the diamagnetic Fe^{II}-Co^{III} units and paramagnetic Fe^{III}-Co^{II} units under thermal or light-induced process via the cyanide bridge (**Figure 1.7**).[11] This property has also been extended to different combinations, such as Fe-Fe, Fe-Mn, Co-W, which may further create synergy between ET and other properties.[12]

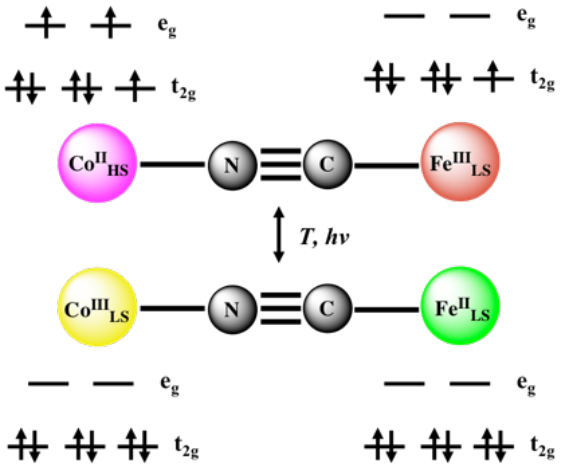

Figure 1.7. Scheme of electron transfer pathways in cyanide-bridged Co-Fe system.

VT was discovered earlier in 1980 in a mononuclear Co complex where an electron transferred from a diamagnetic ligand (cat) to low-spin Co(III) yielding a high-spin Co(II) and a paramagnetic radical (sq) upon heating (**Figure 1.8**). To achieve VT, a redox-active organic ligand is required (which must have an accessible radical form) to drive the intramolecular electron transfer between metal and ligand.[13] Other metal-ligand systems are also under investigation[14] to elucidate additional factors that influence VT such as ancillary ligands, counter ions and intermolecular interactions.[15]

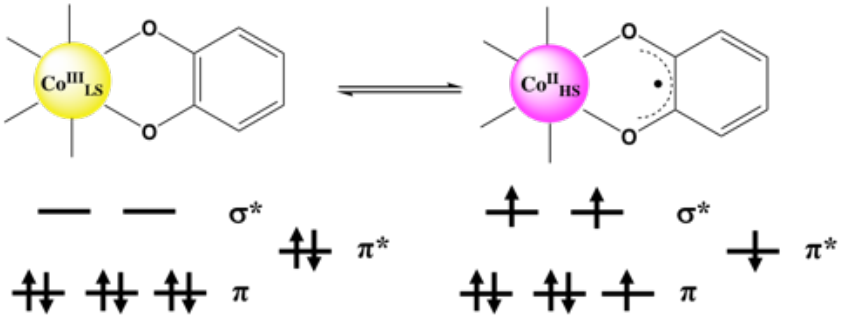

Figure 1.8. Scheme of valence tautomerism in Co complex.

1.2.3 Single-molecule magnets (SMMs)

In 1993, a manganese cluster $[Mn_{12}O_{12}(O_2CMe)_{16}(H_2O)_4]$ showed slow magnetic relaxation and hysteresis at low temperatures (**Figure 1.9**) which resembles to bulk nanomagnets that can be magnetised under magnetic field and remained magnetised after the field is removed.[16] Complexes with this magnetic behaviour are named as single-molecule magnets (SMMs).

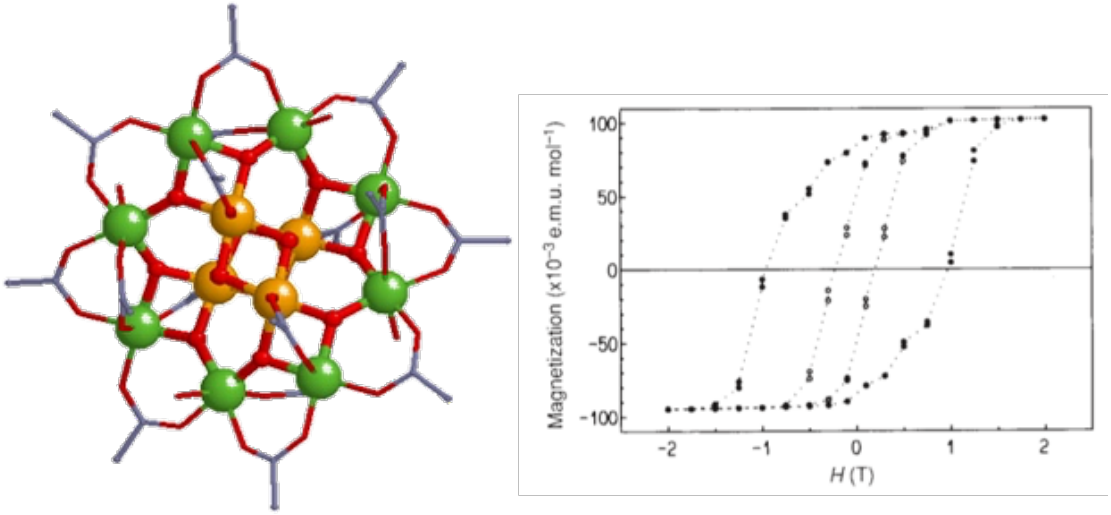

Figure 1.9. Crystal structure (left) and hysteresis loops (right) of $[Mn_{12}O_{12}(O_2CMe)_{16}(H_2O)_4]$.[16] Atom colours: Mn(III), green; Mn(IV), orange; O, red; C, grey.

The slow magnetic relaxation is a consequence of an axial anisotropy due to a negative axial zero field splitting which results in the spin ground state splitting into $(2S+1)$ M_s sub levels from $-S$ to $+S$ in integer steps. These two parameters give rise to an energy barrier which is the lowest energy between degenerate M_s states ($+M_s$ and $-M_s$). The energy barrier is theoretically calculated by $U = |D| S^2$ for integer-spin molecules and $U = (S^2 - ¼) |D|$ for half-integer-spin molecules. The double-well potential energy diagram (**Figure 1.10**) is used to describe the magnetisation and relaxation pathways. Quantum tunnelling of the magnetisation (QTM) occurs when energy levels of two sub-states coincide under an appropriate magnetic field and the states are brought to resonance. This results in an experimental energy barrier (U_{eff}) lower than the theoretically calculated limit due to

tunnelling promoting an overall relaxation process. Energy barrier as well as the magnetic blocking temperature (T_B), which is the highest temperature at which the molecule maintains magnetisation, are used to evaluate an SMM.

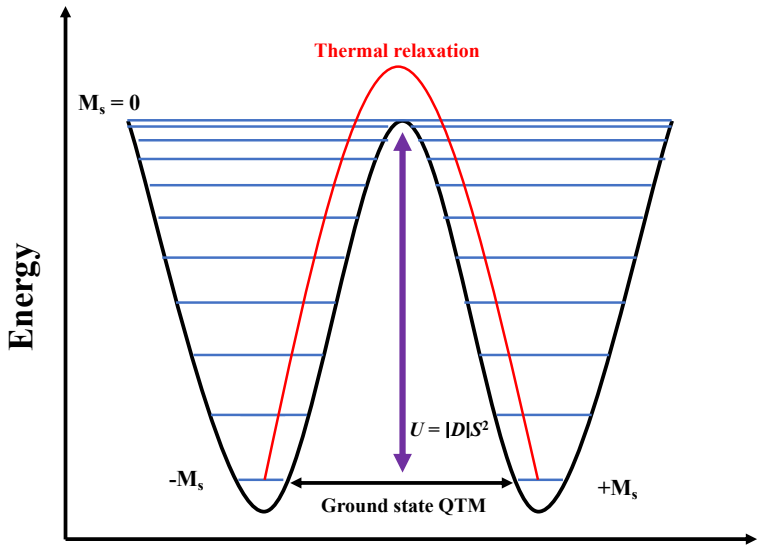

Figure 1.10. A simplified double-well potential energy diagram to show zero-field splitting of M_s levels and the energy barrier (U) between $+M_s$ and $-M_s$ levels.

The SMM behaviour of a metal complex can be intuitively verified according to AC magnetic susceptibility measurements on SQUID, evidenced by the frequency- or temperature-dependent peaks of the in-phase (χ') and out-of-phase (χ'') signals. In order to reduce the QTM occurrences and confirm the pure thermal relaxation regime, a static DC field can be applied in the AC measurements which might lift the degeneracy and result in an energy barrier unaffected by quantum tunnelling. The slow relaxation in magnetisation of a SMM adheres to the Arrhenius law $\tau = \tau_0 \exp(U_{eff}/k_B T)$ for a thermally activated process to overcome the energy barrier, where T is the temperature at which the maximum is observed in the out-of-phase AC susceptibility, and k_B is the Boltzmann constant. The energy barrier U_{eff} and pre-exponential τ_0 can be determined from a plot of $\ln\tau$ vs. $1/T$, where the slope of the plot represents the U_{eff} and from the Arrhenius equation and τ_0 gives the information

about the rate of the spin transition, which must be in a range of 10^{-6} to 10^{-12} to be considered as an SMM.

Research into SMMs initially focused on the 3d transition metal complexes when a series of Mn, Fe, Co, V clusters was reported. These compounds have large spin ground states, but the energy barriers are not always as high as expected. One important reason could be the magnetic couplings between the metal centres are not negligible. In this case, the ligand field and geometry concern have become necessary when designing of transition metal based SMMs. A computational model that takes into account the coordination mode and electronic configuration of the metal is able to predict the magnetic anisotropy of mononuclear SMMs by indicating the favourable coordination environment for large magnetic anisotropy.[17] Particularly for Co(II)-based complexes, which are the largest family of SMMs, the *D* value ranges from -161 to +118 cm^{-1} in different geometries.[18] Up to now, the largest U_{eff} for transition metal based SMMs obtained from a two-coordinated Co(II) complex [(sIPr)CoNDmp] is 413 cm^{-1} (**Figure 1.11** top),[19] while a mixed-valence tetranuclear Co complex has exhibited the highest energy barrier among the SMM clusters (**Figure 1.11** bottom).[20]

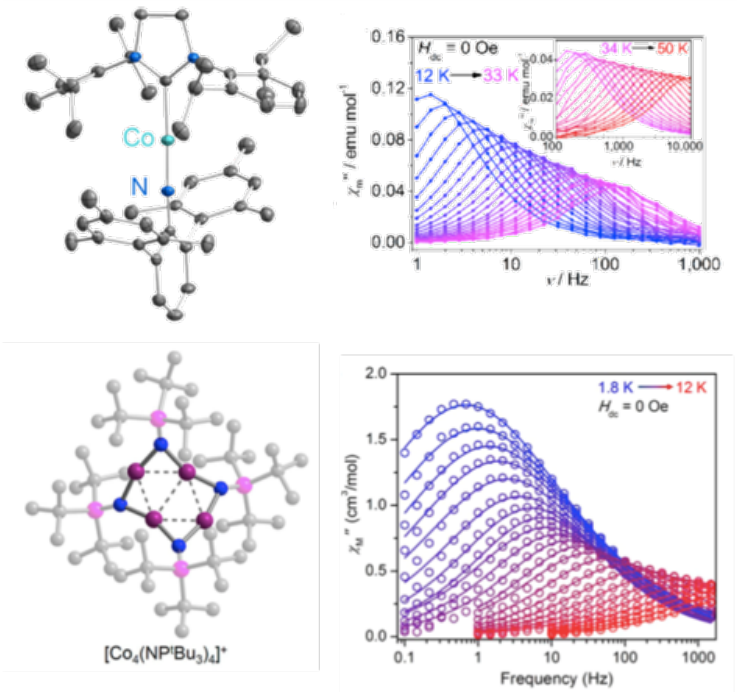

Figure 1.11. Top: Crystal structure and frequency dependence of out-of-phase ac magnetic susceptibilities of [(sIPr)CoNDmp].[19] Atom colours: Co, cyan; C, grey; N, blue. Bottom: Crystal structure and frequency dependence of out-of-phase ac magnetic susceptibilities of the mixed-valence $[Co_4(NP^tBu_3)_4]^+$ demonstrating the SMM behaviours.[20] Atom colours: Co, violet; N, blue; P, pink; C, grey.

In 2003, a double-decker phthalocyanine complex $[Pc_2Tb]^-$ was reported as the first lanthanide-based SMM with an energy barrier as high as 230 cm^{-1}.[21] Since then, 4f elements with extraordinary single-ion anisotropies have been received increasing attention. The orbital contribution to the magnetic moment is large and unquenched among the lanthanide ions, and the ligand effects can be regarded as a small but significant perturbation.[22] The most commonly used ions for SMM are Tb(III), Dy(III), Ho(III), Yb(III) and Er(III) due to the strong angular dependence inherent in the 4f orbitals. Meanwhile, Dy(III) is the most utilised one due to its large magnetic anisotropy and energy gap

between ground state and first-excited m_J levels. A theoretical calculation predicts that $[DyO]^+$ compound in a perfect axial symmetry can obtain an energy barrier as high as 3000 K.[23]

Considering applying the crystal field effect to control the single-ion anisotropy of lanthanides, a model of f-element electronic structure was posted by Long et al.[23-24] As shown in **Figure 1.12**, the shape of the 4f electron densities can be described as prolate (axially elongated) for Pm(III), Sm(III), Er(III), Tm(III) and Yb(III), oblate (equatorially expanded) for Ce(III), Pr(III), Nd(III), Tb(III), Dy(III) and Ho(III), or isotropic (spherical) for Gd(III). The anisotropy of an oblate ion can be maximised through a crystal field where the electron density of the ligand is concentrated above and below the *xy* plane, while a prolate ion prefers an equatorially-coordinated geometry in order to minimise charge contact with the axially-located lanthanide electron density (**Figure 1.13**).

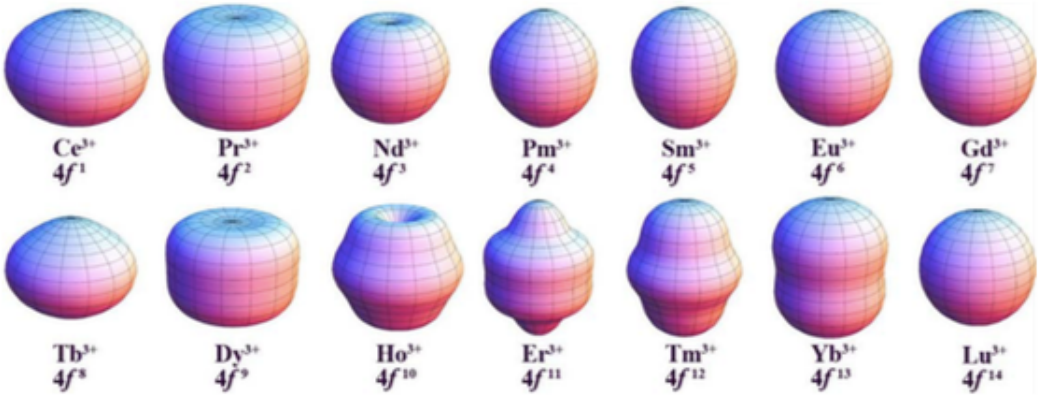

Figure 1.12. Electron density model of 4f orbital of lanthanide ions.[23,24]

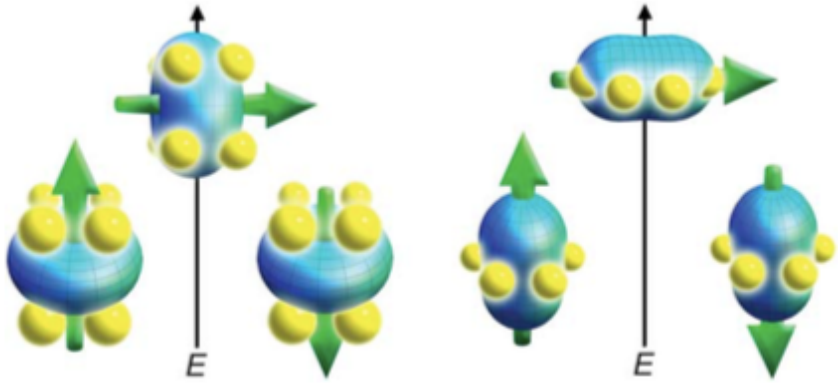

Figure 1.13. Description of the best position of the ligand electron density (yellow) to strengthen magnetic anisotropy for an oblate ion (left) and a prolate ion (right).[23,24]

This guidance is then strongly supported by some representative complexes. Tang et al reported a first equatorially three-coordinated $Er[N(SiMe_3)_2]_3$ complex in a perfect C_{3v} symmetry that exhibited slow magnetic relaxation under zero DC field with an energy barrier of 85 cm^{-1}.[25] Tong et al reported a $[Zn_2Dy(L)_2]^+$ (L = 2,2',2''-(((nitrilotris(ethane-2,1-diyl))tris(azanediyl))tris(methylene))tris-(4-bromo-phenol)) complex which was obtained from $[Zn_2Dy(L)(MeOH)]^+$ by losing the coordination methanol molecule, with the coordination environment of Dy^{3+} changed from D_{5h} (pentagonal bipyramid) to O_h (octahedral).[26] The former complex exhibited a superior slow magnetic relaxation behaviour with an energy barrier of 212 cm^{-1}. Later in 2016, the same group synthesised two Dy^{3+} SMM complexes in D_{5h} geometry, [Dy(bbpen)Br] (bbpen = N,N′-bis(2-hydroxybenzyl)-N,N′-bis(2-methylpyridyl)ethylenediamine) and $[Dy(Cy_3PO)_2(H_2O)_5]^{3+}$ (Cy_3PO = tricyclohexyl phosphine oxide), with an energy barrier of 713 cm^{-1} and a blocking temperature of 20 K, respectively.[27] Since then, many Dy-SMMs with D_{5h} geometry have been reported with recording energy barriers.[28] A Dy metallocene cation with a strong axial crystal field ligand Cp^{iPr5} has shown an effective energy barrier to reversal of the magnetisation of U_{eff} = 1,541 cm^{-1} with a magnetic blocking temperature of T_B = 80 K, which overcomes an essential barrier towards the development of nanomagnet devices that function at practical temperatures (**Figure 1.14**).[29]

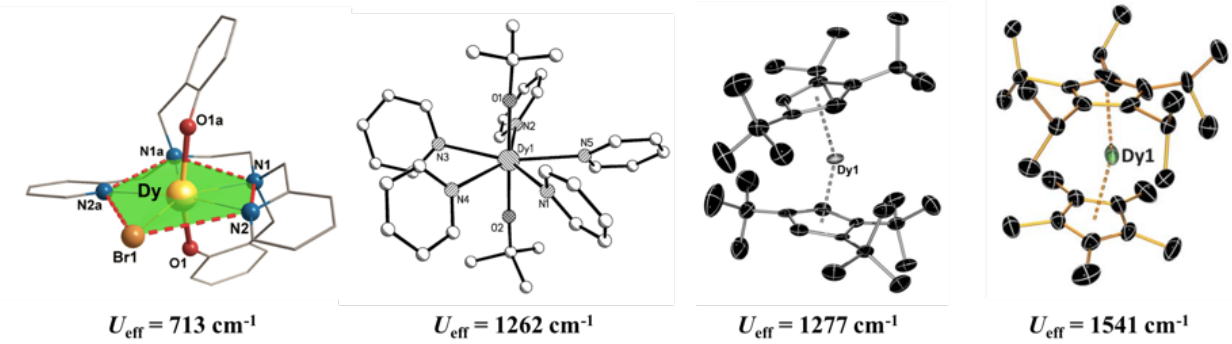

Figure 1.14. Crystal structures of Dy complexes with remarkable energy barriers.[27-29] The non-labelled atoms refer to carbon.

In addition to the requirement of large *D* and *S* values, the magnetic exchange coupling *J* must also be taken into account when designing polynuclear SMMs. It is generally accepted that the diamagnetic linkers provides weak magnetic couplings via an indirect superexchange mechanism, while paramagnetic radical bridges ($S = 1/2$) offer much more stronger and direct interactions between the spin centres due to the direct overlap of the metal-radical orbitals.[30] This strategy has been successfully employed in lanthanide and actinide SMMs,[31] while many transition metal complexes with radical bridges only exhibit strong metal-radical couplings instead of the slow relaxation of magnetisation, and mostly are either mono- or dinuclear structures.

1.3 Lanthanide Luminescence

1.3.1 General concepts of lanthanide

Lanthanide elements display a gradual decrease in ionic radius with increasing atomic number, which is called lanthanide contraction, leading to f-electrons being unable to shield the other valence electrons from the increasing nuclear charge. This is due to the systematically filling of the 4f orbitals with electrons across the lanthanide series. Therefore, the lanthanide elements display similar chemistry. The coordination environment of lanthanide ion is relatively difficult to predict, since the coordination number of the lanthanide ions can vary from two to twelve with different geometries,[32] in which eight and nine are commonly observed in lanthanide complexes. On the other hand, the geometry of lanthanide complexes not only depends on the crystal-field effect but also the ligands.

1.3.2 Luminescence of lanthanide ions

Apart from some useful organic dyes, lanthanides ion are considered as highly luminescent materials because they show advantages across a wide range of emission wavelength distributions

(from visible to near-infrared) with good physical and chemical stabilities. Most of the absorption and emission spectra of lanthanide ions originate from the 4f-4f transition between excited and ground state, which should be formally forbidden by the LaPorte selection rule. Hypersensitive transitions, observed from some characteristic emission peaks, are used to convince the structure and coordination environment of lanthanide complexes.

The emission type for lanthanide complexes relates to the 4f electron and its transitions. The 4f orbitals effectively shielded by the filled $5s^2 5p^6$ orbitals are less affected by external conditions. However, the large spin-orbital coupling constant can result in the splitting of energy level, where the energy gap between the ground state and the lowest excited state can also cause different luminescence. **Figure 1.15** shows the different energy level for lanthanides in aqueous solution.[33] Generally, the 4f-4f transition of lanthanides has three classifications based on the emission characteristics:

(1) Y(III), La(III), Gd(III), and Lu(III). The electronic structure suggests no 4f-4f transition among these ions. Gd(III) emits in the UV region because the lowest excited state is too high to allow an efficient energy transfer.

(2) Sm(III), Eu(III), Dy(III), Tb(III). These ions exhibit strong visible luminescence due to the good match in energy of the ligand triplet and metal excited state levels. The energy transfer efficiency is relatively high.

(3) Pr(III), Nd(III), Er(III), Tm(III), Yb(III). These ions usually have relatively weak luminescence as the small energy gap and high energy density levels that leads to near-infrared emissions.

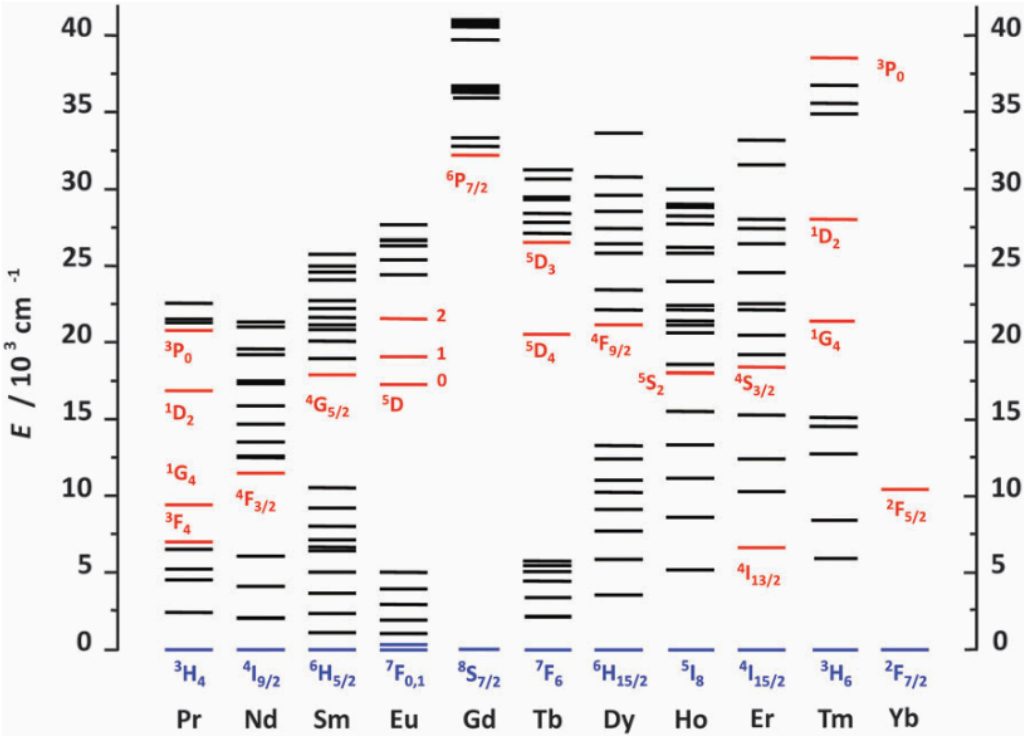

Figure 1.15. Energy level diagram for lanthanide ions in water solution.[33]

The forbidden f-f transfer is so difficult to detect that introducing organic ligands to coordinate with lanthanide ions can improve the optical absorption efficiency for detection, which is defined as antenna effect. The organic ligands can absorb UV light to produce the excited triplet state (T_1) and populate the excited states of Ln centres through intramolecular energy transfer, protecting them from the surroundings to diminish the radiationless deactivation process (**Figure 1.16**). For this reason, effective energy transfer relies on the energy gap between the T_1 state and the emitting level of lanthanide complexes.

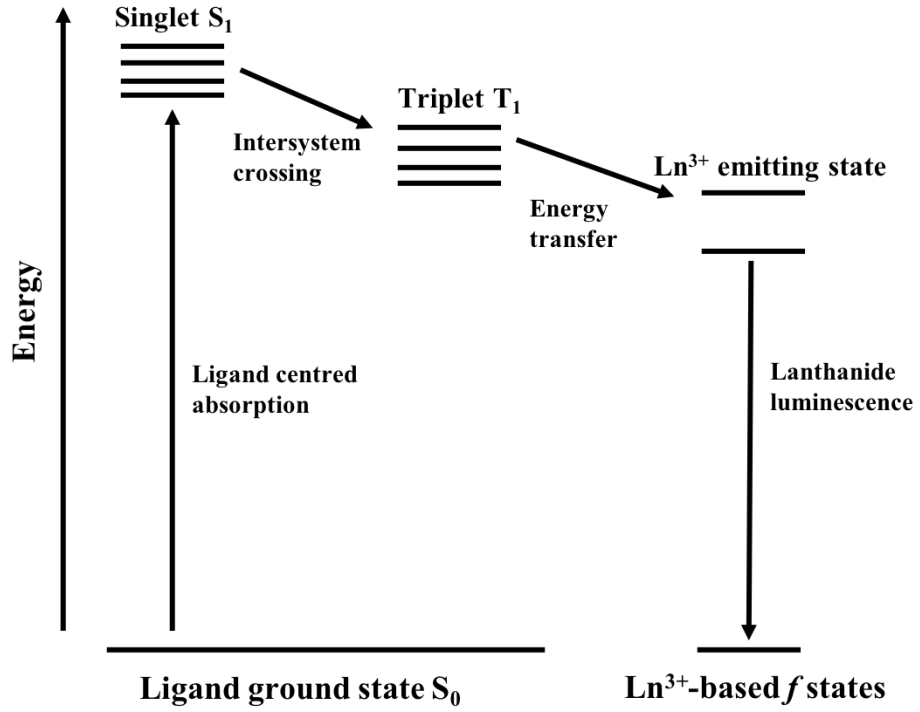

Figure 1.16. Energy transfer diagram from organic ligands to lanthanide ion showing the antenna effect.

The emission efficiency of lanthanide sensitised emission Q_{Ln}^{L} is calculated by $Q_{Ln}^{L} = \eta_{sens} \times Q_{Ln}^{Ln}$. η_{sens} is the efficiency of energy transfer from ligand to lanthanide ions and Q_{Ln}^{Ln} is the quantum yield (Φ) of luminescence complexes, which is calculated by $Q_{Ln}^{Ln} = \frac{\tau_{obs}}{\tau_{rad}}$, where τ_{rad} and τ_{obs} refer to the radiative and observed lifetimes. Lifetimes of lanthanide materials are in a range from nanoseconds to microseconds for near infrared emitted complexes and mostly microseconds for visible emitted complexes, respectively. The efficiency depends on the triplet energy of the organic chromophore and the efficiency of the intersystem crossing from the excited singlet state to the excited triplet state.

1.3.3 Examples of luminescent lanthanide complexes

ß-diketones and some carboxylic acid based ligands are the representative organic ligands and behaves as good antenna in lanthanide complexes. Studies in solid states of Tb-benzonate complexes give an amazing value of 100%, while the recorded quantum yields for Eu^{3+}, Sm^{3+}, Dy^{3+} are 85%, 17% and 19% in their solid states, respectively.[34] In aqueous solution, the overall quantum yields of the lanthanide complexes are relatively small due to possible O-H oscillators for vibrational quenching. The best values for Tb^{3+} is 61% and and Eu^{3+} sits at a range of 20-30%. The less luminescent Sm^{3+} (1%) and Dy^{3+} (3%) complexes are smaller,[35] and it is even more challenging to design the complexes with Pr^{3+}, Ho^{3+}, Tm^{3+} as the largest values obtained for Pr^{3+} only reach 1.3% in $[Pr(hfac)_3(pyrazole)_2]$ (hfac = hexafluoroacetylacetone) complex and are much lower for the other ions. Yb^{3+} complexes achieve the highest quantum yield values of 6.1% which was observed in a deuterated complex $[Yb(tta\text{-}d)_3(DMSO\text{-}d_6)_2]$ (tta = thenoyltrifluoroacetonate) among the NIR-emitting ions because of the large energy gap, while the values for Nd^{3+} complexes ranged between 1-3% in solid state and 0.1-0.5% in solution.

Pikramenou group reported dinuclear Eu^{3+} and Sm^{3+} complexes based on 1,3-bis(3-phenyl-3-oxopropanoyl)benzene (bis-DBM) ligand with simulated triple helix structures.[36] Compared with the mononuclear $[Sm(DBM)_3]$ (DBM = dibenzoylmethane) complex, the efficiency is significantly improved from 1% to 5%. Later crystal structure of a similar complex $[Eu_2(BTB)_3]$ (BTB = 3,3'-bis(4,4,4-trifluoro-1,3-dioxobutyl)biphenyl) was reported where each Eu^{3+} is in a trigondodecahedron geometry.[37] The luminescent signal intensity is 1.33 times higher than $[Eu(BTFA)_3]$ (BTFA = benzoyltrifluoacetone) which is probably due to the structural rigidity.

Some main group or the third row transition metal complexes can act as sensitisers as well because of the low triplet excited states energy and their abilities to strengthen the emission intensity and achieve longer lifetimes. Pecoraro and Petoud et al have developed a series of metallocrown based

lanthanide complexes displaying visible or near-infrared emissions that can be applied in probes, MRI contrasting agents and near-infrared imaging.[38] These molecules are formed by repeating [Metal-N-O] subunits in a manner analogous to classical crown ethers where the oxygen coordination sites can easily bind the lanthanide ions to sensitise lanthanide emission.

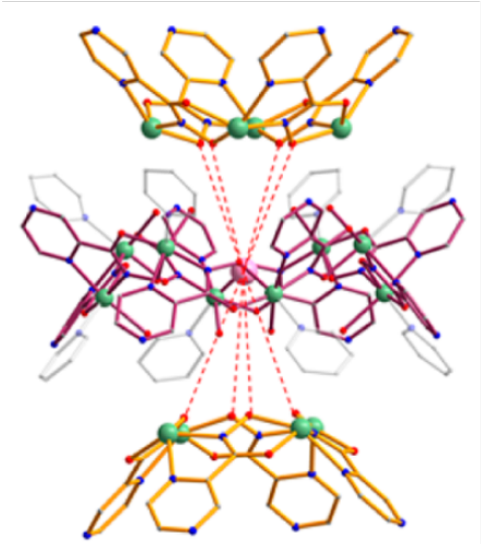

Figure 1.17. An example of a metallocrown based complex $Ln^{3+}[12\text{-}MC_{Zn(II),pyzHA}\text{-}4]_2[24\text{-}MC_{Zn(II),pyzHA}\text{-}8]$ for NIR imaging.[38b] Atom colours: Zn, green; Ln^{3+}, pink; O, red; N, blue; C, yellow and purple.

Acyclic ligands based on polyaminopolycarboxylate systems in which four or more acetic groups are covalently attached to a polyamino skeleton such as ethylendiaminetetraacetic acid (EDTA), tetraazacyclododecanetetraacetic acid (DOTA) or diethylentriaminepentaacetic acid (DTPA) are also important to sensitising lanthanide luminescence. A significant amount of research has been developed based on their good stability and solubility in aqueous medium. Our research group has been interested in DTPA-bisamide derivatives with functional groups for selective reactivity yielding multinuclear, multicolour lanthanide edifices or lanthanide coated nanoparticles (**Figure 1.18**).[39]

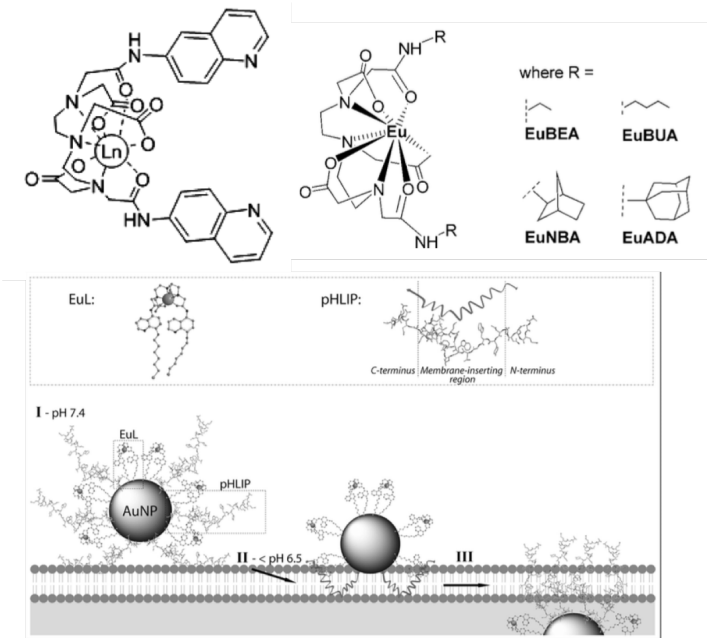

Figure 1.18. Examples of Ln-DTPA complexes and the coating on gold nanoparticles.[39]

1.4 Combination of magnetism and luminescence

Multifunctional molecular materials that combine different physical or chemical properties in one structure have attracted increasing attention and shown applications in catalysis, biomedicine, gas or solvent separations. Of particular interests are the molecular magnetic complexes with additional functions such as luminescence, conductivity and ferroelectricity.[40] Unlike the luminescent complexes that have already been applied in sensors, magnetic resonance imaging and biological assays, molecular magnetic materials are limited in application due to the restrictions from the energy barriers that are too low (normally below liquid nitrogen temperatures) or spin transition temperatures that are not suitable enough to be applied. Moreover, the hysteresis of SCO remains uncommon and unpredictable for use in memorable functions.[41] Recent works combining SMMs or SCO compounds with metal-organic frameworks (MOFs) or nanoparticles have demonstrated precise assemblies and provided additional functions to these molecules.[42]

1.4.1 Luminescent single-molecule magnets

The paramagnetic transition metal ions (Mn, Fe, Co, Ni) generally do not exhibit emission profiles and also quench the luminescence of organic chromophores. Although they are well-employed in SMMs, few complexes show luminescence output. In the pursuit of novel magneto-optical systems, trivalent lanthanide ions with appropriate antenna ligand or luminescent metal centre are ideal candidates to achieve this bi-function.

Tong et al used a blue emissive ligand to synthesis two Dy complexes $[Dy_4(bpt)_4(NO_3)_4(\mu\text{-}OMe)_2(\mu_3\text{-}OH)_2]\cdot 3MeOH$ (bpt = 3,5-bis(pyridin-2-yl)-1,2,4-trizole) in a butterfly core and $[Dy_4(bpt)_4(NO_3)_6(EtOH)_2(\mu\text{-}OH)_2]\cdot 3MeOH$ in a zigzag structure (**Figure 1.19**), which show strong white emission that can be potentially applied in WLEDs.[43] Under a zero DC field, both complexes exhibit slow relaxation of the magnetisation. The first one showed a single relaxation process with an energy barrier of 81 cm^{-1}, while a double relaxation process was observed in the second one with energy barriers of 29 cm^{-1} and 31 cm^{-1}.

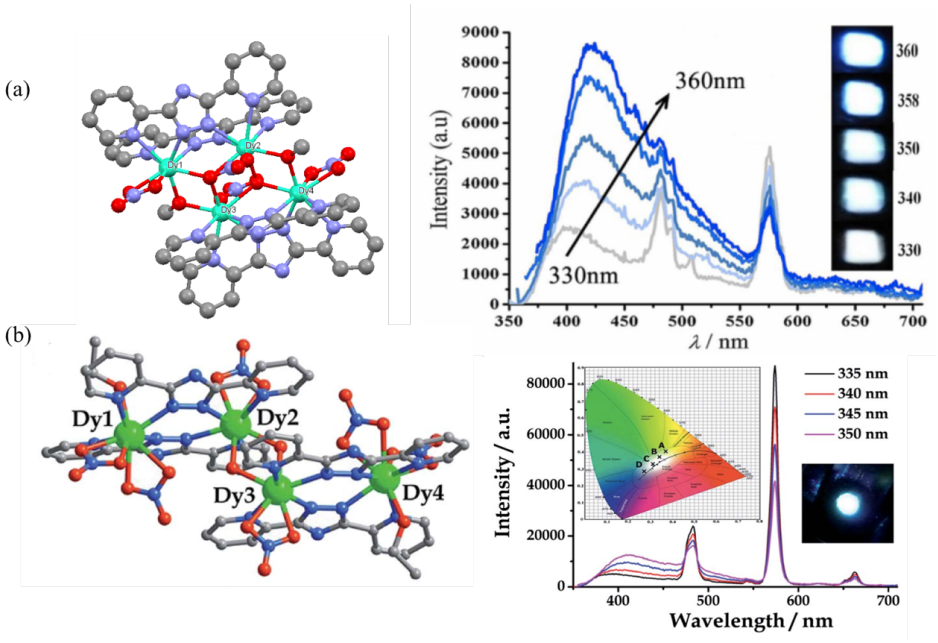

Figure 1.19. Structure and emission spectra of complex $[Dy_4(bpt)_4(NO_3)_4(\mu\text{-}OMe)_2(\mu_3\text{-}OH)_2]\cdot 3MeOH$ (a) and $[Dy_4(bpt)_4(NO_3)_6(EtOH)_2(\mu\text{-}OH)_2]\cdot 3MeOH$ (b).[43]

In the first $DyIr_6$ SMM $[DyIr_6(ppy)_{12}(bpp)_2(bppH)_4](CF_3SO_3)\cdot 8H_2O$ (ppy = 2-phenylpyridine, bpp = 2-pyridylphosphonate, **Figure 1.20**),[44] the Dy^{3+} ion locates in a nearly regular octahedral geometry. Frequency dependent signals can be detected under an 1000 Oe applied DC field, indicating slow magnetic relaxation with an effective anisotropy barrier of 42.9 K. The small anisotropy barrier value is related to the Dy geometry as the strict O_h symmetry is an unfavourable ligand field for Dy-SMM because of the isotropic *g*-tensors. The electronic absorption spectra showed bands at 260 nm attributed to π-π* transitions and a weak absorption tail at 400-480 nm, which is assigned to MLCT transition. The solid state luminescent spectra under excitation at 480 nm gave a broad emission band at 531 nm, indicating the luminescence originates from iridium moieties.

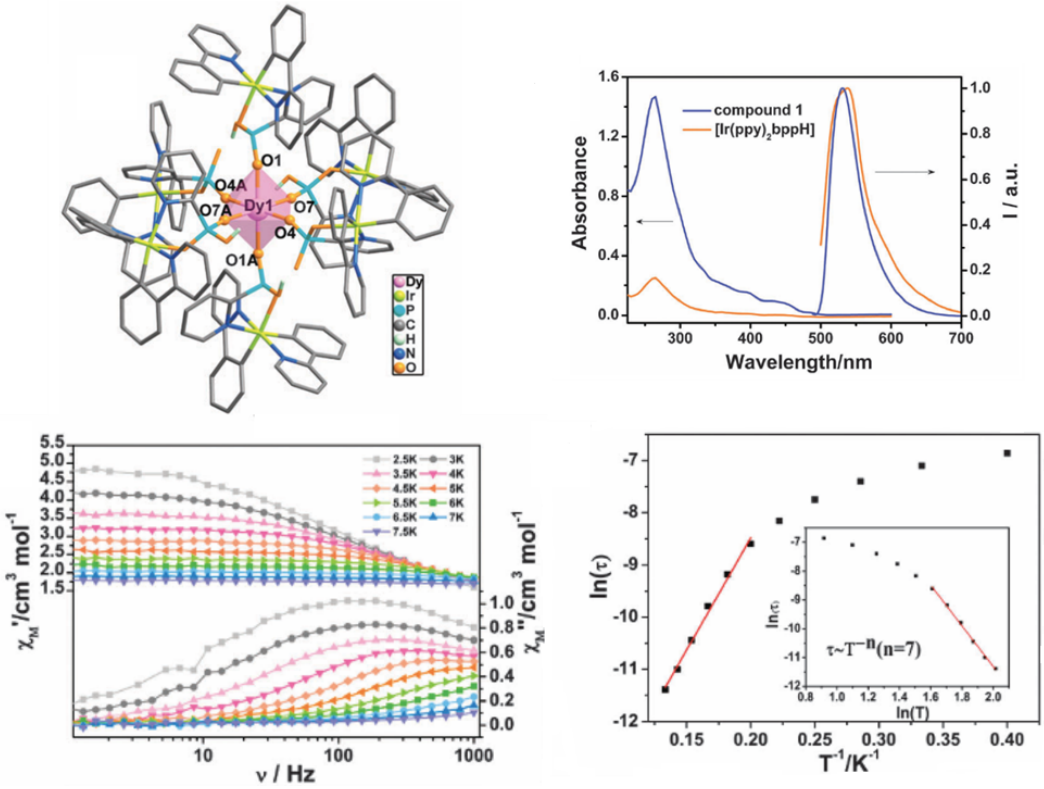

Figure 1.20. Crystal structure, absorption and solid state emission spectra, ac measurement and ln τ vs. T^{-1} plots for $DyIr_6$.[44]

As research into this field grows, the studies of luminescence on lanthanide complexes can also give information of magnetic levels, suggesting a correlation between luminescence and SMM behaviour. The chosen lanthanide ion is crucial because the ion should present a large magnetic moment and magnetic anisotropy to achieve molecular architectures with high energy barriers for the reversal of magnetisation. In addition, they should exhibit well-resolved emission spectra with a long lifetimes.[45] This is the reason why Dy^{3+}, Tb^{3+}, Er^{3+}, and Yb^{3+} ions are the most commonly employed. Meanwhile, the ligands design is still of challenge since they will dictate the coordination environment that is suitable to create a slow relaxation of the magnetisation and the simultaneous sensitisation of the Ln^{3+} ion, to enhance the luminescence efficiency.

The first demonstration of the correlation between the relaxation dynamics and emission was conducted in 2012 in a DyDOTA complex.[46] The value of separation of the energy levels for $^4F_{9/2}$ $^6H_{15/2}$, 53 cm^{-1}, is slightly higher than the energy barrier (42 cm^{-1}) obtained from dynamic magnetic measurements, indicating a weak QTM was involved. Later, an inductive effect between the magnetic field and luminescence has shown in $[CsDy(8\text{-mCND})_4(CH_3OH)(Me_2CO)]_2 \cdot 2Me_2CO$ (8-mCND = 4-hydroxy-8-methyl-1,5-naphthyridine-3-carbonitrile) (**Figure 1.21** a).[47] The complex, under a magnetic field that was pulsed in increasing intervals to 36 T, indicated that the Zeeman splitting occurred at 26 T can induce a separated emission peaks, giving an energy difference value of 100 cm^{-1} between two energy sublevels, ground Kramers doublets state and first excited Kramers doublets state, which is close to the calculated energy gap (90 cm^{-1}) from the emission spectrum under a zero DC field and energy barrier (93 cm^{-1}) from the AC measurement at 1000 Oe applied DC field. Similar study on $[Dy(CyPh_2PO)_2(H_2O)_5]Br_3 \cdot 2CyPh_2PO \cdot EtOH \cdot 3H_2O$ ($CyPh_2PO$ = cyclohexyl(diphenyl)phosphine oxide) complex have also given the energy gap value of 322 cm^{-1} within the range of 353 cm^{-1} and 297 cm^{-1} extracted from ac susceptibilities and *ab initio* calculations (**Figure 1.21** b).[48] The difference between the two values might be due to the precision of luminescent

spectra, different relaxation processes and the magnetic effect on the luminescence. In addition, research on lanthanide SMMs in luminescent molecular thermometers has emerged in recent years, realising this through Dy, Yb and Ho complexes with efficient thermal sensitivities.[49]

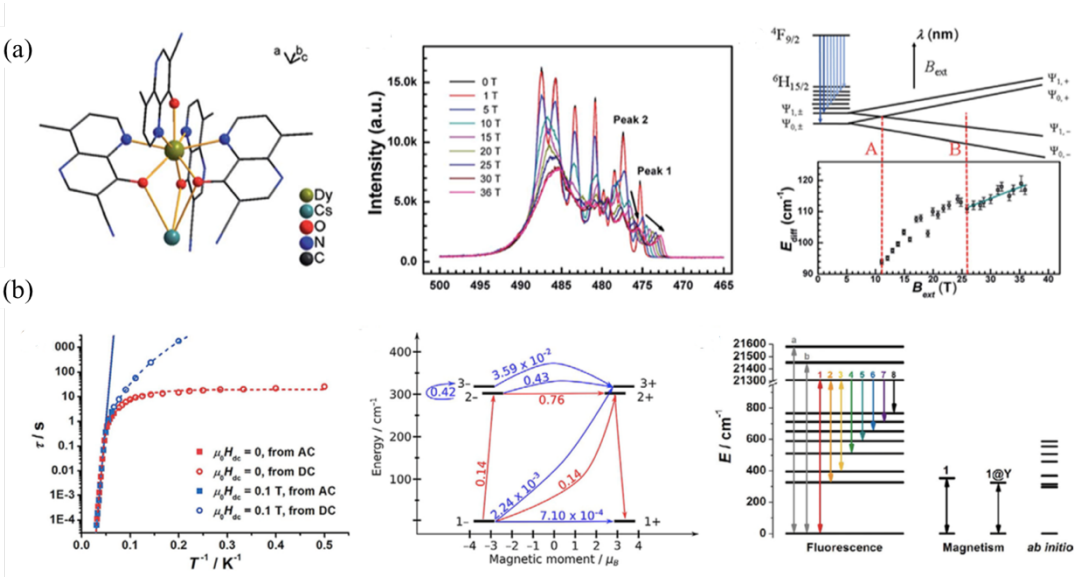

Figure 1.21. (a) Structure, luminescence spectrum under a pulsed magnetic field and diagram for energy splitting by Zeeman effect for $[CsDy(8\text{-}mCND)_4(CH_3OH)(Me_2CO)]_2 \cdot 2Me_2CO$.[47] (b) Temperature dependence graph of relaxation time in zero and 0.1 T dc field, magnetic blocking barrier with probable relaxation route and energy levels determined by fluorescence spectra compared with magnetic energy barrier and *ab initio* calculations for $[Dy(CyPh_2PO)_2(H_2O)_5]Br_3 \cdot 2CyPh_2PO \cdot EtOH \cdot 3H_2O$.[48]

1.4.2 Synergy between spin crossover and luminescence

The construction of luminescent SCO complexes has received considerable attentions due to the possibility of tuning the luminescence signal or detecting physicochemical changes, which may extend the SCO-based applications, particularly as magneto-optical switches. The potential difference in luminescence signal could be explained by energy transfer from the excited energy donor to the low-spin SCO complex leads to the quenching of donor emission, while in the high-spin

SCO complex the donor luminescence is retained due to the reduced spectral overlap between the donor emission and high-spin acceptor absorption.[50]

Two synthetic considerations may be involved in terms of designing luminescent SCO complexes: combining a luminophore with SCO centres into a single entity and doping luminescent entities (metal ions, molecules, etc.) into a SCO material. In 2011 the first structurally characterised SCO–fluorescent dinuclear Fe^{II} complex showed variable emissions at different temperatures (**Figure 1.22** top).[51] Recent approaches have demonstrated the synergy between SCO and luminescence where an abrupt increase of luminescence intensity occurred when switching to high-spin.[52] Highly emissive organic ligands, such as naphthalene, anthracene, rhodamine derivatives, are often applied in this stage. Kou et al used rhodamine 6G-labeled pyridyl aroylhydrazone ligand in a mononuclear Fe complex showing three-step SCO upon heating and a 40 K hysteresis after desolvation exceeding 300 K.[53] The complex exhibited ligand-centred red emission from the rhodamine centre. Temperature-dependent luminescence spectra between clearly demonstrate a synergy that the luminescence intensity is influenced by SCO process and the emission can be quenched by the low-spin Fe(II) entity (**Figure 1.22** bottom). This discovery has also been extended to SCO polymers.[54] A spin-crossover coordination polymer $[Fe\text{-}(L)(bipy)]_n$ (where L = a $N_2O_2^{2-}$ coordinating Schiff base-like ligand bearing a phenazine fluorophore and bipy = 4,4′-bipyridine) exhibited a 48 K wide thermal hysteresis above room temperature ($T_{1/2}\uparrow$ = 371 K and $T_{1/2}\downarrow$= 323 K).[55] The polymer showed two emission peaks under 337 excitation. The photoluminescence intensities of the ratio tracked well with the magnetic susceptibility, indicating that the SCO can be tracked by using fluorescence spectroscopy. Although the results have been fruitful, exhibiting the good combinations, the majority still display no correlation between spin state and luminescence.

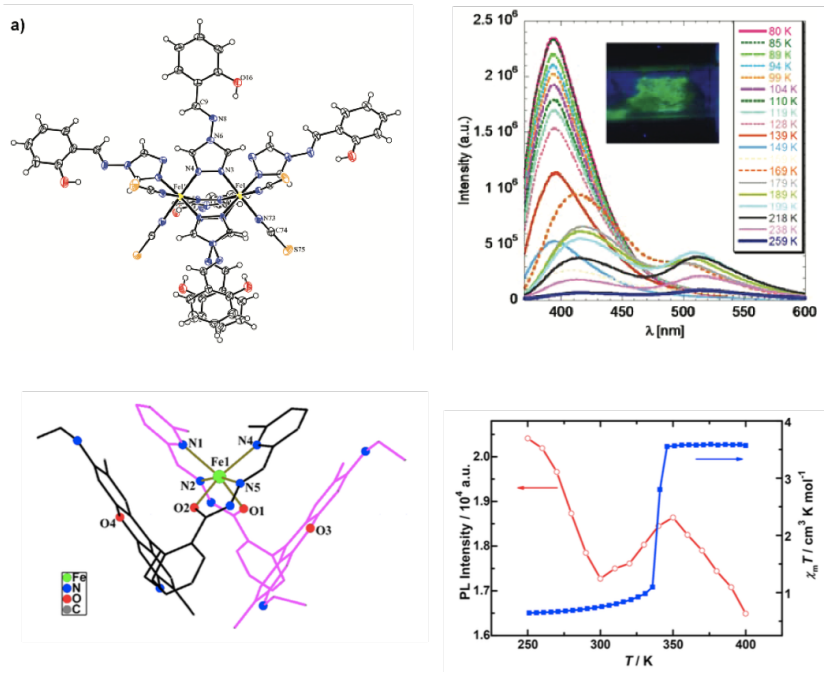

Figure 1.22. Top: Crystal structure and luminescent spectra at different temperatures of a dinuclear Fe complex with *N*-salicylidene-4-amino-1,2,4-triazole ligand.[51] Bottom: Crystal structure and synergy of photoluminescence intensity and magnetic susceptibility of a Fe complex based on a ring-opened rhodamine 6G hydrazone ligand.[53]

1.5 Thesis outline

The aim of this thesis is to design and synthesise multinuclear transition metal and lanthanide complexes to study the magnetic and luminescent properties using supramolecular self-assembly approach, containing the work in both SUSTech and UoB. The results in each chapter will be presented in journal format that are suitable for publication or published manuscript.

Bis-bidentate 3,6-substituted pyridazine ligands pzdz and pydz are introduced in ***Chapter 2*** and ***Chapter 3*** together with versatile azido bridge for the design of tetranuclear Co and Fe complexes. Magnetic studies shows the Co complexes behave as typical field-induced SMMs, while the substitution effect of pyridyl and pyrazoyl is studied in Fe_4 complexes leading to different magnetic performance.

In ***Chapter 4*** and ***Chapter 5***, radical formation of 3,6-subustituted 1,2,4,5-tetrazine ligands bpztz and bptz are adapted in tetranuclear azido-bridged cobalt complexes, respectively. Despite the maintenance of similar tetranuclear architectures, the magnetic interactions between metal and radical are also investigated to compared with the neutral pyridazine bridges. Interestingly, mixed-valence cobalt complexes are successfully isolated and crystallised using the redox active bptz ligand in ***Chapter 5***.

Chapter 6 focuses on the assembly of heterometallic dinuclear lanthanide complexes using an imidodiphosphonate ligand in solution. Significant energy transfer between lanthanide ions are observed.

Lanthanide complexes based on a novel DTPA-bisamide derivative with terpyridine arms are synthesised in ***Chapter 7***. Photophysical studies of the complexes demonstrated the efficient sensitisation of lanthanide ions. In addition, the heterometallic 3d-4f assembly of Eu_2Fe_2 is also studied in solution.

Chapter 8 contains the concluding remarks and future work.

1.6 References

1. N. F. Chilton, R. P. Anderson, L. D. Turner, A. Soncini and K. S. Murray, *J. Comput. Chem.*, 2013, **34**, 1164-1175.
2. L. Cambi and L. Szegö, *Ber. Dtsch. Chem. Ges.*, 1931, **64**, 2591-2598.
3. (a) E. Koenig and K. Madeja, *Inorg. Chem.*, 1967, **6**, 48-55; (b) R. C. Stoufer, D. H. Busch and W. B. Hadley, *J. Am. Chem. Soc.*, 1961, **83**, 3732-3734.
4. I. Šalitroš, N. T. Madhu, R. Boča, J. Pavlik and M. Ruben, *Monatsh Chem*, 2009, **140**, 695-733.
5. (a) S. Decurtins, P. Gütlich, C. P. Köhler, H. Spiering and A. Hauser, *Chem. Phys. Lett.*, 1984, **105**, 1-4; (b) J. J. McGravey and I. Lawthers, *J. Chem. Soc., Chem. Commun.*, 1982, 906-907.

6. G. Chastanet, M. Lorenc, R. Bertoni and C. Desplanches, *C. R. Chim.*, 2018, **21**, 1075-1094.

7. G. Chastanet, C. Desplanches, C. Baldé, P. Rosa, M. Marchivie and P. Guionneau, *Chem. Sq.*, 2018, **2**, 2.

8. J.-F. Létard, L. Capes, G. Chastanet, N. Moliner, S. Létard, J.-A. Real and O. Kahn, *Chem. Phys. Lett.*, 1999, **313**, 115-120.

9. S. Hayami, Z.-z. Gu, Y. Einaga, Y. Kobayasi, Y. Ishikawa, Y. Yamada, A. Fujishima and O. Sato, *Inorg. Chem.*, 2001, **40**, 3240-3242.

10. (a) Y.-S. Meng and T. Liu, *Acc. Chem. Res.*, 2019, **52**, 1369-1379; (b) H.-Y. Sun, Y.-S. Meng and T. Liu, *Chem. Commun.*, 2019, **55**, 8359-8373.

11. Y. Zhang, D. Li, R. Clérac, M. Kalisz, C. Mathonière and S. M. Holmes, *Angew. Chem. Int. Ed.*, 2010, **49**, 3752-3756.

12. (a) C. Mathonière, *Eur. J. Inorg. Chem.*, 2018, **2018**, 248-258; (b) R. Podgajny, S. Chorazy, W. Nitek, M. Rams, A. M. Majcher, B. Marszałek, J. Żukrowski, C. Kapusta and B. Sieklucka, *Angew. Chem. Int. Ed.*, 2013, **52**, 896-900; (c) M. L. Baker, S.-Q. Wu, S. Kang, S. Matsuzawa, M.-A. Arrio, Y. Narumi, T. Kihara, T. Nakamura, Y. Kotani, O. Sato and H. Nojiri, *Inorg. Chem.*, 2019, **58**, 10160-10166; (d) J.-R. Jiménez, J. Glatz, A. Benchohra, G. Gontard, L.-M. Chamoreau, J.-F. Meunier, A. Bousseksou and R. Lescouëzec, *Angew. Chem. Int. Ed.*, 2020, **59**, 8089-8093.

13. T. Tezgerevska, K. G. Alley and C. Boskovic, *Coord. Chem. Rev.*, 2014, **268**, 23-40.

14. (a) A. Lannes, Y. Suffren, J. B. Tommasino, R. Chiriac, F. Toche, L. Khrouz, F. Molton, C. Duboc, I. Kieffer, J.-L. Hazemann, C. Reber, A. Hauser and D. Luneau, *J. Am. Chem. Soc.*, 2016, **138**, 16493-16501; (b) S. Kanegawa, Y. Shiota, S. Kang, K. Takahashi, H. Okajima, A. Sakamoto, T. Iwata, H. Kandori, K. Yoshizawa and O. Sato, *J. Am. Chem. Soc.*, 2016, **138**, 14170-14173; (c) S.-Q. Wu, M. Liu, K. Gao, S. Kanegawa, Y. Horie, G. Aoyama, H. Okajima,

A. Sakamoto, M. L. Baker, M. S. Huzan, P. Bencok, T. Abe, Y. Shiota, K. Yoshizawa, W. Xu, H.-Z. Kou and O. Sato, *Nat. Commun.*, 2020, **11**, 1992; (d) N. Bonanno, Z. Watts, C. Mauws, B. O. Patrick, C. Wiebe, Y. Shibano, K. Sugisaki, H. Matsuoka, D. Shiomi, K. Sato, T. Takui and M. Lemaire, *Chem. Commun.*, 2021, **57**, 6213-6216.

15. O. Drath and C. Boskovic, *Coord. Chem. Rev.*, 2018, **375**, 256-266.
16. D. G. R. Sessoli, A. Caneschi & M. A. Novak, *Nature*, 1993, **365**, 141-143.
17. S. Gomez-Coca, E. Cremades, N. Aliaga-Alcalde and E. Ruiz, *J. Am. Chem. Soc.*, 2013, **135**, 7010-7018.
18. (a) M. Murrie, *Chem. Soc. Rev.*, 2010, **39**, 1986-1995; (b) Y.-Y. Zhu, C. Cui, Y.-Q. Zhang, J.-H. Jia, X. Guo, C. Gao, K. Qian, S.-D. Jiang, B.-W. Wang, Z.-M. Wang and S. Gao, *Chem. Sci.*, 2013, **4**, 1802-1806; (c) S. Vaidya, A. Upadhyay, S. K. Singh, T. Gupta, S. Tewary, S. K. Langley, J. P. S. Walsh, K. S. Murray, G. Rajaraman and M. Shanmugam, *Chem. Commun.*, 2015, **51**, 3739-3742; (d) Y. Rechkemmer, F. D. Breitgoff, M. van der Meer, M. Atanasov, M. Hakl, M. Orlita, P. Neugebauer, F. Neese, B. Sarkar and J. van Slageren, *Nat. Commun.*, 2016, **7**, 10467; (e) Y.-Z. Zhang, S. Gómez-Coca, A. J. Brown, M. R. Saber, X. Zhang and K. R. Dunbar, *Chem. Sci.*, 2016, **7**, 6519-6527; (f) P. C. Bunting, M. Atanasov, E. Damgaard-Møller, M. Perfetti, I. Crassee, M. Orlita, J. Overgaard, J. van Slageren, F. Neese and J. R. Long, *Science*, 2018, **362**, eaat7319; (g) A. K. Mondal, J. Jover, E. Ruiz and S. Konar, *Dalton Trans.*, 2019, **48**, 25-29.
19. X.-N. Yao, J.-Z. Du, Y.-Q. Zhang, X.-B. Leng, M.-W. Yang, S.-D. Jiang, Z.-X. Wang, Z.-W. Ouyang, L. Deng, B.-W. Wang and S. Gao, *J. Am. Chem. Soc.*, 2017, **139**, 373-380.
20. K. Chakarawet, P. C. Bunting and J. R. Long, *J. Am. Chem. Soc.*, 2018, **140**, 2058-2061.
21. N. Ishikawa, M. Sugita, T. Ishikawa, S.-y. Koshihara and Y. Kaizu, *J. Am. Chem. Soc.*, 2003, **125**, 8694-8695.

22. D. N. Woodruff, R. E. P. Winpenny and R. A. Layfield, *Chem. Rev.*, 2013, **113**, 5110-5148.

23. L. Ungur and L. F. Chibotaru, *Phys. Chem. Chem. Phys.*, 2011, **13**, 20086-20090.

24. J. D. Rinehart and J. R. Long, *Chem. Sci.*, 2011, **2**, 2078-2085.

25. P. Zhang, L. Zhang, C. Wang, S. Xue, S.-Y. Lin and J. Tang, *J. Am. Chem. Soc.*, 2014, **136**, 4484-4487.

26. J.-L. Liu, Y.-C. Chen, Y.-Z. Zheng, W.-Q. Lin, L. Ungur, W. Wernsdorfer, L. F. Chibotaru and M.-L. Tong, *Chem. Sci.*, 2013, **4**, 3310-3316.

27. (a) Y.-C. Chen, J.-L. Liu, L. Ungur, J. Liu, Q.-W. Li, L.-F. Wang, Z.-P. Ni, L. F. Chibotaru, X.-M. Chen and M.-L. Tong, *J. Am. Chem. Soc.*, 2016, **138**, 2829-2837; (b) J. Liu, Y.-C. Chen, J.-L. Liu, V. Vieru, L. Ungur, J.-H. Jia, L. F. Chibotaru, Y. Lan, W. Wernsdorfer, S. Gao, X.-M. Chen and M.-L. Tong, *J. Am. Chem. Soc.*, 2016, **138**, 5441-5450.

28. (a) Y.-S. Ding, N. F. Chilton, R. E. P. Winpenny and Y.-Z. Zheng, *Angew. Chem. Int. Ed.*, 2016, **128**, 16305-16308; (b) F.-S. Guo, B. M. Day, Y.-C. Chen, M.-L. Tong, A. Mansikkamäki and R. A. Layfield, *Angew. Chem. Int. Ed.*, 2017, **56**, 11445-11449.

29. F.-S. Guo, B. M. Day, Y.-C. Chen, M.-L. Tong, A. Mansikkamäki and R. A. Layfield, *Science*, 2018, **362**, 1400.

30. (a) C. Benelli and D. Gatteschi, *Chem. Rev.*, 2002, **102**, 2369-2388; (b) S. Demir, I.-R. Jeon, J. R. Long and T. D. Harris, *Coord. Chem. Rev.*, 2015, **289-290**, 149-176; (c) K. E. Preuss, *Coord. Chem. Rev.*, 2015, **289-290**, 49-61.

31. (a) J. T. Coutinho, M. A. Antunes, L. C. J. Pereira, J. Marçalo and M. Almeida, *Chem. Commun.*, 2014, **50**, 10262-10264; (b) B. S. Dolinar, S. Gómez-Coca, D. I. Alexandropoulos and K. R. Dunbar, *Chem. Commun.*, 2017, **53**, 2283-2286; (c) G. Brunet, M. Hamwi, M. A. Lemes, B. Gabidullin and M. Murugesu, *Commun. Chem.*, 2018, **1**, 88; (d) B. S. Dolinar, D. I. Alexandropoulos, K. R. Vignesh, T. A. James and K. R. Dunbar, *J. Am. Chem. Soc.*, 2018, **140**,

908-911; (e) X. Meng, W. Shi and P. Cheng, *Coord. Chem. Rev.*, 2019, **378**, 134-150; (f) Z. Zhu, M. Guo, X.-L. Li and J. Tang, *Coord. Chem. Rev.*, 2019, **378**, 350-364.

32. S. B. Humphrey L.C. Feltham, *Coord. Chem. Rev.*, 2014, **276**, 1-33.
33. D. E. Barry, D. F. Caffrey and T. Gunnlaugsson, *Chem. Soc. Rev.*, 2016, **45**, 3244-3274.
34. J.-C. G. Bünzli, *Coord. Chem. Rev.*, 2015, **293-294**, 19-47.
35. S. Petoud, S. M. Cohen, J.-C. G. Bünzli and K. N. Raymond, *J. Am. Chem. Soc.*, 2003, **125**, 13324-13325.
36. A. P. Bassett, S. W. Magennis, P. B. Glover, D. J. Lewis, N. Spencer, S. Parsons, R. M. Williams, L. D. Cola and Z. Pikramenou, *J. Am. Chem. Soc.*, 2004, **126**, 9413-9424.
37. H.-F. Li, P.-F. Yan, P. Chen, Y. Wang, H. Xu and G.-M. Li, *Dalton Trans.*, 2012, **41**, 900-907.
38. (a) H. Uh and S. Petoud, *C. R. Chim.*, 2010, **13**, 668-680; (b) I. Martinić, S. V. Eliseeva, T. N. Nguyen, V. L. Pecoraro and S. Petoud, *J. Am. Chem. Soc.*, 2017, **139**, 8388-8391; (c) C. Y. Chow, S. V. Eliseeva, E. R. Trivedi, T. N. Nguyen, J. W. Kampf, S. Petoud and V. L. Pecoraro, *J. Am. Chem. Soc.*, 2016, **138**, 5100-5109.
39. (a) D. J. Lewis, F. Moretta, A. T. Holloway and Z. Pikramenou, *Dalton Trans.*, 2012, **41**, 13138-13146; (b) A. Davies, D. J. Lewis, S. P. Watson, S. G. Thomas and Z. Pikramenou, *Proc. Natl. Acad. Sci. U. S. A.*, 2012, **109**, 1862; (c) L. L. Ruston, G. M. Robertson and Z. Pikramenou, *Chem. Asian. J.*, 2010, **5**, 571-580; (d) D. J. Lewis, T. M. Day, J. V. MacPherson and Z. Pikramenou, *Chem. Commun.*, 2006, 1433-1435.
40. J. Long, Y. Guari, R. A. S. Ferreira, L. D. Carlos and J. Larionova, *Coord. Chem. Rev.*, 2018, **363**, 57-70.
41. S. Brooker, *Chem. Soc. Rev.*, 2015, **44**, 2880-2892.
42. (a) M. Mannini, F. Bertani, C. Tudisco, L. Malavolti, L. Poggini, K. Misztal, D. Menozzi, A. Motta, E. Otero, P. Ohresser, P. Sainctavit, G. G. Condorelli, E. Dalcanale and R. Sessoli, *Nat.*

Commun., 2014, **5**, 4582; (b) R. Torres-Cavanillas, R. Sanchis-Gual, J. Dugay, M. Coronado-Puchau, M. Giménez-Marqués and E. Coronado, *Adv. Mater.*, 2019, **31**, 1900039; (c) A. E. Thorarinsdottir and T. D. Harris, *Chem. Rev.*, 2020, **120**, 8716-8789; (d) C. Göbel, C. Hils, M. Drechsler, D. Baabe, A. Greiner, H. Schmalz and B. Weber, *Angew. Chem. Int. Ed.*, 2020, **59**, 5765-5770; (e) G. Mínguez Espallargas and E. Coronado, *Chem. Soc. Rev.*, 2018, **47**, 533-557.

43. P.-H. Guo, Y. M. Meng, Y.-C. Chen, Q.-W. Li, B.-Y. Wang, J.-D. Leng, D.-H. Bao, J.-H. Jia and M.-L. Tong, *J. Mater. Chem. C*, 2014, **2**, 8858-8864.

44. D. Zeng, M. Ren, S.-S. Bao, L. Li and L.-M. Zheng, *Chem. Commun.*, 2014, **50**, 8356-8359.

45. J.-H. Jia, Q.-W. Li, Y.-C. Chen, J.-L. Liu and M.-L. Tong, *Coord. Chem. Rev.*, 2019, **378**, 365-381.

46. G. Cucinotta, M. Perfetti, J. Luzon, M. Etienne, P.-E. Car, A. Caneschi, G. Calvez, K. Bernot and R. Sessoli, *Angew. Chem. Int. Ed.*, 2012, **51**, 1606-1610.

47. Y. Bi, C. Chen, Y.-F. Zhao, Y.-Q. Zhang, S.-D. Jiang, B.-W. Wang, J.-B. Han, J.-L. Sun, Z.-Q. Bian, Z.-M. Wang and S. Gao, *Chem. Sci.*, 2016, **7**, 5020-5031.

48. Y.-C. Chen, J.-L. Liu, Y. Lan, Z.-Q. Zhong, A. Mansikkamäki, L. Ungur, Q.-W. Li, J.-H. Jia, L. F. Chibotaru, Han Jun-Bo, W. Wernsdorfer, X.-M. Chen and M.-L. Tong, *Chem. Eur. J.*, 2017, **23**, 5708-5715.

49. (a) D. Errulat, R. Marin, D. A. Gálico, K. L. M. Harriman, A. Pialat, B. Gabidullin, F. Iikawa, O. D. D. Couto, J. O. Moilanen, E. Hemmer, F. A. Sigoli and M. Murugesu, *ACS Central Science*, 2019, **5**, 1187-1198; (b) J. Wang, J. J. Zakrzewski, M. Zychowicz, V. Vieru, L. F. Chibotaru, K. Nakabayashi, S. Chorazy and S.-i. Ohkoshi, *Chem. Sci.*, 2021, **12**, 730-741; (c) J. Wang, J. J. Zakrzewski, M. Heczko, M. Zychowicz, K. Nakagawa, K. Nakabayashi, B. Sieklucka, S. Chorazy and S.-i. Ohkoshi, *J. Am. Chem. Soc.*, 2020, **142**, 3970-3979.

50. K. Senthil Kumar and M. Ruben, *Coord. Chem. Rev.*, 2017, **346**, 176-205.

51. Y. Garcia, F. Robert, A. D. Naik, G. Zhou, B. Tinant, K. Robeyns, S. Michotte and L. Piraux, *J. Am. Chem. Soc.*, 2011, **133**, 15850-15853.

52. (a) Y. Jiao, J. Zhu, Y. Guo, W. He and Z. Guo, *J. Mater. Chem. C*, 2017, **5**, 5214-5222; (b) C.-F. Wang, G.-Y. Yang, Z.-S. Yao and J. Tao, *Chem. Eur. J.*, 2018, **24**, 3218-3224; (c) J.-L. Wang, Q. Liu, Y.-S. Meng, X. Liu, H. Zheng, Q. Shi, C.-Y. Duan and T. Liu, *Chem. Sci.*, 2018, **9**, 2892-2897.

53. J. Yuan, S.-Q. Wu, M.-J. Liu, O. Sato and H.-Z. Kou, *J. Am. Chem. Soc.*, 2018, **140**, 9426-9433.

54. C. Lochenie, K. Schötz, F. Panzer, H. Kurz, B. Maier, F. Puchtler, S. Agarwal, A. Köhler and B. Weber, *J. Am. Chem. Soc.*, 2018, **140**, 700-709.

55. J.-Y. Ge, Z. Chen, L. Zhang, X. Liang, J. Su, M. Kurmoo and J.-L. Zuo, *Angew. Chem. Int. Ed.*, 2019, **58**, 8789-8793.

Chapter 2

Two Azido-Bridged [2 × 2] Cobalt(II) Grids Featuring Single-Molecule Magnet Behaviours

Zhilin Guo, Yi-Fei Deng, Yipei Zhang, Zoe Pikramenou and Yuan-Zhu Zhang.

A version of this manuscript has been accepted for publication in *Dalton Transactions*.

Reproduced from *Dalton Trans.* 2020, **49**, 9218-9222 with permission from Royal Society of Chemistry.

2.1 Abstract

The self-assembly of Co(II) salts, pyridazine derivatives and azides afforded two azido-bridged [2 × 2] grid-type complexes $\{[(L)_4Co^{II}_4(N_3)_4][BPh_4]_4\}\cdot sol$ (**1**, L = 3,6-bis(3,5-dimethyl-1H-pyrazol-1-yl)pyridazine (pzdz) and sol = $4CH_3CN\cdot 3CHCl_3\cdot 2CH_3OH$ and **2**, L = 3,6-di(pyridin-2-yl)pyridazine (pydz) and sol = $4CH_3CN$). Upon comparison with other related grid-like complexes, the incorporation of end-on azido-bridges resulted in overall intramolecular ferromagnetic couplings, and thus endowed complexes **1** and **2** single-molecule magnet behaviour with field-induced slow magnetic relaxation.

2.2 Introduction

Coordination-driven self-assembly[1] has provided an important strategy in supramolecular chemistry for the synthesis of aesthetical molecular architectures that could exhibit unique physicochemical properties associated with potential applications including catalysis, sensors and electronic devices, etc.[2] The assembly of supramolecular components is dominated by the coordination demand of metal ions together with the coding imposed by particular functional groups of ligands to yield a desired molecular topology, such as grid,[3] polyhedron,[4] cube,[5] etc. For example, the principal requirement for grid formation underlines the presence of the parallel coordination sites of the ligands being utilised to bind the adjacent metal atoms. Furthermore, the incorporation of appropriate bridging linkers is also of significant importance to physical properties, such as magnetic exchange coupling, which is necessary for cluster-based single-molecule magnets (SMMs).[6]

Pyrazolyl- or pyridyl-substituted pyridazine derivatives with parallel coordination sites (**Figure 2.1**) are attractive functional ligands, which indeed have contributed to a series of popular grid-like complexes through the self-assembly process, mainly focusing on the diamagnetic Cu(I), Ag(I) or

Zn(II) species.[7] However, the pyridazine-based grids involving the paramagnetic metal centres did not show interesting magnetic properties such as slow relaxation dynamics; one reason might be the diminished or quenched spin ground state that originated from the intramolecular antiferromagnetic exchange through the diazine bridges. In a well-studied representative $[Co^{II}]_4$ square complex where Co^{II} ions are arranged at the corners via oxygen bridges, overall intramolecular ferromagnetic coupling and typical SMM behaviour were observed.[8] More recently, another square-like tetranuclear Co-based SMM was reported with an effective energy barrier (U_{eff}) up to 87 cm^{-1}, the largest reported to date for a transition metal cluster.[9] Such results and related studies have demonstrated that the ferromagnetic arrangement of anisotropic metal centres may be a neat strategy to design SMMs, for which Co(II) ions are selected due to their appreciable spin–orbit coupling (SOC) with variable zero-field splitting (zfs) parameters from -161 cm^{-1} to +118 cm^{-1}.[10] In addition, the "end-on" (EO) azido bridges have been found to be effective for mediating ferromagnetic couplings and are thus applied for constructing SMMs or single chain magnets.[11] It is worth mentioning that the EO-azido bridges were successfully introduced into a pyridazine-based square compound while no magnetic data were reported.[7h]

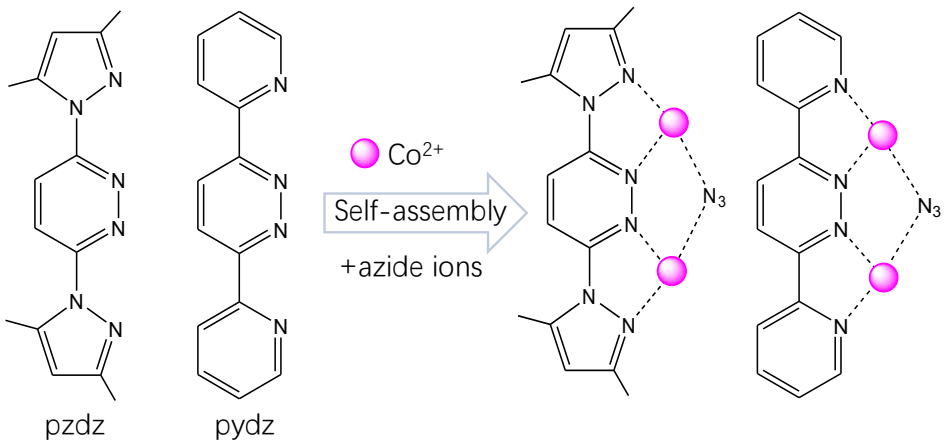

Figure 2.1. The structures of selected pyridazine derivatives and their proposed coordination modes.

In light of the aforementioned considerations, in this chapter, two pyridazine derivatives pzdz and pydz are introduced as the functional ligands with the incorporation of azide ions as the secondary bridges and constructed two [2 × 2] grid-like Co(II) clusters $\{[(L)_4Co^{II}_4(N_3)_4][BPh_4]_4\}\cdot sol$ (**1**, L = pzdz, sol = $4CH_3CN\cdot 3CHCl_3\cdot 2CH_3OH$; **2**, L = pydz, sol = $4CH_3CN$). Remarkably, the overall intramolecular ferromagnetic couplings that benefited from the end-on azido bridges were observed in complexes **1** and **2**, whilst both complexes behaved as single-molecule magnets with field-induced slow magnetic relaxation and effective energy barriers of 36 and 56 K.

2.3 Contribution

I prepared Co complexes and performed the characterisations and magnetic measurements. Co-authors are acknowledged: Yipei Zhang helped with the initial synthesis of pzdz ligand. Dr Yi-Fei Deng helped with the fitting of magnetic data. I wrote the draft manuscript which was then revised by Dr Deng, Prof. Pikramenou and Dr Zhang.

2.4 Experimental Section

2.4.1 Materials and physical measurements

3, 6-di(pyridin-2-yl)pyridazine (pydz) ligand and other chemicals are commercially available and used as received. 3,6-bis(3,5-dimethyl-1H-pyrazol-1-yl)pyridazine (pzdz) was synthesised according to the literature. Elemental analyses (C, H, N) were measured by a vario EL cube CHNOS Elemental Analyzer Elementar Analysensysteme GmbH. FT-IR spectra were recorded in the range 600-4000 cm^{-1} on a Bruker tensor II spectrophotometer. Powder X-ray diffraction (PXRD) measurements were recorded on a Rigaku Smartlab X-ray diffractometer. A PXRD pattern for **1** could not be obtained due to the loss of $CHCl_3$ interstitial solvent molecules. Magnetic measurements were carried out with

a SQUID MPMS3 magnetometer. Magnetic data were corrected for the diamagnetism of the sample holder and for the diamagnetism of the sample using Pascal's constants.

Caution: Although no such behaviour was observed during the experiment, azido salts are potentially explosive and should be handled with care.

X-ray data for **1** and **2** were collected on a Bruker D8 VENTURE diffractometer with graphite monochromated Mo Kα radiation (λ = 0.71073 Å). Lorentz/polarisation corrections were applied during data reduction and the structures were solved by direct methods (SHELXS-97). Refinements were performed by full-matrix least squares (SHELXL-97) on F^2 and empirical absorption corrections (SADABS) were applied. Anisotropic thermal parameters were used for the non-hydrogen atoms. Hydrogen atoms were added at calculated positions and refined using a riding model. Weighted R factors (*w*R) and the goodness-of-fit (S) values are based on F^2; conventional R factors (R) are based on F, with F set to zero for negative F^2. CCDC-1945133 (**1**) and 1945134 (**2**) contain the crystallographic data.

2.4.2 Synthesis

Synthesis of {[Co^{II}_4(pzdz)$_4$(N_3)$_4$][BPh_4]$_4$}·4CH_3CN·3$CHCl_3$·2CH_3OH (**1**). Treatment of $CoCl_2·6H_2O$ (72.5 mg, 0.31 mmol) and $NaBPh_4$ (135 mg, 0.39 mmol) in acetonitrile (5 mL) afforded a blue-greenish solution with white precipitate (NaCl), which was filtered off after 20 min. Pzdz (90 mg, 0.31 mmol) in chloroform 5 mL, and NaN_3 (24.5 mg, 0.38 mmol) in methanol (5 mL), were added to the above solution. The resulting red solution was allowed to stand quietly for several days. Orange plate-like crystals were isolated via filtration, washed with methanol and dried in the air. Yield: 123 mg (48.3% based on Co salt).Selected IR data (cm^{-1}): 2070 (s), 1478 (m), 1432 (s), 1354 (m), 1275 (w), 1137 (w), 1094 (m), 1043 (m), 982 (m). Anal. Calc. $C_{165}H_{166}B_4N_{40}O_2Cl_9Co_4$: C, 61.15; H, 5.20; N, 17.39. Found C, 60.71; H, 5.46; N, 17.15.

Synthesis of {[Co^{II}_4(pydz)$_4$(N_3)$_4$][BPh_4]$_4$}·4CH_3CN (2). The synthesis of **2** was similar to **1** using pydz ligand instead. Orange block crystals were collected by filtration and washed with cold methanol and dried in the air. Yield 150 mg (70% based on Co salt). Selected IR data (cm^{-1}): 2065 (s), 1433 (m), 1354 (m), 986 (m). Anal. Calc. $C_{156}H_{126}B_4Co_4N_{30}$: C, 69.40; H, 4.70; N, 15.56. Found C, 69.48; H, 4.29; N, 15.55.

2.5 Results and discussion

2.5.1 Crystal structures

The treatment of $CoCl_2·6H_2O$ with pzdz or pydz, NaN_3 and $NaBPh_4$ in a 1:1:1:1 ratio gave orange block crystals of **1** and **2**. Single crystal X-ray diffraction study reveals that they crystallise in the triclinic space group *P*-1 for **1** and tetragonal space group $I4_1/a$ for **2**, respectively (**Table 2.1**). The asymmetric unit of **1** contains four symmetrically related Co^{II} ions, while only one crystallographically independent Co^{II} ion is involved in **2** due to the four-fold symmetry. Despite these different symmetries, both complexes feature a [2 × 2] grid-shaped structure in which the neighbouring Co^{II} ions reside in alternate corners and are linked by two pyridazine N atoms and a single EO-azido bridge (**Figure 2.2**). Each Co^{II} ion is located in a highly distorted octahedral coordination sphere formed by six N atoms from the EO azides and the pzdz or pydz ligands. The Co–N bond lengths are in the range of 2.064–2.175 Å (for **1**) and 2.068–2.174 Å (for **2**), consistent with the high spin Co^{II} species (**Table 2.2** and **Table 2.3**).10 The bridging M–N_{azide}–M angle is found to be 118.5 – 119.9° for **1** and 116.9° for **2**, respectively. The dihedral angles between the pyrazolyl- or pyridyl- and pyridazine rings are around 4.19/26.06° (**1**) and 10.61/11.51° (**2**), suggesting a relatively poor coplanarity. The adjacent Co···Co distances of **1** remain nearly the same (3.57–3.60 Å) while the four Co···Co···Co vertex angles (86.95–92.97°) for this molecular square deviate

significantly from being ideal. The [Co^{II}_4] core in **2** is arranged in a nearly perfect square shape where the adjacent Co···Co distance is 3.54 Å and the Co···Co···Co vertex angle is 89.91°. Both square molecules are well isolated by the counteranions BPh_4^- and interstitial solvents, giving the shortest intermolecular Co···Co distance of 12.7 Å and 11.4 Å for **1** and **2**, respectively (**Figure 2.3**). No significant intermolecular interactions are found.

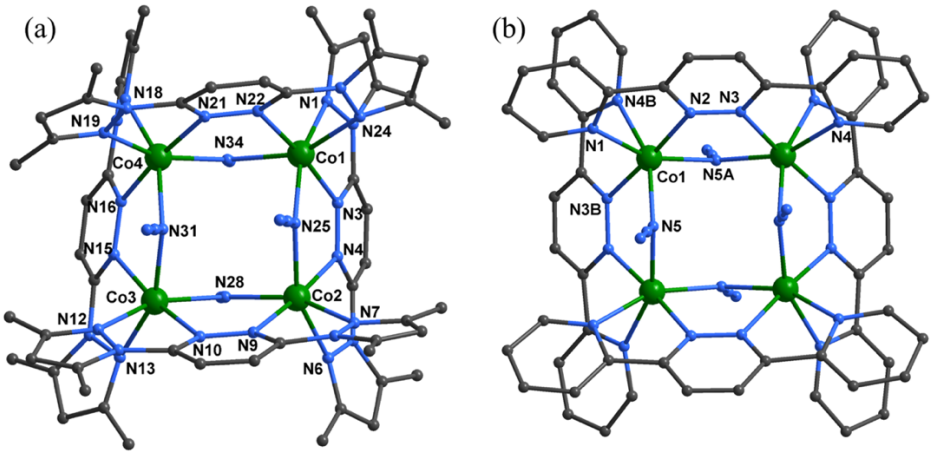

Figure 2.2. Molecular structure of **1** (a) and **2** (b). All the hydrogen atoms, interstitial solvents and counter ions are omitted for the sake of clarity.

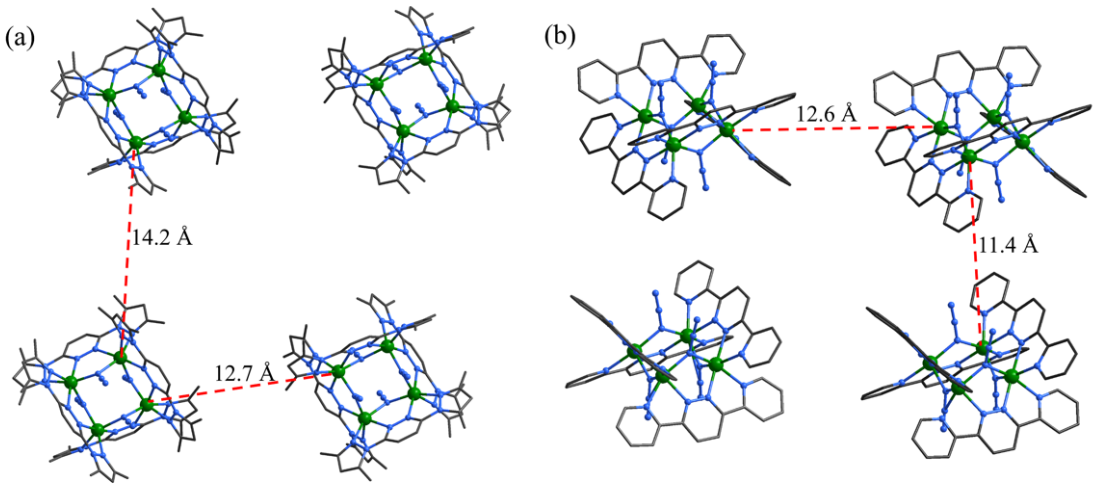

Figure 2.3. The packing diagram of **1** (a) and **2** (b). The dashed line shows the nearest intermolecular Co···Co separation. Hydrogen atoms, counter anions and interstitial solvent molecules are omitted for clarity. Colour codes: Co(II), green; C, grey; N, light blue.

Table 2.1. Crystallographic data for **1** and **2**.

	1	**2**
Empirical formula	$C_{165}H_{166}B_4N_{40}O_2Cl_9Co_4$	$C_{156}H_{126}B_4Co_4N_{30}$
Molecular weight/g mol^{-1}	3339.38	2699.82
Temperature, K	100(2)	150(2)
Crystal system	triclinic	tetragonal
Space group	P-1	$I4_1/a$
a/Å	17.9901(18)	17.3694(14)
b/Å	19.0049(19)	17.3694(14)
c/Å	28.923(3)	43.223(6)
α/°	89.170(5)	90
β/°	72.435(5)	90
γ/°	62.773(5)	90
V, Å^3	8293.6(14)	13040(3)
Z	2	4
D_{cal}/g cm^{-3}	1.337	1.375
Radiation	MoKα	MoKα
2θ range/^{o}	1.49 to 55.14	4.69 to 55.19
completeness	98.6%	99.9%
residual map, e Å^{-3}	1.409/-1.112	0.263/-0.327
Goodness-of-fit on F^2	1.080	1.030
Final indices[I>2σ(I)]	R_1 = 0.0523 wR_2 = 0.1294	R_1 = 0.0357 wR_2 = 0.0688
R indices (all data)	R_1 = 0.0684 wR_2 = 0.1411	R_1 = 0.0616 wR_2 = 0.0759

Table 2.2. Selected bond lengths [Å] and angles [deg] for **1**.

Co(1)-N(22)	2.175(2)	Co(2)-N(28)	2.071(2)
Co(1)-N(25)	2.076(2)	Co(2)-N(4)	2.171(2)
Co(1)-N(3)	2.157(2)	Co(2)-N(7)	2.112(2)
Co(1)-N(24)	2.119(2)	Co(2)-N(25)	2.092(2)
Co(1)-N(34)	2.078(2)	Co(2)-N(9)	2.167(2)
Co(1)-N(1)	2.122(2)	Co(2)-N(6)	2.120(2)
Co(3)-N(15)	2.171(2)	Co(4)-N(16)	2.140(2)
Co(3)-N(28)	2.064(2)	Co(4)-N(34)	2.087(2)
Co(3)-N(13)	2.146(2)	Co(4)-N(18)	2.134(2)
Co(3)-N(10)	2.161(2)	Co(4)-N(31)	2.093(2)
Co(3)-N(31)	2.095(2)	Co(4)-N(21)	2.137(2)
Co(3)-N(12)	2.112(2)	Co(4)-N(19)	2.126(2)
N(25)-Co(1)-N(22)	89.35(8)	N(28)-Co(3)-N(15)	91.21(8)
N(25)-Co(1)-N(3)	86.61(8)	N(28)-Co(3)-N(13)	93.47(8)
N(25)-Co(1)-N(24)	96.63(8)	N(28)-Co(3)-N(10)	87.13(8)
N(25)-Co(1)-N(34)	97.39(8)	N(28)-Co(3)-N(31)	97.59(8)
N(25)-Co(1)-N(1)	159.40(8)	N(28)-Co(3)-N(12)	158.46(8)
N(3)-Co(1)-N(22)	174.21(8)	N(13)-Co(3)-N(15)	73.72(8)
N(24)-Co(1)-N(22)	74.21(8)	N(13)-Co(3)-N(10)	114.38(8)
N(24)-Co(1)-N(3)	110.37(8)	N(10)-Co(3)-N(15)	171.81(8)
N(24)-Co(1)-N(1)	84.67(8)	N(31)-Co(3)-N(15)	86.13(8)
N(34)-Co(1)-N(22)	85.29(8)	N(31)-Co(3)-N(13)	157.20(8)
N(34)-Co(1)-N(3)	91.12(8)	N(31)-Co(3)-N(10)	86.13(8)
N(34)-Co(1)-N(24)	154.95(8)	N(31)-Co(3)-N(12)	91.30(8)
N(34)-Co(1)-N(1)	89.38(8)	N(12)-Co(3)-N(15)	109.02(8)
N(1)-Co(1)-N(22)	110.66(8)	N(12)-Co(3)-N(13)	85.46(8)
N(1)-Co(1)-N(3)	73.78(8)	N(12)-Co(3)-N(10)	73.88(8)
N(28)-Co(2)-N(4)	91.75(8)	N(34)-Co(4)-N(16)	86.49(8)
N(28)-Co(2)-N(7)	157.64(8)	N(34)-Co(4)-N(18)	89.80(8)
N(28)-Co(2)-N(25)	101.15(8)	N(34)-Co(4)-N(31)	102.55(8)

N(28)-Co(2)-N(9)	86.81(8)	N(34)-Co(4)-N(21)	87.17(8)
N(28)-Co(2)-N(6)	91.88(8)	N(34)-Co(4)-N(19)	159.67(8)
N(7)-Co(2)-N(4)	108.90(8)	N(18)-Co(4)-N(16)	73.96(8)
N(7)-Co(2)-N(9)	73.26(8)	N(18)-Co(4)-N(21)	108.39(8)
N(7)-Co(2)-N(6)	85.88(8)	N(31)-Co(4)-N(16)	86.91(8)
N(25)-Co(2)-N(4)	85.50(8)	N(31)-Co(4)-N(18)	156.63(8)
N(25)-Co(2)-N(7)	89.26(8)	N(31)-Co(4)-N(21)	92.16(8)
N(25)-Co(2)-N(9)	90.35(8)	N(31)-Co(4)-N(19)	85.61(8)
N(25)-Co(2)-N(6)	156.11(8)	N(21)-Co(4)-N(16)	173.24(8)
N(9)-Co(2)-N(4)	175.27(8)	N(19)-Co(4)-N(16)	112.76(8)
N(6)-Co(2)-N(4)	74.06(8)	N(19)-Co(4)-N(18)	89.48(8)
N(6)-Co(2)-N(9)	110.47(8)	N(19)-Co(4)-N(21)	73.81(8)

Table 2.3. Selected bond lengths [Å] and angles [deg] for **2**.

Co(1)-N(1)	2.142(1)	Co(1)-N(2)	2.124(1)
Co(1)-N(3B)	2.137(1)	Co(1)-N(4B)	2.174(1)
Co(1)-N(5)	2.068(1)	Co(1)-N(5A)	2.077(1)
N(1)-Co(1)-N(5)	92.99(5)	N(1)-Co(1)-N(5A)	157.97(5)
N(1)-Co(1)-N(2)	75.21(5)	N(1)-Co(1)-N(3B)	104.29(5)
N(1)-Co(1)-N(4B)	81.07(5)	N(2)-Co(1)-N(5)	98.58(5)
N(2)-Co(1)-N(4B)	101.10(5)	N(2)-Co(1)-N(5A)	85.84(5)
N(2)-Co(1)-N(3B)	175.65(5)	N(3B)-Co(1)-N(5A)	93.75(5)
N(3B)-Co(1)-N(4B)	74.57(5)	N(3B)-Co(1)-N(5)	85.76(5)
N(4B)-Co(1)-N(5)	157.19(5)	N(4B)-Co(1)-N(5A)	91.90(5)
N(5)-Co(1)-N(5A)	100.96(7)		

Symmetry transformations used to generate equivalent atoms:

A: y+1/4, -x+7/4, -z+3/4 B: -y+7/4, x-1/4, -z+3/4

2.5.2 Magnetic properties

The magnetic susceptibility data for **1** and **2** were collected at an applied direct current (dc) field of 1000 Oe in a temperature range of 2–300 K (**Figure 2.4**). The χT products for **1** and **2** at 300 K are 12.15 cm^3 K mol^{-1} and 11.50 cm^3 K mol^{-1}, respectively, which are in good agreement with the expected values for the four isolated high-spin Co^{II} ions with unquenched orbital momentum.[12] Upon cooling, the χT products of both complexes increased steadily to a maximum of 25.37 cm^3 K mol^{-1} (at 12 K for **1**) and 20.26 cm^3 K mol^{-1} (at 16 K for **2**) and then dropped to 21.23 cm^3 K mol^{-1} (for **1**) and 18.12 cm^3 K mol^{-1} (for **2**) at 2 K.

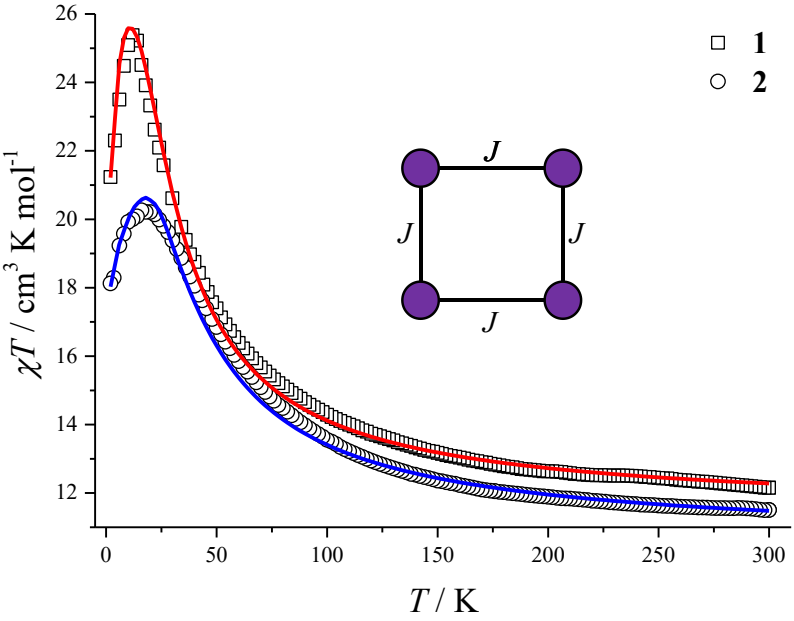

Figure 2.4. Temperature dependence of magnetic susceptibility for **1** (□) and **2** (○) at 1000 Oe dc field. The solid lines represent the fit based on eq. 2.1. Inset shows the magnetic exchange pathways.

Fitting the data above 50 K by the Curie-Weiss law gave the positive Weiss constants of +19.2 K for **1** and +20.2 K for **2**. Such behaviours are indicative of dominant ferromagnetic interactions between the neighbouring Co(II) centres, while the decrease at low temperatures is likely attributed to the intermolecular antiferromagnetic interaction, the spin–orbit coupling and/or the blocking

dynamics. To gain insight into the magnetic anisotropy and coupling strength of the Co(II) centres, the χT vs. T data were fitted with the PHI programme[13] based on a square model (the inset of **Figure 2.4**) with the following spin Hamiltonian (eq. 2.1):

$$\hat{H} = -2J(\hat{S}_1\hat{S}_2 + \hat{S}_2\hat{S}_3 + \hat{S}_3\hat{S}_4 + \hat{S}_1\hat{S}_4) + \sum_{i=1}^{4}(D_{Co,i}\hat{S}_{z,i}^{\ 2} + g_{Co,i}\mu_B\hat{S}_{Co,i}B) \qquad \text{(eq. 2.1)}$$

where D_{Co}, μ_B, g_{Co}, B, and J correspond to the axial zero-field splitting (zfs) parameter, Bohr magneton, Landé factor, magnetic field vector and magnetic exchange between Co(II) metal centres, respectively. The best set of parameters gave J = +3.2 cm^{-1}, g = 2.46 and D = +6.2 cm^{-1} for **1** and J = +3.7cm^{-1}, g = 2.37 and D = +10.2 cm^{-1} for **2**. No acceptable fittings can be achieved with a negative D value. The positive J values further confirmed the intramolecular ferromagnetic interactions and suggested an S = 6 ground state for both **1** and **2**. Noting that the diazine ligands usually transfer weak antiferromagnetic interactions in Co^{II} complexes,[14] the overall intramolecular ferromagnetic couplings in both the complexes should be dominated by the contribution from EO-azido bridges.

As depicted in **Figure 2.5**, the reduced magnetisation plots for both complexes exhibited non-superposition between the isofield curves and a continuous increase with high-field non-saturation (9.41 $N\beta$ for **1** and 8.07 $N\beta$ for **2** at 2.0 K and 70 kOe), indicating the presence of significant magnetic anisotropy. Using an S = 6 macro-spin model with the following spin Hamiltonian (eq. 2.2), the data were fitted with the PHI programme to extract the axial (D) and transverse (E) zfs parameters of the entire molecule:

$$\hat{H} = D\hat{S}_z^{\ 2} + E(\hat{S}_x^{\ 2} + \hat{S}_y^{\ 2}) + g\mu_B\hat{S}\cdot B \qquad \text{(eq. 2.2)}$$

The best fit gave D = +6.5 cm^{-1}, E = -0.6 cm^{-1}, and g = 2.36 for **1** and D = +4.5 cm^{-1}, E = -0.8 cm^{-1}, and g = 2.11 for **2**. It should be noted that both negative and positive D values can be used for fitting the experimental data. However, the large $|E/D|$ ratios that exceed the theoretical limit[15] ($|E/D|$ = 1/3)

are observed for both complexes when correlated with a negative *D* value, suggesting that only positive *D* values are reasonable and corroborate the easy-plane magnetic anisotropy for **1** and **2**.

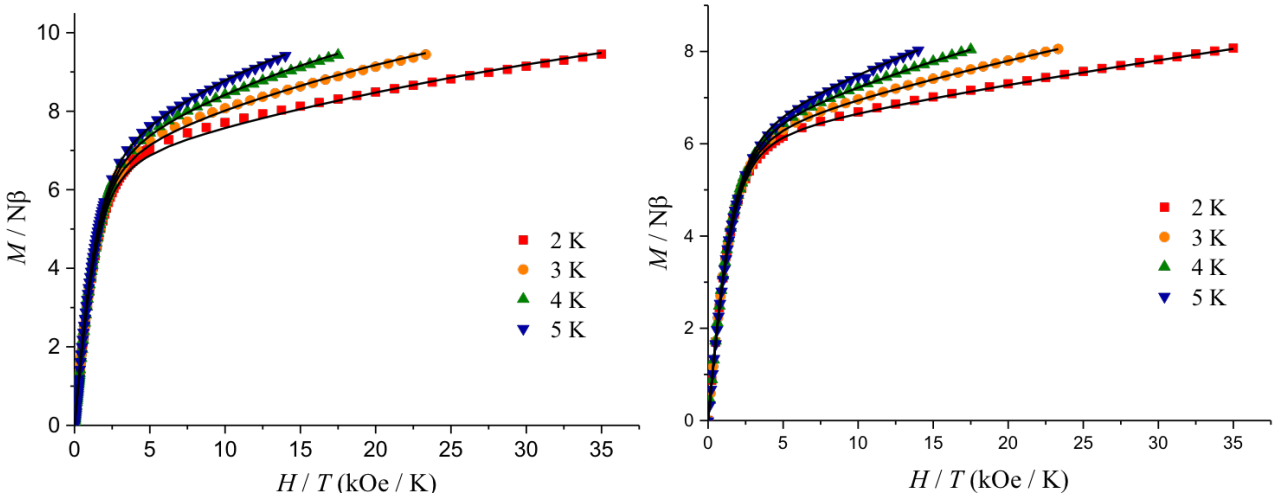

Figure 2.5. Reduced magnetisation data for **1** (left) and **2** (right) at 2-5 K. The solid lines represent the fit to the data based on eq. 2.2.

Accordingly, the alternating current (ac) susceptibility measurements were conducted to probe the SMM behaviour. Under a zero dc field, no out-of-phase (χ'') signals were observed for both complexes, suggesting serious quantum tunnelling of magnetisation (QTM).[16] Ac susceptibility data under different applied dc fields were thus collected to determine the optimum field at which the QTM effects are minimised; 1500 Oe (for **1**) and 2000 Oe (for **2**) dc fields were determined on the basis of both the enhanced relaxation times and appreciable signal intensity, under which clear frequency-dependent signals with out-of-phase (χ'') peaks were observed (**Figure 2.6** and **Figure 2.7**). The relaxation times (τ) of **1** and **2** were extracted from fitting the Cole–Cole plots based on the generalised Debye model,[17] and were further plotted as ln τ versus T^{-1} to generate the Arrhenius-like diagram. The high-temperature relaxation times follow the Arrhenius law $\tau = \tau_0 \exp(U_{eff}/k_BT)$ (τ_0 is the pre-exponential factor),[18] leading to an effective energy barrier (U_{eff}) of 36 K ($\tau_0 = 3.2\times10^{-9}$ s) for **1** and 56 K ($\tau_0 = 6.4\times10^{-10}$ s) for **2**. Those τ_0 and U_{eff} values are comparable to the reported Co^{II}-

SMMs. It may be mentioned that no hysteresis loop of magnetisation was observed for both complexes at a normal sweeping rate below 100 Oe s^{-1} (**Figure 2.8**).

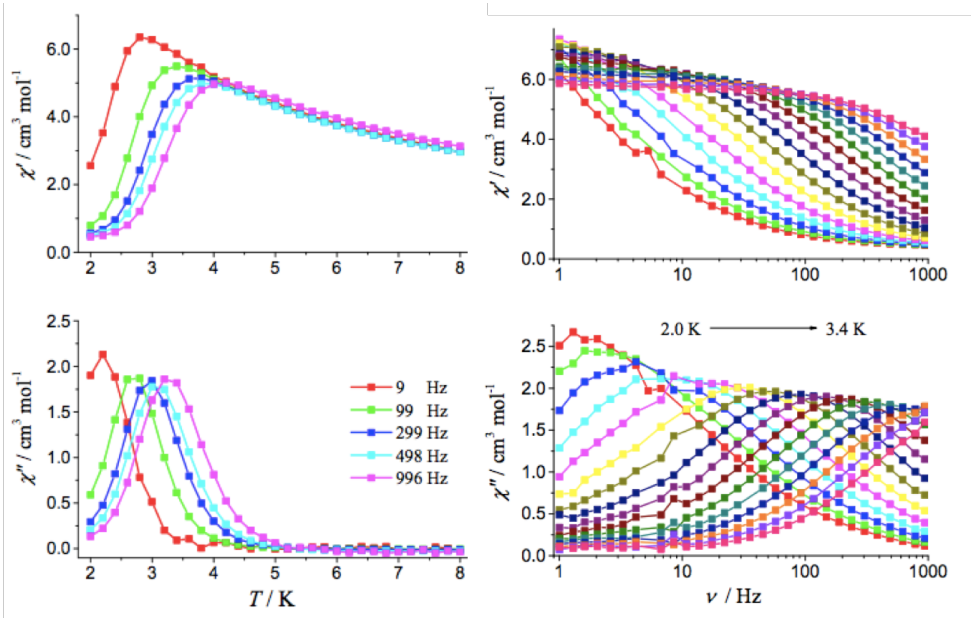

Figure 2.6. Temperature dependence (left) and frequency dependence (right) of the in-phase (χ') and out-of-phase (χ'') ac susceptibility for **1** under 1500 Oe dc field. Solid lines are guides for the eye.

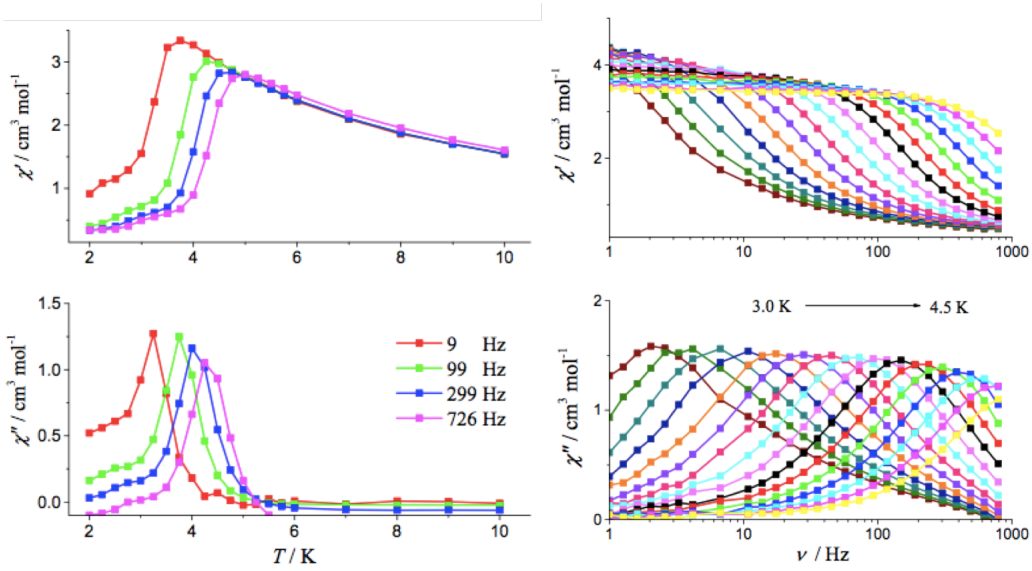

Figure 2.7. Temperature dependence (left) and frequency dependence (right) of the in-phase (χ') and out-of-phase (χ'') ac susceptibility for **2** under 2000 Oe dc field. Solid lines are guides for the eye.

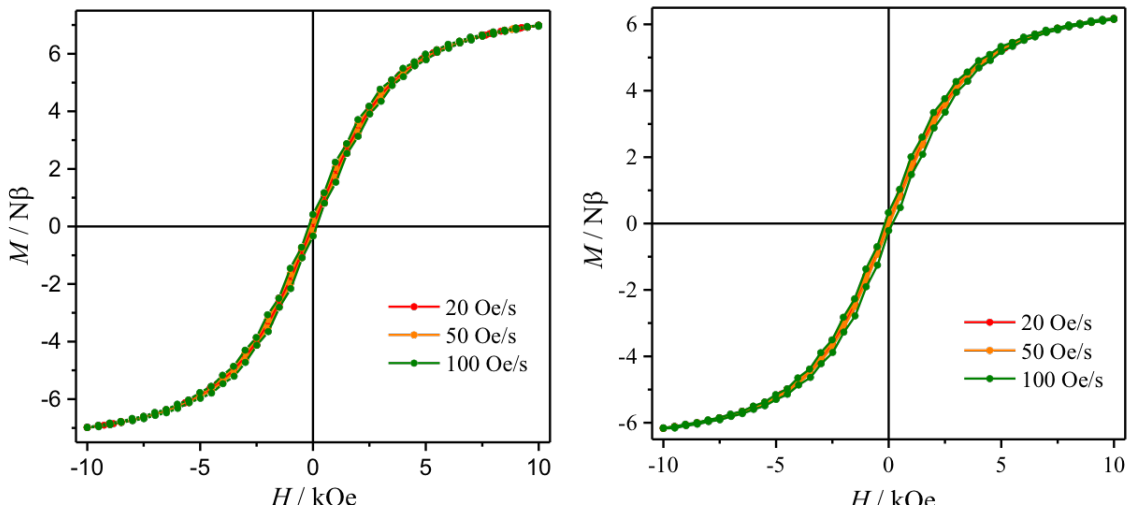

Figure 2.8. Magnetic hysteresis measurements of **1** and **2** recorded at 2.0 K with field sweep rate of 20, 50 and 100 Oe/s.

2.6 Conclusion

In summary, two azido-bridged [2 × 2] grid-like cobalt(II) complexes were constructed with two pyridazine derivatives of pydz and pzdz as coding ligands and the incorporation of end-on azido ions as secondary bridges. Magnetic studies indicated the overall intramolecular ferromagnetic couplings and field-induced slow magnetic relaxation for both the complexes. Investigation on assembling metal ions with tetrazine derivatives for further modulating the magnetic communications in these grid-like structures is currently in progress.

2.7 References

1. (a) M. Fujita, M. Tominaga, A. Hori and B. Therrien, *Acc. Chem. Res.*, 2005, **38**, 369-378; (b) M. Ruben, J.-M. Lehn and P. Müller, *Chem. Soc. Rev.*, 2006, **35**, 1056-1067; (c) R. Chakrabarty,

P. S. Mukherjee and P. J. Stang, *Chem. Rev.*, 2011, **111**, 6810-6918; (d) T. R. Cook and P. J. Stang, *Chem. Rev.*, 2015, **115**, 7001-7045.

2. (a) M. Ruben, E. Breuning, J.-M. Lehn, V. Ksenofontov, F. Renz, P. Gütlich and G. B. M. Vaughan, *Chem. Eur. J.*, 2003, **9**, 4422-4429; (b) M. Ruben, J. Rojo, F. J. Romero-Salguero, L. H. Uppadine and J.-M. Lehn, *Angew. Chem. Int. Ed.*, 2004, **43**, 3644-3662; (c) J. W. Steed, *Chem. Soc. Rev.*, 2009, **38**, 506-519; (d) M. D. Pluth, R. G. Bergman and K. N. Raymond, *Acc. Chem. Res.*, 2009, **42**, 1650-1659; (e) D. B. Amabilino, D. K. Smith and J. W. Steed, *Chem. Soc. Rev.*, 2017, **46**, 2404-2420.

3. (a) L. N. Dawe, K. V. Shuvaev and L. K. Thompson, *Chem. Soc. Rev.*, 2009, **38**, 2334-2359; (b) H. T. Chifotides and K. R. Dunbar, *Acc. Chem. Res.*, 2013, **46**, 894-906; (c) B. Schäfer, J.-F. Greisch, I. Faus, T. Bodenstein, I. Šalitroš, O. Fuhr, K. Fink, V. Schünemann, M. M. Kappes and M. Ruben, *Angew. Chem. Int. Ed.*, 2016, **55**, 10881-10885; (d) M. Steinert, B. Schneider, S. Dechert, S. Demeshko and F. Meyer, *Inorg. Chem.*, 2016, **55**, 2363-2373; (e) J. W. L. Wong, S. Demeshko, S. Dechert and F. Meyer, *Inorg. Chem.*, 2019, **58**, 13337-13345.

4. (a) P. Mal, B. Breiner, K. Rissanen and J. R. Nitschke, *Science*, 2009, **324**, 1697; (b) K. Harris, D. Fujita and M. Fujita, *Chem. Commun.*, 2013, **49**, 6703-6712; (c) A. M. Castilla, W. J. Ramsay and J. R. Nitschke, *Acc. Chem. Res.*, 2014, **47**, 2063-2073.

5. (a) G. C. Dismukes, R. Brimblecombe, G. A. N. Felton, R. S. Pryadun, J. E. Sheats, L. Spiccia and G. F. Swiegers, *Acc. Chem. Res.*, 2009, **42**, 1935-1943; (b) J. J. Henkelis and M. J. Hardie, *Chem. Commun.*, 2015, **51**, 11929-11943; (c) P. Yang and U. Kortz, *Acc. Chem. Res.*, 2018, **51**, 1599-1608.

6. (a) M. Murugesu, M. Habrych, W. Wernsdorfer, K. A. Abboud and G. Christou, *J. Am. Chem. Soc*, 2004, **126**, 4766-4767; (b) C. J. Milios, A. Vinslava, W. Wernsdorfer, S. Moggach, S. Parsons, S. P. Perlepes, G. Christou and E. K. Brechin, *J. Am. Chem. Soc*, 2007, **129**, 2754-

2755; (c) B. S. Dolinar, S. Gómez-Coca, D. I. Alexandropoulos and K. R. Dunbar, *Chem. Commun.*, 2017, **53**, 2283-2286; (d) B. S. Dolinar, D. I. Alexandropoulos, K. R. Vignesh, T. A. James and K. R. Dunbar, *J. Am. Chem. Soc.*, 2018, **140**, 908-911; (e) U. Albold, H. Bamberger, P. P. Hallmen, J. van Slageren and B. Sarkar, *Angew. Chem. Int. Ed.*, 2019, **58**, 9802-9806.

7. (a) M.-T. Youinou, N. Rahmouni, J. Fischer and J. A. Osborn, *Angew. Chem. Int. Ed.*, 1992, **31**, 733-735; (b) N. S. Oxtoby, A. J. Blake, N. R. Champness and C. Wilson, *Dalton Trans.*, 2003, 3838-3839; (c) B. L. Schottel, J. Bacsa and K. R. Dunbar, *Chem. Commun.*, 2005, 46-47; (d) B. L. Schottel, H. T. Chifotides, M. Shatruk, A. Chouai, L. M. Pérez, J. Bacsa and K. R. Dunbar, *J. Am. Chem. Soc.*, 2006, **128**, 5895-5912; (e) E. C. Constable, S. Decurtins, C. E. Housecroft, T. D. Keene, C. G. Palivan, J. R. Price and J. A. Zampese, *Dalton Trans.*, 2010, **39**, 2337-2343; (f) S. E. Bodman and C. M. Fitchett, *Dalton Trans.*, 2014, **43**, 12606-12613; (g) N. Marino, R. Bruno, A. Bentama, A. Pascual-Álvarez, F. Lloret, M. Julve and G. De Munno, *CrystEngComm*, 2019, **21**, 917-924; (h) H. Gao, Z.-H. Zhang, P. Jiang and X.-R. Li, *Transition Met Chem*, 2006, **31**, 1088-1092.

8. D. Wu, D. Guo, Y. Song, W. Huang, C. Duan, Q. Meng and O. Sato, *Inorg. Chem.*, 2009, **48**, 854-860.

9. K. Chakarawet, P. C. Bunting and J. R. Long, *J. Am. Chem. Soc.*, 2018, **140**, 2058-2061.

10. (a) J. M. Zadrozny and J. R. Long, *J. Am. Chem. Soc*, 2011, **133**, 20732-20734; (b) J. Vallejo, I. Castro, R. Ruiz-García, J. Cano, M. Julve, F. Lloret, G. De Munno, W. Wernsdorfer and E. Pardo, *J. Am. Chem. Soc*, 2012, **134**, 15704-15707; (c) X. Liu, L. Sun, H. Zhou, P. Cen, X. Jin, G. Xie, S. Chen and Q. Hu, *Inorg. Chem.*, 2015, **54**, 8884-8886; (d) A. V. Palii, D. V. Korchagin, E. A. Yureva, A. V. Akimov, E. Y. Misochko, G. V. Shilov, A. D. Talantsev, R. B. Morgunov, S. M. Aldoshin and B. S. Tsukerblat, *Inorg. Chem.*, 2016, **55**, 9696-9706; (e) Y.-Z. Zhang, S. Gómez-Coca, A. J. Brown, M. R. Saber, X. Zhang and K. R. Dunbar, *Chem. Sci.*, 2016, **7**,

6519-6527; (f) Y. Rechkemmer, F. D. Breitgoff, M. van der Meer, M. Atanasov, M. Hakl, M. Orlita, P. Neugebauer, F. Neese, B. Sarkar and J. van Slageren, *Nat. Commun.*, 2016, **7**, 10467; (g) J. M. Frost, K. L. M. Harriman and M. Murugesu, *Chem. Sci.*, 2016, **7**, 2470-2491; (h) X.-N. Yao, J.-Z. Du, Y.-Q. Zhang, X.-B. Leng, M.-W. Yang, S.-D. Jiang, Z.-X. Wang, Z.-W. Ouyang, L. Deng, B.-W. Wang and S. Gao, *J. Am. Chem. Soc.*, 2017, **139**, 373-380; (i) M. Feng and M.-L. Tong, *Chem. Eur. J.*, 2018, **24**, 7574-7594; (j) B. Yao, Y.-F. Deng, T. Li, J. Xiong, B.-W. Wang, Z. Zheng and Y.-Z. Zhang, *Inorg. Chem.*, 2018, **57**, 14047-14051; (k) P. C. Bunting, M. Atanasov, E. Damgaard-Møller, M. Perfetti, I. Crassee, M. Orlita, J. Overgaard, J. van Slageren, F. Neese and J. R. Long, *Science*, 2018, **362**, eaat7319.

11. (a) T.-F. Liu, D. Fu, S. Gao, Y.-Z. Zhang, H.-L. Sun, G. Su and Y.-J. Liu, *J. Am. Chem. Soc*, 2003, **125**, 13976-13977; (b) Y.-Z. Zhang, W. Wernsdorfer, F. Pan, Z.-M. Wang and S. Gao, *Chem. Commun.*, 2006, 3302-3304; (c) X.-Y. Wang, Z.-M. Wang and S. Gao, *Chem. Commun.*, 2008, 281-294; (d) Y.-F. Zeng, X. Hu, F.-C. Liu and X.-H. Bu, *Chem. Soc. Rev.*, 2009, **38**, 469-480; (e) H.-L. Sun, Z.-M. Wang and S. Gao, *Coord. Chem. Rev.*, 2010, **254**, 1081-1100; (f) X.-C. Huang, C. Zhou, H.-Y. Wei and X.-Y. Wang, *Inorg. Chem.*, 2013, **52**, 7314-7316; (g) Y.-Z. Zhang, S. Gao and O. Sato, *Dalton Trans.*, 2015, **44**, 480-483; (h) S. Dhers, H. L. C. Feltham and S. Brooker, *Coord. Chem. Rev.*, 2015, **296**, 24-44.

12. (a) M. Murrie, *Chem. Soc. Rev.*, 2010, **39**, 1986-1995; (b) G. A. Craig and M. Murrie, *Chem. Soc. Rev.*, 2015, **44**, 2135-2147.

13. N. F. Chilton, R. P. Anderson, L. D. Turner, A. Soncini and K. S. Murray, *J. Comput. Chem.*, 2013, **34**, 1164-1175.

14. (a) A. Escuer, R. Vicente, B. Mernari, A. El Gueddi and M. Pierrot, *Inorg. Chem.*, 1997, **36**, 2511-2516; (b) S. Brooker, D. J. de Geest, R. J. Kelly, P. G. Plieger, B. Moubaraki, K. S. Murray and G. B. Jameson, *J. Chem. Soc., Dalton Trans.*, 2002, 2080-2087; (c) Y. Lan, D. K.

Kennepohl, B. Moubaraki, K. S. Murray, J. D. Cashion, G. B. Jameson and S. Brooker, *Chem. Eur. J.*, 2003, **9**, 3772-3784.

15. R. Carlin, *Magnetochemistry*, Springer, 1986.
16. D. Gatteschi and R. Sessoli, *Angew. Chem. Int. Ed.*, 2003, **42**, 268-297.
17. R. Schenker, M. N. Leuenberger, G. Chaboussant, D. Loss and H. U. Güdel, *Physical Review B*, 2005, **72**, 184403.
18. D. Gatteschi, R. Sessoli and R. Villain, *Molecular Nanomagnets*, Oxford University Press, 2006.

Chapter 3

An azido-bridged [Fe^{II}_4] molecule showing spin crossover behaviour

Zhilin Guo, Maolin You, Yi-Fei Deng, Qiang Liu, Yin-Shan Meng, Zoe Pikramenou and Yuan-Zhu Zhang

A version of this manuscript has been accepted for publication in *Dalton Transaction*.

Reproduced from *Dalton Trans*. 2021, **50**, 14303-14308 with permission from Royal Society of Chemistry

3.1 Abstract

The supramolecular self-assembly synthetic strategy provides a valid tool to obtain polynuclear Fe(II) complexes having effective communications between the metal centres and distinct spin crossover behaviour. Despite the great success in constructing various magnetic molecules, progress has not been made in SCO complexes based on azido bridges. In this article, the coordination-driven supramolecular assembly based on 3,6-substituted pyridazine and azide is presented to afford two Fe(II) grid-like complexes: $[(L)_4Fe^{II}_4(N_3)_4][BPh_4]_4 \cdot sol$ (**1**, L = 3,6-bis(3,5-dimethyl-1H-pyrazol-1-yl)pyridazine; **2**, L = 3,6-di(pyridin-2-yl)pyridazine). The substitution of pyridinyl groups in **2** instead of pyrazolyl ones in **1** led to the only example exhibiting spin-crossover behaviour ($T_{1/2}$ = 230 K) among the azido-bridged complexes. In addition, a temperature-dependent photoluminescence study of **2** demonstrates a visible synergetic effect between the SCO event and the luminescence.

3.2 Introduction

The great advances in the area of spin crossover (SCO) complexes in the last thirty years have concentrated on Fe(II) complexes, which display a distinct spin transition between high spin (HS) and low spin (LS).[1] Such materials are expected to be applied in next-generation molecule-based devices for sensing, switching, and information storage owing to their rapid response to external stimuli such as magnetic field, temperature, light, pressure, etc.[2] In addition to the change in magnetic properties, the spin transition is usually accompanied by changes in the colour,[3] volume (negative thermal expansion in special cases),[4] electrical resistance (conductivity),[5] or other functions,[6] thus making them popular candidates for multi-functional materials. Of particular interest are those molecules that exhibit a synergistic effect between SCO and luminescence,[7] for example those showing great potential for application in nanosized sensing devices.[8]

Coordination-driven self-assembly is an appealing approach for the design of diverse molecular materials whose functionalities can be manipulated by selection of metal and ligands.[9] The control of architecture based on coordination principles and multitopic ligand design as well as the versatility of the assembly modular approach can address the increasing demand polynuclear SCO complexes, in which the active metal centres may be chemically distinguishable, thus exhibiting site-selectivity[10] or step-wise transitions.[11] In particular, the supramolecular tetranuclear grid architecture mediated by various bridges has received growing attention in this area.[12] Furthermore, the enhanced intramolecular interaction in these multinuclear clusters is supposed to yield stronger cooperative effect when effective bridges are applied.[13]

As one of the most effective bridges, the azide ion has been widely explored in the construction of enormous magnetic complexes because it may engender appreciable and predictable ferro- or antiferro- magnetic coupling depending on the metal species as well as the bridging modes (end-on (EO) or end-end (EE)).[14] Nevertheless, the azido-Fe(II) system is relatively less studied, only a few exhibited magnetic bistability.[15] Surprisingly, no azido-bridged SCO complex has yet been reported, although there have been some reports of spin-transition related mononuclear iron complexes using azide ion as a terminal ligand.[16] Recently, we and others successfully incorporated azide ions as secondary bridges and constructed a series of square complexes $[M^{II}_4]$ (M = Co, Ni), in which the 3,6-substituted pyridazine or tetrazine derivatives adopt *cis*-bridging modes as dictated by the EO-azido bridges, in which the cobalt analogues exhibited interesting SMM behaviour.[17] With continuous interest in this programmable system, herein, we prepared the Fe(II) analogues: $[(L)_4Fe^{II}_4(N_3)_4][BPh_4]_4 \cdot sol$ (**1**, L = 3,6-bis(3,5-dimethyl-1H-pyrazol-1-yl)pyridazine (pzdz), sol = $3MeCN \cdot 2MeOH \cdot 3CHCl_3$; **2**, L = 3,6-di(pyridin-2-yl)pyridazine (pydz), sol = 4MeCN), where the Fe(II) ions are co-bridged by the end-on (EO) azide and the diazine. Interestingly, the substitution of

pyridinyl groups in **2** instead of pyrazolyl ones in **1** set up the first SCO example ($T_{1/2}$ = 230 K) of azido-bridged complexes.

3.3 Contribution

I performed the syntheses and characterisations of the iron complexes, including SCXRD at different temperatures, static magnetic measurement and variable-temperature luminescent measurement. Other co-authors are acknowledged: Maolin You, Dr Qiang Liu and Dr Yin-Shan Meng helped with the Mössbauer spectra. Dr Yi-Fei Deng helped with setting up the photomagnetic measurements and data interpretation. The draft manuscript was written by me and revised by Prof. Pikramenou and Dr. Zhang.

3.4 Experimental section

3.4.1 General methods

All synthetic procedures were carried out under an inert atmosphere using a glove box. 3,6-di(pyridin-2-yl)pyridazine (pydz) ligand and other chemicals are commercially available and used as received. Distilled and degassed solvents were obtained from a solvent purification system and stored with molecular sieves in the glove box. 3,6-bis(3,5-dimethyl-1H-pyrazol-1-yl)pyridazine (pzdz) was prepared according to the previous literature.[18] Elemental analyses (C, H, N) were measured by a vario EL cube CHNOS Elemental Analyzer Elementar Analysensysteme GmbH. Powder X-ray diffraction (PXRD) measurements were recorded on a Rigaku Smartlab X-ray diffractometer. FT-IR spectra were recorded in the range 600-4000 cm^{-1} on a Bruker tensor II spectrophotometer. Solid-state UV-vis spectra were recorded on Aglient Cary 5000 UV-Vis spectrometer using an integrating sphere. Magnetic measurements were carried out with a SQUID MPMS3 magnetometer. Magnetic

data were corrected for the diamagnetism of the sample holder and for the diamagnetism of the sample using Pascal's constants. Photomagnetic irradiation was performed on fresh sample at 10 K. Diode Pumped Solid State Lasers was guided via a flexible optical fibre into SQUID magnetometer. Luminescence spectra were recorded on an Edinburgh Instruments FLSP920 steady-state and time-resolved spectrometer with F900 software and on a Photon Technology International spectrometer. The spectra are corrected for lamp/photomultiplier tube/instrument response.

X-ray data for **1** and **2** were collected on a Bruker D8 VENTURE diffractometer with graphite monochromated Mo Kα (λ = 0.71073 Å) and Cu Kα (λ = 1.54178 Å) radiation. Lorentz/polarisation corrections were applied during data reduction and the structures were solved with the SHELXT solution program using Intrinsic Phasing. Refinements were performed by full-matrix least squares minimisation (SHELXL) on F^2. Anisotropic thermal parameters were used for the non-hydrogen atoms. Hydrogen atoms were added at calculated positions and refined using a riding model. Weighted R factors (wR) and the goodness-of-fit (S) values are based on F^2; conventional R factors (R) are based on F, with F set to zero for negative F^2. Since the solvent molecules in 1 could not be completely modelled due to the disorder, a part of Q peaks were subtracted by the SQUEEZE program implemented in Olex2. As a result, 272.6 electrons were found in a total solvent accessible volume of 1035.3 $Å^3$ for **1** per unit cell. Combined with the definition in the residual density map, we attribute this to the presence of four $CHCl_3$ and two CH_3OH per unit cell which account for 268 electrons that is consistent with the SQUEEZE calculations. CCDC-2015661 (**1**), 2015655 (**2**-100 K), 2078512 (**2**-150 K), 2015657 (**2**-200 K) and 2015660 (**2,** 300 K) contain the crystallographic data.

3.4.2 Synthesis

Caution: Azido salts are potentially explosive and should be handled with only small amount and great care.

Synthesis of $[(pzdz)_4Fe^{II}_4(N_3)_4][BPh_4]_4 \cdot 3MeCN \cdot 2MeOH \cdot 3CHCl_3$ (1). $FeCl_2 \cdot 4H_2O$ (19.8 mg, 0.10 mmol) and $NaBPh_4$ (34.2 mg, 0.10 mmol) were dissolved in 5 mL mixed solvents of methanol and acetonitrile (5 mL, v/v = 1/1) and stirred for two minutes, to which pzdz (27.1 mg, 0.10 mmol) in 5 mL chloroform was added, followed by the addition of NaN_3 (6.5 mg, 0.10 mmol) in 5 mL methanol. Black crystals of **1** were obtained by slow evaporation at room temperature in a week and collected by filtration. Yield 21.7 mg (28 % based on Fe salt). Selected IR data (cm^{-1}): 2069 (s, azido bridges), 1476 (m), 1429 (s), 1353 (m). Anal. Calc. for $C_{152}H_{144}B_4Fe_4N_{36}(CHCl_3)_2(CH_3OH)$: C 61.80 %, H 5.02 %, N 16.74 %; Found: C 62.32%, H 4.76%, N 16.46%.

Synthesis of $[(pydz)_4Fe^{II}_4(N_3)_4][BPh_4]_4 \cdot 4MeCN$ (2). The synthetic procedure for **2** was similar to that of **1** using pydz ligand in 5 mL dichloromethane instead. Black crystals of **2** obtained within a week were collected by filtration and washed with cold water and acetonitrile. Yield, 37.6 mg (36 % based on the Fe salt). Selected IR data (cm^{-1}): 2065 (s, azido bridges), 1458 (m), 1417 (m), 1261 (w). Anal. Calc. for $C_{156}H_{126}B_4Fe_4N_{30}(H_2O)_4$ C 67.90 %, H 4.89 %, N 15.23 %. Found C 67.84 %, H 4.78 %, N 14.75 %.

3.5 Results and discussion

3.5.1 Crystallographic studies

Slow evaporation of the methanol/acetonitrile/chloroform solution of $FeCl_2 \cdot 4H_2O$, pzdz (or pydz), NaN_3 and $NaBPh_4$ in stoichiometric ratio of 1:1:1:1 gave dark block crystals of **1** and **2**, respectively. Single crystal X-ray diffraction (SCXRD) studies at 100 K revealed that **1** crystallised in the triclinic space group *P*-1 while **2** in the tetragonal space group $I4_1/a$, and each is isomorphous to their Co(II) analogues (**Table 3.1** and **Table 3.2**). Selected bond distances and angles are listed in **Table 3.3** and **Table 3.4**.The powder XRD pattern of **2** under ambient atmosphere matches well with its SCXRD

simulation, indicating the purity and air-stability of the bulk products, while no peak was observed for the sample of **1** due to the serious loss of interstitial solvent molecules.

Table 3.1. Selected crystallographic data for **1**.

Empirical formula	$C_{168}H_{173}B_4Cl_{15}Fe_4N_{40}O_3$
Formula weight	3598.85
Temperature	100 K
Radiation	MoKα (λ = 0.71073)
Crystal size/mm^3	0.30 × 0.25 × 0.15
Crystal system	Triclinic
Space group	P-1
a/Å	18.0455(8)
b/Å	19.1164(8)
c/Å	28.9018(12)
α/°	89.217(2)
β/°	72.662(2)
γ/°	62.820(2)
Volume/Å^3	8377.7(6)
Z	2
ρ_{calc}g/cm^3	1.212
μ/mm^{-1}	0.449
F(000)	3192.0
2θ range /°	2.628 to 55.018
Reflections collected/unique	200342/37759
R_{int}	0.0545
R_{sigma}	0.0473
Goodness-of-fit on F^2	1.030
Final R indexes [I>2σ(I)]	R_1 = 0.0493, wR_2 = 0.1181
Final R indexes [all data]	R_1 = 0.0759, wR_2 = 0.1322
Largest diff. peak/hole / e Å^{-3}	0.59/-0.98

Table 3.2. Selected Crystallographic data of **2** at different temperatures.

Empirical formula	$C_{156}H_{126}B_4Fe_4N_{30}$			
Formula weight	2687.50			
Radiation	CuKα (λ = 1.54178)			
Crystal size/mm^3	0.25 × 0.25 × 0.20			
Crystal system	Tetragonal			
Space group	$I4_1/a$			
Temperature/K	100	150	200	300
a/Å	17.2401(3)	17.2652(8)	17.3036(3)	17.4466(3)
b/Å	17.2401(3)	17.2652(8)	17.3036(3)	17.4466(3)
c/Å	42.898(1)	43.062(3)	43.1803(10)	43.6969(13)
α/°	90	90	90	90
β/°	90	90	90	90
γ/°	90	90	90	90
Volume/Å^3	12750.2(5)	12836.1(1)	12928.8(5)	13300.6(6)
Z	4	4	4	4
ρ_{calc}g/cm^3	1.400	1.391	1.381	1.342
μ/mm^{-1}	4.124	4.097	4.067	3.954
F(000)	5584.0	5584.0	5584.0	5584.0
2θ range /°	8.03 to 136.6	5.51 to 130.3	10.2 to 136.8	7.91 to 130.3
Reflections collected/unique	37412/5831	26305/5831	26305/5831	26215/5667
R_{int}	0.0565	0.0794	0.0490	0.0622
R_{sigma}	0.0307	0.0739	0.0325	0.0590
Goodness-of-fit on F^2	1.068	0.996	1.057	1.024
Final R indexes [I>2σ(I)]	R_1 = 0.0369, wR_2 = 0.0965	R_1 = 0.0660, wR_2 = 0.1707	R_1 = 0.0335, wR_2 = 0.0904	R_1 = 0.0479, wR_2 = 0.1238
Final R indexes [all data]	R_1 = 0.0459, wR_2 = 0.1011	R_1 = 0.1027, wR_2 = 0.1994	R_1 = 0.0466, wR_2 = 0.0958	R_1 = 0.0748, wR_2 = 0.1408
Largest diff. peak/hole / e Å^{-3}	0.70/-0.23	0.54/-0.31	0.34/-0.27	0.28/-0.14

Table 3.3. Selected bond distance [Å] and angles [deg] of **1** at 100 K.

Fe1-N1	2.159(2)	Fe4-N16	2.183(2)	N4-Fe2-N9	175.67(8)
Fe1-N3	2.208(2)	Fe4-N18	2.179(2)	N4-Fe2-N7	109.22(9)
Fe1-N19	2.155(2)	Fe4-N22	2.195(2)	N4-Fe2-N34	93.30(9)
Fe1-N21	2.219(2)	Fe4-N24	2.160(2)	N4-Fe2-N25	84.56(8)
Fe1-N25	2.084(2)	Fe4-N28	2.101(2)	N4-Fe2-N6	72.65(9)
Fe1-N28	2.124(2)	Fe4-N31	2.121(2)	N15-Fe3-N10	172.35(8)
Fe2-N4	2.222(2)	N3-Fe1-N21	175.04(8)	N15-Fe3-N12	108.85(9)
Fe2-N6	2.154(2)	N3-Fe1-N19	111.07(8)	N15-Fe3-N34	93.04(9)
Fe2-N7	2.159(2)	N3-Fe1-N28	91.64(8)	N15-Fe3-N31	85.96(9)
Fe2-N9	2.221(2)	N3-Fe1-N25	85.99(9)	N15-Fe3-N13	72.46(8)
Fe2-N25	2.124(2)	N3-Fe1-N1	72.44(9)	Fe1-N25-Fe2	120.97
Fe2-N34	2.082(2)	N16-Fe4-N22	173.90(8)	Fe1-N28-Fe4	118.86
Fe3-N10	2.212(2)	N16-Fe4-N24	113.53(8)	Fe3-N34-Fe2	120.46
Fe3-N12	2.156(2)	N16-Fe4-N31	86.92(9)	Fe3-N31-Fe4	118.90
Fe3-N13	2.179(2)	N16-Fe4-N28	87.43(9)		
Fe3-N15	2.221(2)	N16-Fe4-N18	72.67(8)		
Fe3-N31	2.119(2)				
Fe3-N34	2.079(2)				

Table 3.4. Selected bond distance [Å] and angles [deg] of **2** at different temperatures.

	100 K	150 K	200 K	300 K
Fe1-N1	1.976(0)	1.999(4)	1.985(8)	2.150(3)
Fe1-N2	1.920(9)	1.940(4)	1.938(7)	2.141(2)
Fe1-N3C	1.930(6)	1.938(4)	1.945(8)	2.140(3)
Fe1-N4C	1.989(8)	1.986(4)	2.003(4)	2.179(3)
Fe1-N5	2.005(7)	2.002(3)	2.003(4)	2.069(3)
Fe1-N5C	2.011(8)	2.008(3)	2.017(4)	2.080(3)
N1-Fe1-N2	80.96(6)	80.60(15)	80.60(6)	74.84(10)
N1-Fe1-N3C	99.47(6)	98.04(15)	99.63(6)	103.44(9)
N1-Fe1-N4C	83.66(6)	83.35(14)	83.36(6)	81.89(10)
N1-Fe1-N5	166.43(6)	165.09(15)	165.88(7)	158.05(10)
N1-Fe1-N5C	93.42(6)	94.47(15)	93.49(6)	94.13(10)
N5-Fe1-N5C	91.80(9)	91.9(2)	92.24(9)	98.66(14)

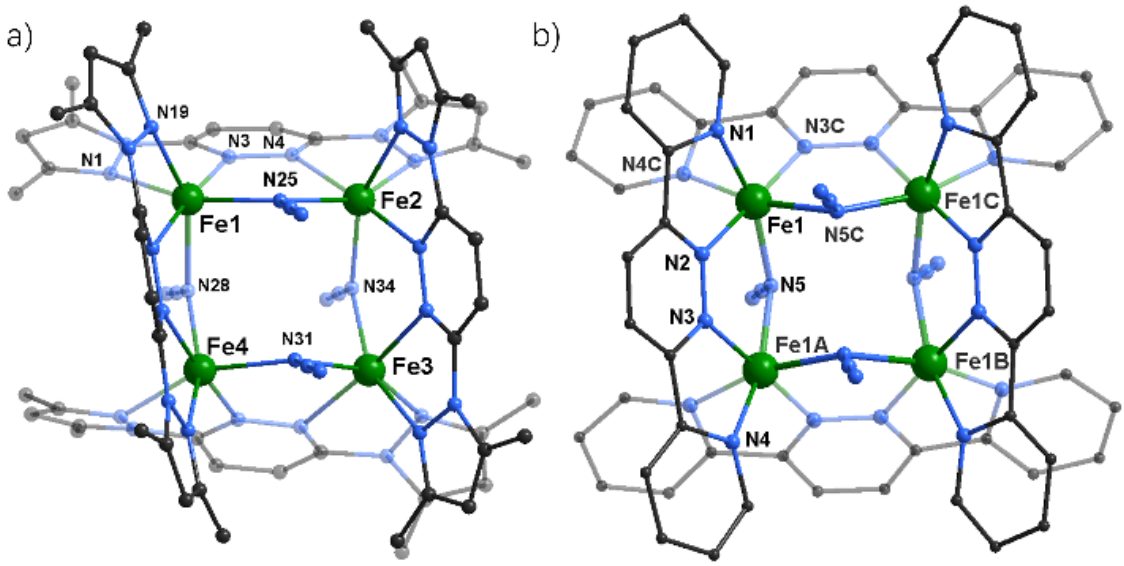

Figure 3.1. Crystal structures of **1** (a) and **2** (b) at 100 K with numbering scheme. Hydrogen atoms, counter ions and solvent molecules are omitted for clarity. Colour codes: Fe(II), green; C, grey; N, light blue.

As shown in **Figure 3.1**, both **1** and **2** feature a [2 × 2] grid-like structure, where the Fe^{II} ions reside in the corners and the neighbouring ions are linked simultaneously by one pyridazine and one EO-azido bridges. The asymmetric unit of **1** contains four crystallographically independent Fe^{II} ions, while only one is involved in the case of **2**. Each Fe^{II} ion displays a distorted octahedral geometry formed by six N atoms from two azides and two pzdz (for **1**) or pydz (for **2**) ligands. The Fe-N bond lengths are in the range of 2.080 – 2.222 Å (avg. 2.159 Å) for **1** and 1.920 – 2.011 Å (avg. 1.972 Å) for **2**, corresponding to the HS and LS states, respectively. This result demonstrated that the pydz ligands in **2** are able to stabilise the LS Fe(II) ion at low temperatures owing to a stronger ligand field. The bridging Fe-N_{azide}-Fe angles for **1** are 118.84° and 120.93°, slightly larger than those (117.30 and 117.54°) for **2**. The dihedral angles between the pyrazolyl- (or pyridyl-) and pyridazine rings are varying from 5.00 to 27.82° for **1** while in a narrow range of 11.27 - 11.40° for **2**. It should be mentioned that the [Fe^{II}_4] core in **1** displays a rather distorted square shape with the adjacent Fe···Fe

distances of 3.612 - 3.662 Å and the Fe···Fe···Fe vertex angles of 86.74 – 93.05°. Instead, the [Fe^{II}_4] core in **2** is in a nearly perfect square shape with the vertex angle of 89.97° and the adjacent Fe···Fe distance of 3.435 Å. The square molecules are well isolated by counter anions $[BPh_4]^-$ and interstitial solvents, with the shortest intermolecular Fe···Fe distance of 12.7 Å and 11.4 Å for **1** and **2**, respectively (**Figure 3.2** and **Figure 3.3**).

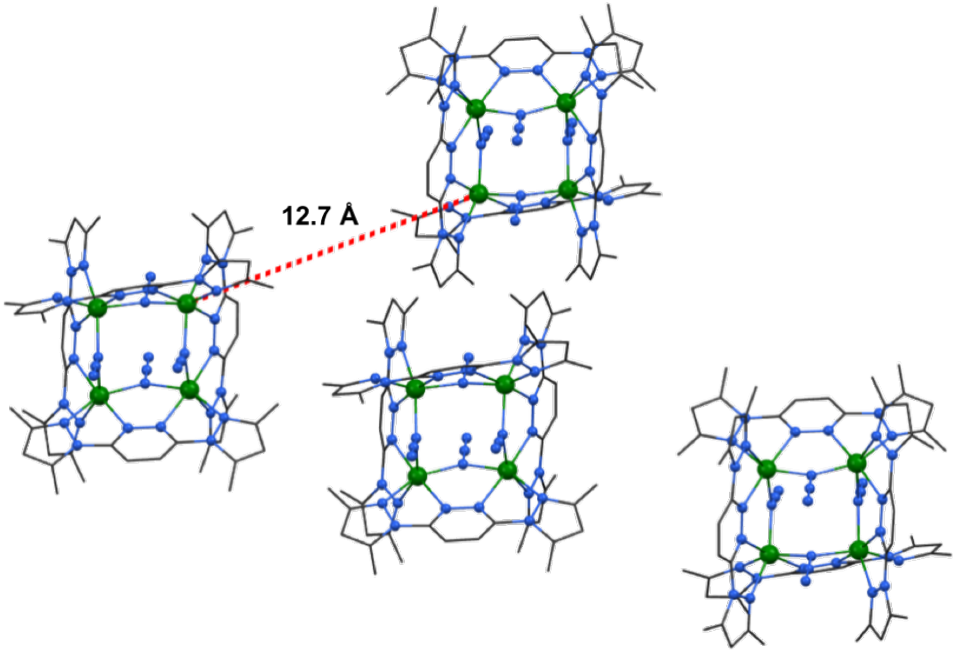

Figure 3.2. The packing diagram of **1**. Hydrogen atoms, counter ions and solvent molecules are omitted for clarity. The dashed lines show the nearest intermolecular Co···Co separation. Colour codes: Fe(II), green; C, grey; N, light blue.

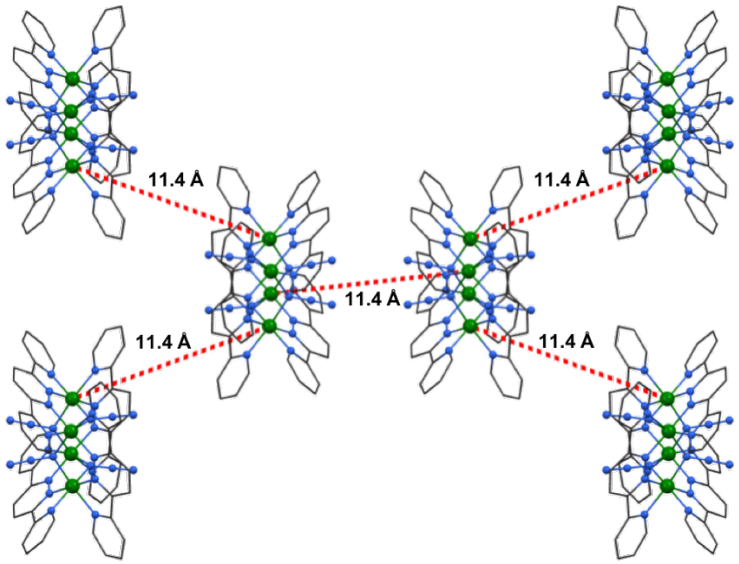

Figure 3.3. The packing diagram of **2**. Hydrogen atoms, counter ions and solvent molecules are omitted for clarity. The dashed lines show the nearest intermolecular Co···Co separation. Colour codes: Fe(II), green; C, grey; N, light blue.

Additional crystallographic data for **2** were further collected at selected temperatures of 150, 200, and 300 K, under a slow warming mode between the measurements. No change in the space group was found at all temperatures, while significant changes in the Fe-N bond distances were discovered. The average Fe-N bond lengths at 100, 150 and 200 K are nearly steady within the low-spin range, giving the values of 1.972, 1.979 and 1.985 Å, respectively. At 300 K the average Fe-N bond distance increased abruptly to 2.127(7) Å which is clearly assigned to the high-spin phase (**Table 3.5** and **Figure 3.4**). Such a clear elongation manifests the occurrence of thermally induced LS-to-HS SCO process in **2**. Correspondingly, the side Fe–Fe distance for the $[Fe^{II}_4]$ core increases slightly to 3.551 Å at 300 K. In addition, the distortion indices Σ (the sum of the deviations from 90° of the twelve cis-angles of the iron) and Θ (the sum of the deviations from 60° of the 24 unique torsion angles between adjacent N donors on opposite triangular faces of the octahedron) in the $[FeN_6]$ octahedral geometry can also be used to track the spin state change.[19] For **2** the Σ and Θ values are calculated to be 68.21°

and 188.01° at 100 K, which are dramatically smaller than those (Σ = 101.46° and Θ = 272.77°) at 300 K. This is in accordance with the general agreement that a HS Fe(II) ion displays a more plastic octahedral structure with larger distortion parameters than its LS one.[20]

Table 3.5. Distortion indices and average Fe-N bond distances of **2** at different temperatures.

Temp. / K	100	150	200	300
Σ / °	68.21	70.62	70.98	101.46
Θ / °	188.01	192.95	194.29	272.77
Avg. Fe-N Bond distances / Å*	1.972(19)	1.979(9)	1.985(15)	2.127(7)

* The average errors are calculated by the root mean square of the errors on the individual bond lengths.

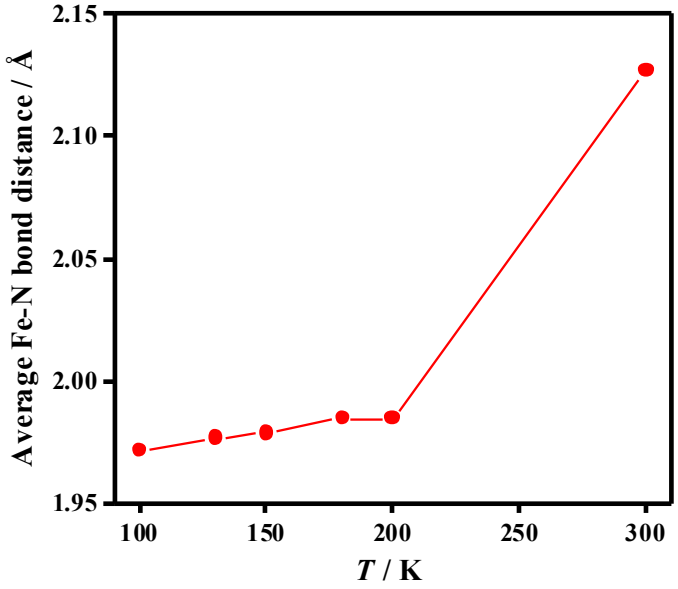

Figure 3.4. Temperature dependence of average Fe-N bond distances for complex **2**.

3.5.2 Mössbauer spectroscopy

The ^{57}Fe solid Mössbauer spectrum for **2** was further collected to determine the SCO process (**Figure 3.5**). At 300 K, the Mössbauer spectrum revealed a doublet with an isomer shift (δ) of 0.78 mm s^{-1} and a quadrupole splitting (ΔE_Q) of 1.81 mm s^{-1}, in well consistent with those HS Fe(II) complexes. Upon cooling to 80 K, the spectrum is fitted to δ = 0.30 mm sec^{-1}and ΔE_Q = 0.60 mm sec^{-1}, indicating the presence of LS Fe(II) ions.[21] It should be mentioned that the weak signals may hide the possible HS portion, which was observed by the magnetic study (vide infra) as well as the slightly longer Fe-N bond lengths at low temperatures (vide supra). It should be noted that the asymmetry of the doublet at 300 K might be attributed to the anisotropic orientations of crystals, because the sample was prepared via the fresh crystals without grinding. Another possible reason for the asymmetry could be the Goldanskii-Karyagin effect. Nevertheless, this dramatic change clearly confirms the occurrence of SCO event and is in good accordance with the crystallographic analysis.

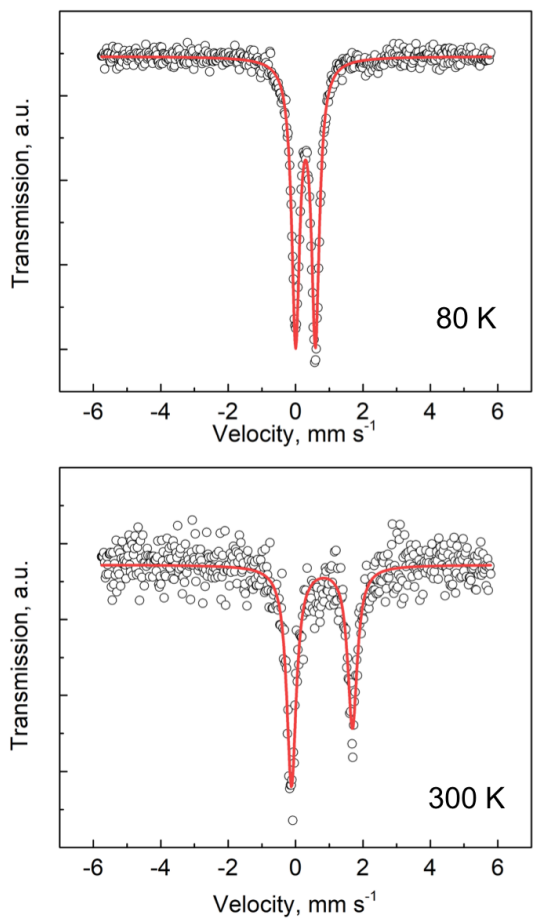

Figure 3.5. Mössbauer spectra of **2** measured at 80 K and 300 K. Solid lines are the best fittings to the data.

3.5.3 Magnetic studies

Variable-temperature magnetic susceptibilities for **1** and **2** were collected over the range of 2-300 K under an applied field of 1 kOe (**Figure 3.6**) with a 2 K min^{-1} sweeping rate. For **1**, the χT product of 12.77 cm^3 mol^{-1} K at 300 K agrees well with the sum of four isolated HS octahedral Fe^{II} ions (S = 2), assigned as $[Fe^{II,HS}_4]$. Upon cooling, the χT product of **1** decreases gradually until 5 K, and then more quickly to 6.66 cm^3 mol^{-1} K at 2 K, likely due to zero-field splitting and/or intermolecular antiferromagnetic coupling. The data was then fitted based on a square molecular model by the PHI programme[22] using the following Hamiltonian equation (eq. 3.1):

$$\hat{H} = -2J(\hat{S}_1\hat{S}_2 + \hat{S}_2\hat{S}_3 + \hat{S}_3\hat{S}_4 + \hat{S}_1\hat{S}_4) + \sum_{i=1}^{4}(D_{Fe,i}\hat{S}_{z,i}^{\ 2} + g_{Fe,i}\mu_B\hat{S}_{Fe,i}B) \quad \text{(eq. 3.1)}$$

where D_{Fe}, μ_B, g_{Fe}, B, J corresponds to the axial zero-field splitting (zfs) parameter, Bohr magneton, Landé factor, magnetic field vector and magnetic exchange between Fe(II) centres, respectively. Considering four high-spin Fe(II) ions are in a similar coordination environment, the best fitting gave D_{Fe} = -28.6 cm^{-1}, J = -0.04 cm^{-1} and g_{Fe} = 2.09. The small value of J indicates the negligible intra-cluster Fe-Fe interaction, which is not surprised because of the competitive and comparable ferromagnetic *vs*. antiferromagnetic (AF) coupling through the EO-azido bridge ($J \approx +3$ cm^{-1}) and diazine bridge ($J \approx -3$ cm^{-1}), respectively.[15a, 23] The obtained D parameter is comparable to those of high-spin Fe(II) ions in similar coordination environments. Field dependence of the magnetisation data exhibited continuous increase with a high-field non-saturation value of 6.29 Nβ at 2.0 K and 70 kOe (**Figure 3.7**), suggesting the presence of significant magnetic anisotropy. It should be noted that the attempts to either fit the χT-T and M-H data only failed due to the limit of the Hamiltonian matrix. To further verify the fitting results, simulations of the M-H plots were performed using the obtained spin Hamiltonian parameters. As a result, the simulated magnetisation data for **1** are in reasonable agreement with the experimental data, which could justify the reliability of the obtained parameters to a certain extent. No slow magnetic relaxation behaviour was observed, excluding the possible single-molecule magnet of **1**. Such behaviour may be possibly correlated with the anisotropic arrangements between the four Fe(II) metal ions, which may counteract each other leading to the decreased magnetic anisotropy for the entire molecule.

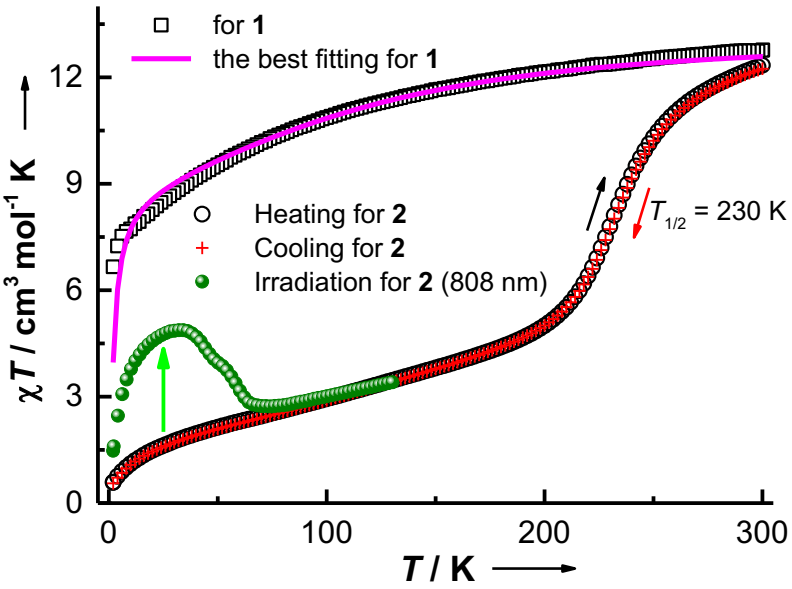

Figure 3.6. Temperature dependence of magnetic susceptibility data for **1** (□) and **2** (○, heating; +, cooling) collected in the dark (1 kOe) and after light irradiation at 808 nm for **2** (green, 10 kOe). The violet line represents the fitting based on eq. 3.1.

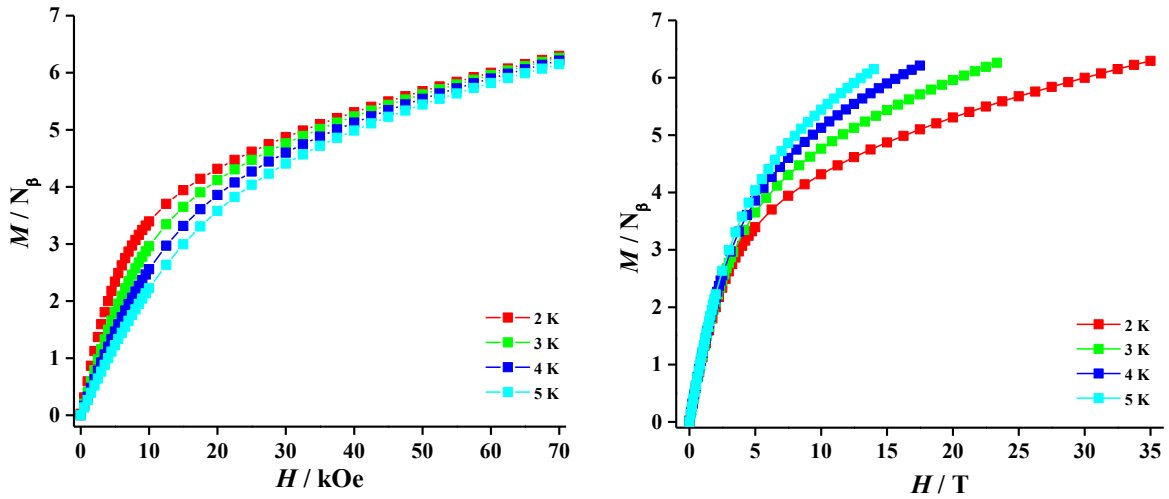

Figure 3.7. Reduced magnetisation plots for **1** at 2-5 K.

For **2**, the χT value of 12.34 cm^3 mol^{-1} K at 300 K is also consistent with the presence of four uncoupled HS Fe^{II} ions. Upon lowering the temperature, the χT product decreased gradually before an abrupt drop with the values changing from 11.5 cm^3 mol^{-1} K at 270 K to 5.0 cm^3 mol^{-1} K at 200

K, indicating an incomplete SCO event with a certain amount of residual HS components. The $T_{1/2}$ is estimated to be 230 K. Below 200 K, the χT value went through a slow and gradual decrease which may be attributed to the continuously transition to low-spin Fe(II) state, as implied by the variable-temperature crystallographic analysis (**Figure 3.4**). Similar trends were also found in other SCO complexes.[24] The final χT value reaches 0.59 cm^3 mol^{-1} K at 2 K, suggesting a nearly complete SCO conversion to LS state.[25] On warming back to 300 K, the χT product follows the same variation as seen in the cooling cycle, while no thermal hysteresis is observed.

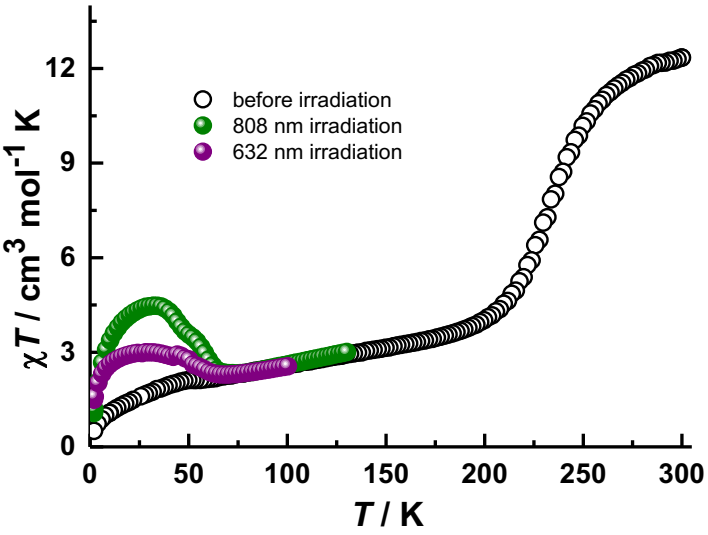

Figure 3.8. Magnetic susceptibility measurement of **2** under 10 kOe before and after 632 and 808 nm irradiation at 10 K.

To probe the possible LIESST effect of **2**, the photomagnetic behaviour were further investigated at low temperatures under light irradiation. Under a selected laser light (808 nm, 10 mW, based on the MLCT band, *vide supra*) at 10 K, the χT products increased abruptly and reached a maximum of 3.77 cm^3 mol^{-1} K in 8 h, suggesting that the diamagnetic [$Fe^{II,LS}_4$] phase were partially converted (36 %, in reference to the corresponding χT value of **1**) to the paramagnetic [$Fe^{II,HS}_4$] state. After

switching the light off and heating with 1 K min^{-1}, the χT values increased slowly to the maximum of 4.87 cm^3 mol^{-1} K at 32 K, corresponding to 19% photoconversion, which is attributed to the intermolecular antiferromagnetic interactions and/or the magnetic anisotropy of metal centres. Upon further heating, the metastable state undergoes the continuous decrease and finally relaxes back to the thermodynamic diamagnetic LS phase at ca. 65 K. Similar LIESST effect with less photoconversion was also observed when applying a laser light with 632 nm (**Figure 3.8**) which may be due to the light penetration.[26] The relaxation temperature T(LIESST) was determined to be 51 K and 59 K at 632 and 808 nm irradiation, respectively.

3.5.4 Photophysical studies

The UV-vis absorption spectra of **2** as well as pydz ligand were recorded in both solution and solid state at room temperature (**Figure 3.9**). The solid state absorption of **2** shows a broad peak in the visible range centred at 632 nm which are possibly attributed to the MLCT transition (also observed in solution of a broad peak centred at 547 nm) or low-lying d-d states.[27] Broad bands in the ultraviolet region <300 nm and around 400 nm are observed which are attributed to the π-π* transition of the ligand. The red shift of the ligand and **2** in solid state may be due to packing effects.

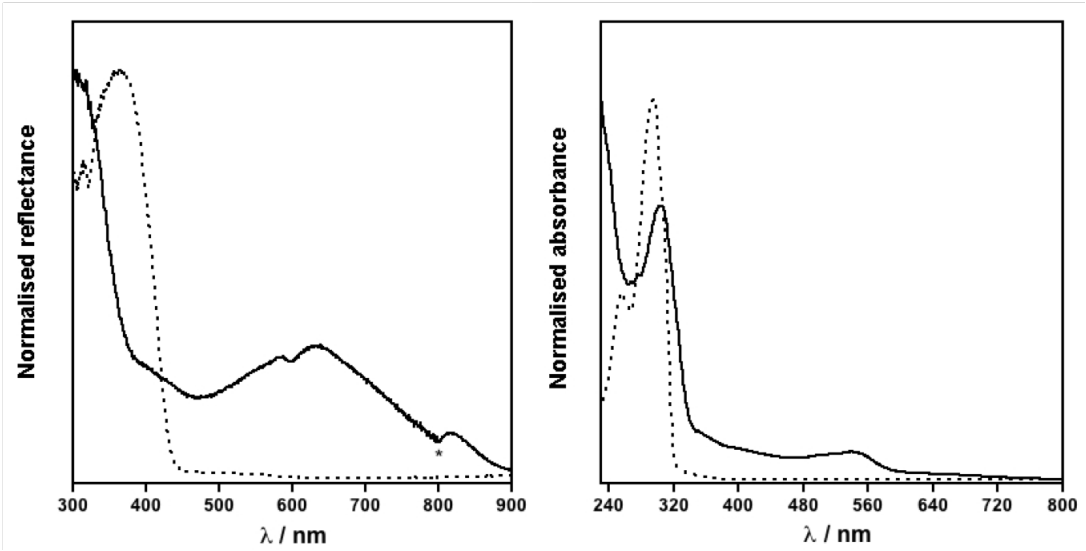

Figure 3.9. Solid state (left) and acetonitrile solution (right) UV-vis spectra of **2** (solid line) and pydz ligand (dashed line) at room temperature (* is an artefact due to lamp change at 800 nm).

To further probe the possible synergetic effect between SCO and luminescence, variable-temperature solid-state luminescent spectra of **2** were measured in the range of 77-300 K. As depicted in **Figure 3.10**, a broad emission with two distinct peaks at 435 nm and 465 nm was observed. This can be attributed to the emission of the π-π* of the pydz ligand as previously observed in frozen glass.[28] We examined the correlation of the magnetic susceptibility with the luminescence signal (integrated intensity). Unlike the commonly observed increasing of the intensity around the SCO transition temperature, the emission intensity of **2** showed a continued decreasing trend upon heating; yet it is interesting to observed that the rate of decrease of the luminescence signal changes at the exact SCO transition temperature of 230 K. Thermal quenching is usually decreased as temperature rises but the characteristic change is attributed to a synergistic effect of the paramagnetic iron quenching the luminescence signal by electron transfer.

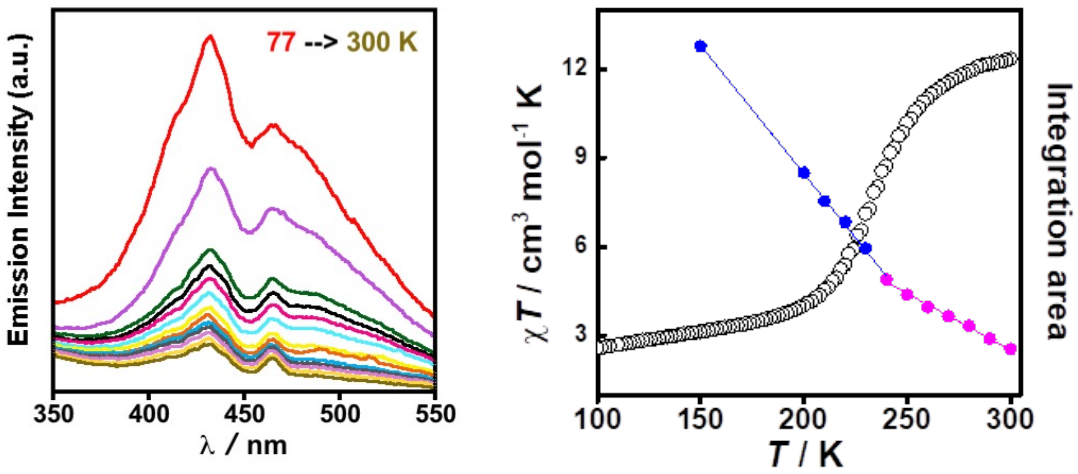

Figure 3.10. (left) Temperature dependent luminescence spectra of **2** under 300 nm excitation. (right) Overlay diagram of magnetic susceptibility and luminescence integration. Blue and purple solid lines indicate different decreasing rate of photoluminescence.

3.6 Conclusion

In conclusion, two novel [Fe^{II}_4] grids were constructed based on the coordination-driven supramolecular strategy for which **2** exhibited interesting SCO behaviour and a clear synergetic effect between the SCO and the luminescence. Remarkably, rational modification of the coordination surroundings of Fe(II) centres by using stronger ligands into the azido-bridged systems proved to be feasible and thus afforded the first example of azido-bridged SCO complexes. To extend this idea to other azido-bridged systems towards more SCO functionalised complexes and to realise site-selectivity SCO behaviour by using asymmetric ligands in this programmable family are under way.

3.7 References

1. P. Gütlich, Y. Garcia and H. A. Goodwin, *Chem. Soc. Rev.*, 2000, **29**, 419-427.

2. (a) S. Brooker, *Chem. Soc. Rev.*, 2015, **44**, 2880-2892; (b) K. S. Kumar and M. Ruben, *Angew. Chem. Int. Ed.*, 2019, **59**, 2-22.

3. Y. Garcia, F. Robert, A. D. Naik, G. Zhou, B. Tinant, K. Robeyns, S. Michotte and L. Piraux, *J. Am. Chem. Soc.*, 2011, **133**, 15850-15853.

4. L. Wiehl, G. Kiel, C. P. Koehler, H. Spiering and P. Guetlich, *Inorg. Chem.*, 1986, **25**, 1565-1571.

5. H. Phan, S. M. Benjamin, E. Steven, J. S. Brooks and M. Shatruk, *Angew. Chem. Int. Ed.*, 2015, **54**, 823-827.

6. (a) K. Senthil Kumar and M. Ruben, *Coord. Chem. Rev.*, 2017, **346**, 176-205; (b) Y.-S. Meng and T. Liu, *Acc. Chem. Res.*, 2019, **52**, 1369-1379; (c) H.-Y. Sun, Y.-S. Meng and T. Liu, *Chem. Commun.*, 2019, **55**, 8359-8373.

7. (a) Y. Jiao, J. Zhu, Y. Guo, W. He and Z. Guo, *J. Mater. Chem. C*, 2017, **5**, 5214-5222; (b) C. Lochenie, K. Schötz, F. Panzer, H. Kurz, B. Maier, F. Puchtler, S. Agarwal, A. Köhler and B. Weber, *J. Am. Chem. Soc.*, 2018, **140**, 700-709; (c) J. Yuan, S.-Q. Wu, M.-J. Liu, O. Sato and H.-Z. Kou, *J. Am. Chem. Soc.*, 2018, **140**, 9426-9433; (d) J.-Y. Ge, Z. Chen, L. Zhang, X. Liang, J. Su, M. Kurmoo and J.-L. Zuo, *Angew. Chem. Int. Ed.*, 2019, **58**, 8789-8793.

8. B. Benaicha, K. Van Do, A. Yangui, N. Pittala, A. Lusson, M. Sy, G. Bouchez, H. Fourati, C. J. Gómez-García, S. Triki and K. Boukheddaden, *Chem. Sci.*, 2019, **10**, 6791-6798.

9. (a) K. S. Murray, *Eur. J. Inorg. Chem.*, 2008, **2008**, 3101-3121; (b) R. W. Hogue, S. Singh and S. Brooker, *Chem. Soc. Rev.*, 2018, **47**, 7303-7338.

10. (a) N. O. Moussa, G. Molnár, S. Bonhommeau, A. Zwick, S. Mouri, K. Tanaka, J. A. Real and A. Bousseksou, *Phys. Rev. Lett.*, 2005, **94**, 107205; (b) C.-H. Shih, C.-F. Sheu, K. Kato, K. Sugimoto, J. Kim, Y. Wang and M. Takata, *Dalton Trans.*, 2010, **39**, 9794-9800; (c) T. Jasper-

Toennies, M. Gruber, S. Karan, H. Jacob, F. Tuczek and R. Berndt, *Nano Lett.*, 2017, **17**, 6613-6619.

11. (a) C.-J. Zhang, K.-T. Lian, G.-Z. Huang, S. Bala, Z.-P. Ni and M.-L. Tong, *Chem. Commun.*, 2019, **55**, 11033-11036; (b) Y.-Y. Peng, S.-G. Wu, Y.-C. Chen, W. Liu, G.-Z. Huang, Z.-P. Ni and M.-L. Tong, *Inorg. Chem. Front.*, 2020, **7**, 1685-1690.
12. (a) E. Breuning, M. Ruben, J.-M. Lehn, F. Renz, Y. Garcia, V. Ksenofontov, P. Gütlich, E. Wegelius and K. Rissanen, *Angew. Chem. Int. Ed.*, 2000, **39**, 2504-2507; (b) B. Schneider, S. Demeshko, S. Dechert and F. Meyer, *Angew. Chem. Int. Ed.*, 2010, **49**, 9274-9277; (c) R.-J. Wei, Q. Huo, J. Tao, R.-B. Huang and L.-S. Zheng, *Angew. Chem. Int. Ed.*, 2011, **50**, 8940-8943; (d) T. Matsumoto, G. N. Newton, T. Shiga, S. Hayami, Y. Matsui, H. Okamoto, R. Kumai, Y. Murakami and H. Oshio, *Nat. Commun.*, 2014, **5**, 3865.
13. (a) A. I. Nesterov, Y. S. Orlov, S. G. Ovchinnikov and S. V. Nikolaev, *Phys. Rev. B*, 2017, **96**, 134103; (b) B. Weber, *Coord. Chem. Rev.*, 2009, **253**, 2432-2449.
14. (a) A. Escuer, J. Esteban, S. P. Perlepes and T. C. Stamatatos, *Coord. Chem. Rev.*, 2014, **275**, 87-129; (b) A. Escuer and G. Aromí, *Eur. J. Inorg. Chem.*, 2006, **2006**, 4721-4736; (c) Y.-F. Zeng, X. Hu, F.-C. Liu and X.-H. Bu, *Chem. Soc. Rev.*, 2009, **38**, 469-480.
15. (a) D. I. Alexandropoulos, K. R. Vignesh, T. C. Stamatatos and K. R. Dunbar, *Chem. Sci.*, 2019, **10**, 1626-1633; (b) A. K. Boudalis, B. Donnadieu, V. Nastopoulos, J. M. Clemente-Juan, A. Mari, Y. Sanakis, J.-P. Tuchagues and S. P. Perlepes, *Angew. Chem. Int. Ed.*, 2004, **43**, 2266-2270.
16. (a) E. Andris, R. Navrátil, J. Jašík, G. Sabenya, M. Costas, M. Srnec and J. Roithová, *Angew. Chem. Int. Ed.*, 2017, **56**, 14057-14060; (b) I. Nemec, R. Herchel, R. Boča, Z. Trávníček, I. Svoboda, H. Fuess and W. Linert, *Dalton Trans.*, 2011, **40**, 10090-10099; (c) D. J. Rudd, C. R.

Goldsmith, A. P. Cole, T. D. P. Stack, K. O. Hodgson and B. Hedman, *Inorg. Chem.*, 2005, **44**, 1221-1229.

17. (a) Z. Guo, Y.-F. Deng, Y. Zhang, Z. Pikramenou and Y.-Z. Zhang, *Dalton Trans.*, 2020, **49**, 9218-9222; (b) R. Bruno, N. Marino, J. Cano, A. P. Alvarez, A. Ben Tama, F. Lloret, M. Julve and G. De Munno, *Crys. Growth Des.*, 2020, **20**, 6478-6492; (c) Z. Guo, Y.-F. Deng, Z. Pikramenou, K. R. Dunbar and Y.-Z. Zhang, *Inorg. Chem.*, 2021, **60**, 3651-3656.
18. L. K. Thompson, T. C. Woon, D. B. Murphy, E. J. Gabe, F. L. Lee and Y. Le Page, *Inorg. Chem.*, 1985, **24**, 4719-4725.
19. M. A. Halcrow, *Chem. Soc. Rev.*, 2011, **40**, 4119-4142.
20. (a) L. J. Kershaw Cook, R. Kulmaczewski, S. A. Barrett and M. A. Halcrow, *Inorg. Chem. Front.*, 2015, **2**, 662-670; (b) J.-T. Chen, X.-H. Zhao and Y.-Z. Zhang, *Dalton Trans.*, 2020, **49**, 5949-5956.
21. (a) T. Shiga, Y. Sato, M. Tachibana, H. Sato, T. Matsumoto, H. Sagayama, R. Kumai, Y. Murakami, G. N. Newton and H. Oshio, *Inorg. Chem.*, 2018, **57**, 14013-14017; (b) T. Shiga, D. Ishikawa, M. Tachibana, R. Saiki, G. N. Newton and H. Oshio, *J. Magn. Magn. Mater.*, 2019, **485**, 16-20.
22. N. F. Chilton, R. P. Anderson, L. D. Turner, A. Soncini and K. S. Murray, *J. Comput. Chem.*, 2013, **34**, 1164-1175.
23. A. Chatterjee, K. L. Thompson and K. S. Dey, *Magnetochemistry*, 2018, **4**.
24. (a) C. A. Tovee, C. A. Kilner, S. A. Barrett, J. A. Thomas and M. A. Halcrow, *Eur. J. Inorg. Chem.*, 2010, 1007-1012; (b) Y.-T. Wang, S.-T. Li, S.-Q. Wu, A.-L. Cui, D.-Z. Shen and H.-Z. Kou, *J. Am. Chem. Soc.*, 2013, **135**, 5942-5945.
25. S. Zaiter, C. Kirk, M. Taylor, Y. M. Klein, C. E. Housecroft, N. F. Sciortino, J. E. Clements, R. I. Cooper, C. J. Kepert and S. M. Neville, *Dalton Trans.*, 2019, **48**, 7337-7343.

26. S. De, L.-M. Chamoreau, H. El Said, Y. Li, A. Flambard, M.-L. Boillot, S. Tewary, G. Rajaraman and R. Lescouëzec, *Front. Chem.*, 2018, **6**, 326.

27. (a) L. Li, N. Saigo, Y. Zhang, D. J. Fanna, N. D. Shepherd, J. K. Clegg, R. Zheng, S. Hayami, L. F. Lindoy, J. R. Aldrich-Wright, C.-G. Li, J. K. Reynolds, D. G. Harman and F. Li, *J. Mater. Chem. C*, 2015, **3**, 7878-7882; (b) S. De, L.-M. Chamoreau, H. El Said, Y. Li, A. Flambard, M.-L. Boillot, S. Tewary, G. Rajaraman and R. Lescouëzec, *Front. Chem.*, 2018, **6**; (c) S. De, S. Tewary, D. Garnier, Y. Li, G. Gontard, L. Lisnard, A. Flambard, F. Breher, M.-L. Boillot, G. Rajaraman and R. Lescouëzec, *Eur. J. Inorg. Chem.*, 2018, **2018**, 414-428.

28. G. Denti, L. Sabatino, G. De Rosa, A. Bartolotta, G. Di Marco, V. Ricevuto and S. Campagna, *Inorg. Chem.*, 1989, **28**, 3309-3313.

Chapter 4

Strong Coupling and Slow Relaxation of the Magnetisation for an Air-Stable [Co_4] Square with Both Tetrazine Radicals and Azido Bridges

Zhilin Guo, Yi-Fei Deng, Zoe Pikramenou, Kim R. Dunbar and Yuan-Zhu Zhang.

A version of this manuscript has been accepted for publication in *Inorganic Chemistry*.

Reproduced with permission from [*Inorg. Chem.* 2021, **60**, 3651-3656].

4.1 Abstract

Introducing both tetrazine radical and azido bridges afforded two air-stable square complexes $[M^{II}_4(bpztz^{\bullet-})_4(N_3)_4]$ (M = Zn^{2+}, **1**; Co^{2+}, **2**; bpztz = 3,6-bis(3,5-dimethyl-pyrazolyl)-1,2,4,5-tetrazine), where the metal ions are co-bridged by $\mu_{1,1}$-azido bridges and tetrazine radicals. Magnetic studies revealed strong antiferromagnetic metal-radical interaction with a coupling constant of -64.7 cm^{-1} in the 2*J* formalism in **2**. Remarkably, **2** exhibits slow relaxation of magnetisation with an effective barrier for spin reverse of 96 K at zero applied field.

4.2 Introduction

Coordination-driven self-assembly[1] of supramolecular architectures continues to produce fascinating results in many interdisciplinary fields with various fundamental applications[2] including sensors, optics, spintronics, and catalysis. Elegant and intricate structures such as metallacycles, molecular knots, metal-organic polyhedra, metallocages, and interlocked molecules have been reported owing to the structural versatility of the metal ions and the directionality of the metal-ligand interactions based on coordination algorithm.[3] A key underpinning of research on this topic is the design of specific organic linkers that are coded to produce a desired topology. Of specific interest to the present work is the use of organic radical linkers in supramolecular architectures that exhibit strong direct magnetic couplings.[4]

The literature is replete with examples of compounds featuring metal spins coupled through closed-shell bridging ligands via an indirect super-exchange mechanism but many of these magnetic interactions are relatively weak especially when the bridging ligand spans a large distance. Although the chemistry is more challenging, the use of free radical bridges[5] is capable of propagating efficient spin exchange beyond the limit of distance and gives rise to much stronger magnetic interactions due

to the direct overlap of orbitals that bears the unpaired electrons. The growing body of research in this area has demonstrated that higher blocking temperatures for single-molecule magnets (SMMs) are achieved with paramagnetic bridges.[6] A remarkable recent example is a radical bridged dinuclear Co(II) compound that exhibits significantly higher relaxation times and hysteresis up to 15 K, among the very best properties reported for transition metal based SMMs.[6c]

The most common motif for supramolecular metallacycles is the molecular square which is due to the ease of satisfying the requirement for 90° angles between the metal corners with the use of linear organic linkers. Specifically, 3,6-substituted pyridazine and tetrazine derivatives have been used for the formation of various polygonal topologies including triangles, squares and pentagons mostly through the trans-bridging mode.[7] Such pre-programed topologies with tetrazine radical ligands haven been incorporated into coordination complexes including recent work from Dunbar and Murugesu groups who demonstrated that much stronger ferromagnetic or antiferromagnetic coupling up to $J \approx \pm 100$ cm^{-1} (in 2J formalism) between tetrazine radicals and paramagnetic metal ions can be realised, however less SMM behaviour was observed.[8] Given that the contribution to the spin reversal barrier in most transition metal complexes is dominated by axial zero-field splitting (D) and the magnetic coupling (J) these parameters are important to control.[9] It is well-known that the end-on (EO, $\mu_{1,1}$) azido bridge would engender appreciable and predictable ferromagnetic coupling, and we recently incorporated azide ions as secondary bridges and constructed two [Co_4] square complexes, in which the neutral pyridazine derivatives adopt *cis*- bridging modes as dictated by the EO-azido bridge (**Figure 4.1**). The ferromagnetic coupling constant was found to be approximately +4 cm^{-1} and both compounds exhibit typical field-induced slow relaxation in magnetisation.[10]

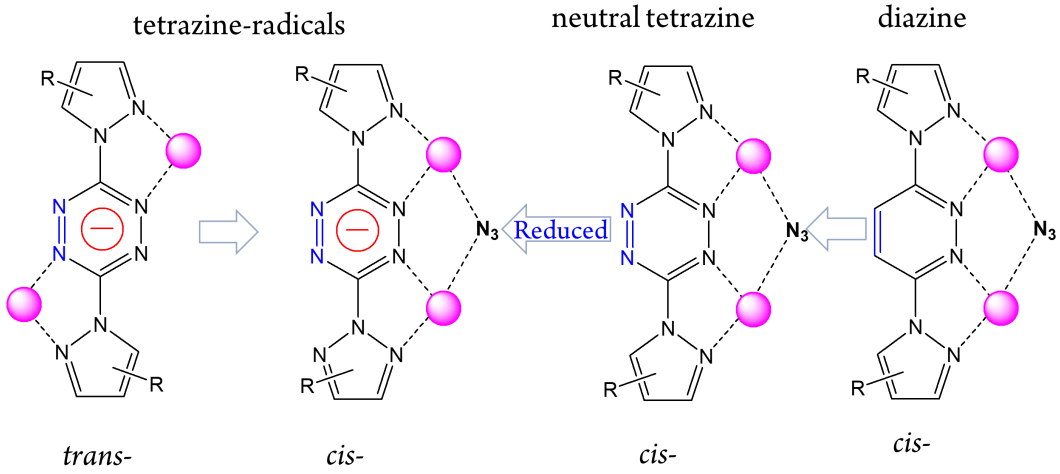

Figure 4.1. Coordination modes of tetrazine/diazines.

With this prior work as a backdrop as well as the above considerations, the related tetrazine derivative of bpztz anion radical formation was thus explored in the assembly of metal complexes within the selected topology bearing azide bridging ligand to further improve the magnetic communication. Herein we report the synthesis, structures and magnetic studies of the air-stable azido-bpztz co-bridged molecular squares $[M^{II}_4(bpztz^{\bullet-})_4(N_3)_4]$ (M = Zn^{2+}, **1**; Co^{2+}, **2**). Crystallographic and magnetic studies revealed a rare *cis*-tetrazine radical bridged $[M_4]$ square structure with magnetic coupling for **2** being significantly enhanced for the radical versus the diamagnetic bridging ligand. As a result, high-performance behaviour with an effective energy barrier of 96 K of **2** at zero dc field and clear magnetic hysteresis loops below 5 K were observed, which is the first example of *cis*-tetrazine radical bridged $[Co_4]$ square and among the highest relaxation barriers for the reported polynuclear Co(II) compounds.

4.3 Contribution

I started the project by doing the synthesis of the complexes and their characterisations including SCXRD, PXRD, UV-vis, CV, EPR measurements. I also did the magnetic measurements of the complexes. Dr Yi-Fei Deng helped with further characterisation on the metamagnetism of the complex as well as fitting of the magnetic data. I wrote the first draft of the manuscript then Dr Yi-Fei Deng, Prof Pikramenou, Prof Dunbar and Dr Zhang helped to revise.

4.4 Experimental Section

4.4.1 General methods

All syntheses were carried out under an argon atmosphere using a glove box. The starting materials are from commercially available sources and were used as received. Acetonitrile and dichloromethane were purified using a solvent purification system and stored over molecular sieves in the glove box. Anhydrous methanol was purchased from Energy Chem and stored over molecular sieves in a glove box.

Caution. Although no such issues were observed during the present work, azido and perchlorate salts are potentially explosive and should be handled with extreme caution.

X-ray data for were collected on a Bruker APEX-II CCD diffractometer using graphite monochromated Cu Kα radiation (λ = 1.54178 Å). The structure was solved with the ShelXT structure solution program using Intrinsic Phasing and refined in the ShelXL refinement package using Least Squares minimisation. Hydrogen atoms were added at calculated positions and refined using a riding model. Weighted R factors (wR) and the goodness-of-fit (S) values are based on F^2; conventional R factors (R) are based on F, with F set to zero for negative F^2. Powder X-ray Diffraction (PXRD) measurements were recorded on a Rigaku Smartlab X-ray diffractometer. FT-IR spectra were

recorded in the range 600-4000 cm^{-1} on a Bruker tensor II spectrophotometer. Elemental analyses (C, H, N) were measured by a vario EL cube CHNOS Elemental Analyzer Elementar Analysensysteme GmbH. UV-vis absorption spectra were recorded on an Agilent Cary 5000 UV-vis spectrophotometer. Solid state reflectance spectra were recorded on the same instrument with a corresponding integrating sphere from Agilent. Cyclic voltammetry (CV) measurements were carried out on a CHI760E electrochemical workstation (Chenhua Co. Ltd., China) equipped with a Pt working electrode. Ag/AgCl was used as the reference electrode. The measurements were performed under nitrogen atmosphere in dichloromethane solution with a 0.4 mM concentration of the complex in the presence of 0.1 M $[_nBu_4N][PF_6]$ as the supporting electrolyte at a scan rate of 0.1 $V \cdot s^{-1}$. The specific heat measurements were conducted using a PPMS DynaCool-9T system. Magnetic measurements were carried out on a SQUID MPMS3 magnetometer. Diamagnetic corrections were calculated from Pascal constants and applied to all the constituent atoms and sample holder.

4.4.2 Synthesis

Synthesis of $[Zn_4(bpztz^{\bullet-})_4(N_3)_4]$ (1): $[Zn(H_2O)_6][ClO_4]_2$ (37.2 mg, 0.1 mmol) and L-ascorbic acid (26.5 mg, 0.15 mmol) were dissolved in 3 mL acetonitrile and 1 mL methanol, to which bpztz (27.2 mg, 0.1 mmol) in 4 mL dichloromethane was added, followed by NaN_3 (9.1 mg, 0.14 mmol) in 4 mL methanol. The resulting brown solution was slowly evaporated at room temperature for three days which yielded black block crystals of **1**. The product was collected by filtration and washed with acetonitrile. Yield 9.6 mg (26 % based on bpztz). Anal. Calc. for $C_{48}H_{56}Zn_4N_{44}$ C, 38.16 %; H, 3.74 %; N, 40.79 %. Found C, 38.34 %; H, 3.88 %; N, 40.29 %. Selected IR data (cm^{-1}): 2361 (m), 2338 (w), 2074 (s), 1573 (m), 1477 (m), 1408 (s), 1320 (m), 1294 (m), 1121 (m), 1063 (m), 1043 (m), 985 (m).

Synthesis of $[Co_4(bpztz^{\bullet-})_4(N_3)_4]$ (2): Black block crystals of **2** were obtained by following a similar procedure to that of **1** with the starting material $[Co(H_2O)_6][ClO_4]_2$ (36.8 mg, 0.1 mmol). Yield 13.4 mg (36 % based on bpztz). Anal. Calc. for $C_{48}H_{56}Co_4N_{44}$ C, 38.82 %; H, 3.80 %; N, 41.50 %.

Found C, 38.65 %; H, 3.49 %; N, 41.25 %. Selected IR data (cm^{-1}): 2363 (m), 2338 (w), 2053 (s), 1571 (m), 1478 (m), 1411 (s), 1323 (m), 1283 (m), 1125 (m), 1065 (m), 1041 (m), 987 (m).

4.5 Results and discussion

4.5.1 Crystal Structures

Treatment of $[Zn(H_2O)_6][ClO_4]_2$ or $[Co(H_2O)_6][ClO_4]_2$ with bpztz ligand in 1:1 ratio with slightly excess of sodium azide and L-ascorbic acid in an inert atmosphere yielded compounds **1** and **2**. Single-crystal X-ray diffraction (SCXRD) studies revealed that **1** and **2** crystallise in the tetragonal space group $I4_1/acd$ (**Table 4.1**). Select bond distances and angles are listed in **Table 4.2**. Bond valence sum (BVS) calculations (**Table 4.3**) indicate the presence of 2+ oxidation state of Co and Zn which, considering overall charge balance, means that all bpztz ligands have been reduced to radicals. This was further confirmed by room-temperature EPR data of **1** in solid state which g_{rad} = 2.003 (**Figure 4.2**). Powder X-ray diffraction patters of **1** and **2** under ambient condition matched well with the SCXRD simulation, indicating high purity and air stability for the compound.

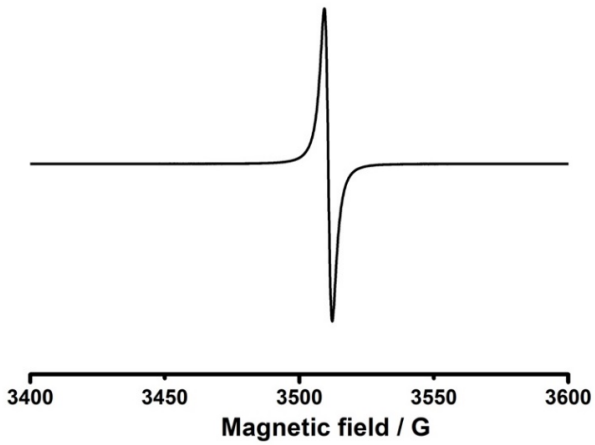

Figure 4.2. EPR spectrum of **1** in the solid state at room temperature giving g_{rad} = 2.003.

Table 4.1. Crystallographic data of **1** and **2**.

	1	**2**
Empirical formula	$C_{48}H_{56}N_{44}Zn_4$	$C_{48}H_{56}Co_4N_{44}$
Formula weight	1510.84	1485.08
Temperature/K	150(2)	100(2)
Crystal system	tetragonal	tetragonal
Space group	$I4_1/acd$	$I4_1/acd$
a/Å	17.3851(8)	17.3642(5)
b/Å	17.3851(8)	17.3642(5)
c/Å	42.117(2)	41.7879(12)
α/°	90	90
β/°	90	90
γ/°	90	90
Volume/Å^3	12729.6(13)	12599.7(8)
Z	8	8
ρ_{calc}g/cm^3	1.577	1.566
μ/mm^{-1}	2.333	8.734
F(000)	6176	6080
Crystal size/mm^3	0.2 × 0.2 × 0.15	0.21 × 0.18 × 0.07
Radiation	CuKα (λ = 1.54178)	CuKα (λ = 1.54178)
2θ range for data collection/°	11.01 to 136.96	8.35 to 136.81
Reflections collected	30639	27656
Independent reflections	2930 [R_{int} = 0.0487]	2898 [R_{int} = 0.0754]
Goodness-of-fit on F^2	1.077	1.037
completeness	99.8 %	99.9 %
Final R indexes [I>2σ(I)][a,b]	R_1 = 0.0417, wR_2 = 0.1007	R_1 = 0.0379, wR_2 = 0.0866
Final R indexes [all data]	R_1 = 0.0492, wR_2 = 0.1060	R_1 = 0.0488, wR_2 = 0.0923
Largest diff. peak/hole/ e Å^{-3}	0.65/-0.41	0.65/-0.42

Table 4.2. Selected bond distances (Å) and bond angles (deg) for **1** and **2**.

1		**2**	
Zn1-N2	2.183(2)	Co1-N1	2.158(2)
Zn1-N2A	2.183(2)	Co1-N1A	2.158(2)
Zn1-N9	2.096(2)	Co1-N2	2.052(2)
Zn1-N9A	2.096(2)	Co1-N2A	2.052(2)
Zn1-N1A	2.218(2)	Co1-N9A	2.119(2)
Zn1-N1	2.218(2)	Co1-N9	2.119(2)
Zn2-N9	2.132(2)	Co2-N4A	2.185(2)
Zn2-N9B	2.132(2)	Co2-N4B	2.185(2)
Zn2-N3	2.082(2)	Co2-N3A	2.121 (2)
Zn2-N3B	2.082(2)	Co2-N3B	2.121(2)
Zn2-N4	2.231(3)	Co2-N9	2.091(2)
Zn2-N4B	2.231(3)	Co2-N9C	2.091(2)
N2-N3	1.378(3)	N2-N3	1.377(3)
N6-N7	1.400(3)	N6-N7	1.397(3)
N2-Zn1-N1A	111.08(8)	N2-Co1-N1A	105.73(8)
N2-Zn1-N1	71.23(8)	N2-Co1-N1	74.51(8)
N2-Zn1-N9A	94.34(9)	N2-Co1-N9A	85.77(8)
N2-Zn1-N9	83.76(9)	N2-Co1-N9	94.04(8)
N9-Zn1-N9A	99.14(14)	N1-Co1-N1A	84.67(12)
N9A-Zn1-N1	94.46(9)	N1-Co1-N9	89.51(8)
N1-Zn1-N1A	84.05(12)	N9-Co1-N9A	103.84(12)
N9-Zn1-N9B	102.20(13)	N4A-Co2-N4B	83.39(11)
N9-Zn1-N4B	90.41(11)	N3B-Co2-N4B	72.42(7)
N3-Zn2-N9	86.79(9)	N3A-Co2-N4B	111.92(8)
N3-Zn2-N9B	95.97(9)	N9-Co2-N4B	93.94(8)
N3B-Zn2-N4	103.59(10)	N9-Co2-N3A	83.93(8)
N3-Zn2-N4	73.04(9)	N9-Co2-N3B	92.54(8)
N4-Zn2-N4B	84.49(18)	N9-Co2-N9C	100.00(12)

Symmetry operation for **1**. A*:* 5/4-y, 5/4-x, 5/4-z; B*:* 1-x, 3/2-y, z

Symmetry operation for **2**. A: 1-x, 1/2-y, z; B: 3/4-y, 3/4-x, 3/4-z; C: 1/4+y, -1/4+x, 3/4-z

Table 4.3. Bond Valence Sum (BVS) calculations for **1** and **2**.

1		**2**		
	Zn^{II}		Co^{II}	Co^{III}
Zn1	2.08(0)	Co1	2.10(9)	1.94(5)
Zn2	2.18(6)	Co2	1.98(0)	1.82(6)

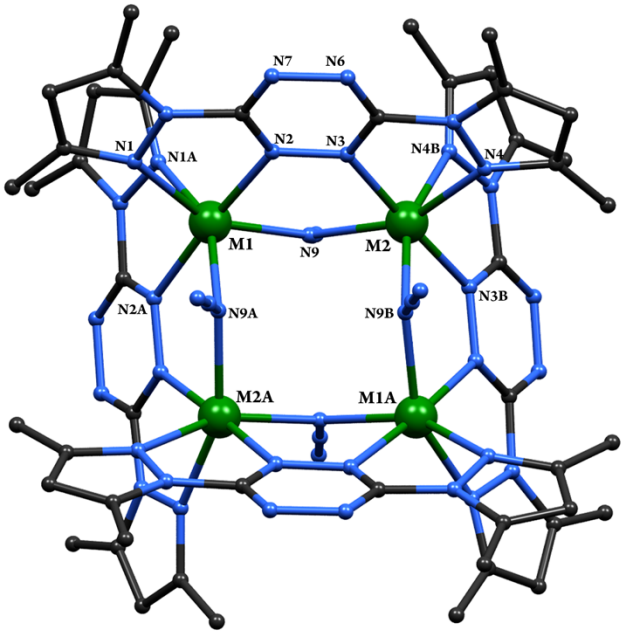

Figure 4.3. A ball-and-stick structure of **1** (M = Zn^{2+}) and **2** (M = Co^{2+}) with a numbering scheme. Hydrogen atoms were omitted for the sake of clarity.

As shown in **Figure 4.3**, the neighbouring metal ions reside at corners and are linked by one bpztz ligand in a *cis* mode and one $\mu_{1,1}$-azido bridge to form a neutral molecular square [M_4]. There are two crystallographically independent metal ions (M1 and M2) in the asymmetric unit. Each M^{II} ion adopts a distorted octahedral coordination geometry formed by four N atoms from two different bpztz ligands and two N atoms from azido ligands. The M-N bond distances and the *cis* N-M-N angles are in the range of 2.082 - 2.231 Å and 71.23 - 111.08° for **1**, 2.052 - 2.185 Å and 74.51 - 111.92° for **2**,

respectively. The Co-N bond distances in **2** are consistent with those for a high spin Co(II) ion. The bridging M-N_{azido}-M angle is 117.63° for **1** and 117.89° for **2**, respectively. Significant elongation of the N-N intra-tetrazine bond distances of 1.378 Å (N2-N3) and 1.400 Å (N6-N7) in **1**, 1.377 Å (N2-N3) and 1.397 Å (N6-N7) in **2**, respectively, compared with the neutral tetrazine ligand (~ 1.32 Å) strongly support the formation of tetrazine radical in **1** and **2**.[8c, 11] It should be mentioned that the dihedral angles between the pyrazolyl and tetrazine rings of the bpztz ligand in **2** are 3.32 and 10.21°, indicating increased coplanarity compared to the previously reported diamagnetic analogues (4.19 - 26.06°). Moreover, the chelating N_{pz}-M-N_{tz} (N1-Co1-N2 and N3-Co2-N4) angles of 74.51 and 72.41° in **2** are significantly smaller than those for the related [Co_4] complexes in a *trans* binding mode. The [Co_4] core is nearly planar with adjacent Co···Co distances of 3.606 Å and vertex Co-Co-Co angles of 92.83° and 87.17° for **2** with similar parameters of 3.617 Å, 92.38° and 87.62° for **1**. The shortest intermolecular M···M separation is 9.98 Å and 10.29 Å for **1** and **2**, respectively. It is worth noting that extensive short contacts were found throughout the 3D packing arrangement involving weak $H_{pz}\cdots N_{azide}$ hydrogen bonds (**1**, 3.042 Å; **2**, 3.142 Å), non-covalent C-H···π interactions (**1**, 2.455-3.217 Å; **2**, 2.418-3.232 Å) and edge-to-edge (**1**, 4.107 Å; **2**, 4.072 Å) π···π interactions (**Figure 4.4** and **Figure 4.5**). Such supramolecular interactions give rise to appreciable intermolecular magnetic interactions which accounts for the long-range antiferromagnetic ordering for this large spin system (*vide infra*).

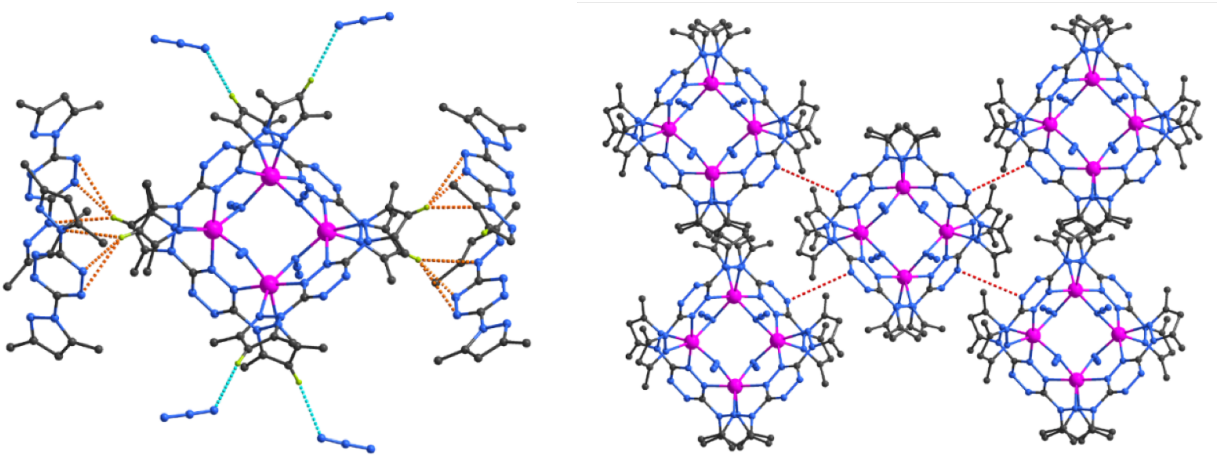

Figure 4.4. Ball and stick view of **1** highlighting the short contacts around the square (left) and between the packed molecules (right). The turquoise, orange and red dashed lines indicate the hydrogen bonds (3.042 Å), C···H···π couplings (2.455-3.217 Å) and edge-to-edge π···π interactions (4.107 Å), respectively. Colour codes: Zn, pink; C, grey; N, blue; H, lime. Other hydrogen or metal atoms are omitted for clarity.

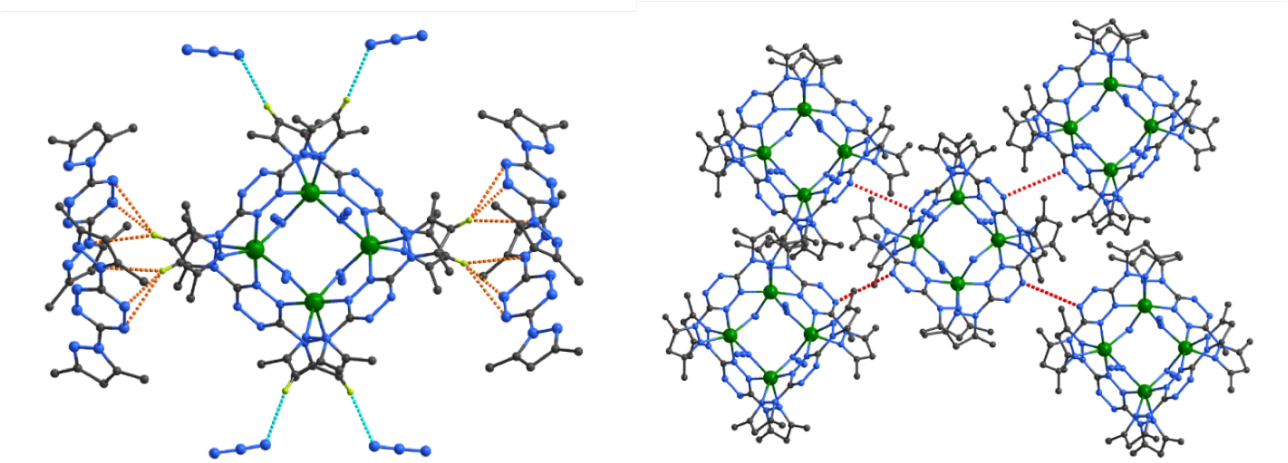

Figure 4.5. Ball and stick view of **2** highlighting the short contacts around the perimeter of the square (left) and between the packed molecules (right). The turquoise, orange and red dashed lines indicate the hydrogen bonds (3.142 Å), C···H···π couplings (2.418-3.232 Å) and edge-to-edge π···π interactions (4.072 Å). Colour codes: Co, green; C, grey; N, blue; H, lime. Other hydrogen or metal atoms are omitted for clarity.

4.5.2 UV-vis spectroscopy

UV-vis spectroscopy is also performed to study the tetrazine radical formation. In solution, neutral bpztz ligand shows a strong π-π* transition at 298 nm and less intense n-π* transition bands at visible region.[12] For **1** and **2**, the π-π* transition absorption bands are blue-shifted to 280 nm due to decreased conjugation. The absorption bands at visible region show clear red shift which is the influence of n-π* contributions upon coordination. This is consistent with the previously reported N-heterocylic radicals,[13] which clearly supports the tetrazine radicals in **1** and **2** (**Figure 4.6**). In solid state (**Figure 4.7**), the band at 530 nm of the spectrum can be possibly attributed to excimer formation. The bands of **1** and **2** in solid state can be also attributed to packing or extensive electronic communication between ligands which alters the HOMO-LUMO of n-π* transition.

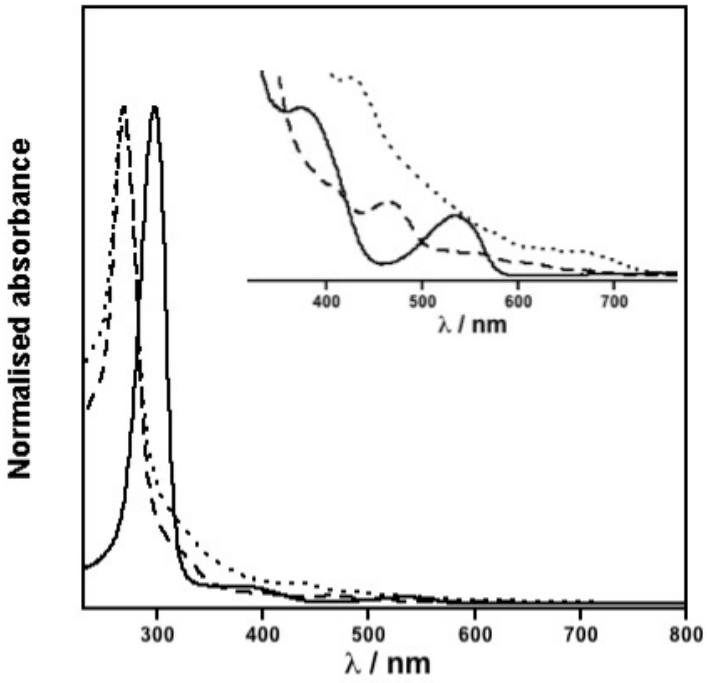

Figure 4.6. UV-vis spectra of bpztz ligand (solid line), **1** (dashed line) and **2** (dotted line) in CH_2Cl_2 solution.

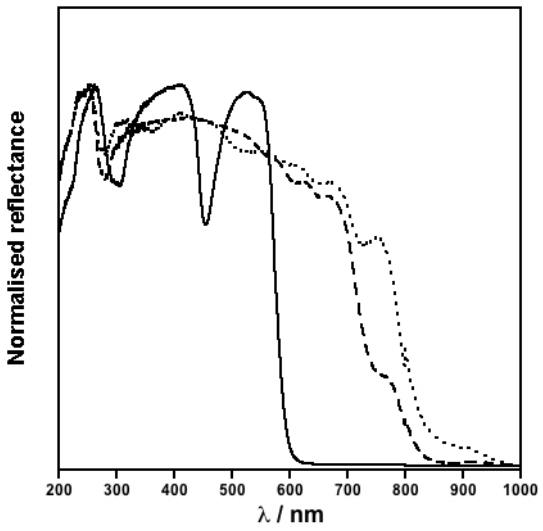

Figure 4.7. Solid state absorption spectra of neutral bpztz ligand (solid line), **1** (dashed line) and **2** (dotted line).

4.5.3 Electrochemical properties

The electrochemical property of **2** studied by cyclic voltammetry method in dichloromethane revealed four consecutive and reversible redox potentials at $E_{1/2}$ = +0.31, +0.47, +0.63 and +0.79 V (vs Ag/AgCl, **Figure 4.8**), which were assigned to the four one-electron oxidation processes of $[Co^{III}_1Co^{II}_3]^{+}$, $[Co^{III}_2Co^{II}_2]^{2+}$, $[Co^{III}_3Co^{II}_1]^{3+}$ and $[Co^{III}_4]^{4+}$ states, respectively. In addition, the reversible one-electron reduction at $E_{1/2}$ = -1.3 V is most likely attributed to bpztz radical reduction. Given that ΔE (the redox potential difference) is the same (0.16 V) for the four redox waves, the calculated comproportionation constants (*K*c) based on $Kc = \exp(F\Delta E/RT)$ were found to be 5.07×10^2, indicating the intermediated stability of mixed valence states.

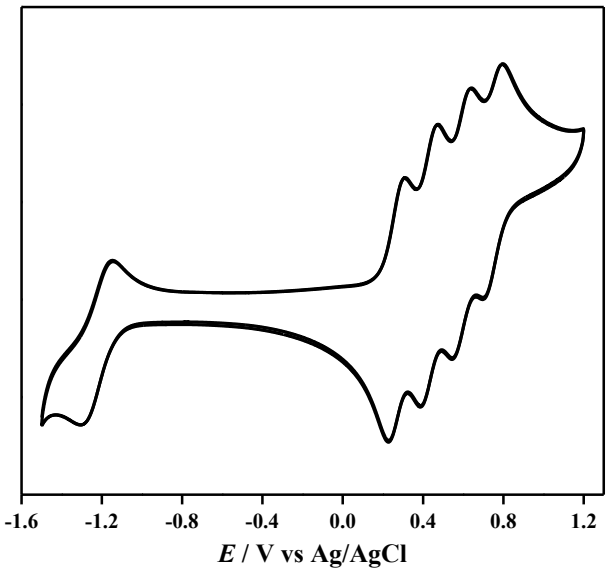

Figure 4.8. Cyclic voltammetry spectrum of **2** in CH_2Cl_2 solution (in 0.1 M $[_nBu_4N][PF_6]$ supporting electrolyte) with a Pt working electrode at a scan rate of 0.1 V/s at room temperature.

4.5.4 Magnetic studies

Variable-temperature magnetic susceptibility data for **1** and **2** were collected with applied direct current (dc) fields of 0.1 and 1 kOe (**Figure 4.9**). The χT value at 300 K of 1.46 cm^3 mol^{-1} K for **1** is consistent with four non-interacting $bpztz^{\bullet-}$ radicals (S_{rad} = 1/2, g = 2.003). Upon cooling, the χT value remains essentially constant down to 50 K and then decreases to 0.122 cm^3 K mol^{-1} at 2 K, indicating antiferromagnetic (AF) interactions between the radicals. In the case of **2**, the χT value of 13.67 cm^3 K mol^{-1} at 300 K is significantly higher than the theoretically calculated for four isolated high-spin Co^{II} ions (1.85 cm^3 K mol^{-1} each) and four uncoupled $bpztz^{\bullet-}$ radicals, indicating the significant orbital contribution.[14] Upon cooling, the χT value increases continuously to a maximum of 29.16 cm^3 mol^{-1} K at 37 K and then decreases to 0.64 cm^3 K mol^{-1} at 2 K, likely due to the presence of inter-molecular AF interactions, magnetic anisotropy and/or blocking dynamics.

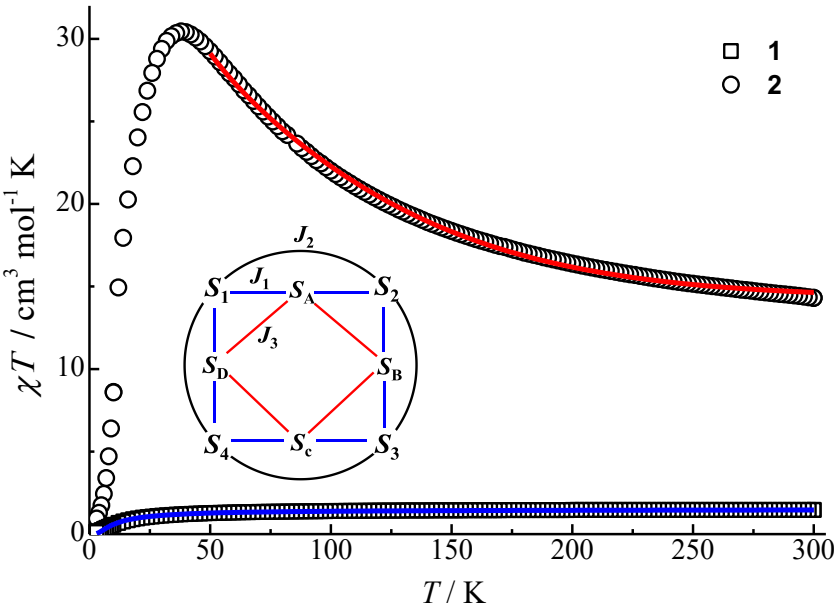

Figure 4.9. Variable-temperature magnetic susceptibility data for **1**(□) and **2**(O) under an applied dc field of 1 kOe. Solid lines represent the fittings based on eq. 1 and eq. 2. Inset shows the magnetic exchange pathways in **2**.

To probe the magnetic coupling between the spin carriers, the magnetic susceptibility data for **1** (2-300 K) and **2** (50-300 K) were fitted using the PHI programme[15] based on the following spin Hamiltonian (eq. 1 for **1** and eq. 2 for **2**):

$$\hat{H} = -2J_3(\hat{S}_A\hat{S}_B + \hat{S}_B\hat{S}_C + \hat{S}_C\hat{S}_D + \hat{S}_D\hat{S}_A) + (\sum_{i=A}^{D} g_{rad}\mu_B\hat{S}_i H) \qquad \cdots\cdots \text{eq. 1}$$

$$\hat{H} = -2J_1(\hat{S}_1\hat{S}_A + \hat{S}_A\hat{S}_2 + \hat{S}_2\hat{S}_B + \hat{S}_B\hat{S}_3 + \hat{S}_3\hat{S}_C + \hat{S}_C\hat{S}_4 + \hat{S}_4\hat{S}_D + \hat{S}_D\hat{S}_1) + (\sum_{i=A}^{D} g_{rad}\mu_B\hat{S}_i H)$$
$$+(\sum_{i=1}^{4} g_{Co}\mu_B\hat{S}_i H) - 2J_2(\hat{S}_1\hat{S}_2 + \hat{S}_2\hat{S}_3 + \hat{S}_3\hat{S}_4 + \hat{S}_4\hat{S}_1) - 2J_3(\hat{S}_A\hat{S}_B + \hat{S}_B\hat{S}_C + \hat{S}_C\hat{S}_D + \hat{S}_D\hat{S}_A)$$
$$\cdots\cdots \text{eq. 2}$$

where S_1 to S_4 = S_{Co} = 3/2, S_A to S_D = S_{rad} = 1/2, μ_B is the Bohr magneton, H is the magnetic field vector, g_{Co} and g_{rad} (2.003 as determined by EPR studies) are the Lande factors for Co(II) ion and bpztz$^{\bullet-}$ radical, respectively; J_1 to J_3 correspond to the magnetic couplings for Co···radical, Co···Co

and the neighbouring radicals, respectively. It should be mentioned that no acceptable fitting of χT vs T plots was achieved over the 2-300 K temperature range using an anisotropic spin model, possibly due to the low temperature complexity including the metamagnetism, antiferromagnetic ordering and relaxation dynamics. In addition, the incorporation of more anisotropic parameters in this advanced model would lead to the over-parameterisation. On the basis that the high temperature magnetic susceptibility should be dominated by the strong exchange couplings mediated by bpztz$^{\bullet-}$ radical bridges, the χT vs T plots at above 50 K were thus fitted with an isotropic spin model. Moreover, given that the [Zn_4] analogue can be unambiguously characterised over the entire temperature, the coupling constant between the neighbouring bpztz$^{\bullet-}$ radicals was thus restrained as the same across the two data sets of **1** and **2** to avoid the over-parameterisation. With the addition of the intermolecular couplings (*zj'*) based on the mean-field approximation,[16] the best fitting gave J_3 = -4.7 cm^{-1}, and *zj'* = -0.2 cm^{-1} for **1**. For **2**, *zj'* can be neglected in the high-temperature range, and J_3 was fixed to -4.7 cm^{-1} in the fitting process to reduce the parameter space. The best set of parameters are J_1 = -64.7 cm^{-1}, J_2 = +4.9 cm^{-1}, g_{Co} = 2.81. It should be noted that attempts to fit the susceptibility data of **2** with a free J_3 parameter did not improve the quality significantly and gave similar results. The obtained $J_{Co}\cdots$rad value is similar to that observed for bptz$^{\bullet-}$ radical bridged [Co^{II}_3] (-67.5 cm^{-1}) and [Co^{II}_4] (-66.8 cm^{-1}) complexes and confirms the strong AF coupling between the Co(II) metal centres and bpztz$^{\bullet-}$ radicals.

The isothermal field-dependent magnetisation of **2** measured at 2 K exhibits a pronounced sigmoidal behaviour with an initial slow increase (**Figure 4.10**), corresponding to an *AF* ordered state, and then a sharp transition to a superparamagnetic state, reaching an unsaturated value of 11.4 Nβ at 70 kOe, typical for a metamagnet with the critical field of 32.5 kOe, extracted from the peak in its dM/dH curve (**Figure 4.11**). Such behaviour is indicative of metamagnetic behaviour which comes from the weak inter-square couplings. The lack of saturation reveals the presence of magnetic

anisotropy.[17] Further studies revealed that the critical fields decrease at higher temperatures and the *S*-shape disappears at temperatures above 12 K. The metamagnetic behaviour is further supported by the field-cooled (FC) magnetisation measurements under fields of 1 to 35 kOe (**Figure 4.12**). Moreover, specific heat measurements reveal a λ-shaped peak at ~11.5 K under zero field and disappeared under an applied dc field of 30 kOe (**Figure 4.13**), which corroborated the antiferromagnetic ordering and metamagnetic behaviour of **2**.

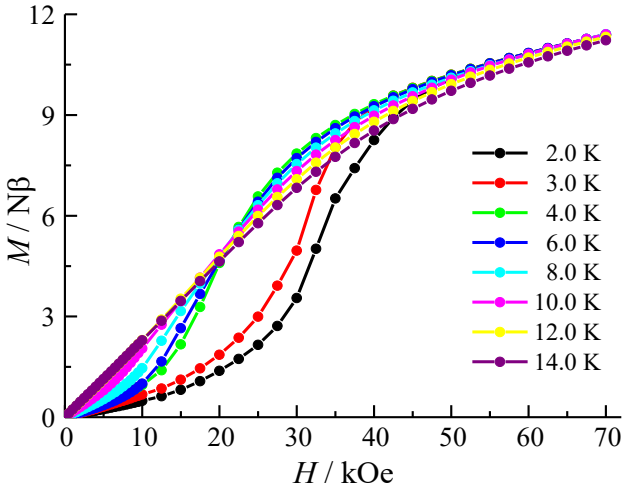

Figure 4.10. Field dependence of the magnetisation for **2** between 2 and 14 K. Solid lines are guides for the eye.

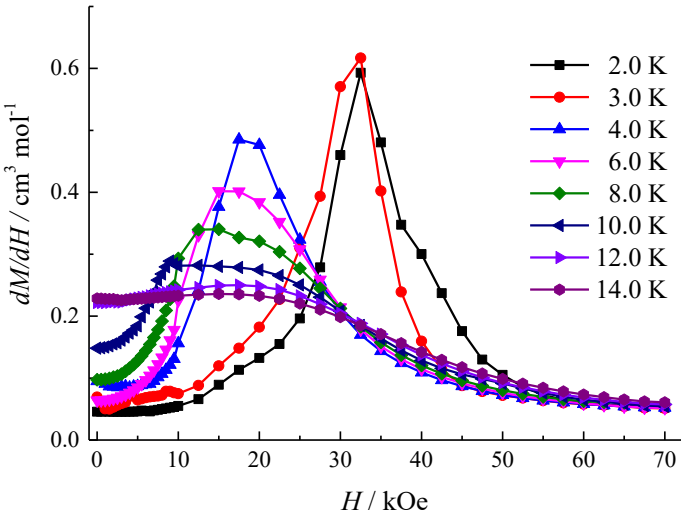

Figure 4.11. First field derivative of the magnetisation as a function of the applied dc field for **2** between 2 and 14 K. Solid lines are guides for the eye.

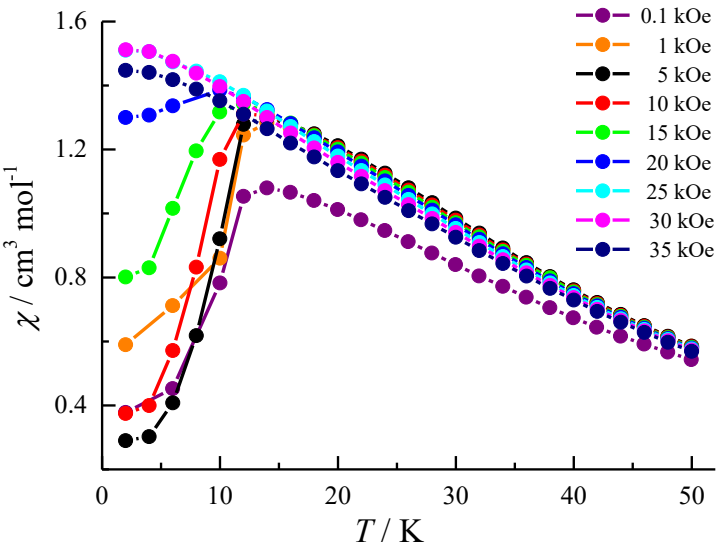

Figure 4.12. Temperature dependence of the magnetic susceptibility for **2** as a function of applied dc fields. Solid lines are guides for the eye.

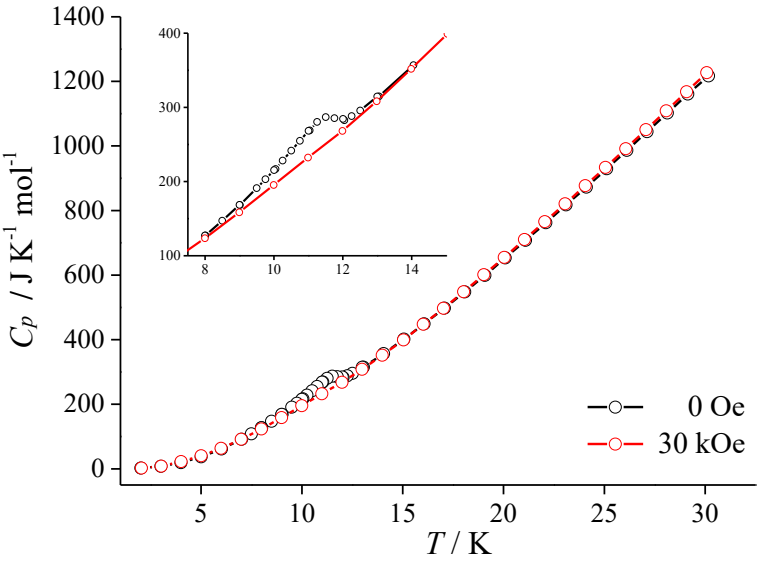

Figure 4.13. Variable temperature heat-capacity plot of **2** under zero and 30 kOe dc fields. Inset shows the enlarged plots over the temperature range of 8-14 K.

Remarkably, step-wise magnetic hysteresis loops at a field sweep rate of 20 Oe/s were observed below 4.0 K (**Figure 4.14**). At 2 K, a wide step-wise hysteresis loop with a coercive field of 9 kOe

and a remnant magnetisation (M_R) of 2.2 Nβ was observed. The loops exhibit narrowing at higher temperatures and disappear at temperatures above 4 K. In terms of the ZFC-FC experiments, under an applied dc field of 50 Oe, the ZFC-FC splitting at about 12 K is much higher than the blocking temperature where the hysteresis closes (**Figure 4.15** left), which may be caused by the coexistence of AF ordering and magnetic relaxation. To better address this, the ZFC-FC plots were further measured under an applied dc field of 30 kOe where the AF ordering is overcome (**Figure 4.15** right). As a result, the observed divergence for the ZFC-FC plots at about 4.5 K is in well agreement with the blocking temperature extracted from the hysteresis measurements, indicating that the ZFC-FC splitting is attributed to the blocking dynamics rather than the long-range magnetic ordering.

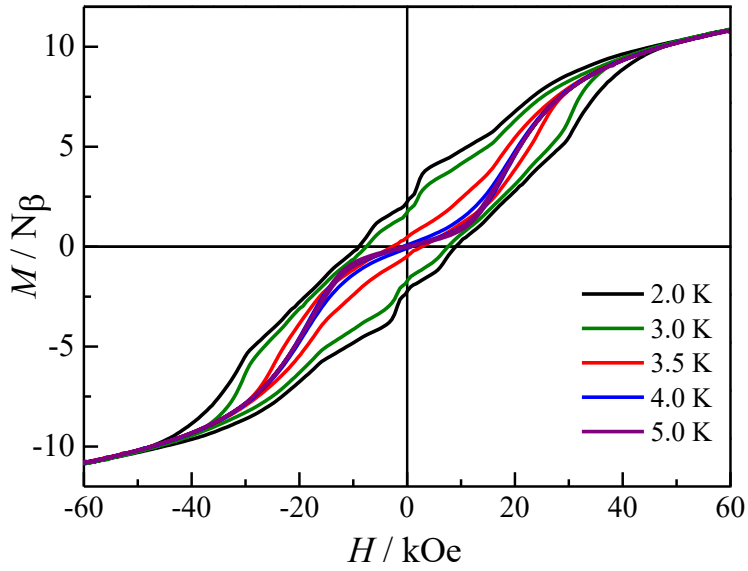

Figure 4.14. Hysteresis loops of **2** measured at 2-5 K with a field sweep rate of 20 Oe/s. Solid lines are guides for the eye.

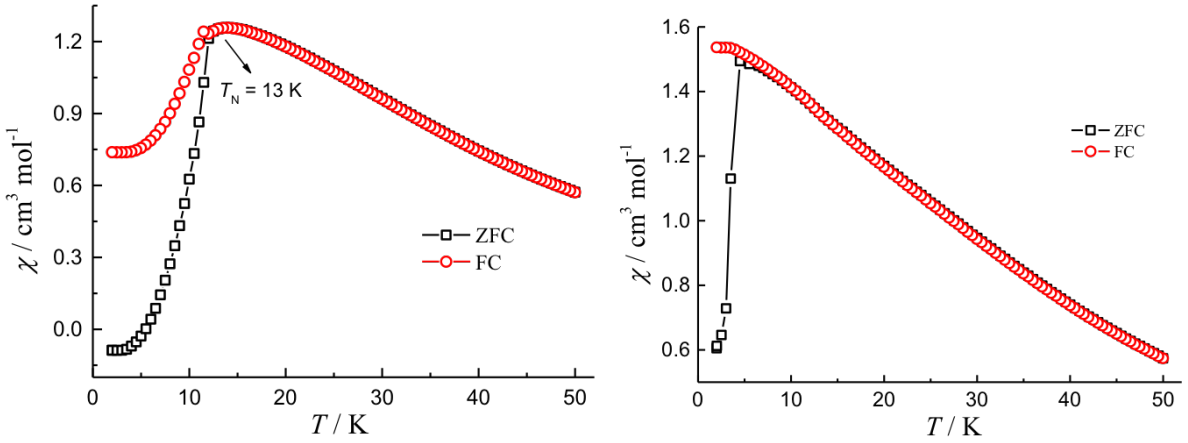

Figure 4.15. ZFC and FC magnetisation data for **2** measured with an applied dc field of 50 Oe (left) and 30 kOe (right).

To investigate the relaxation dynamics of **2**, ac susceptibility data were collected under zero and 30 kOe applied dc fields. The in-phase (χ') signals under a zero dc field exhibit frequency-independent signals maximum at 13 K with the out-of-phase (χ'') component remaining zero around this temperature (**Figure 4.16**). This is not unexpected for antiferromagnets and agrees well with the dc results. Interestingly, strong frequency dependent behaviour in the temperature range of 4 - 10 K was observed, although the signals are weak. Under an applied dc field of 30 kOe (above the critical field) in order to overcome the intercluster *AF* interactions, both the in-phase and out-of-phase ac susceptibilities exhibit obvious frequency dependence, with the χ'' maximum shifting from 4.8 K at 29 Hz to 5.9 K at 898 Hz **.** The intensities of the out-of-phase signals increase ten times. The Mydosh parameter $\varphi = (\Delta T_p/T_p)/(\Delta \log f)$ was estimated to be 0.13, which is larger than a canonical spin glass and closer to a normal value for superparamagnetic behaviour.[18] The relaxation time (τ) derived from the χ'' peaks follows the Arrhenius law $\tau = \tau_0 \exp(U_{eff}/k_B T)$.[19] The obtained effective energy barriers of 96 K ($\tau_0 = 5.2 \times 10^{-10}$ s; zero field) and 83 K ($\tau_0 = 1.7 \times 10^{-10}$ s; 30 kOe dc field) are among the largest reported for polynuclear d-block compounds.[20] The coexistence of long-range magnetic ordering and slow magnetic relaxation is not unexpected for an anisotropic system.[21] It should be

noted that the relaxation time obtained from ac susceptibility measurements seems much lower than those account for the pronounced ZFC-FC and hysteresis curves. Based on the 3D supramolecular structure and AF ordering dictated by extensive short contacts between the [Co_4] squares, such abnormality is reminiscent of some high-dimensional magnetic systems[22] wherein much lower pre-exponential factor and relaxation time are observed due to the variable system size, intermolecular interactions and/or random defects.

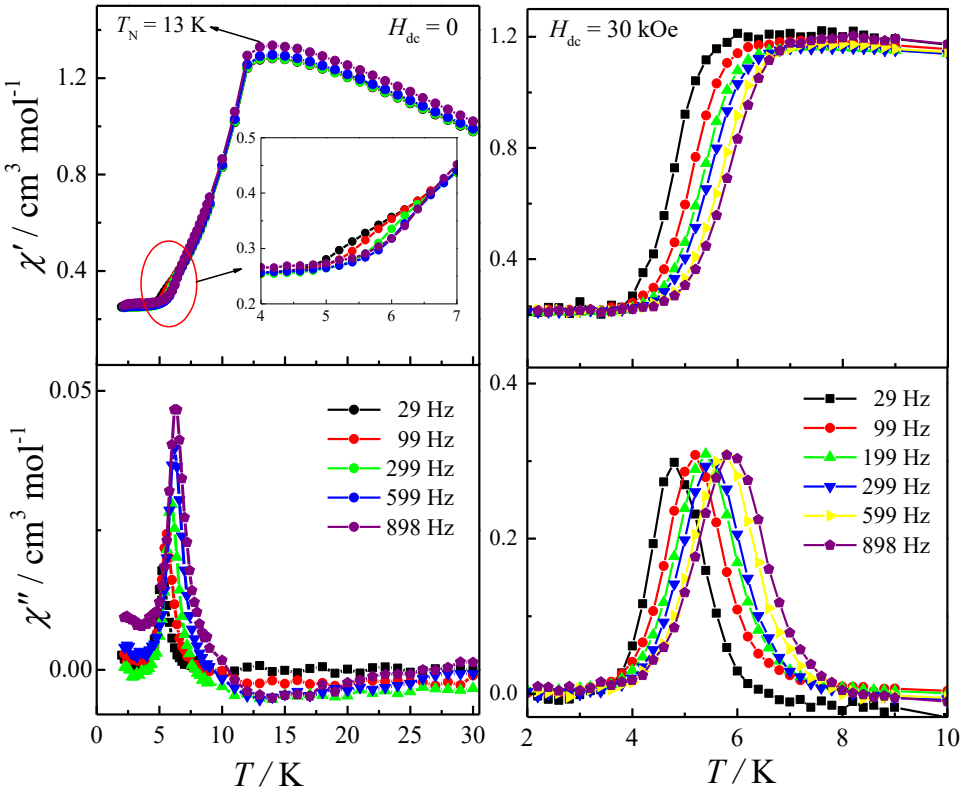

Figure 4.16. Temperature dependence of the in-phase (χ') and out-of-phase (χ'') ac susceptibility data for **2** at zero (left) and 30 kOe (right) dc fields.

4.6 Conclusions

In summary, two new azido-bridged square complexes with *cis*-bpztz radical bridges are reported. Magnetic studies revealed the introduction of tetrazine radicals into [Co^{II}_4] square system is an

effective strategy for engendering direct and strong magnetic interactions between metal spin centres and the radicals. The slow magnetic relaxation behaviour of **2** is significantly enhanced compared to the neutral pyridazine-bridged analogues, demonstrating the potential of topological control coupled with magnetic properties of radical bridges. Future work is being directed at synthesising combinations of various paramagnetic 3d transition metals and tetrazine type ligands in the context of these studies.

4.7 References

1. (a) M. Fujita, M. Tominaga, A. Hori and B. Therrien, *Acc. Chem. Res.*, 2005, **38**, 369-378; (b) R. Chakrabarty, P. S. Mukherjee and P. J. Stang, *Chem. Rev.*, 2011, **111**, 6810-6918.
2. (a) M. D. Pluth, R. G. Bergman and K. N. Raymond, *Acc. Chem. Res.*, 2009, **42**, 1650-1659; (b) A. J. McConnell, C. S. Wood, P. P. Neelakandan and J. R. Nitschke, *Chem. Rev.*, 2015, **115**, 7729-7793; (c) H. Sepehrpour, W. Fu, Y. Sun and P. J. Stang, *J. Am. Chem. Soc*, 2019, **141**, 14005-14020.
3. (a) M. Ruben, J. Rojo, F. J. Romero-Salguero, L. H. Uppadine and J.-M. Lehn, *Angew. Chem. Int. Ed.*, 2004, **43**, 3644-3662; (b) L. N. Dawe, K. V. Shuvaev and L. K. Thompson, *Chem. Soc. Rev.*, 2009, **38**, 2334-2359; (c) D. A. Roberts, B. S. Pilgrim and J. R. Nitschke, *Chem. Soc. Rev.*, 2018, **47**, 626-644.
4. (a) L. E. Darago, M. L. Aubrey, C. J. Yu, M. I. Gonzalez and J. R. Long, *J. Am. Chem. Soc*, 2015, **137**, 15703-15711; (b) L. Qu, H. Iguchi, S. Takaishi, F. Habib, C. F. Leong, D. M. D'Alessandro, T. Yoshida, H. Abe, E. Nishibori and M. Yamashita, *J. Am. Chem. Soc*, 2019, **141**, 6802-6806; (c) A. E. Thorarinsdottir and T. D. Harris, *Chem. Rev.*, 2020, **120**, 8716-8789.
5. (a) S. Kaizaki, *Coord. Chem. Rev.*, 2006, **250**, 1804-1818; (b) J. P. Malrieu, R. Caballol, C. J. Calzado, C. de Graaf and N. Guihéry, *Chem. Rev.*, 2014, **114**, 429-492.

6. (a) J. D. Rinehart, M. Fang, W. J. Evans and J. R. Long, *J. Am. Chem. Soc*, 2011, **133**, 14236-14239; (b) S. Demir, I.-R. Jeon, J. R. Long and T. D. Harris, *Coord. Chem. Rev.*, 2015, **289-290**, 149-176; (c) U. Albold, H. Bamberger, P. P. Hallmen, J. van Slageren and B. Sarkar, *Angew. Chem. Int. Ed.*, 2019, **58**, 9802-9806.

7. (a) H. Gao, Z.-H. Zhang, P. Jiang and X.-R. Li, *Transition Metal Chemistry*, 2006, **31**, 1088-1092; (b) B. L. Schottel, H. T. Chifotides, M. Shatruk, A. Chouai, L. M. Pérez, J. Bacsa and K. R. Dunbar, *J. Am. Chem. Soc*, 2006, **128**, 5895-5912; (c) H. T. Chifotides and K. R. Dunbar, *Acc. Chem. Res.*, 2013, **46**, 894-906; (d) H. T. Chifotides, I. D. Giles and K. R. Dunbar, *J. Am. Chem. Soc*, 2013, **135**, 3039-3055; (e) S. E. Bodman, A. C. Crowther, P. B. Geraghty and C. M. Fitchett, *CrystEngComm*, 2015, **17**, 81-89; (f) B. S. Dolinar, D. I. Alexandropoulos, K. R. Vignesh, T. A. James and K. R. Dunbar, *J. Am. Chem. Soc*, 2018, **140**, 908-911; (g) B. Li, X.-N. Wang, A. Kirchon, J.-S. Qin, J.-D. Pang, G.-L. Zhuang and H.-C. Zhou, *J. Am. Chem. Soc*, 2018, **140**, 14581-14585; (h) N. Marino, R. Bruno, A. Bentama, A. Pascual-Álvarez, F. Lloret, M. Julve and G. De Munno, *CrystEngComm*, 2019, **21**, 917-924.

8. (a) M. Ruben, J.-M. Lehn and P. Müller, *Chem. Soc. Rev.*, 2006, **35**, 1056-1067; (b) T. J. Woods, M. F. Ballesteros-Rivas, S. M. Ostrovsky, A. V. Palii, O. S. Reu, S. I. Klokishner and K. R. Dunbar, *Chem. Eur. J.*, 2015, **21**, 10302-10305; (c) D. I. Alexandropoulos, B. S. Dolinar, K. R. Vignesh and K. R. Dunbar, *J. Am. Chem. Soc*, 2017, **139**, 11040-11043; (d) M. A. Lemes, G. Brunet, A. Pialat, L. Ungur, I. Korobkov and M. Murugesu, *Chem. Commun.*, 2017, **53**, 8660-8663; (e) T. J. Woods, H. D. Stout, B. S. Dolinar, K. R. Vignesh, M. F. Ballesteros-Rivas, C. Achim and K. R. Dunbar, *Inorg. Chem.*, 2017, **56**, 12094-12097; (f) M. A. Lemes, H. N. Stein, B. Gabidullin, K. Robeyns, R. Clérac and M. Murugesu, *Chem. Eur. J.*, 2018, **24**, 4259-4263.

9. D. Gatteschi, R. Sessoli and R. Villain, *Molecular Nanomagnets*, Oxford University Press, 2006.

10. Z. Guo, Y.-F. Deng, Y. Zhang, Z. Pikramenou and Y.-Z. Zhang, *Dalton Trans.*, 2020, **49**, 9218-9222.

11. S. Patra, B. Sarkar, S. Ghumaan, J. Fiedler, W. Kaim and G. K. Lahiri, *Inorg. Chem.*, 2004, **43**, 6108-6113.

12. (a) P. Audebert, S. Sadki, F. Miomandre, G. Clavier, M. Claude Vernières, M. Saoud and P. Hapiot, *New J. Chem.*, 2004, **28**, 387-392; (b) M. Plugge, V. Alain-Rizzo, P. Audebert and A. M. Brouwer, *Journal of Photochemistry and Photobiology A: Chemistry*, 2012, **234**, 12-20.

13. (a) G. A. Heath, L. J. Yellowlees and P. S. Braterman, *J. Chem. Soc., Chem. Commun.*, 1981, DOI: 10.1039/C39810000287, 287-289; (b) P. S. Braterman, J. I. Song and R. D. Peacock, *Inorg. Chem.*, 1992, **31**, 555-559.

14. M. Murrie, *Chem. Soc. Rev.*, 2010, **39**, 1986-1995.

15. N. F. Chilton, R. P. Anderson, L. D. Turner, A. Soncini and K. S. Murray, *J. Comput. Chem.*, 2013, **34**, 1164-1175.

16. D. J. Scalapino, Y. Imry and P. Pincus, *Physical Review B*, 1975, **11**, 2042-2048.

17. (a) M. R. Saber and K. R. Dunbar, *Chem. Commun.*, 2014, **50**, 12266-12269; (b) Y.-Z. Zhang, S. Gómez-Coca, A. J. Brown, M. R. Saber, X. Zhang and K. R. Dunbar, *Chem. Sci.*, 2016, **7**, 6519-6527.

18. J. Mydosh, *Spin Glass: An Experimental Introduction*, London: CRC Press, 1993.

19. R. Carlin, *Magnetochemistry*, Springer, 1986.

20. (a) C. J. Milios, A. Vinslava, W. Wernsdorfer, S. Moggach, S. Parsons, S. P. Perlepes, G. Christou and E. K. Brechin, *J. Am. Chem. Soc*, 2007, **129**, 2754-2755; (b) K. Chakarawet, P. C. Bunting and J. R. Long, *J. Am. Chem. Soc*, 2018, **140**, 2058-2061.

21. (a) H. Miyasaka, K. Takayama, A. Saitoh, S. Furukawa, M. Yamashita and R. Clérac, *Chem. Eur. J.*, 2010, **16**, 3656-3662; (b) Y.-Z. Zhang, H.-H. Zhao, E. Funck and K. R. Dunbar, *Angew. Chem. Int. Ed.*, 2015, **54**, 5583-5587.

22. S. Dhers, H. L. C. Feltham and S. Brooker, *Coord. Chem. Rev.*, 2015, **296**, 24-44.

Chapter 5

Tetranuclear Co Square Complexes Based on a Redox Active Tetrazine Ligand

5.1 Abstract

Organic radicals have been attractive in the design of molecular magnetic materials, creating direct and efficient magnetic interaction pathways between spin carriers. Tetrazine derivatives are of particular interest due to their unique and active redox properties which may produce anion radical after one-electron reduction. Herein, 3,6-bispyridyl-1,2,4,5-tetrazine (bptz) is introduced to molecular grid architecture accompanied with the azido bridges. Three cobalt-based complexes $[Co^{II}_4(bptz^{\bullet-})_4(N_3)_4]\cdot MeOH$ (**1**), $[Co^{2.5}_4(bptz^{\bullet-})_4(N_3)_4](ClO_4)_2\cdot 5MeOH$ (**2**) and $[Co^{II}_2Co^{III}_2(Hbptz)_4(N_3)_4](OTF)_2\cdot solvents$ (**3**) are successfully prepared and characterised by single-crystal X-ray diffraction, UV-vis and cyclic voltammetry methods. Anion radicals of $bptz^{\bullet-}$ were obtained in **1** and **2**, while hydrogenated $Hbptz^-$ was observed in **3**. Magnetic measurements of the complexes show typical antiferromagnetic interaction between Co and $bptz^{\bullet-}$ radicals in **1** as well as slow magnetic relaxation with an effective energy barrier of 57 K at zero field. Tuning the oxidation state of Co(II) ions, slow magnetic relaxation performance was observed in **2** and further switched off in **3**.

5.2 Introduction

Tremendous development in coordination driven self-assembly coordination complexes has been made in recent years, producing intricate supramolecular architectures with a defined geometry of metal centre, including grids, cages, capsules, polyhedral and interlocked structures.[1] These functional nanoscale molecular materials exhibit great potentials in catalysis, optics, sensors, recognition and molecular magnetism throughout various systems.[2] The chelate ligands and appropriate organic bridges have then become key to design polymetallic complexes with desired topology. More importantly, in the field of designing molecular magnetic materials, incorporating

radical bridges has been proven to be effective in creating direct magnetic communication and stronger magnetic couplings when compared to the indirect super-exchange interactions through diamagnetic linkers,[3] leading to exceptional performance in transition metal and lanthanide complexes.

Molecular squares, first described by Stang and Fujita, are deemed to be the most common motif of metallacycles due to their good stability and steerability. Specifically, 3,6-substituded tetrazine derivatives have been well-employed in pre-programmed polygonal architectures with supramolecular anion-π interactions.[4] The low-lying π* orbital located at the tetrazine ring and highly electron deficiency provide active and reversible redox properties of the ligands and related metal complexes.[5] Looking at bptz ligand, stable anion radical is formed through one-electron reduction and it can be further reduced to the non-radical hydrogenated formation (**Figure 5.1**). The tetrazine radical formations have been observed in homo- and hetero-dinuclear Cu, Re, Os, Ru complexes and their mixed-valence species, many of which were observed in solution via the *in situ* electrochemical process and show remarkable control on the redox behaviours.[6] Notably, mixed-valence $Cu^{1.5}Cu^{1.5}$ complexes using neutral asymmetric tetrazine ligand were reported and considered to be class-III type mixed-valence system where the single electron is delocalised between the two metal centres.[7] Nevertheless, the crystallisation of tetrazine radical based complexes are found to be difficult due to the challenges posed by reactivity and sensitivity towards protons, oxygen and other electrophiles in solution.

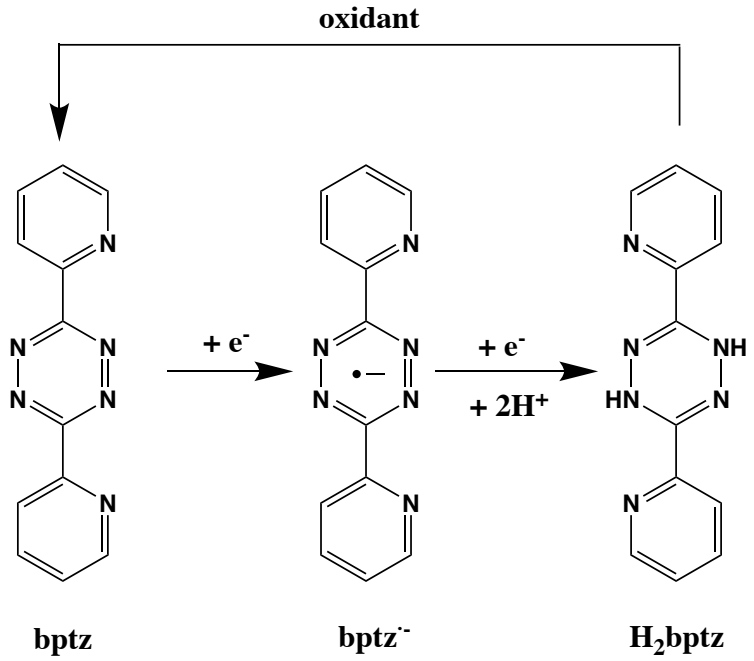

Figure 5.1. The redox scheme of bptz ligand.

Moreover, reduction of neutral tetrazine can switch off the anion-π interaction while the resulting radical is still able to bind cationic and neutral donor molecules to facilitate direct exchange interactions and lead to stronger ferromagnetic or antiferromagnetic couplings up to $J \approx \pm 100$ cm^{-1} between tetrazine radicals and paramagnetic metal ions, demonstrated by the latest work from Dunbar and Murugesu groups.[8] Despite the first report of dinuclear tetrazine radical (bmtz$^{\bullet-}$) bridged Co^{II} SMM, our recent progress has led to successful assembling tetrazine radical (bpztz$^{\bullet-}$) with azido bridges into a Co^{II} grid complex where the antiferromagnetic coupling constant was found to be -64.7 cm^{-1} in addition to slow relaxation of magnetisation with an barrier up to 96 K.[9]

With continuous interest in this area and by using similar synthetic strategies, herein we report the synthesis of three cobalt-based molecular grid-like complexes based on bptz ligand and azido-bridge: one [Co$^{II}_4$] SMM (**1**) and mixed-valence [Co$^{2.5}$]$_4$ (**2**) with tetrazine radicals followed by a [Co$^{II}_2$Co$^{III}_2$] complex (**3**) with hydrogenated tetrazine. The mixed-valence state of the complexes are supported by

crystallography, UV-vis and cyclic voltammetry measurements. Both **1** and **2** behave as typical SMMs under zero field, while **3** does not show slow relaxation of magnetisation.

5.3 Experimental Section

5.3.1 General Methods

All chemicals are commercially available and used as received. 3,6-di(pyridin-2-yl)-1,4-dihydro-1,2,4,5-tetrazine ligand (H_2bptz) was prepared according to the literature method.[10] Syntheses of the metal complexes were carried out in a glove box under an argon atmosphere. Acetonitrile and dichloromethane were purified using a solvent purification system and stored over molecular sieves in the glove box. Anhydrous methanol was purchased from Energy Chem and stored over molecular sieves in a glove box.

5.3.2 Physical measurements

Suitable single crystals were selected and put on a Bruker APEX-II CCD diffractometer using graphite monochromated Cu Kα (λ = 1.54178) or Mo Kα (λ = 0.71073) radiation at 100 K. The structure was solved with the ShelXT structure solution program using Intrinsic Phasing and refined in the ShelXL refinement package using Least Squares minimisation. Hydrogen atoms were added at calculated positions and refined using a riding model. Weighted R factors (wR) and the goodness-of-fit (S) values are based on F^2; conventional R factors (R) are based on F, with F set to zero for negative F^2. Highly disordered solvent molecules in **2** and **3** were squeezed using solvent mask in Olex2. FT-IR spectra were recorded in the range 600-4000 cm^{-1} on a Bruker tensor II spectrophotometer. Elemental analyses (C, H, N) were obtained on a vario EL cube CHNOS Elemental Analyzer Elementar Analysensysteme GmbH. UV-vis spectra were recorded on a Agilent Cary 5000 spectrometer. Cyclic voltammetry experiments were carried out on a CHI760E electrochemical

workstation (Chenhua Co. Ltd., China) with a Pt working electrode. Ag/AgCl was used as the reference electrode and 0.1 M acetonitrile solution of [n-Bu_4N][PF_6] was used as supporting electrolyte. Magnetic measurements were carried out on a SQUID MPMS3 magnetometer. Diamagnetic corrections were calculated from Pascal constants and applied to all the constituent atoms and sample holder.

5.3.3 Synthesis

Caution. Although no such issues were observed during the present work, azido and perchlorate salts are potentially explosive and should be handled with extreme caution.

Synthesis of [$Co_4(bptz^{\bullet-})_4(N_3)_4$]·MeOH (1). [$Co(H_2O)_6$][OTF]$_2$ (46.6 mg, 0.1 mmol) and L-ascorbic acid (26.0 mg, 0.14 mmol) were dissolved in 5 mL MeOH, to which H_2bptz (23.8, 0.1 mmol) in 4 mL dichloromethane was added, followed by sodium azide (9.1 mg, 0.14 mmol) in 4 mL MeOH. The resulting solution was left to slowly evaporate at room temperature. Black block crystals appeared in a few days which were collected via filtration, washed with cold acetonitrile and dried. Yield 11.9 mg (35% based on H_2bptz). Anal. Calc. (%) for $C_{48}H_{32}Co_4N_{36}(CH_3OH)(H_2O)_2$ C, 41.54; H, 2.85; N, 35.59. Found C, 41.19; H, 2.90; N, 35.91. Selected IR data (cm^{-1}): 2358 (m), 2340 (w), 2060 (s), 1598 (m), 1385 (m), 1321 (m), 1278 (m), 1254 (m), 1150 (m).

Synthesis of [$Co_4(bptz^{\bullet-})_4(N_3)_4$]($ClO_4$)$_2$·5MeOH (2). [$Co(H_2O)_6$][$ClO_4$]$_2$ (36.8 mg, 0.1 mmol) and L-ascorbic acid (26.2 mg) were dissolved in 5 mL MeOH, to which bptz (23.6, 0.1 mmol) in 4 mL dichloromethane was added, followed by sodium azide (9.1 mg, 0.14 mmol) in 4 mL MeOH. The resulting black mixture left undisturbed for three hours before filtration. The filtrate was left to slowly evaporate at room temperature. Black block crystals were collected via filtration after a few days. Yield 7.8 mg (21% based on ligand). Anal Calc. (%) for $C_{48}H_{32}Co_4N_{36}(ClO_4)_2(CH_3OH)_5$ C, 37.27; H, 3.07; N, 29.52. Found C, 36.92; H, 2.74; N, 29.18. Selected IR data (cm^{-1}): 2358 (m), 2340 (w), 2066 (s), 1600 (m), 1394 (m), 1252 (m), 1077 (br).

Synthesis of $[Co_4(Hbptz)_4(N_3)_4](OTF)_2 \cdot$solvents (3). $[Co(H_2O)_6][OTF]_2$ (36.8 mg, 0.1 mmol) and L-ascorbic acid (26.2 mg) were dissolved in 5 mL MeOH, to which bptz (23.6, 0.1 mmol) in 4 mL dichloromethane was added, followed by sodium azide (9.1 mg, 0.14 mmol) in 4 mL MeOH. The resulting mixture was left undisturbed for three hours before filtration. The filtrate was left to slowly evaporate at room temperature. Black plate crystals appeared in a week which were collected via filtration. Yield 6.3 mg (21% based on ligand). Anal. Calc. (%) for $C_{48}H_{36}Co_4N_{36}(CF_2SO_3)_2(CH_3OH)_2(CH_2Cl_2)_2$ C, 34.41; H, 2.57; N, 26.75; S, 3.40. Found C, 34.91; N, 27.78; H, 2.22; S, 3.83.Selected IR data (cm^{-1}): 2360 (m), 2340 (w), 2061 (s), 1600 (m), 1397 (m), 1247 (m), 1223 (w), 1027 (s).

5.4 Results and discussion

5.4.1 Syntheses and Structures

Compounds **1**-**3** were prepared in similar conditions by the reaction of equivalent molar of Co^{II} salt and H_2bptz (for **1**) or bptz ligand (for **2** and **3**) in the presence of slightly excess sodium azide and L-ascorbic acid. Notably, **1** can also be synthesised using $[Co(H_2O)_6][ClO_4]_2$ and bptz with less L-ascorbic acid but the yield is much lower. Interestingly, these complexes are found to be quasi-reversible in syntheses as evidenced by the crystallographic measurements (**Figure 5.2**): complex **2** or **3** can convert to **1** in solution under excess $NaNO_2$, while **2** can be obtained by **3** by anion substitution with excess $NaClO_4$. The mechanism of the reactions are still under investigation. The powder X-ray diffraction pattern of the bulk products cannot be obtained due to the loss of solvent in the crystal lattice.

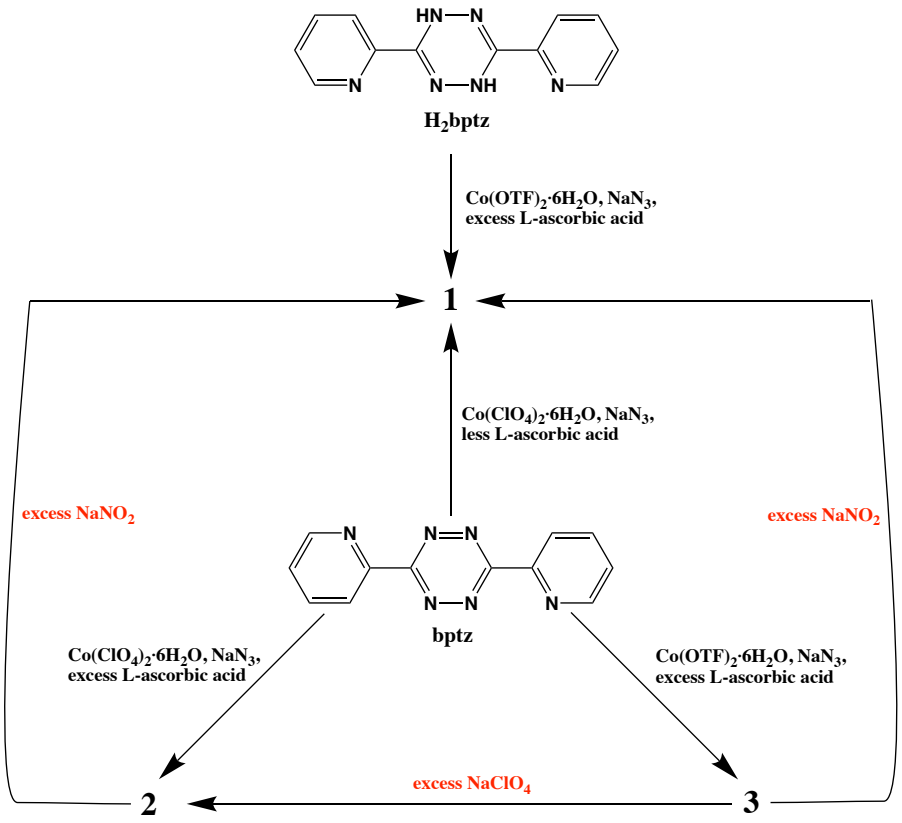

Figure 5.2. Synthetic scheme of the complexes.

All three complexes reveal similar square structures where the metal ions are capped by two bptz or Hbptz ligands and bridged by EO-azide and tetrazine rings in a *cis* position (**Figure 5.3** - **Figure 5.5**). Crystallographic information are summarised in **Table 5.1**. The average intra-tetrazine N-N bond lengths in **1** and **2** are 1.387 Å and 1.377 Å, respectively, which firmly support the anion radical formation of bptz.[8a, 11] Interestingly, the average N-N bond distance of tetrazine in **3** has increased to 1.428 Å, which is in line with the crystallographic data of $Hbptz^-$ formation and related metal complexes,[12] suggesting the absence of radical bridges in **3**.

Table 5.1. Selected crystallographic information of **1**-**3**.

	1	**2**	**3**
Empirical formula	$C_{49}H_{36}Co_4N_{36}O$	$C_{52}H_{47}Cl_2Co_4N_{36}O_{12}$	$C_{98}H_{72}Co_8F_6N_{72}O_6S_2$
Formula weight	1380.86	1674.87	3003.83
Crystal system	monoclinic	monoclinic	monoclinic
Space group	C2/c	$P2_1/n$	$P2_1/n$
a/Å	40.1008(15)	12.2788(8)	16.5772(18)
b/Å	15.6242(5)	24.1285(17)	27.580(3)
c/Å	19.5565(5)	23.3690(16)	32.190(4)
α/°	90	90	90
β/°	116.361(3)	104.180(2)	97.6840(10)
γ/°	90	90	90
Volume/Å^3	10978.8(7)	6712.6(8)	14585(3)
Z	8	4	4
ρ_{calc}g/cm^3	1.671	1.657	1.368
μ/mm^{-1}	9.951	1.139	0.994
F(000)	5584.0	3396.0	6056.0
Crystal size/mm^3	0.15 × 0.09 × 0.07	0.35 × 0.15 × 0.08	0.25 × 0.24 × 0.22
Radiation	CuKα (λ = 1.54178)	MoKα (λ = 0.71073)	MoKα (λ = 0.71073)
Goodness-of-fit on F^2	1.025	1.031	1.049
Final R indexes [I>=2σ (I)]	R_1 = 0.0442, wR_2 = 0.1168	R_1 = 0.0973, wR_2 = 0.2037	R_1 = 0.0522, wR_2 = 0.1366
Final R indexes [all data]	R_1 = 0.0563, wR_2 = 0.1248	R_1 = 0.1558, wR_2 = 0.2399	R_1 = 0.0764, wR_2 = 0.1541

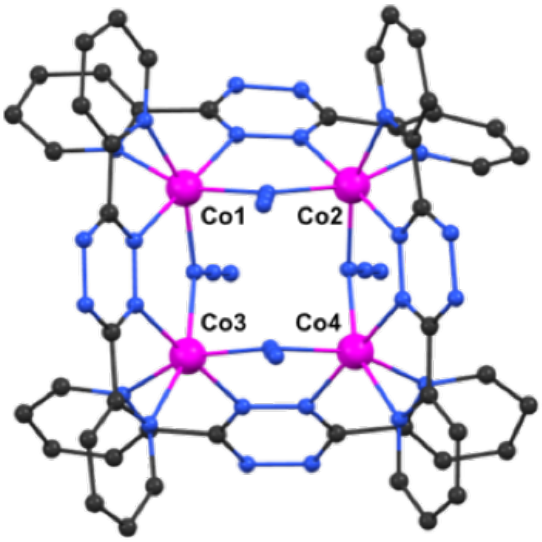

Figure 5.3. Asymmetric unit of **1**. Hydrogen atoms, solvent molecules are omitted for clarity. Atom colours: N, blue; C, black.

1 crystallised in a monoclinic C2/c space group, where the asymmetric unit contains one unique [Co_4] square and one methanol molecule (**Figure 5.3**). Selected bond distances and angles are listed in **Table 5.2**. Considering the overall charge balance and the bond valence sum (BVS) calculation (**Table 5.5**), each Co ion is in a 2+ oxidation state. All Co^{II} ions are located in distorted octahedral environments formed by two N atom from azide and four from two different bptz ligands, giving the average Co-N bond lengths for Co1, Co2, Co3, Co4 are 2.113 Å, 2.109 Å, 2.116 Å and 2.112 Å, respectively, suggesting the presence of high-spin Co^{II} ions. The *cis*-N-Co-N angles are in the range of 73.98-106.55° and the Co-N_{azide}-Co angle ranges from 116.66° to 118.10°. The bptz radicals are not planar and bow inward towards the azide, giving an average dihedral angles between pyridine and tetrazine rings of 8.2°. Unlike the bpztz radical-bridged Co_4 analogue, the pyridine substitution cuts off the supramolecular interactions in **1**, giving the closest intermolecular Co-Co distance of 8.434 Å.

Table 5.2. Selected bond lengths (Å) and angles [deg] for **1**.

Co1-N8	2.070(3)	Co3-N16	2.062(3)
Co1-N31	2.091(3)	Co3-N34	2.123(3)
Co1-N7	2.161(3)	Co3-N20	2.151(3)
Co1-N2	2.072(3)	Co3-N22	2.044(3)
Co1-N25	2.096(3)	Co3-N19	2.203(3)
Co1-N1	2.193(3)	Co3-N28	2.088(3)
Co2-N15	2.064(3)	Co4-N31	2.101(3)
Co2-N14	2.161(3)	Co4-N21	2.075(3)
Co2-N4	2.162(3)	Co4-N11	2.170(3)
Co2-N25	2.098(3)	Co4-N9	2.059(3)
Co2-N3	2.057(3)	Co4-N10	2.188(3)
Co2-N28	2.111(3)	Co4-N34	2.104(3)
N8-Co1-N31	85.19(10)	N16-Co3-N34	92.94(11)
N8-Co1-N7	75.18(10)	N16-Co3-N20	105.83(12)
N8-Co1-N2	178.21(11)	N16-Co3-N19	73.98(11)
N8-Co1-N25	93.73(11)	N16-Co3-N28	86.58(11)
N8-Co1-N1	105.97(11)	N34-Co3-N20	159.31(12)
N31-Co1-N7	158.58(11)	N34-Co3-N19	93.98(11)
N31-Co1-N25	97.85(11)	N20-Co3-N19	83.17(11)
N31-Co1-N1	94.86(11)	N22-Co3-N16	176.26(12)
N7-Co1-N1	82.64(10)	N22-Co3-N34	84.52(11)
N2-Co1-N31	96.00(11)	N22-Co3-N20	76.30(12)
N2-Co1-N7	103.84(11)	N22-Co3-N19	103.42(12)

N2-Co1-N25	84.79(11)	N22-Co3-N28	96.57(12)
N2-Co1-N1	75.29(11)	N28-Co3-N34	100.50(11)
N25-Co1-N7	91.98(11)	N28-Co3-N20	89.46(11)
N25-Co1-N1	157.36(11)	N28-Co3-N19	156.33(12)
N15-Co2-N14	74.95(11)	N31-Co4-N11	158.52(11)
N15-Co2-N4	106.73(11)	N31-Co4-N10	91.51(11)
N15-Co2-N25	92.33(11)	N31-Co4-N34	98.39(11)
N15-Co2-N28	86.21(11)	N21-Co4-N31	94.75(11)
N14-Co2-N4	88.79(11)	N21-Co4-N11	104.87(11)
N25-Co2-N14	90.91(11)	N21-Co4-N10	74.80(11)
N25-Co2-N4	160.15(11)	N21-Co4-N34	84.40(11)
N25-Co2-N28	99.77(11)	N11-Co4-N10	85.39(11)
N3-Co2-N15	177.61(11)	N9-Co4-N31	85.41(11)
N3-Co2-N14	106.01(11)	N9-Co4-N21	178.64(12)
N3-Co2-N4	75.54(11)	N9-Co4-N11	75.18(11)
N3-Co2-N25	85.49(11)	N9-Co4-N10	106.55(11)
N3-Co2-N28	93.20(11)	N9-Co4-N34	94.23(11)
N28-Co2-N14	158.73(11)	N34-Co4-N11	92.24(11)
N28-Co2-N4	87.25(11)	N34-Co4-N10	157.65(11)

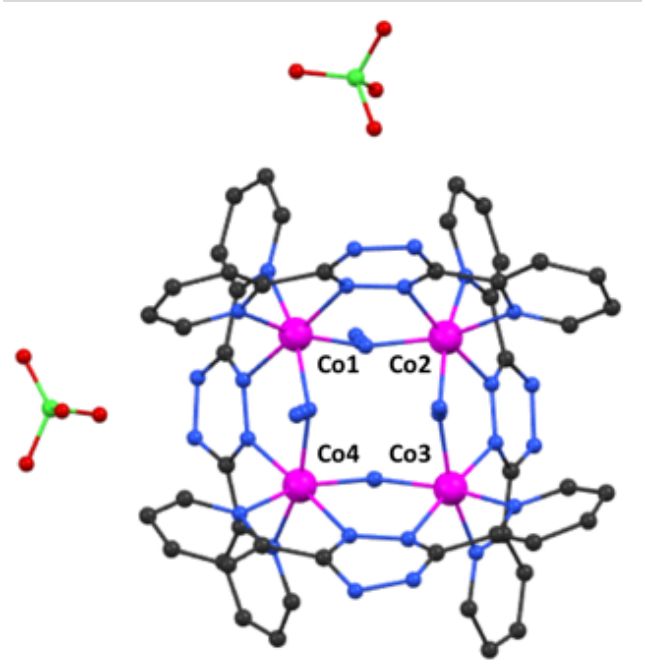

Figure 5.4. Crystal structure of **2**. Hydrogen atoms, solvent molecules are omitted for clarity. Atom colours: Cl, green; O, red; N, blue; C, black.

Both **2** and **3** crystallised in monoclinic $P2_1/n$ space group. The asymmetric unit of **2** contains one $[Co_4]$ core with two perchlorate anions and solvent molecules (**Figure 5.4**). All Co ions are located in distorted octahedral geometry with six N atoms coordinated. The average Co-N bond lengths are 2.021 Å, 2.044 Å, 2.002 Å and 2.048 Å for Co1, Co2, Co3 and Co4, respectively (see **Table 5.3** for selected bond lengths and angles), which are either too long for low-spin $Co^{II/III}$ (~1.9 Å) or too short for high-spin Co^{II} (~2.1 Å). The charge balance consideration suggests the four Co ions distribute an overall +10 charge. Moreover, the BVS calculation indicates a delocalisation of positive charges around cobalt ions (+2.5 each) instead of accurate identification of the oxidation state (**Table 5.5**). To the best of our knowledge, this has not yet been found in any Co intervalent cluster. The Co-N_{azide}-Co angle ranges from 116.84° to 118.21°. The $[Co_4]$ units are separated by the perchlorate ions and

solvent molecules with no significant intermolecular interaction. The closest intermolecular distance of Co-Co is 8.143 Å.

Table 5.3. Selected bond lengths [Å] and angles [deg] of **2**.

Co1-N1	2.037(5)	Co3-N4	2.023(6)
Co1-N3	1.995(5)	Co3-N13	2.026(6)
Co1-N6	2.039(7)	Co3-N20	1.999(8)
Co1-N14	2.013(8)	Co3-N24	1.966(7)
Co1-N19	2.009(7)	Co3-N25	1.976(7)
Co1-N23	2.035(6)	Co3-N28	2.024(9)
Co2-N2	2.055(5)	Co4-N6	2.056(7)
Co2-N14	2.068(8)	Co4-N7	2.056(6)
Co2-N15	1.998(6)	Co4-N8	2.074(6)
Co2-N16	2.071(6)	Co4-N9	2.029(6)
Co2-N20	2.063(8)	Co4-N11	2.023(5)
Co2-N22	2.017(7)	Co4-N28	2.057(10)
N1-Co1-N6	166.1(2)	N4-Co3-N13	92.4(3)
N3-Co1-N1	79.6(2)	N4-Co3-N28	165.7(3)
N3-Co1-N6	86.5(2)	N20-Co3-N4	87.5(2)
N3-Co1-N14	93.9(3)	N20-Co3-N13	165.9(3)
N3-Co1-N19	177.7(3)	N20-Co3-N28	91.4(3)
N3-Co1-N23	99.6(3)	N24-Co3-N4	79.8(3)
N14-Co1-N1	89.2(2)	N24-Co3-N13	95.8(3)
N14-Co1-N6	93.2(3)	N24-Co3-N20	98.0(3)

N14-Co1-N23	166.4(3)	N24-Co3-N25	175.7(3)
N19-Co1-N1	98.3(3)	N24-Co3-N28	86.3(3)
N19-Co1-N6	95.5(3)	N25-Co3-N4	99.3(3)
N19-Co1-N14	86.9(3)	N25-Co3-N13	80.0(3)
N19-Co1-N23	79.5(3)	N25-Co3-N20	86.1(3)
N23-Co1-N1	92.5(2)	N25-Co3-N28	94.8(3)
N23-Co1-N6	88.3(2)	N28-Co3-N13	92.1(3)
N2-Co2-N14	88.3(2)	N6-Co4-N7	163.2(2)
N2-Co2-N16	91.7(3)	N6-Co4-N8	89.3(2)
N2-Co2-N20	163.9(2)	N6-Co4-N28	97.4(3)
N14-Co2-N16	164.1(3)	N7-Co4-N8	91.1(3)
N15-Co2-N2	78.5(2)	N7-Co4-N28	87.4(3)
N15-Co2-N14	98.5(3)	N9-Co4-N6	96.7(3)
N15-Co2-N16	97.1(3)	N9-Co4-N7	99.9(3)
N15-Co2-N20	85.5(3)	N9-Co4-N8	78.3(3)
N15-Co2-N22	175.6(3)	N9-Co4-N28	83.7(3)
N20-Co2-N14	94.5(3)	N11-Co4-N6	85.4(2)
N20-Co2-N16	89.9(3)	N11-Co4-N7	78.0(2)
N22-Co2-N2	99.6(3)	N11-Co4-N8	99.9(3)
N22-Co2-N14	85.4(3)	N11-Co4-N9	177.3(3)
N22-Co2-N16	78.9(3)	N11-Co4-N28	97.9(3)
N22-Co2-N20	96.4(3)	N28-Co4-N8	161.5(3)

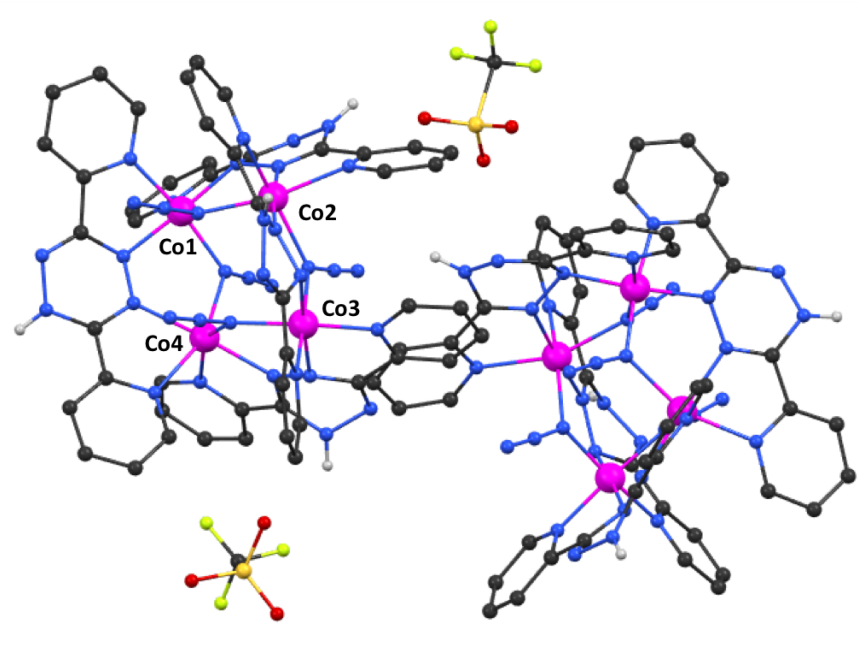

Figure 5.5. Asymmetric unit structure of **3**. Solvent molecules and hydrogen atoms of pyridine are omitted for clarity. Atom colours: S, yellow; O, red; F, light green; N, blue; C, black.

In the case of **3**, the asymmetric unit contains two OTF anions and two independent [Co_4] squares showing similar structural parameters (**Figure 5.5**), so only one square (Co1-Co4) will be discussed in detail. All Co ions are in six N coordination environment, resulting in distorted octahedral geometry. According to the BVS calculation (**Table 5.5**), Co1 and Co3 are more likely assigned to low-spin Co^{III} where the average Co-N bond lengths are 1.952 Å and 1.939 Å, while Co2 and Co4 are close to high-spin Co^{II} with the average Co-N bond lengths of 2.112 Å and 2.122 Å. The distance of the adjacent Co ions inside square is within the range of 3.478-3.488 Å and the diagonal Co ions is 5.411 and 4.378 Å. The Co-N_{azide}-Co angle ranges from 115.71° to 118.18°. The square molecules are separated by counter anions, giving the closest intermolecular Co-Co distance of 7.394 Å. Strong hydrogen bond interaction was observed between OTF anion and neighbouring Hbptz, with the closest O···H and F···H distances of 2.338 Å and 2.598 Å, respectively, as well as azide and $Hbptz^-$ (N···H distance is 2.386 Å).

Table 5.4. Selected bond lengths (Å) and angles of **3**.

Co1-N8	1.939(3)	Co3-N3	1.942(3)
Co1-N12	1.953(3)	Co3-N10	1.953(3)
Co1-N15	1.954(3)	Co3-N11	1.947(3)
Co1-N17	1.948(3)	Co3-N25	1.936(3)
Co1-N20	1.936(3)	Co3-N35	1.921(3)
Co1-N24	1.971(3)	Co3-N41	1.936(3)
Co2-N1	2.060(3)	Co4-N4	2.072(3)
Co2-N3	2.123(3)	Co4-N7	2.072(3)
Co2-N6	2.153(3)	Co4-N11	2.121(3)
Co2-N12	2.105(3)	Co4-N16	2.152(3)
Co2-N21	2.067(3)	Co4-N24	2.140(3)
Co2-N33	2.136(3)	Co4-N44	2.147(3)
N8-Co1-N12	89.55(12)	N3-Co3-N10	89.41(11)
N8-Co1-N15	81.96(12)	N3-Co3-N11	86.93(12)
N8-Co1-N17	94.93(12)	N11-Co3-N10	170.38(12)
N8-Co1-N24	93.71(12)	N25-Co3-N3	89.23(12)
N12-Co1-N15	171.51(12)	N25-Co3-N10	94.47(12)
N12-Co1-N24	88.15(12)	N25-Co3-N11	94.37(12)
N15-Co1-N24	92.12(12)	N25-Co3-N41	83.11(12)
N17-Co1-N12	90.13(12)	N35-Co3-N3	94.60(12)
N17-Co1-N15	90.85(12)	N35-Co3-N10	82.05(12)
N17-Co1-N24	171.18(11)	N35-Co3-N11	89.37(12)
N20-Co1-N8	176.26(12)	N35-Co3-N25	174.79(12)

N20-Co1-N12	93.15(12)	N35-Co3-N41	93.13(12)
N20-Co1-N15	95.34(12)	N41-Co3-N3	172.22(12)
N20-Co1-N17	82.50(12)	N41-Co3-N10	92.50(12)
N20-Co1-N24	88.96(12)	N41-Co3-N11	92.31(12)
N1-Co2-N3	94.62(11)	N4-Co4-N7	174.97(12)
N1-Co2-N6	75.88(11)	N4-Co4-N11	103.03(11)
N1-Co2-N12	83.41(11)	N4-Co4-N16	75.68(11)
N1-Co2-N21	174.70(11)	N4-Co4-N24	82.34(11)
N1-Co2-N33	106.88(11)	N4-Co4-N44	99.63(12)
N3-Co2-N6	85.18(11)	N7-Co4-N11	81.53(11)
N3-Co2-N33	157.91(11)	N7-Co4-N16	102.80(11)
N12-Co2-N3	99.75(11)	N7-Co4-N24	98.53(11)
N12-Co2-N6	159.06(11)	N7-Co4-N44	75.45(11)
N12-Co2-N33	87.96(11)	N11-Co4-N16	85.59(11)
N21-Co2-N3	82.20(11)	N11-Co4-N24	105.96(11)
N21-Co2-N6	99.56(11)	N11-Co4-N44	153.87(12)
N21-Co2-N12	101.27(11)	N24-Co4-N16	157.07(11)
N21-Co2-N33	75.98(11)	N24-Co4-N44	89.71(11)
N33-Co2-N6	95.00(11)	N44-Co4-N16	87.60(11)

Table 5.5. Bond Valence Sum (BVS) calculation of **1**-**3**.

1		**2**			**3**		
	Co^{II}		Co^{II}	Co^{III}		Co^{II}	Co^{III}
Co1	2.257	Co1	2.658	2.451	Co1	2.314[a]	2.951
Co2	2.142	Co2	2.502	2.307	Co2	2.085[b]	
Co3	2.156	Co3	2.802	2.583	Co3	2.396[a]	3.056
Co4	2.108	Co4	2.471	2.278	Co4	2.033[b]	

[a] Simulating with low-spin Co(II) parameters.

[b] Simulating with high-spin Co(II) parameters.

5.4.2 UV-vis spectroscopy studies

The absorption spectra of all complexes as well as the ligands are measured at room temperature in solution (**Figure 5.6**). The neutral bptz ligand shows a strong π-π* transition at 295 nm as well as less intense n-π* transition bands at the visible region. The π-π* transition bands in **1** and **2** are blue-shifted which is indicative of decreased conjugation. Meanwhile, the absorption bands at the visible region for **1** and **2** show clear red shift that can be attributed the effect of coordination to n-π* transition. This is consistent with the previously reported N-heterocylic radicals[13] and the Co_4bpztz analogue, which clearly supports the tetrazine radical formation. No obvious visible absorption observed for H_2bptz ligand and **3** may support the absence of tetrazine radicals and further reduction of tetrazine into the hydrogenated formation.

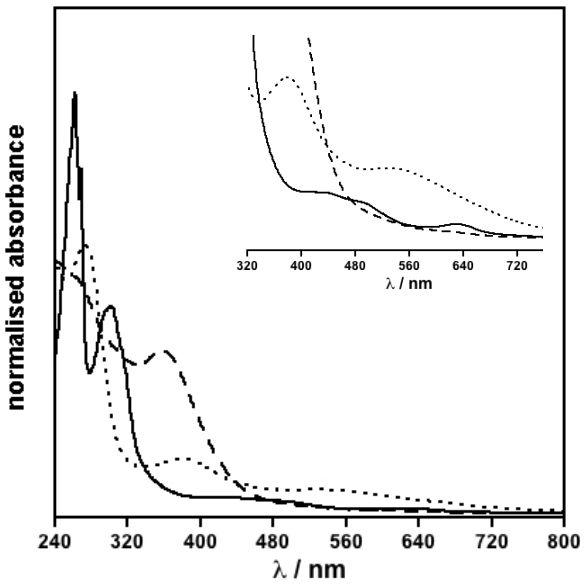

Figure 5.6. UV-vis absorption spectra of **1** (solid line), **2** (dotted line) and **3** (dashed line) in acetonitrile solution.

5.4.3 Electrochemistry studies

To gain an insight of the electrochemistry of the complexes, cyclic voltammetry spectra of the complexes were recorded at room temperature in acetonitrile solution. The CV spectrum of **1** shows four consecutive and reversible Co^{II} oxidation peaks at +0.048, +0.31, +0.54 and +0.73 V (**Figure 5.7** left) under a positive scan mode. Further scanning to negative region an irreversible peak at -0.88 V appeared which possibly correspond to the tetrazine radical reduction (**Figure 5.7** right). The shift of the oxidation potentials under a negative scan mode may be due to the overlap of an unknown oxidation process. A comproportionation constant *K*c calculated by $Kc = \exp(F\Delta E/RT)$ is used to evaluate the relative stability of the mixed valence states with respect to their reduced and oxidation forms. The *K*c values for each oxidation process of 5.03×10^4, 7.76×10^3 and 1.63×10^3 indicates intermediated stability of $[Co^{III}_2Co^{II}_2]$, $[Co^{III}_3Co^{II}_1]$ and $[Co^{III}_4]$ state.

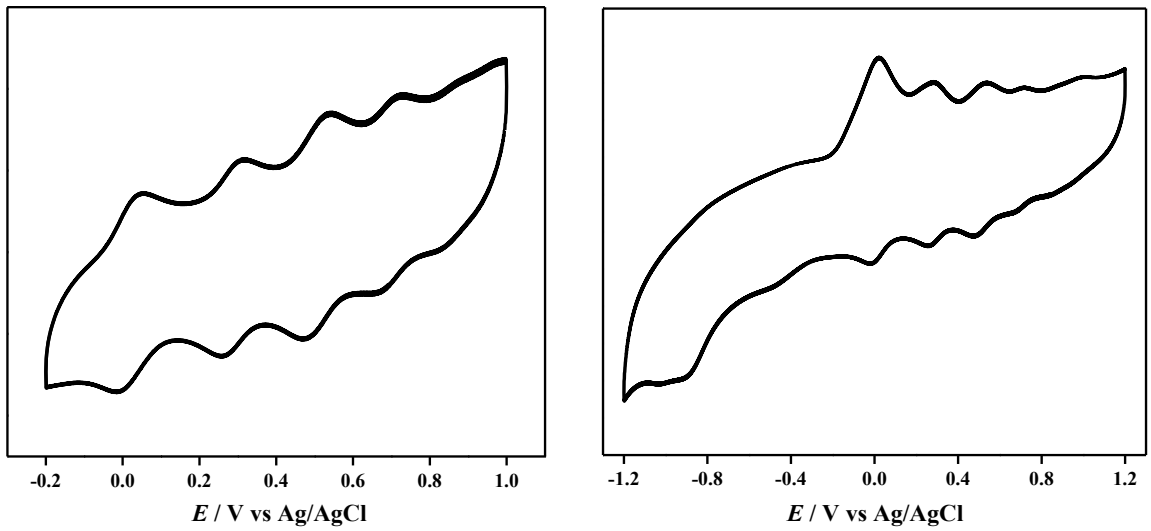

Figure 5.7. Cyclic voltammetry of **1**: (left) a positive scan mode with a scan rate of 50 mV/s and (right) negative scan mode of 100 mV/s.

In the case of **2** (**Figure 5.8**), a broad oxidation band appeared in the range of 0.5-1.5 V along with obvious reduction process of metal ions in the negative region, however it is difficult to assign each process. Such an overall quasi-reversible curve may be an evidence of delocalisation of Co^{II}/Co^{III}. The one-electron irreversible reduction peak at -1.16 V is likely attributed to the bptz radical reduction. The CV spectrum of **3** (**Figure 5.9**) displays two quasi-reversible $Co^{II/III}$ oxidation processes at +0.49 V and 0.68 V as well as two $Co^{III/II}$ reductions at -0.37 V and -0.52 V. No obvious peak was observed after -0.8 V. The close overlap of $Co^{II/III}$ oxidation could be due to the redox events occurring at the Co(II) sites occupying opposing vertices inside the square.[14] This is also consistent with crystallographic assignments.

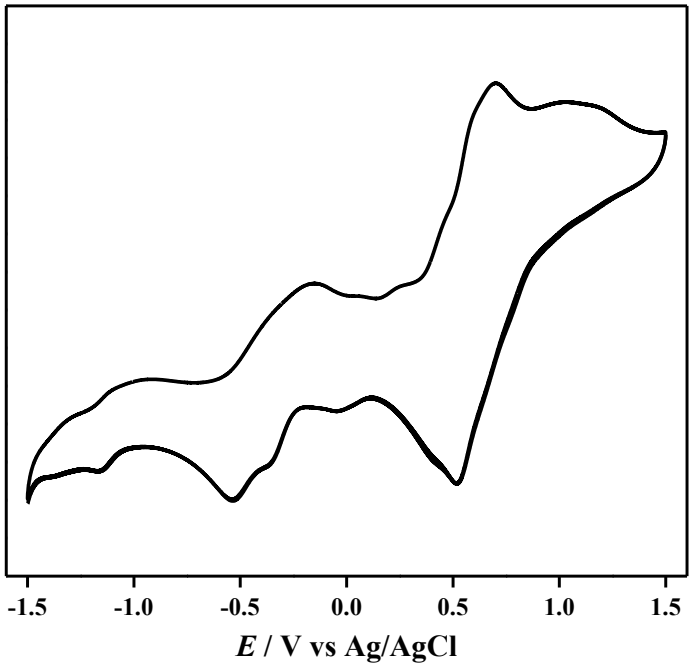

Figure 5.8. Cyclic voltammetry of **2** in acetonitrile with a scan rate of 100 mV/s.

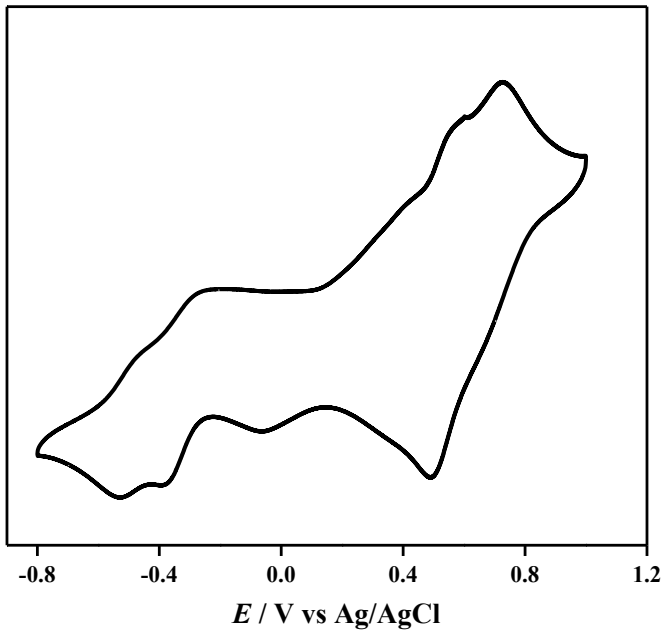

Figure 5.9. Cyclic voltammetry of **3** in acetonitrile with a scan rate of 100 mV/s.

5.4.4 Magnetic studies

Static magnetic properties of the complexes were measured under 1000 Oe field from 300 to 2 K. As shown in **Figure 5.10**, the χT value of **1** at 300 K is 12.29 cm^3 mol^{-1} K, which is significantly higher than the sum of four non-interacting Co^{II} ions (1.89 cm^3 mol^{-1} K each) with unquenched orbital momentum and four isolated tetrazine radicals (0.375 cm^3 mol^{-1} K each), suggest strong orbital contribution.[15] The χT product remained nearly static to 150 K before an increase to a maximum of 16.76 cm^3 mol^{-1} K at 16 K. The decrease of χT to 14.73 cm^3 mol^{-1} K at 2 K might be due to antiferromagnetic interactions and/or spin-orbit coupling.

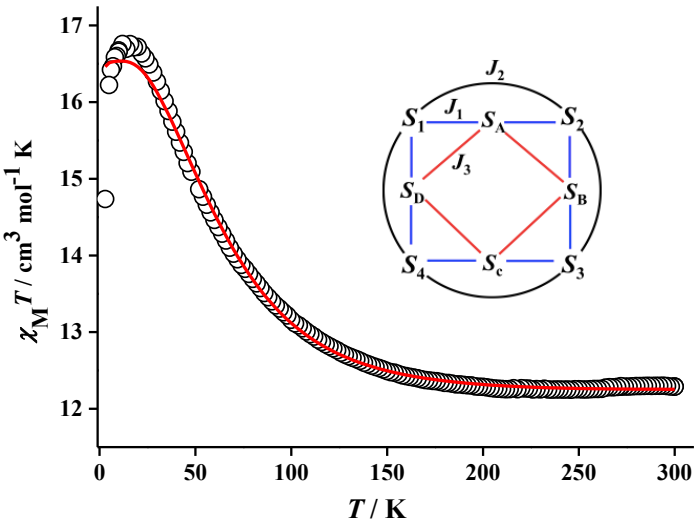

Figure 5.10. Variable-temperature magnetic susceptibilities of **1** under 1000 Oe applied field. Solid lines represent the best fittings using eq. 5.1. Inset shows the magnetic exchange pathways in **1**.

To gain an insight of the magnetic couplings of the spin carriers, the full-range magnetic susceptibility data were fitted using PHI programme[16] based on the following Hamilton similar to the Co_4bpztz complex

$$\hat{H} = -2J_1(\hat{S}_1\hat{S}_A + \hat{S}_A\hat{S}_2 + \hat{S}_2\hat{S}_B + \hat{S}_B\hat{S}_3 + \hat{S}_3\hat{S}_C + \hat{S}_C\hat{S}_4 + \hat{S}_4\hat{S}_D + \hat{S}_D\hat{S}_1) + (\sum_{i=A}^{D} g_{rad}\mu_B\hat{S}_i H)$$
$$+(\sum_{i=1}^{4} g_{Co}\mu_B\hat{S}_i H) - 2J_2(\hat{S}_1\hat{S}_2 + \hat{S}_2\hat{S}_3 + \hat{S}_3\hat{S}_4 + \hat{S}_4\hat{S}_1) - 2J_3(\hat{S}_A\hat{S}_B + \hat{S}_B\hat{S}_C + \hat{S}_C\hat{S}_D + \hat{S}_D\hat{S}_A) \qquad \text{(eq. 5.1)}$$

where S_1 to $S_4 = S_{Co} = 3/2$, S_A to $S_D = S_{rad} = 1/2$, μ_B is the Bohr magneton, H is the magnetic field vector, g_{Co} is the Lande factors for Co^{II} ion and g_{rad} is fixed to be 2.003 for $bptz^{\bullet-}$ radical, respectively; J_1 to J_3 correspond to the magnetic couplings for Co···radical, Co···Co, and the neighbouring radicals, respectively. The best fitted parameters gave $J_1 = -23.11$ cm^{-1}, $J_2 = 6.34$ cm^{-1}, $J_3 = -8.36$ cm^{-1} and $g_{Co} = 2.42$. The negative value of J_1 indicates antiferromagnetic interaction between Co^{II} and bptz radical as expected, however it is much smaller than the previously reported Co_4bpztz compound and $bptz^{\bullet-}$ bridged squares. J_2 represents metal-metal exchange coupling mediated by both the $bptz^{\bullet-}$ radicals and EO-azido bridges and the obtained value is close to that of Co_4bpztz compound, while the negative J_3 indicates the $bptz^{\bullet-}$ radicals are antiferromagnetically coupled. The addition of axial zero-field-splitting parameter D to the Hamiltonian did not significantly improve the fitting quality by giving $D = -0.85$ cm^{-1}, $J_1 = -22.9$ cm^{-1}, $J_2 = 5.98$ cm^{-1}, $J_3 = -7.82$ cm^{-1} and $g = 2.43$.

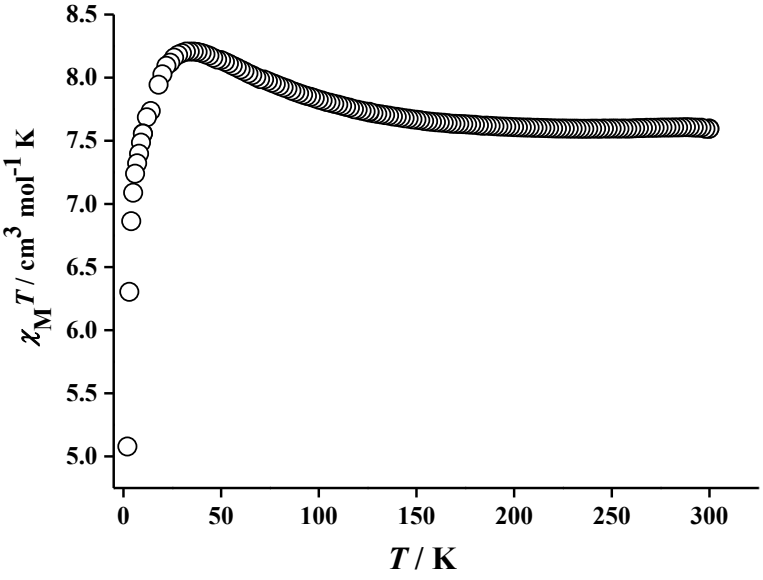

Figure 5.11. Variable-temperature magnetic susceptibilities of **2** under 1000 Oe applied field.

In the case of **2**, the χT value is 7.59 cm^3 mol^{-1} K at 300 K, which agrees well with the considerations of four bptz$^{\bullet-}$ radicals and two non-interacting Co^{II} ions (**Figure 5.11**). The χT value gradually increased to 8.21 cm^3 mol^{-1} K at 32 K then dropped abruptly to 5.08 cm^3 mol^{-1} K at 2 K. The data fitted by Curie-Weiss law gave a positive Weiss constant of +2.5 K, indicating an overall ferromagnetic interaction of the clusters. Due to the lack of spin-delocalisation model for the present system, no reasonable fitting of the magnetic exchange coupling parameters could be obtained. Fitting the data by PHI programme considering the entire molecule to extract the axial (D) and transverse (E) zfs parameters was not successful by giving $|E/D|$ values exceeding the theoretical limit ($|E/D|$ = 1/3).[17]

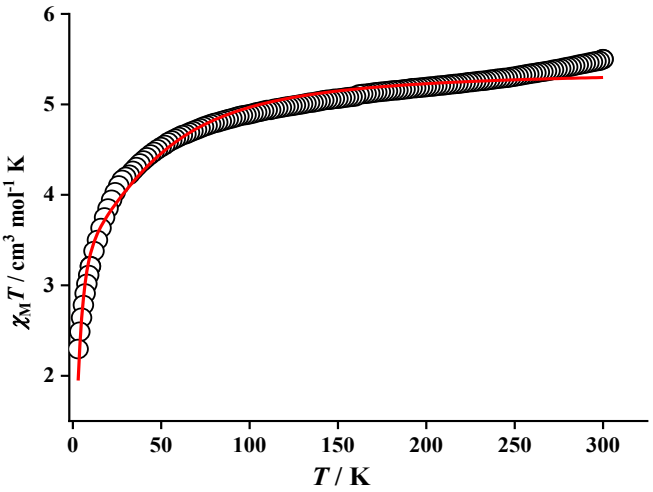

Figure 5.12. Variable-temperature magnetic susceptibilities of **3** under 1000 Oe applied field. Solid lines represent the fittings by eq. 5.2.

For **3**, the χT value of 5.50 cm^3 mol^{-1} K at 300 K is higher than the sum of two independent Co^{II} ions (1.89 cm^3 mol^{-1} K each, g = 2.0) with unquenched orbital momentum, indicating strong orbital contribution (**Figure 5.12**). Upon cooling, the value decreased gradually to 2.02 cm^3 mol^{-1} K at 2.0 K, which may be due to intermolecular antiferromagnetic coupling and/or zero-field splitting. The data fitted by Curie-Weiss law gave a negative Weiss constant of -11.7 K, indicating the overall antiferromagnetic interaction of the molecule. The data were further fitted by PHI programme[16] using the following spin Hamilton model

$$\hat{H} = -2J\hat{S}_1\hat{S}_2 + \sum_{i=1}^{2}(D_{Co,i}\hat{S}_{z,i}^{\ 2} + g_{Co,i}\mu_B\hat{S}_{Co,i}B) \qquad \text{(eq. 5.2)}$$

where $S_1 = S_2 = 3/2$ for high-spin Co(II) ion, D and J represents axial zero-field splitting parameters and the magnetic interaction between two Co^{II} ions, respectively. Both positive and negative D values can be used for fitting. The best set gives similar parameters with D = +15.0 cm^{-1}, J = -0.31 cm^{-1} and g = 2.38, or D = -15.8 cm^{-1}, J = -0.14 cm^{-1} and g = 2.38. The small and negative J value indicates the weak intramolecular antiferromagnetic interaction. This is not surprise because the two diagonal Co^{II}

ions are relatively independent. To accurately determine the *D* value, high-field EPR measurements at low temperatures may be required.

The reduced magnetisation (*M* - *H*) curves of **1-3** measured at 2 – 5 K did not saturate up to 7 kOe (**Figure 5.13** - **Figure 5.15**), reaching 7.47, 5.23 and 3.40 N_β for **1**, **2** and **3**, respectively. The non-superposition of the isofield curves also indicates the presence of magnetic anisotropy in these grid complexes.[15]

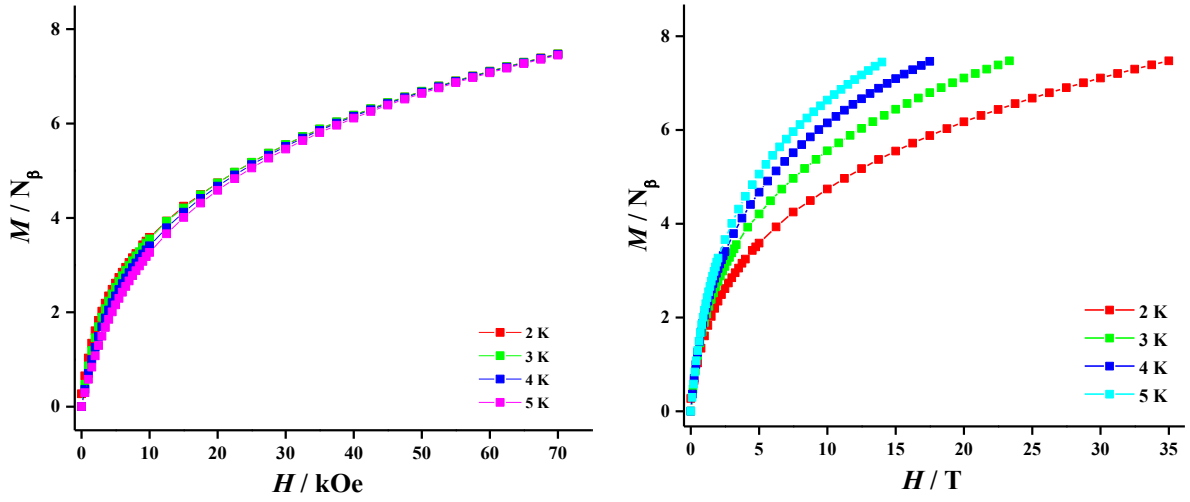

Figure 5.13. Field dependence of the magnetisation for **1** at 2-5 K. The solid lines are guided to the eye.

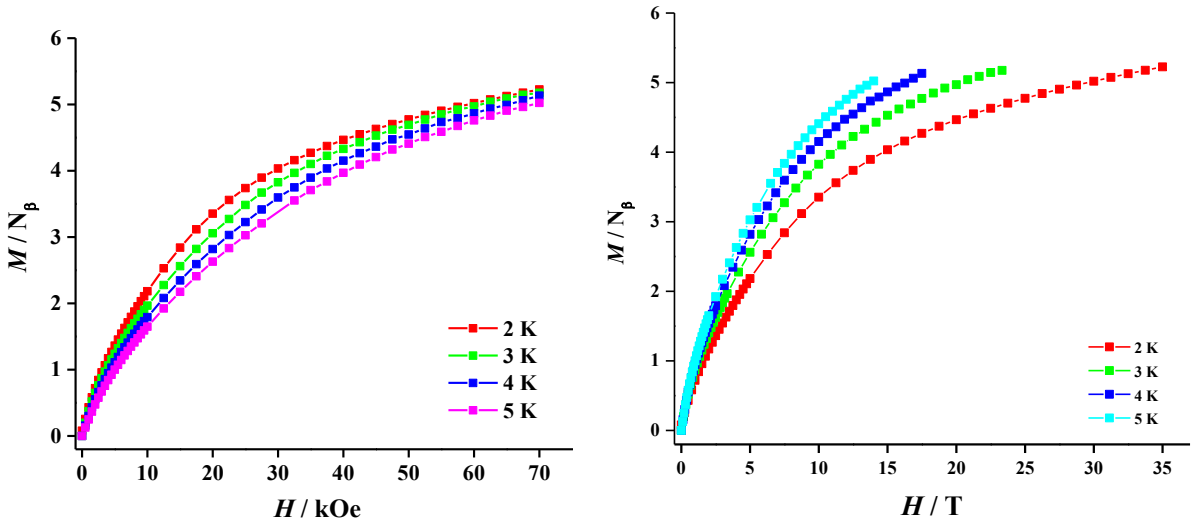

Figure 5.14. Field dependence of the magnetisation for **2** at 2-5 K. The solid lines are guided to the eye.

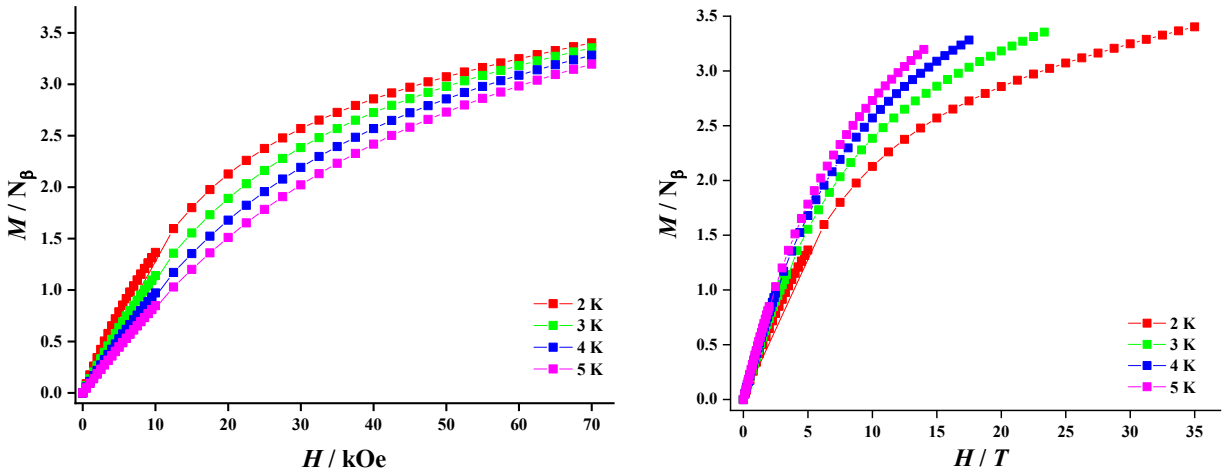

Figure 5.15. Field dependence of the magnetisation for **3** at 2-5 K. The solid lines are guided to the eye.

Hysteresis loops were observed for **1** (**Figure 5.16**) and **2** (**Figure 5.17**) at 2 K under low sweep rates, which may suggest the presence of slow magnetic relaxation.

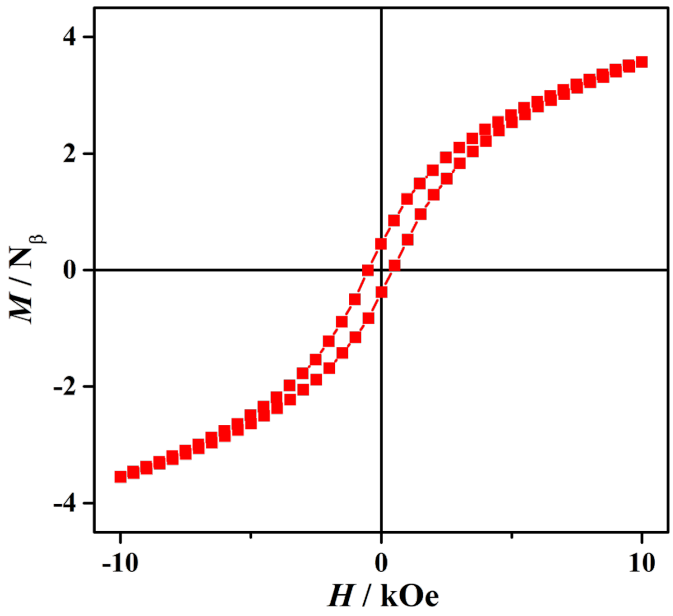

Figure 5.16. Hysteresis loop of **1** at 2 K with a sweep rate of 30 Oe/s.

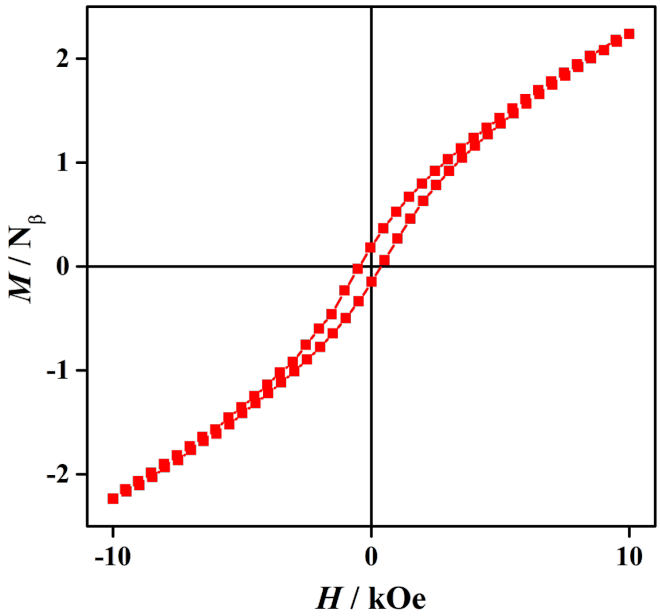

Figure 5.17. Hysteresis loop of **2** at 2 K with a sweep rate of 50 Oe/s.

To further investigate the dynamic magnetic properties of the complexes, alternate current (ac) magnetic measurements were carried out under zero applied field. Both **1** and **2** exhibit strong frequency-dependent and temperature-dependent peaks in in-phase and out-of-phase magnetic susceptibility plots (**Figure 5.18** and **Figure 5.19**), indicating typical slow magnetisation relaxation. The Cole-Cole plots of **1** fitted with Debye model at different temperatures show a single relaxation process. The relaxation time (τ) derived from the χ" peaks follows the Arrhenius law $\tau = \tau_0 \exp(U_{eff}/k_BT)$. The estimated energy barrier is 65 K with a preexponential factor (τ_0) of 1.43×10^{-11} s. Further measurement under different applied fields did not improve the relaxation of magnetisation behaviour.

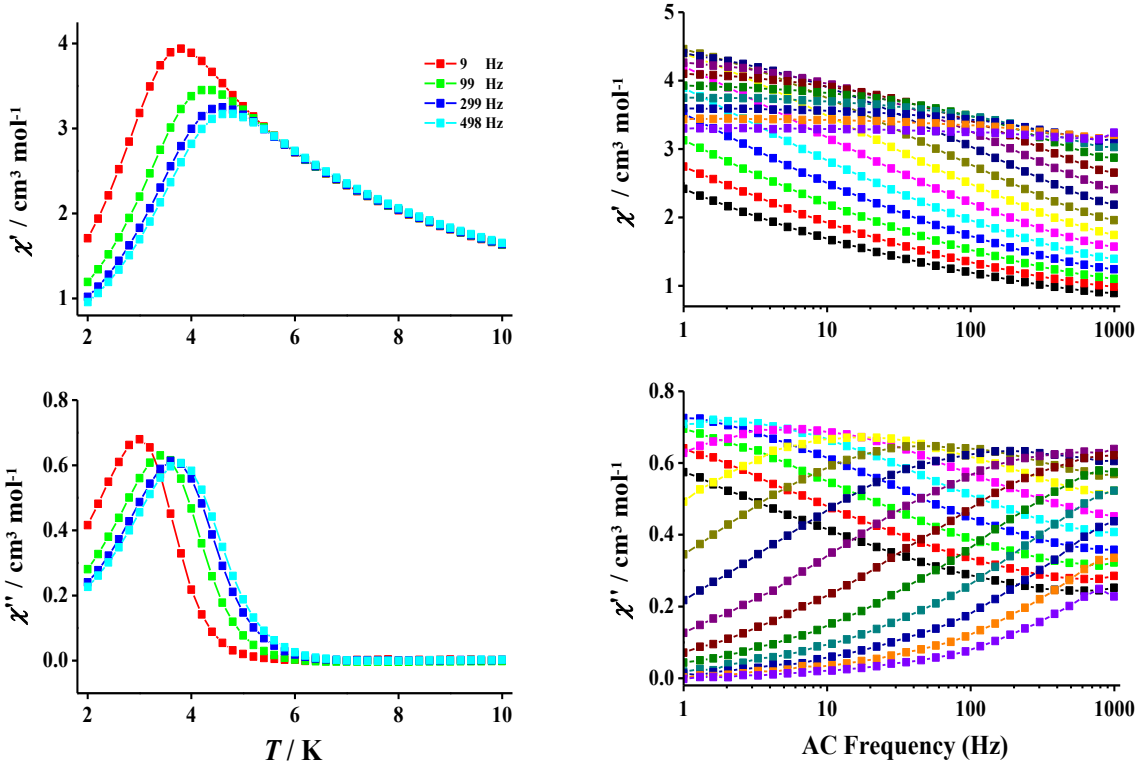

Figure 5.18. Frequency dependence (left) and temperature dependence (right) of the in-phase (χ') and out-of-phase (χ") ac susceptibilities for **1** at zero field.

In the case of **2**, the Mydosh parameter $\varphi = (\Delta Tp/Tp)/(\Delta \log f)$ (Tp is the peak temperature from out-of-phase ac susceptibility and f is the frequency) is estimated to be 0.11 which is close to a normal value for superparamagnetic behaviour. The energy barrier extracted from the frequency-dependent data is 49 K based on Arrhenius law $\tau = \tau_0 \exp(\Delta/k_B T)$. The τ_0 value of 1.5×10^{-9} s is within the range of the reported Co-SMMs. In addition, no obvious frequency-dependent or temperature-dependent peaks were observed for **3** under zero or 1000 Oe applied field which can be due to the presence of fast quantum tunnelling of magnetisation. The energy barriers of **1** and **2** are smaller than the bpztz analogue but still higher than the neutral pyridazine-bridged complexes and within the leading values in azido-bridged systems, demonstrating again that the introduction of radical bridge into selected topologies can effectively enhance the magnetic performance.

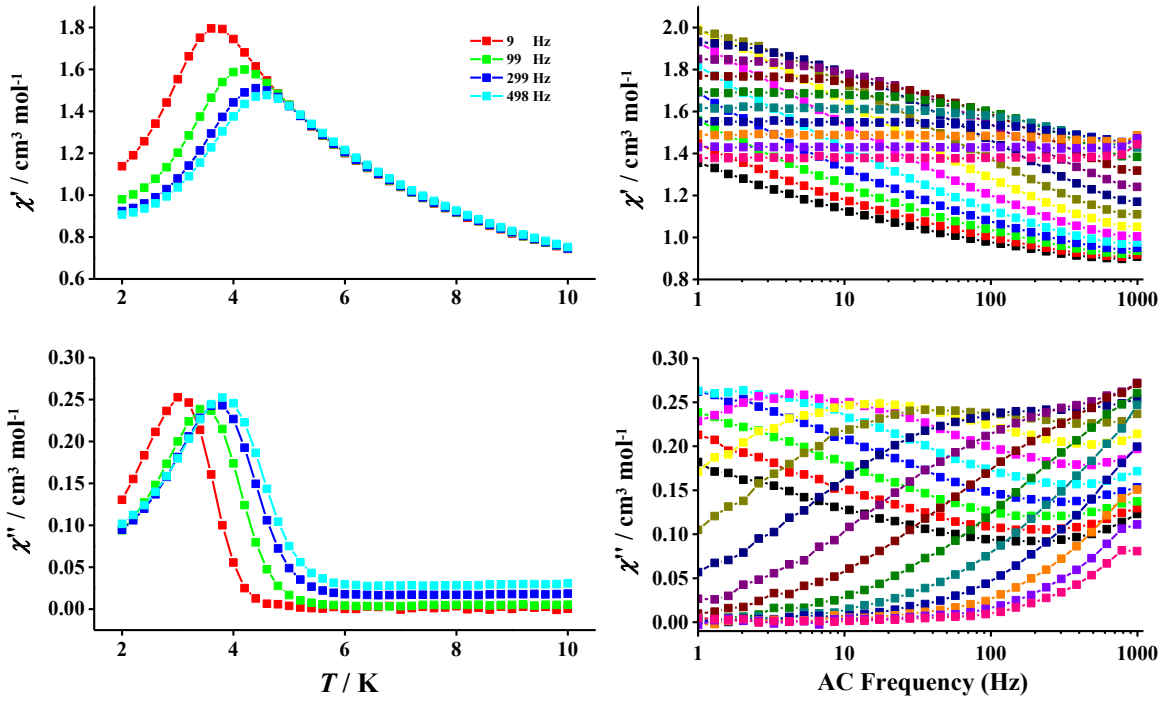

Figure 5.19. Frequency dependence (left) and temperature dependence (right) of the in-phase (χ') and out-of-phase (χ'') ac susceptibilities for **2** at zero field.

5.5 Conclusion

Three novel Co grids were successfully prepared using a redox-active bptz ligand, including a tetrazine radical and azido co-bridged [Co^{II}_4] grid (**1**) and two mix-valent [$Co^{2.5}_4$] (**2**), [$Co^{II}_2Co^{III}_2$] (**3**) grids with tetrazine radical and hydrogenated tetrazine. Magnetic studies of the complexes demonstrated again that direct antiferromagnetic coupling between Co and tetrazine radical leads to the enhancement of single-molecule magnetism in the square complexes compared to the neutral pyridazine analogues. The related DFT calculations on the mixed-valence state are currently in progress.

5.6 References

1. R. Chakrabarty, P. S. Mukherjee and P. J. Stang, *Chem. Rev.*, 2011, **111**, 6810-6918.
2. (a) M. J. Hannon, *Chem. Soc. Rev.*, 2007, **36**, 280-295; (b) N. Busschaert, C. Caltagirone, W. Van Rossom and P. A. Gale, *Chem. Rev.*, 2015, **115**, 8038-8155; (c) D. B. Amabilino, D. K. Smith and J. W. Steed, *Chem. Soc. Rev.*, 2017, **46**, 2404-2420.
3. S. Demir, I.-R. Jeon, J. R. Long and T. D. Harris, *Coord. Chem. Rev.*, 2015, **289-290**, 149-176.
4. (a) B. L. Schottel, H. T. Chifotides and K. R. Dunbar, *Chem. Soc. Rev.*, 2008, **37**, 68-83; (b) H. T. Chifotides and K. R. Dunbar, *Acc. Chem. Res.*, 2013, **46**, 894-906; (c) M. Savastano, C. García-Gallarín, M. D. López de la Torre, C. Bazzicalupi, A. Bianchi and M. Melguizo, *Coord. Chem. Rev.*, 2019, **397**, 112-137.
5. (a) W. Kaim, *Coord. Chem. Rev.*, 2002, **230**, 127-139; (b) G. Clavier and P. Audebert, *Chem. Rev.*, 2010, **110**, 3299-3314.
6. (a) S. K. Tripathy, M. van der Meer, A. Sahoo, P. Laha, N. Dehury, S. Plebst, B. Sarkar, K. Samanta and S. Patra, *Dalton Trans.*, 2016, **45**, 12532-12538; (b) S. Chellamma and M.

Lieberman, *Inorg. Chem.*, 2001, **40**, 3177-3180; (c) S. Patra, B. Sarkar, S. Ghumaan, J. Fiedler, W. Kaim and G. K. Lahiri, *Inorg. Chem.*, 2004, **43**, 6108-6113; (d) M. Schwach, H.-D. Hausen and W. Kaim, *Inorg. Chem.*, 1999, **38**, 2242-2243; (e) C. Kavakli, A. Gabrielsson, M. Sieger, B. Schwederski, M. Niemeyer and W. Kaim, *J. Organomet. Chem.*, 2007, **692**, 3151-3155; (f) P. Audebert, S. Sadki, F. Miomandre, G. Clavier, M. Claude Vernières, M. Saoud and P. Hapiot, *New J. Chem.*, 2004, **28**, 387-392; (g) T. Scheiring, J. Fiedler and W. Kaim, *Organometallics*, 2001, **20**, 1437-1441.

7. O. Stetsiuk, S. R. Petrusenko, L. Sorace, A. Lupan, A. A. A. Attia, V. N. Kokozay, A. El-Ghayoury and N. Avarvari, *Dalton Trans.*, 2019, **48**, 11966-11977.

8. (a) D. I. Alexandropoulos, B. S. Dolinar, K. R. Vignesh and K. R. Dunbar, *J. Am. Chem. Soc.*, 2017, **139**, 11040-11043; (b) M. A. Lemes, G. Brunet, A. Pialat, L. Ungur, I. Korobkov and M. Murugesu, *Chem. Commun.*, 2017, **53**, 8660-8663; (c) T. J. Woods, H. D. Stout, B. S. Dolinar, K. R. Vignesh, M. F. Ballesteros-Rivas, C. Achim and K. R. Dunbar, *Inorg. Chem.*, 2017, **56**, 12094-12097; (d) M. A. Lemes, H. N. Stein, B. Gabidullin, K. Robeyns, R. Clérac and M. Murugesu, *Chem. Eur. J.*, 2018, **24**, 4259-4263.

9. Z. Guo, Y.-F. Deng, Z. Pikramenou, K. R. Dunbar and Y.-Z. Zhang, *Inorg. Chem.*, 2021, **60**, 3651-3656.

10. R. M. Versteegen, R. Rossin, W. ten Hoeve, H. M. Janssen and M. S. Robillard, *Angew. Chem. Int. Ed.*, 2013, **52**, 14112-14116.

11. B. S. Dolinar, D. I. Alexandropoulos, K. R. Vignesh, T. A. James and K. R. Dunbar, *J. Am. Chem. Soc.*, 2018, **140**, 908-911.

12. (a) M. R. Caira, R. G. F. Giles, L. R. Nassimbeni, G. M. Sheldrick and R. G. Hazell, *Acta Cryst. B*, 1976, **32**, 1467-1469; (b) M. Maekawa, T. Miyazaki, K. Sugimoto, T. Okubo, T. Kuroda-

Sowa, M. Munakata and S. Kitagawa, *Dalton Trans.*, 2013, **42**, 4258-4266; (c) K. Wzgarda-Raj, A. J. Rybarczyk-Pirek, S. Wojtulewski and M. Palusiak, *Acta Crys. E*, 2019, **75**, 86-88.

13. (a) G. A. Heath, L. J. Yellowlees and P. S. Braterman, *J. Chem. Soc., Chem. Commun.*, 1981, 287-289; (b) P. S. Braterman, J. I. Song and R. D. Peacock, *Inorg. Chem.*, 1992, **31**, 555-559.
14. H. T. Chifotides, I. D. Giles and K. R. Dunbar, *J. Am. Chem. Soc.*, 2013, **135**, 3039-3055.
15. M. Murrie, *Chem. Soc. Rev.*, 2010, **39**, 1986-1995.
16. N. F. Chilton, R. P. Anderson, L. D. Turner, A. Soncini and K. S. Murray, *J. Comput. Chem.*, 2013, **34**, 1164-1175.

Chapter 6

Energy Transfer of Heterodinuclear Lanthanide Complexes Based on a Pentaphenyl Diimidotriphosphate Ligand

6.1 Abstract

The employment of a pentaphenyl diimidotriphosphate H_2bistpOp afforded a series of homodinulcear lanthanide complexes [Ln_2bistpOp_3] (Ln = Sm, Eu, Gd, Tb, Dy, Yb, **1**-**6**). The complexes are synthesised by the reaction of K_2bistpOp and corresponding $LnCl_3 \cdot 6H_2O$. The 2:3 stoichiometry of Ln : bistpOp is supported by mass spectrometry, luminescence titration and solid state magnetic measurements. Photophysical measurements of the complexes display characteristic visible emissions of Eu^{3+}, Tb^{3+}, Dy^{3+} and Sm^{3+} as well as near-infrared emission of Yb^{3+}. Long lifetimes are observed for [Eu_2bistpOp_3] (**2**) and [Tb_2bistpOp_3] (**4**) complexes. On the other hand, the *in situ* formation of heterometallic [DyEubistpOp_3] and [EuYbbistpOp_3] dimers in solution were investigated, monitoring by luminescence titration experiments and mass spectrometry. [DyEubistpOp_3] dimer displays dual colour emission while [EuYbbistpOp_3] shows both visible and near-infrared emission. The energy transfer efficiency of Dy^{3+} to Eu^{3+} and Eu^{3+} to Yb^{3+} for both dimers calculated by time-resolved luminescent lifetime are above 50%.

6.2 Introduction

Luminescent lanthanide complexes have wide applications in sensing, biological imaging, optical devices and telecommunications.[1] Due to the forbidden 4f-4f transition of single lanthanide ions, organic ligand is always introduced as an antenna to achieve the characteristic luminescence output of lanthanide ions with long lifetimes and high quantum yields. However, it is challenging for a single organic ligand to sensitise all lanthanide ions since the luminescent signal is related to the photosensitising process from the ligand and the reduction of nonradiative quenching pathways mainly from high-energy vibrations in the proximity of the lanthanide coordination site and the presence of charge transfer bands. As a result, the ligand design requires an effective energy transfer between the triplet state of a ligand and the emitting level of the lanthanide ion.

Polynuclear lanthanide systems have garnered growing attentions in exploring new functions such as catalysts, magnetism, optical-magnetic probe, upconversion and biological assays.[2] Of particular interest are the dinuclear complexes bearing proper bridges or well-designed multidentate chelating ligands, including homo- and hetero- dinuclear lanthanide complexes and dinulear lanthanide-transition metal complexes. Research into a series of homodinuclear lanthanide complexes has demonstrated significant enhancement of luminescent output in intensity, lifetimes and quantum yields when compared to their mononuclear species,[1d-f] including our previous work based on bis-diketonate ligands for dinuclear Eu and Sm complexes.[3] Meanwhile, the supramolecular heterodinuclear lanthanide complexes that exhibit dual emissions and effective energy transfer are also of great interest.[4] However, the syntheses and isolation remain difficult due to the stereochemical and coordination preference of the lanthanide ions. To assemble heterodinuclear lanthanide complexes, the control of the ligand to match the lanthanide size or stepwise formation and reactions is also challenging.[5]

Imidodiphosphinate ligands, which provides bidentate bindings to lanthanide ions to form a six-membered ring, are proved to be effective antennas to sensitise lanthanide luminescence with dominant quantum yields and lifetimes.[6] Recently, we adopted a bidentate HtpOp ligand to coordinate with lanthanide ions demonstrating a flexible shielding enhancement on visible and near infrared emission.[7] A bis-bidentate formation ligand H_2bistpOp (pentaphenyl diimidotriphosphate, **Figure 6.1**),[8] which offers an extra coordination position compared to HtpOp ligand, has then drawn our attention. Similar to the triketonate ligands that have been studied due to their ability of to form dinuclear complexes while maintaining local symmetry,[9] this ligand can also afford linear arrays for metal ions upon coordination. Herein we investigated the assembly of H_2bistpOp in a series of homodinuclear lanthanide complexes [Ln_2(bistpOp)$_3$] (Ln = Sm, Eu, Gd, Tb, Dy, Yb, **1**-**6**) with a

detailed photophysical study of the complexes. Meanwhile, heterodinuclear assemblies of lanthanide ions are investigated via luminescence titration.

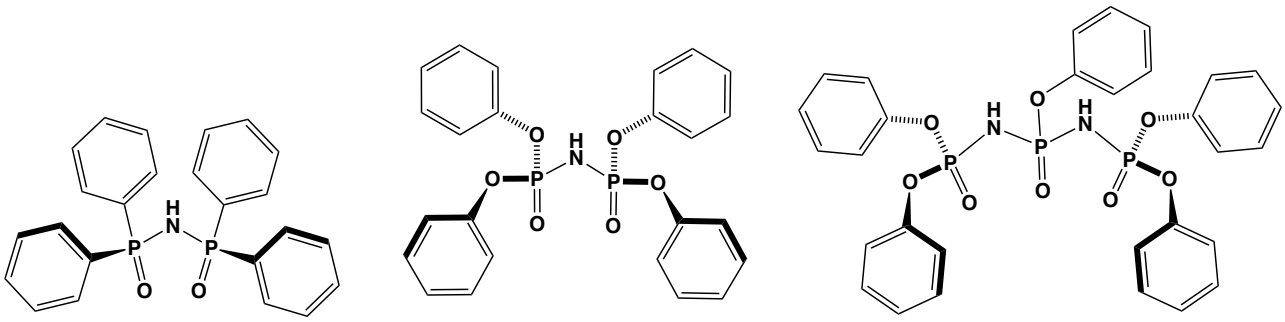

Figure 6.1. Structures of Htpip, HtpOp and H_2bistpOp ligands.

6.3 Contribution

The ligands (H_2bistpOp and K_2bistpOp) and the homodinulcear lanthanide complexes were previously reported by the Pikramenou research group.[10] I reproduced the synthesis of the ligand and lanthanide complexes to ensure full characterisations and more detailed photophysical measurements. I also extended the research on magnetic properties of homodinuclear lanthanide complexes (Gd, Tb, Dy and Yb) and investigation of heterodinuclear assemblies.

6.4 Experimental Section

6.4.1 General methods

All the chemicals and solvents were commercially available from Sigma-Aldrich, Alfa Aesar or Fisher. NaH (60% dispersion in mineral oil) and KH (35% dispersion in mineral oil) was removed prior to use by successively washed with hexane. NMR spectra were obtained on Bruker AC 300, AV

300, AMX 400, AV 400 or DRX 500 spectrometers. Electrospray mass spectra were recorded on a Micromass LC-TOF machine. Single crystal data were collected on Bruker D8 Adventure diffractometer with CuKα (λ = 154178) radiation and kept at 100 K for H_2bistpOp and 298 K for K_2bistpOp during data collection. The structures were solved with the ShelXT structure solution program[11] with Olex2 programme[12] using Intrinsic Phasing and refined with the ShelXL refinement package[13] using Least Squares minimisation. Elemental analyses were recorded on a Carlo Erba EA1110 simultaneous CHN elemental analyser. Magnetic measurements were carried out on an SQUID MPMS3 magnetometer. Magnetic data were corrected for the diamagnetism of the sample holder and for the diamagnetism of the sample using Pascal's constants.

6.4.2 Photophysical measurements

UV-vis absorption spectra were recorded on Agilent Cary 60 UV-Vis spectrophotometer. Emission and excitation data were recorded on the Edinburgh Instrument FLSP920 steady state with F900 software and corrected by Xenon lamp and visible/NIR photomultiplier tube (PMT). Time-resolved lifetime measurements were carried out by using flash lamp as excitation source and collected on the Edinburgh Instrument. The quantum yields were measured by integrating sphere. The data was analysed and fitted by global fitting on FAST software.

6.4.3 Synthesis

Synthesis of [Ln_2(bistpOp)$_3$] (Ln = Sm, Eu, Gd, Tb, Dy, Yb) complexes. H_2bistpOp and K_2bistpOp were prepared according to previously reported methods.[10] To a stirring solution of K_2bistpOp (0.075 mmol) in ethanol (10 mL), $LnCl_3 \cdot 6H_2O$ (0.05 mmol) in ethanol (1 mL) and H_2O (1 mL) were added dropwise. The mixture was stirred for one hour at room temperature. Water was added to form white precipitate, which was collected by filtration, washed with hexane (3 × 5 mL) and water then dried under vacuum.

$[Sm_2(bistpOp)_3]$ (**1**). Yield 23.5 mg, 43% (based on ligand). MALDI-MS *m/z*: 2204 $[M + H]^+$, 1422 $[M – Sm(bistpOp)+ 2H]^+$. Elemental analysis Calc. (%) for $C_{90}H_{75}N_6O_{24}P_9Sm_2(H_2O)_6$: C, 46.75; H, 3.79; N, 3.63; found C, 46.47; H, 3.54; N, 3.81; UV-vis (CH_3CN): λ in nm (log ε) 263 (3.8).

$[Eu_2(bistpOp)_3]$ (**2**). Yield: 25.8 mg, 47% (based on ligand). MALDI-MS *m/z*: 2209 $[M + H]^+$, 1423 $[M - Eu(bistpOp) + 2H]^+$. Elemental analysis Calc. (%) for $C_{90}H_{75}N_6O_{24}P_9Eu_2(H_2O)$: C, 48.58; H, 3.49; N, 3.78; found C, 48.79; H, 3.40; N, 3.85; UV- vis (CH_3CN): λ in nm (log ε) 263 (3.7).

$[Gd_2(bistpOp)_3]$ (**3**). Yield: 20.4 mg, 36% (based on ligand). MALDI-MS *m/z*: 2219 $[M + H]^+$, 1428 $[M - Gd(bistpOp)+2H]^+$. Elemental analysis Calc. (%) for $C_{90}H_{75}N_6O_{24}P_9Gd_2(H_2O)_4$: C, 47.21; H, 3.65; N, 3.67; found C, 46.89; H, 3.21; N, 3.71; UV-vis (CH_3CN): λ in nm (log ε) 263 (3.8).

$[Tb_2(bistpOp)_3]$ (**4**). Yield: 27.3 mg, 50% (based on ligand). MALDI-MS *m/z*: 2222 $[M + H]^+$, 1429 $[M -Tb(bistpOp) + 2H]^+$. Elemental analysis Calc. (%) for $C_{90}H_{75}N_6O_{24}P_9Tb_2(H_2O)_5$: C, 46.77; H, 3.71; N, 3.64; found C, 46.74; H, 3.53; N, 3.78; UV-vis (CH_3CN): λ in nm (log ε) 263 (3.8).

$[Dy_2(bistpOp)_3]$ (**5**). Yield: 26.2 mg, 47% (based on ligand). MALDI-MS *m/z*: 2228 $[M + H]^+$, 1434 $[M - Dy(bistpOp)+ 2H]^+$. Elemental analysis Calc. (%) for $C_{90}H_{75}N_6O_{24}P_9Dy_2(H_2O)_4$: C, 46.99; H, 3.64; N, 3.65; found C, 46.92; H, 3.56; N, 3.85; UV-vis (CH_3CN): λ in nm (log ε) 263 (3.7).

$[Yb_2(bistpOp)_3]$ (**6**). Yield: 30.2 mg, 55% (based on ligand). MALDI-MS *m/z*: 2251 $[M + H]^+$, 1444 $[M - Yb(bistpOp) + 2H]^+$. Elemental analysis Calc. (%) for $C_{90}H_{75}N_6O_{24}P_9Yb_2(H_2O)_4$: C, 46.56; H, 3.60; N, 3.62; found C, 46.21; H, 3.36; N, 3.76; UV-vis (CH_3CN): λ in nm (log ε) 263 (3.6).

6.5 Results and discussion

6.5.1 Crystal structures of ligands

H_2bistpOp ligand was synthesised by reaction of diphenyl phosphoramidate, NaH, and triphenyl phosphate in a 2:2:1 ratio and the NMR characterisation agreed with previously reported results.[10]

Single crystals of H_2bistpOp were obtained by slow evaporation from a chloroform solution at room temperature. The asymmetric unit contains two H_2bistpOp molecules (**Figure 6.2**) where two oxygen atoms (O3 and O5) are in *cis* arrangement with respect to each other in a distance of 3.00 Å, whereas O5 and O8 have anti- conformation. The O-P•••P-O torsion angles in the two chelate rings of the ligand are within the range of 166.4° and 175.5°. The average P=O bond length of 1.46 Å indicates the double bonding between P and O with localised π-electrons. The P-N bond lengths ranges from 1.67 to 1.63 Å. Intermolecular hydrogen bonding interaction was observed between the two units from the two hydrogen atoms on two nitrogen atoms and two *cis* oxygen atoms within the distance range of 1.98 to 2.08 Å, which results in an one dimensional chain packing structure (**Figure 6.3**).

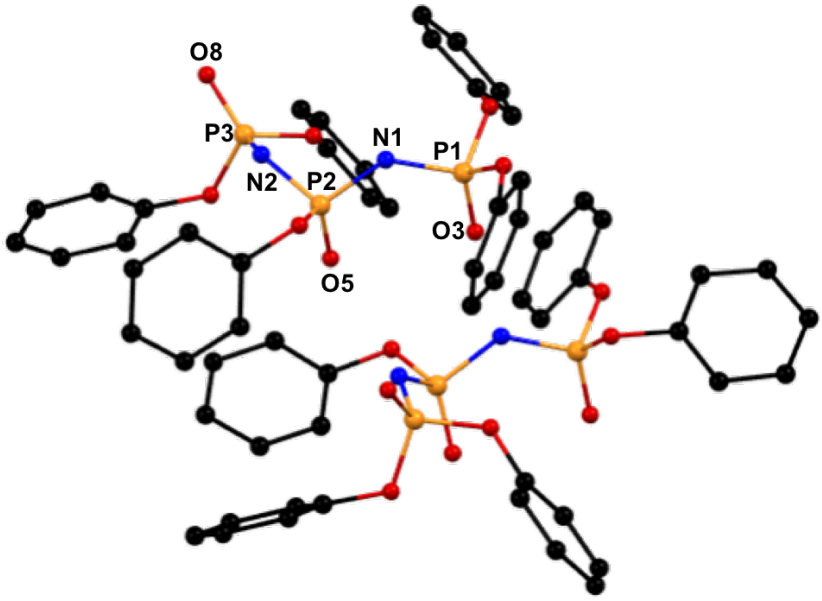

Figure 6.2. Crystal structure of H_2bistpOp with numbering scheme. Hydrogen atoms are omitted for clarity.

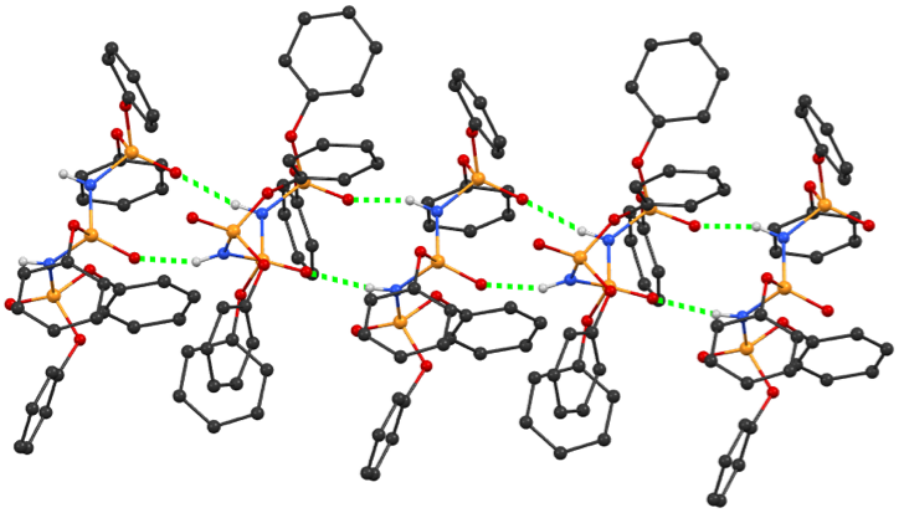

Figure 6.3. Hydrogen bonding interactions (green dashed line) in the stacking structure of H_2bistpOp along a axis.

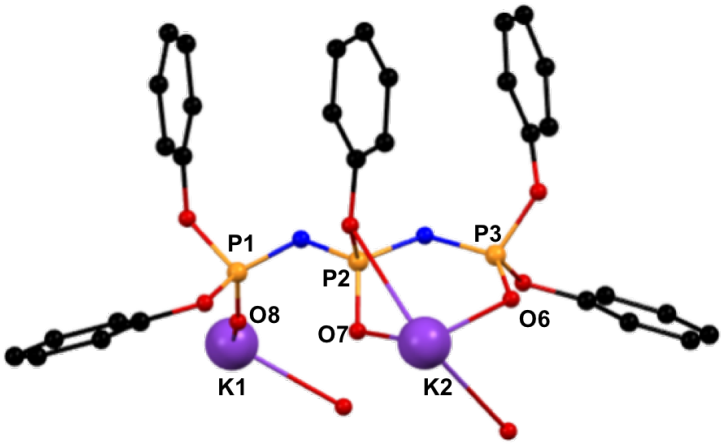

Figure 6.4. Asymmetric unit structure of K_2bistpOp. Hydrogen atoms are omitted for clarity.

Single crystals of K_2bistpOp were grown by slow evaporation of a 1:1 mixed solvents of ethanol and methanol at 4°C. The asymmetric unit contains two K^+ ions and one $bistpOp^{2-}$ ligand (**Figure 6.4**). The three oxygen atoms are arranged in a near *cis* position upon coordination with K^+ ion. The O-P•••P-O torsion angles are 57.4° and 36.2°, which are significantly smaller than H_2bistpOp. One potassium ion (K2) is coordinated by two O from bistpOp ligand and one H_2O, while the other (K1)

is coordinated by one O from bistpOp and an addition water molecule. The average P-N bond distance of 1.57 Å is shorter than H_2bistpOp and the average P=O distance of 1.48 Å are also slightly longer than the free ligand. This indicates the delocalisation of π-electrons around the binding unit, which is consistent with those observed for HtpOp and KtpOp. The packing of K_2bistpOp results in a polymeric structure (**Figure 6.5** top). Interestingly, the view along b axis (**Figure 6.5** bottom) shows the potassium ions are in a square arrangement bridging by the middle oxygen atom from bistpOp and four water molecules. No significant intermolecular interactions are observed.

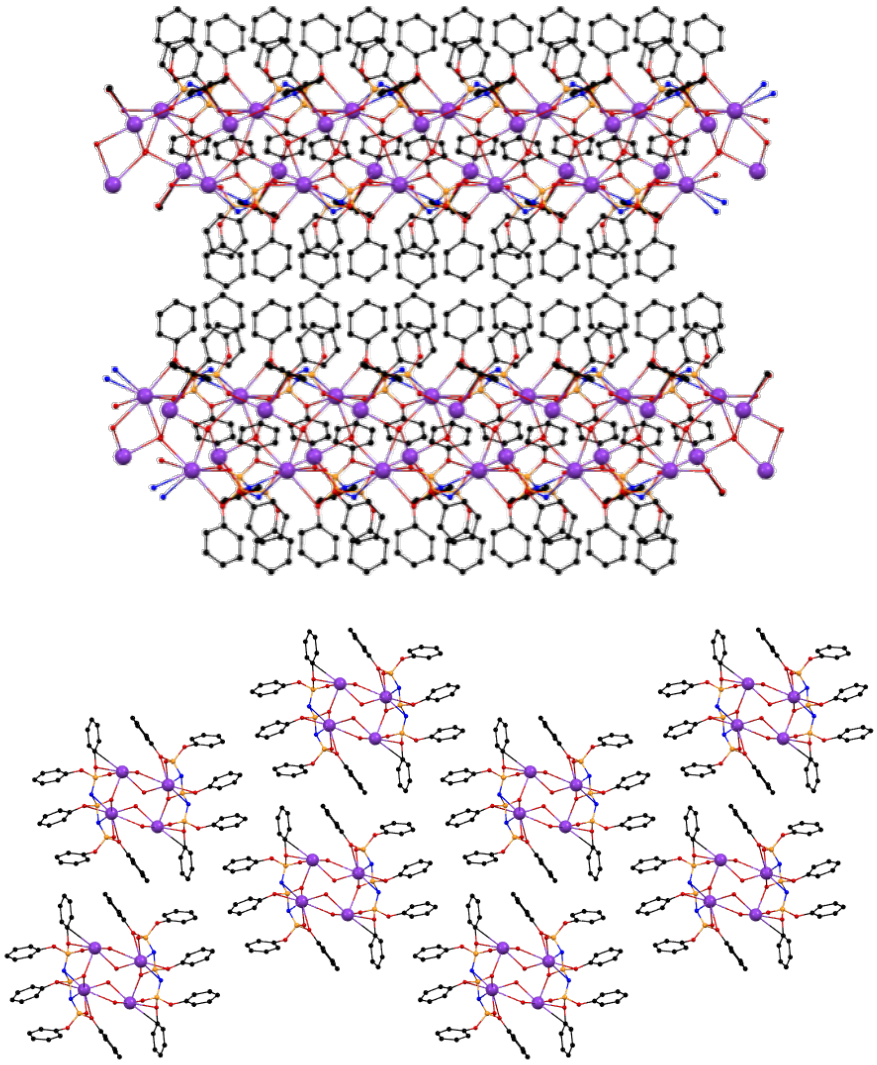

Figure 6.5. Packing of K_2bistpOp along a (top) and b (bottom) axis.

Table 6.1. Crystallographic data of H_2bistpOp and K_2bistpOp.

	H_2bistpOp	K_2bistpOp
Empirical formula	$C_{30}H_{27}N_2O_8P_3$	$C_{30}H_{29}K_2N_2O_{10}P_3$
Formula weight	636.45	748.66
Temperature/K	120	298
Crystal system	Triclinic	Monoclinic
Space group	P -1	$P2_1/n$
a/Å	10.3971(3)	15.3086(7)
b/Å	13.8413(4)	6.2807(3)
c/Å	22.5648(6)	35.0594(17)
α/°	75.526(2)	90
β/°	79.698(2)	98.868(3)
γ/°	72.849(2)	90
Volume/Å^3	2984.94(15)	3330.6(3)
Z	4	4
ρ_{cal}cg/cm^3	1.416	1.493
μ/mm^{-1}	0.253	4.389
F(000)	1320	1544.0
Crystal size/mm^3	0.08 × 0.03 × 0.01	0.12 × 0.02 × 0.02
Radiation	MoKα (λ = 0.71073)	CuKα (λ = 1.54178)
2Θ range for data collection/°	3.08 to 25.03°	8.89 to 130.712
Index ranges	-12<=h<=12, -16<=k<=16, -26<=l<=26	-16 ≤ h ≤ 18, -7 ≤ k ≤ 7, -40 ≤ l ≤ 41
Reflections collected	43335	24772
Independent reflections	10509 [R_{int} = 0.0991]	5673 [R_{int} = 0.1005, R_{sigma} = 0.0752]
Data/restraints/parameters	10509/0/775	5673/0/440
Goodness-of-fit on F^2	1.129	0.985
Final R indexes [I>=2σ (I)]	R_1 = 0.0965, wR_2 = 0.1932	R_1 = 0.0548, wR_2 = 0.1426
Final R indexes [all data]	R_1 = 0.1587, wR_2 = 0.2295	R_1 = 0.0829, wR_2 = 0.1610
Largest diff. peak/hole / e Å^{-3}	1.134/-0.485	0.27/-0.27

6.5.2 Characterisation of Ln complexes

Reaction of $LnCl_3 \cdot 6H_2O$ and K_2bistpOp in a 2:3 ratio results in the formation of $[Ln_2(bistpOp)_3]$ (M = Sm, Eu, Gd, Tb, Dy, Yb). The formation of the complexes are supported by MALDI mass spectra with the correct $[M + H]^+$ peak assignments. All spectra provide the signal occurring at the predicted mass-to-charge ratio value for the dinuclear species, confirming the formulation of the complexes in 2:3 ratio of metal to ligand. These peaks are in good agreement with the theoretical isotope pattern.

6.5.3 Magnetic studies

Static magnetic properties of **3**-**6** were measured at 300 – 2 K under 1000 Oe field (**Figure 6.6**). The $\chi_M T$ values for $[Gd_2(bistpOp)_3]$ (**3**), $[Tb_2(bistpOp)_3]$ (**4**), $[Dy_2(bistpOp)_3]$ (**5**) and $[Yb_2(bistpOp)_3]$ (**6**) at 300 K are 16.21, 24.30, 28.77 and 5.02 $cm^3\ mol^{-1}\ K$, respectively, which are consistent with the theoretical sum of two non-interacting Ln^{3+} ions (for each Ln^{3+}, Gd^{3+} 7.88 $cm^3\ mol^{-1}\ K$, Tb^{3+} 11.85 $cm^3\ mol^{-1}\ K$, Dy^{3+} 14.19 $cm^3\ mol^{-1}\ K$ and Yb^{3+} 2.57 $cm^3\ mol^{-1}\ K$). Upon cooling, the $\chi_M T$ value of **3** remains nearly constant before an abrupt drop from 50 K to 2 K to the lowest of 12.87 $cm^3\ mol^{-1}\ K$, while the $\chi_M T$ values for **4**, **5** and **6** decrease gradually, reaching 21.53 $cm^3\ mol^{-1}\ K$, 15.16 $cm^3\ mol^{-1}\ K$ and 2.31 $cm^3\ mol^{-1}\ K$ at 2 K, respectively. This can be due to the antiferromagnetic interaction between the lanthanide ions and/or Stark sublevels spin-orbital coupling. Fitting the data of **4**, **5** and **6** above 50 K with Curie-Weiss law gave negative Weiss constants of -19.16, -9.26 and -58.53 K, respectively. Considering the absence of orbital angular momentum in Gd^{3+} ions, the magnetic susceptibility data of $[Gd_2(bistpOp)_3]$ were fitted by PHI programme[14] based on the Hamiltonian

$$\hat{H} = -J\hat{S}_1\hat{S}_2 + g\beta H(\hat{S}_1 + \hat{S}_2) \qquad \text{(eq. 6.1)}$$

where $\hat{S}_1 = \hat{S}_2 = S_{Gd} = 7/2$ and J represents magnetic interaction between two Gd^{3+} ions. The best fit gives J = -0.03 cm^{-1} and g = 2.03. The negative and small J value indicates weak antiferromagnetic interaction between the two Gd^{3+} ions, which behaves similarly to those reported oxygen-bridged

dinuclear lanthanide complexes.[15] It should be mentioned that no significant slow relaxation of magnetisation of **4**, **5** and **6** was observed under zero or applied fields. These results also support the stoichiometry of two lanthanides with three bistpOp ligands in the bulk products and weak magnetic communications between the two lanthanide ions.

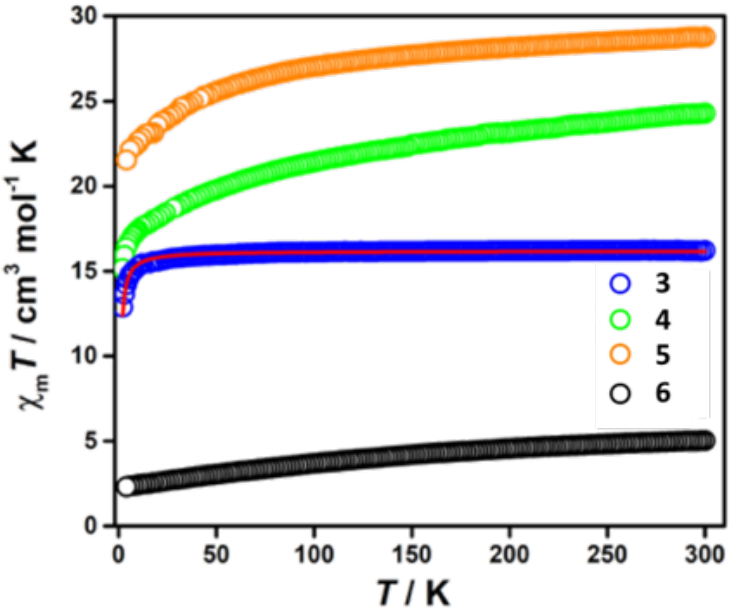

Figure 6.6. Magnetic susceptibility measurement for **3**-**6**. The red line represents the fitting from PHI programme based on eq. 6.1.

6.5.4 Photophysical studies

The lanthanide complexes absorb lights in the UV region attributed to the H_2bistpOp ligand. The absorption spectrum of **4** shows an intense absorption band at 264 nm along with a weaker one at 270 nm (**Figure 6.7**), which are assigned to the $\pi \rightarrow \pi^*$ transitions of phenoxide aromatic groups. The excitation spectrum monitoring the $^5D_0 \rightarrow {}^7F_3$ transition at 620 nm overlapped with absorption spectrum, indicating an efficient energy transfer from ligand to the lanthanide centre.

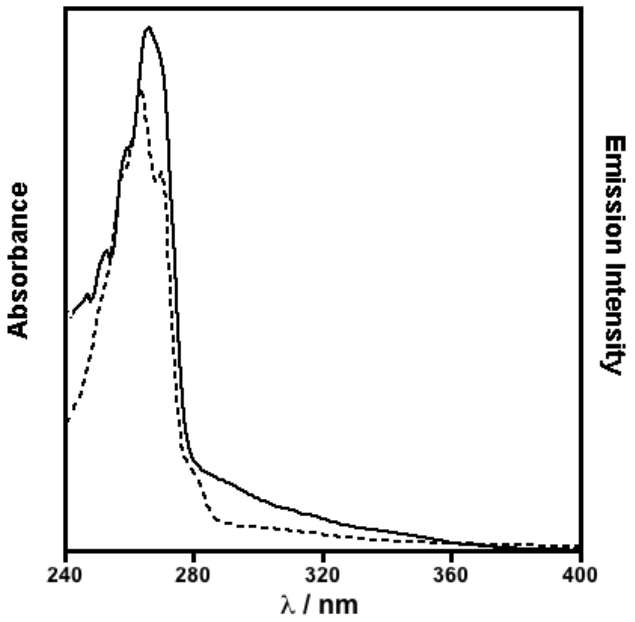

Figure 6.7. Absorption (dashed line) and excitation spectra (solid line) of **4** in dry acetonitrile (λ_{em} = 545 nm, excitation spectra was corrected by PMT response).

Upon excitation at 270 nm, characteristic emission signals in visible region were observed for [Ln_2(bistpOp)$_3$] (Ln = Eu, Tb, Dy and Sm) complexes in dry MeCN solution at room temperature (**Figure 6.8**). [Eu_2(bistpOp)$_3$] (**2**) shows emission bands at 577, 591, 612, 653 and 701 nm which are attributed to the transitions of $^5D_0 \rightarrow {}^7F_J$ (J = 0, 1, 2, 3, 4). The highest intensity is dominated by the hypersensitive $^5D_0 \rightarrow {}^7F_2$ transition at 612 and 621nm. This stronger band than that of the $^5D_0 \rightarrow {}^7F_1$ indicates the asymmetric environment of Eu^{3+} ions in solution.[16] Only one peak in $^5D_0 \rightarrow {}^7F_0$ transition at 577 nm suggests a single chemical environment around Eu^{3+} ions. For [Tb_2(bistpOp)$_3$] (**4**), emission at 487, 544, 585, 619, 650, 668 and 681 nm are attributed to the $^5D_4 \rightarrow {}^7F_J$ (J = 6, 5, 4, 3, 2, 1, 0) transitions. The most intense emission at 544 nm corresponds to the hypersensitive transition $^5D_4 \rightarrow {}^7F_5$. The emission of [$Dy_2$(bistpOp)$_3$] (**5**) shows sharp emission bands at 484, 576, 663 and 753 nm assigned to $^4F_{9/2} \rightarrow {}^6H_J$ (J = 15/2, 13/2, 11/2, 9/2) transitions, while [Sm_2(bistpOp)$_3$]

(**1**) exhibits luminescence at 560, 600, 644 and 705 that are assigned to the $^4G_{5/2} \rightarrow {}^6H_J$ (J = 5/2, 7/2, 9/2) transitions.

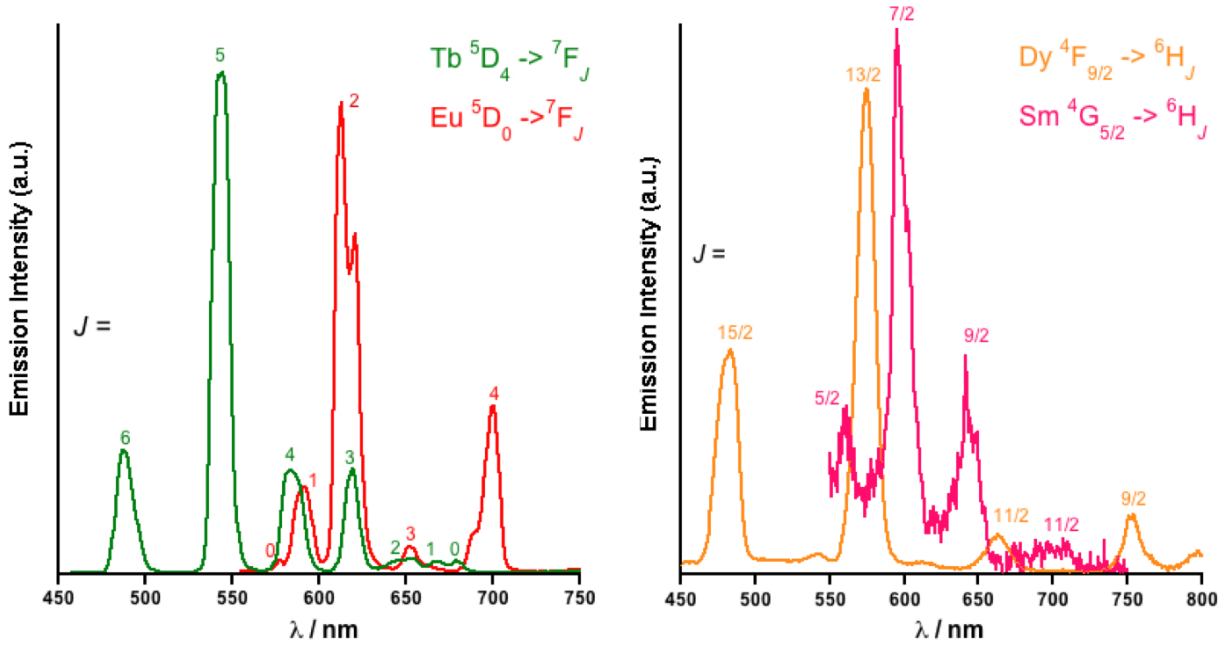

Figure 6.8. Emission spectra of **2** (red), **4** (green), **5** (yellow) and **1** (pink) in dry acetonitrile at room temperature (λ_{exc} = 270 nm, corrected by PMT response).

Only $[Yb_2(bistpOp)_3]$ (**6**) shows near-infrared emission in solution with a broad band at 984 nm which is assigned to the $^2F_{5/2} \rightarrow {}^2F_{7/2}$ transition (**Figure 6.9**). Sensitisation of the NIR luminescence is further supported by the excitation spectrum of **6**, which clearly demonstrates the antenna effect of the ligand with component matching the absorption bands of the electronic spectrum.

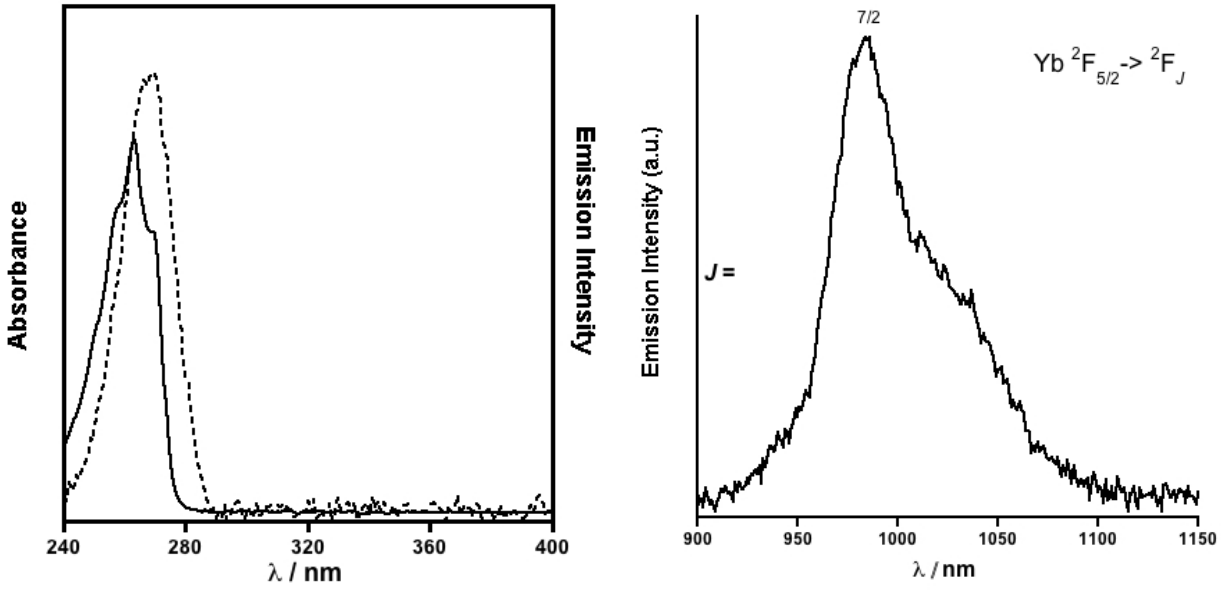

Figure 6.9. (left) Absorption (solid line) and excitation spectra (dotted line) of **6** in dry acetonitrile. (right) Emission spectra of **6** in dry acetonitrile at room temperature (λ_{exc} = 270 nm, corrected by PMT response).

The triplet excited state energy of the ligand was measured by the room temperature and 77 K emission of $[Gd_2(bistpOp)_3]$ (**3**) complex in MeOH/EtOH (1:4) in the previous report (**Figure 6.10**).[10] The lowest T_1 excited state energy was evaluated to be 28736 cm^{-1} and the singlet state energy level of the H_2bistpOp is estimated at 37038 cm^{-1}, which is significantly higher than HtpOp (27397 cm^{-1}) and may be responsible for the less sensitisation efficiency of bistpOp ligand.

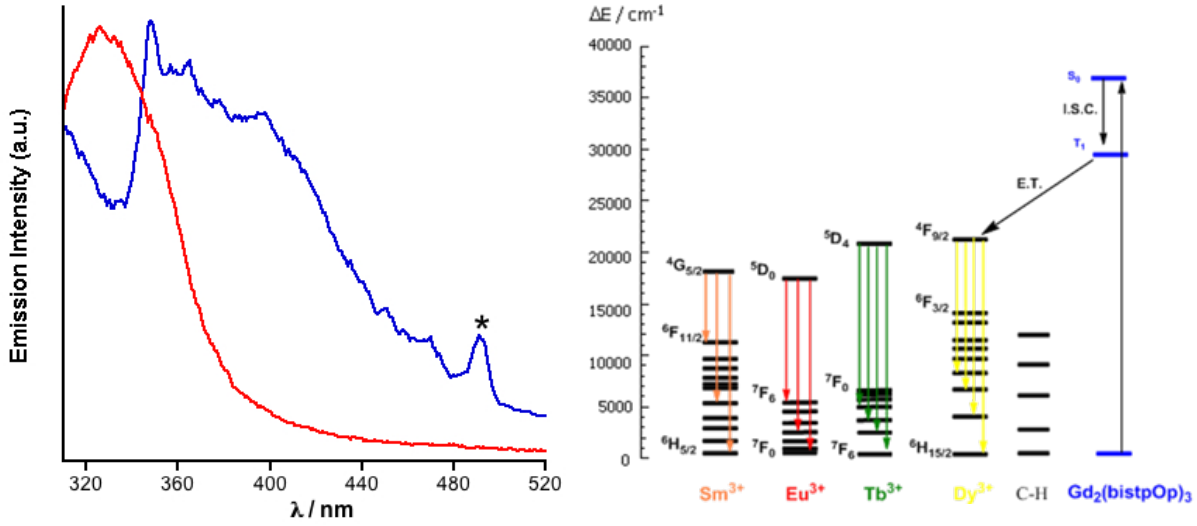

Figure 6.10. (left) Room temperature emission spectra (blue) and 77 K spectra (red) of **3** in EtOH:MeOH = 4:1 (λ_{exc} = 270 nm, * = scattered light). (right) Energy level diagram to show the energy transfer process. Reproduced Figure 3.24 and Scheme 3.5 from ref 10.

In addition, a luminescence titration of $TbCl_3 \cdot 6H_2O$ into K_2bistpOp in MeOH solution was performed in order to investigate the stoichiometry of lanthanide complexes as well as the in situ formation of the complexes in solution (**Figure 6.11**). Upon the addition of Tb^{3+}, the emission intensity increased until reaching a plateau after two equiv of Tb^{3+}. After this point no more Tb^{3+} is accommodated due to the saturated binding sites of the ligand. The result demonstrates the 3:2 stoichiometry of ligand to metal in the lanthanide complexes and the *in situ* formation in solution.

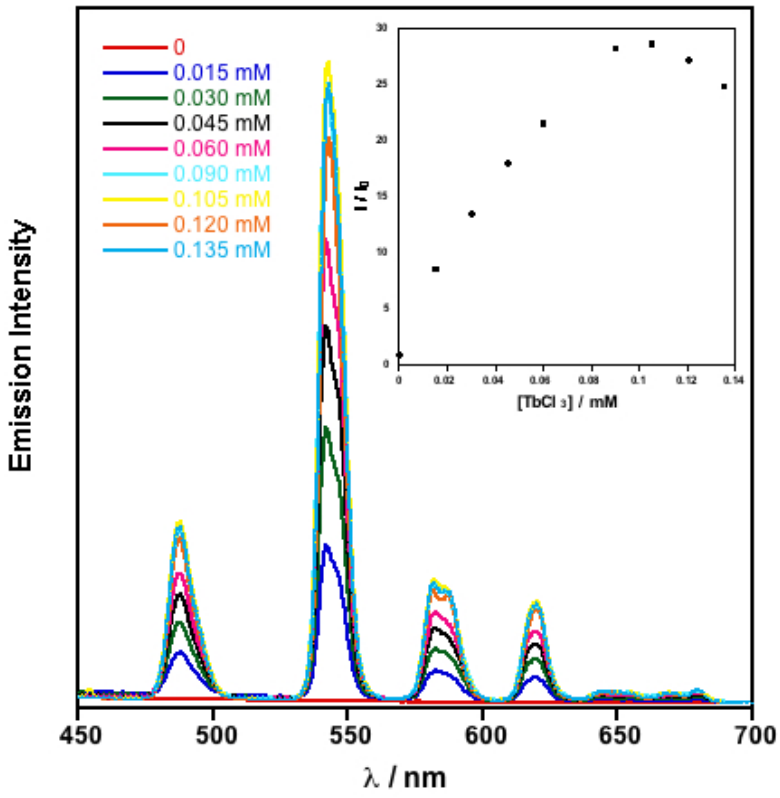

Figure 6.11. Luminescence titration of $TbCl_3 \cdot 6H_2O$ (2 mM) into K_2bistpOp (0.15 mM) in MeOH (λ_{exc} = 270 nm). Inset: Relative integrated emission area vs. concentrations of Tb^{3+} upon titration.

The luminescence lifetimes of $[Ln_2(bistpOp)_3]$ (Ln = Eu, Tb and Dy) complexes were measured in solution under excitation at ligand-centred band. The results are summarised in **Table 6.2**. The time-resolved emission profiles for both $[Eu_2(bistpOp)_3]$ and $[Tb_2(bistpOp)_3]$ reveal single-exponential decay. No significant improvements in fit were obtained when applying a secondary exponential component, which indicates the two Ln^{3+} ions are in the same coordination environment in solution. $[Dy_2(bistpOp)_3]$ display a biexponential lifetime with a major long component of 0.15 ms (84%) and a short component of 0.056 ms (16%). The lifetimes of $[Sm_2(bistpOp)_3]$ and $[Yb_2(bistpOp)_3]$ are too small to adjust the value in the experimental condition. The lifetimes of $[Eu_2(bistpOp)_3]$ and

$[Dy_2(bistpOp)_3]$ in solution are better compared to the previously reported data,[10] which can be due to a drier solvent and less water present in the sample.

The variation of lifetimes can be explained by the energy gap ΔE between the emissive state of the Ln ion and the highest ground state. The ΔE of Tb^{3+} (14,800 cm^{-1}) and Eu^{3+} (12,300 cm^{-1}) are larger than Dy^{3+} (7850 cm^{-1}) and Sm^{3+} (7400 cm^{-1}), therefore, only the high energy O-H oscillators contribute to the quenching of the luminescent states, while the smaller gaps result in lower frequency vibrations causing significant deactivation and the shorter lifetimes.[17]

Table 6.2. Luminescent lifetimes and quantum yields of $[Ln_2(bistpOp)_3]$ (Ln = Eu, Tb, Dy) in dry MeCN monitoring 545, 612 and 574 nm, respectively (λ_{exc} = 270 nm).

Complex	τ_L / ms	QY / %
$[Eu_2(bistpOp)_3]$	2.1	0.8*
$[Tb_2(bistpOp)_3]$	2.5	23.6*
$[Dy_2(bistpOp)_3]$	0.056 (16%), 0.15 (84%)	--

*: errors are estimated to be 5% relative to the quoted values.

The overall sensitisation efficiency was also examined by the quantum yields. In dry MeCN by monitoring the hypersensitive transition of the $[Eu_2(bistpOp)_3]$ and $[Tb_2(bistpOp)_3]$, the quantum yields were measured to be 0.8% and 23.6%, respectively. The improved quantum yield of $[Tb_2(bistpOp)_3]$ compared to the previously reported value[10] may be due to an improved synthesis and less water present of the sample. The values of other lanthanide complexes were hardly obtained,

which clearly demonstrates that the more efficient emitters of bistpOp complexes are Tb^{3+} and Eu^{3+} ions.

The results show that H_2bistpOp is a less efficient sensitiser than the than the HtpOp ligand but similar to Htpip. One possible reason can be due to the large energy gap between the triplet state of H_2bistpOp and the excited state of lanthanides. The values are also smaller than our previously reported dinuclear Eu and Sm complexes based on bis-diketonate ligands which are considered as good antenna due to the well-matched position of the ligand-centred triplet state.

Another possibility causing the quantum yield reduction could be due to the short Ln^{3+} - Ln^{3+} distance, when the distance is less than 8.4 Å concentration quenching will be involved.[18] A model of $[Y_2(bistpOp)_3]$ was achieved by molecular mechanic calculations using the MM2 force field from ChemBio3D software, excluding any coordinated solvent molecules.[19] As shown in **Figure 6.12**, $bistpOp^{2-}$ ligands provide good shielding around the lanthanide ions with a close distance of about 3.7 Å, which further confirms the possible concentration quenching.

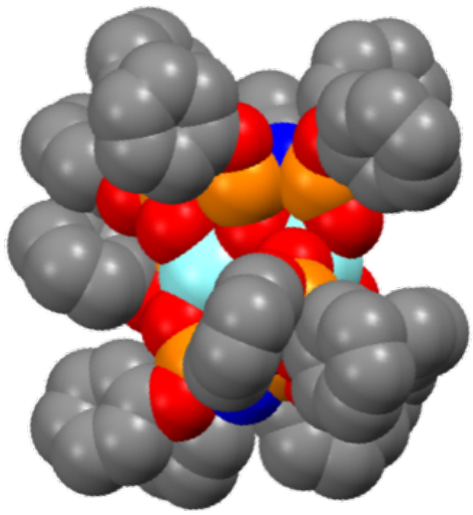

Figure 6.12. Space filled model of $[Y_2(bistpOp)_3]$.

6.5.5 Heterometallic assembly

The two binding positions of bistpOp ligand allow us to investigate the possible heterometallic assembly of lanthanide ions. In this case, luminescence titration experiments were performed to track the formation of [DyEu(bistpOp)$_3$] and [EuYb(bistpOp)$_3$] complexes.

To a methanol solution of K_2bistpOp, $DyCl_3 \cdot 6H_2O$ dissolved in methanol was added until a 1:3 ratio of Ln:bistpOp for the *in situ* formation of $[DybistpOp_3]^{3-}$, by monitoring Dy^{3+} emission under 270 nm excitation. After that $EuCl_3 \cdot 6H_2O$ in methanol was added to reach a final 2:3 ratio of Ln:bistpOp by monitoring Eu^{3+} emissions at 616 nm. With the addition of Eu^{3+}, increasing Eu^{3+} emission was detected during the titration while Dy^{3+} emission intensity decreased to 60% compared to $[DybistpOp_3]^{3-}$ by integration, indicating the occurrence of energy transfer from Dy^{3+} to Eu^{3+} (**Figure 6.13**).

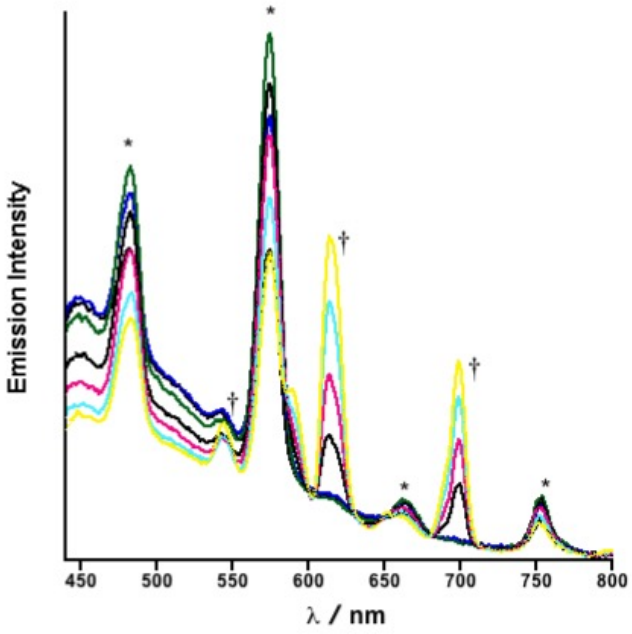

Figure 6.13. Luminescence titration of Dy^{3+} and Eu^{3+} into a K_2bistpOp in MeOH solution monitoring the emission of Dy^{3+} and Eu^{3+} (λ_{exc} = 270 nm). *: emission of Dy^{3+}, †: emission of Eu^{3+}.

Using a similar titration procedure, the in situ formation of [EuYb(bistpOp)$_3$] was performed by the addition of Eu^{3+} into K_2bistpOp in methanol and followed by Yb^{3+} to a final 2:3 ratio of Ln:bistpOp, monitoring Eu^{3+} and Yb^{3+} emission under 270 nm excitation. During the titration, Yb^{3+} emission at 975 nm in NIR region was observed with the decreasing intensities of Eu^{3+} emission signal by 32% of [EubistpOp$_3$]$^{3-}$ species, which suggests an energy transfer from Eu^{3+} to Yb^{3+} (**Figure 6.14**). No more Yb^{3+} was accommodated, indicating the 2:3 ratio of Ln:bistpOp in solution.

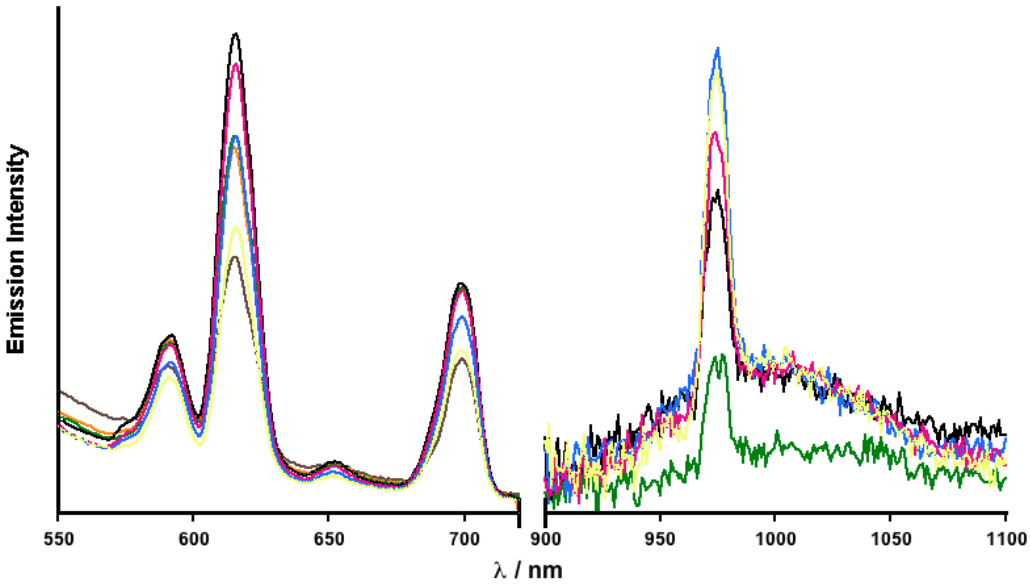

Figure 6.14. Luminescence titration of Eu^{3+} and Yb^{3+} into a K_2bistpOp in MeOH solution monitoring the emission of Eu^{3+} and Yb^{3+} (λ_{exc} = 270 nm).

The formation of the heterodinuclear complexes were further confirmed by the mass spectrometry after titration. As shown in **Figure 6.15** and **Figure 6.16**, the observed peaks at 2219.6 and 2230.12 agreed with the theoretical isotopes of {DyEu(bistpOp)$_3$ + H$^+$} and {EuYb(bistpOp)$_3$ + H$^+$}, respectively, which indicate the formation of heterdinuclear species in solution.

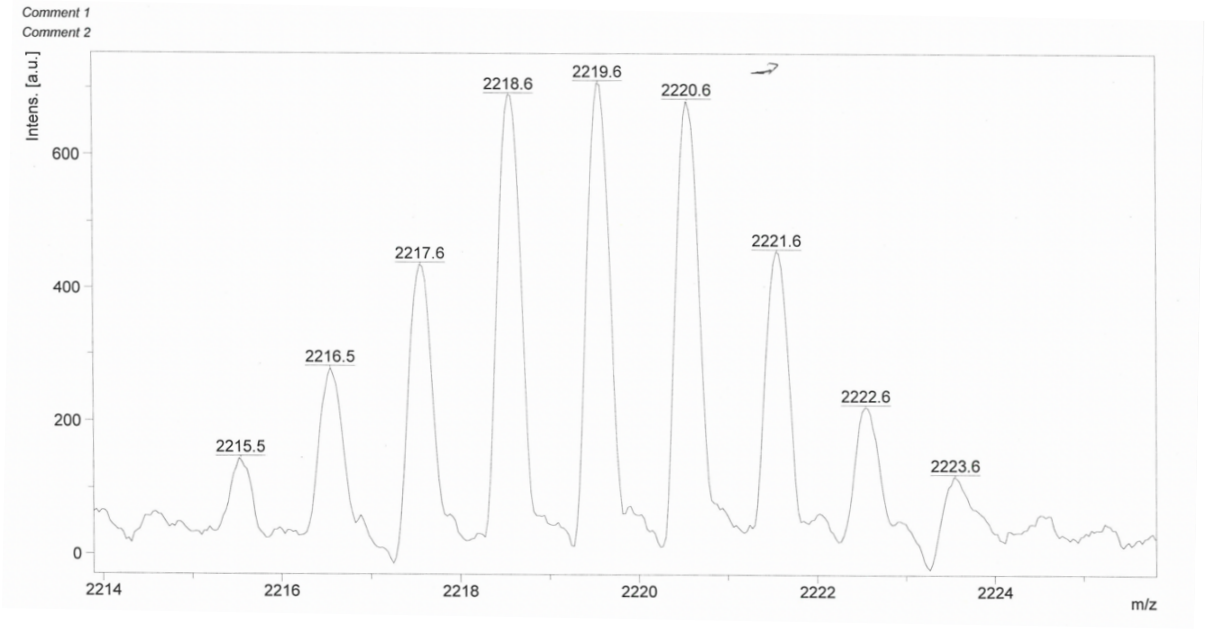

Figure 6.15. MALDI mass spectrometry diagram for {DyEu(bistpOp)$_3$ + H$^+$} after titration showing the formation of heterodinuclear complex.

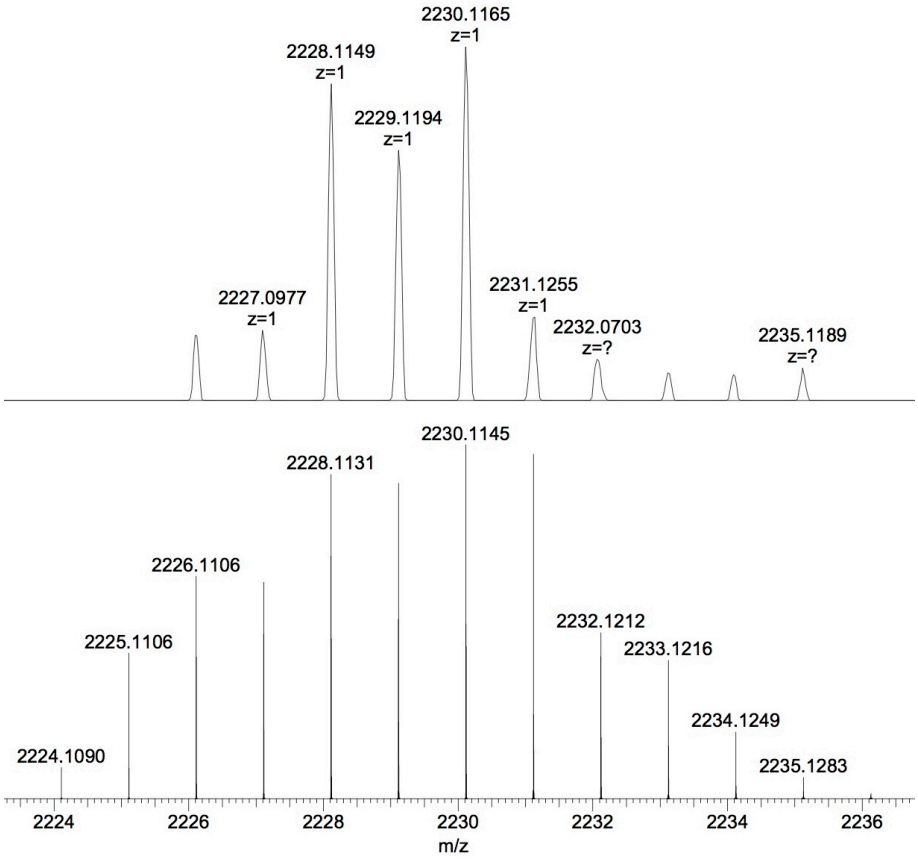

Figure 6.16. ESI^+ mass spectrometry diagram for {EuYb(bistpOp)$_3$ + H^+} after titration (top) with simulated pattern (bottom) showing the formation of heterodinuclear complex.

A combination of equimolar amounts of $DyCl_3 \cdot 6H_2O$ and $EuCl_3 \cdot 6H_2O$ or $EuCl_3 \cdot 6H_2O$ and $YbCl_3 \cdot 6H_2O$ with K_2bistpOp led to a quasi-statistical mixture of homo- and hetero- dimers based on the mass spectroscopy results. The isolations of [DyEu(bistpOp)$_3$] and [EuYb(bistpOp)$_3$] complexes are performed by an immediate evaporation of the solution after titration and their photophysical properties are studied in dry MeCN solution.

Under 270 nm excitation at room temperature, [DyEu(bistpOp)$_3$] display both characteristic Dy^{3+} and Eu^{3+} emissions (**Figure 6.17**). Upon direct excitation of Dy^{3+} at 349 nm, not only the Dy^{3+} emission is observed, but also the Eu^{3+} emission particularly in 680-700 nm region that correspond to $^5D_0 \rightarrow {}^7F_4$ transition can be detected, indicating the significant energy transfer process from Dy^{3+}

to Eu^{3+}. In the case of [EuYb(bistpOp)$_3$], strong Eu^{3+} emission and less-intense Yb^{3+} emission was detected due to the possible inefficient energy transfer from bistpOp ligand to Yb^{3+}. However, strong NIR emission of Yb^{3+} at 975 nm can be observed (**Figure 6.18**) upon direct excitation at Eu^{3+} (394 nm). This is also an evidence of energy transfer from Eu^{3+} to Yb^{3+} in solution.

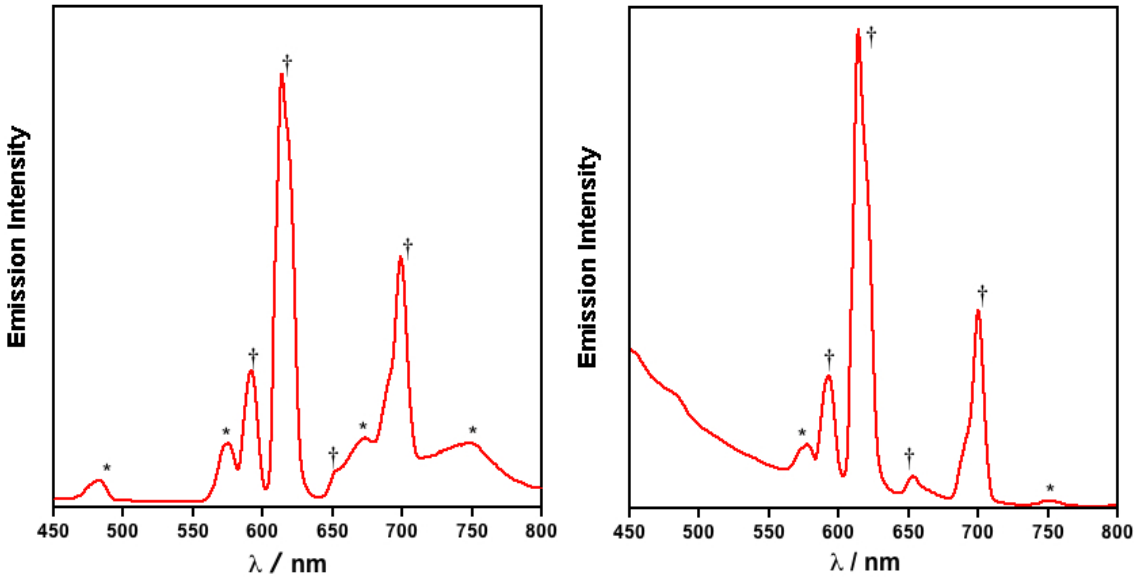

Figure 6.17. Emission spectrum of [DyEu(bistpOp)$_3$] complex in dry MeCN under 270 nm (left) and 349 nm (right) excitations. *: emission of Dy^{3+}, †: emission of Eu $^{3+}$.

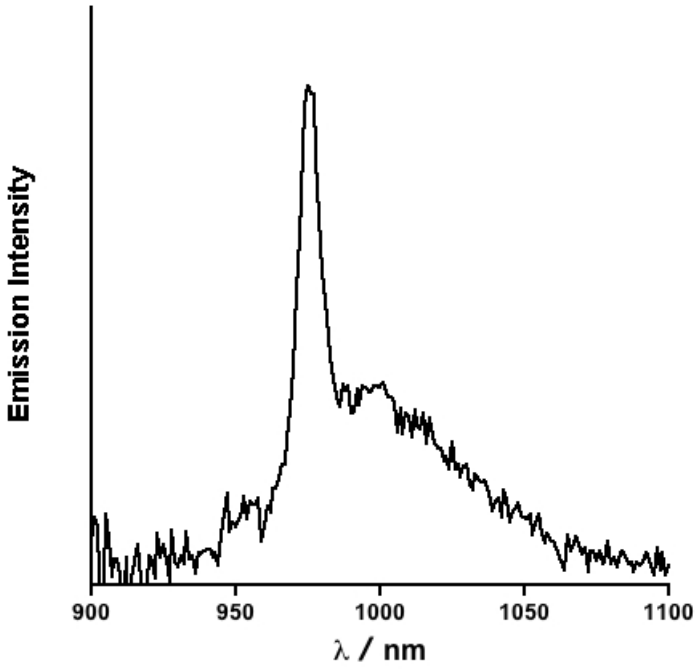

Figure 6.18. NIR emission of Yb^{3+} in [EuYb(bistpOp)$_3$] under 394 nm excitation in dry MeCN solution.

Luminescence lifetimes of the heterodinulcear complexes were determined in solution to study the energy transfer efficiency and the results are summarised in **错误!书签自引用无效。**. To avoid the possible overlap of the visible emissions, we monitored the Dy $^4F_{9/2} \rightarrow {}^6H_{15/2}$ transition at 484 nm for [Dy_2(bistpOp)$_3$] and [DyEu(bistpOp)$_3$]. Under 270 nm excitation, the lifetime of [DyEu(bistpOp)$_3$] solution was found to be 32.7 μs with a shorter component of 4.2 μs (6.14%). Both components are two-third reduced compared to [Dy_2(bistpOp)$_3$]. In addition, no emission was detected for [Eu_2(bistpOp)$_3$] at this wavelength, indicating the shortened lifetime in [DyEu(bistpOp)$_3$] at 484 nm has no contribution from Eu^{3+} luminescence and must be caused only by a reduction of Dy^{3+} luminescent lifetime. Similarly for [EuYb(bistpOp)$_3$] monitoring $^5D_0 \rightarrow {}^7F_2$ transition of Eu^{3+} upon excitation to the ligand, the lifetime was fitted to two components where the longer one (1.6 ms) was

slightly smaller than [Eu_2(bistpOp)$_3$]. The direct excitation to Eu^{3+} gave much more efficient energy transfer, evidenced by the significant reduction of lifetime from 2.0 ms to 0.86 ms.

Table 6.3. Luminescence lifetimes for homo- and hetero- dinuclear complexes in dry MeCN.

	λ_{exc} = 270 nm		λ_{exc} = 394 nm	
	τ_{L1}	τ_{L2}	τ_{L1}	τ_{L2}
[Dy_2(bistpOp)$_3$]	26.5 μs (21.75 %)	97.2 μs (78.25 %)		
[DyEu(bistpOp)$_3$]	4.2 μs (6.14 %)	32.7 μs (93.86 %)		
[Eu_2(bistpOp)$_3$]	2.1 ms	-	2.0 ms	-
[EuYb(bistpOp)$_3$]	0.22 ms (6.56 %)	1.60 ms (93.44 %)	0.18 ms (18.80 %)	0.86 ms (81.20 %)

Considering the mechanism of energy transfer as a dipole-dipole process, the energy transfer efficiency (η) follows the equation[4a, 20]

$$\eta = 1 - (\tau_L/\tau_{L0}) = \frac{1}{[1 + (R/R_0)^6]} \quad \text{(eq. 6.2)}$$

where τ_L and τ_{L0} refer to the luminescent lifetime of Eu^{3+} centre in hetero- and homodimers, R is the distance of the two metal centres and R_0 is the critical distance for 50 % energy transfer. The energy transfer efficiency of Dy^{3+} to Eu^{3+} and Eu^{3+} to Yb^{3+} was calculated to be 66.4% and 59.0%, respectively. Considering the energy transfer is a Fröster mechanism and the distance of two lanthanide ions are similar, the R_0 values of 4.2 Å and 4.5 Å are determined. These distances are close

to other reported values for heterometallic systems. A simplified energy diagram in **Figure 6.19** and **Figure 6.20** is used to demonstrate the energy transfer pathways in [DyEu(bistpOp)$_3$] and [EuYb(bistpOp)$_3$].

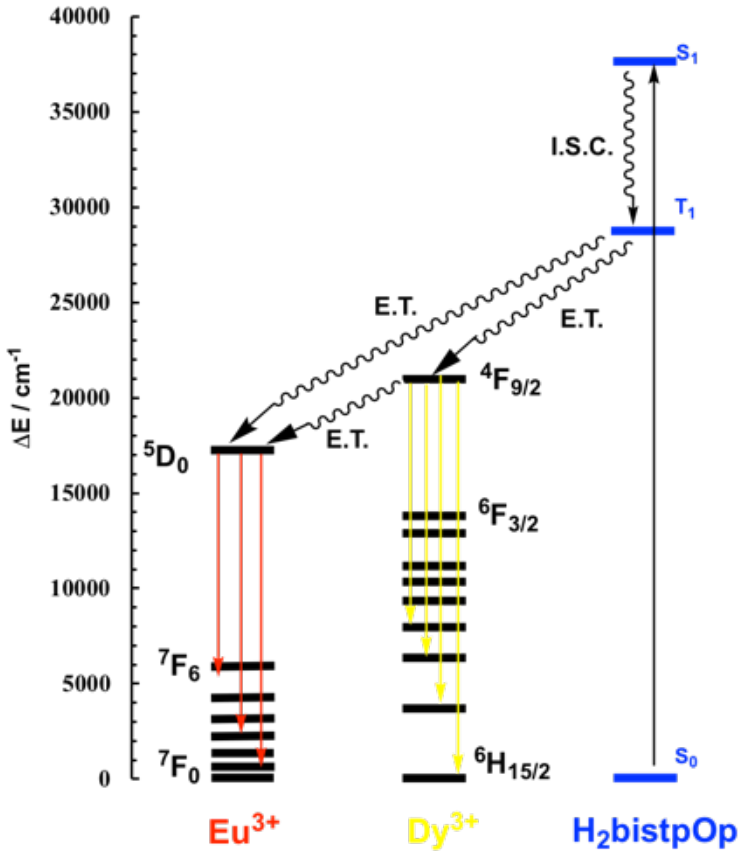

Figure 6.19. Simplified energy diagram of relevant energy levels showing the energy transfer from Dy^{3+} to Eu^{3+}.

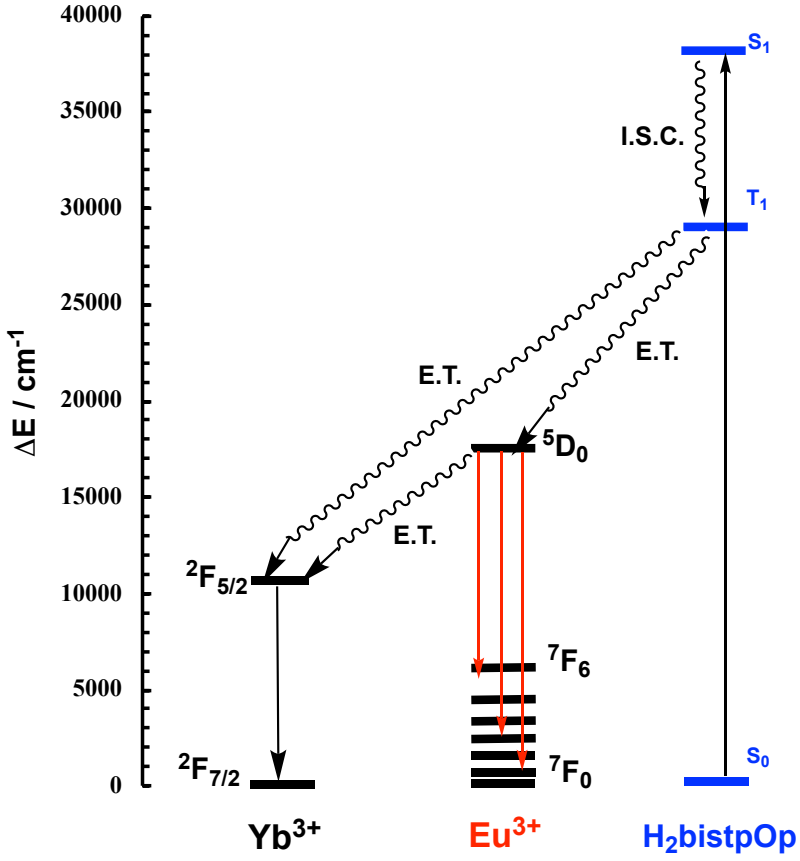

Figure 6.20. Simplified energy diagram of relevant energy levels showing the energy transfer from Eu^{3+} to Yb^{3+}.

In addition, we also attempted to investigated the solid state luminescence of $[Eu_2(bistpOp)_3]$ and $[EuYb(bistpOp)_3]$. Under ligand excitation, the powder emission spectrum of $[Eu_2(bistpOp)_3]$ displays characteristic emissions at 577, 591, 612, 651 and 698 nm are attributed to the transitions of $^5D_0 \rightarrow {}^7F_J$ (J = 0, 1, 2, 3, 4) where the hypersensitive $^5D_0 \rightarrow {}^7F_2$ transition at 612 nm as the most prominent one. The emission of Yb^{3+} could not be observed under this condition either. Moving on to 394 nm excitation at 77 K, strong and intense Eu^{3+} and NIR-Yb^{3+} emission was detected at 976 nm along with a shoulder at 984 nm (**Figure 6.21**). More surprisingly, the lifetime of Yb^{3+} is obtained and fitted to be 14.4 μs, while the longest component of Eu^{3+} lifetimes for $[Eu_2(bistpOp)_3]$ and $[EuYb(bistpOp)_3]$ are estimated to be 1.40 and 0.73 ms, respectively. The reduction of Eu^{3+} lifetimes

and the observation of Yb^{3+} lifetime also support the energy transfer from Eu^{3+} to Yb^{3+} in solid state and the efficiency is 48%. The luminescence intensity decreased significantly for both Eu^{3+} and Yb^{3+} emission upon increasing temperature of [EuYb(bistpOp)$_3$], which can be mainly due to the thermal quenching effect.

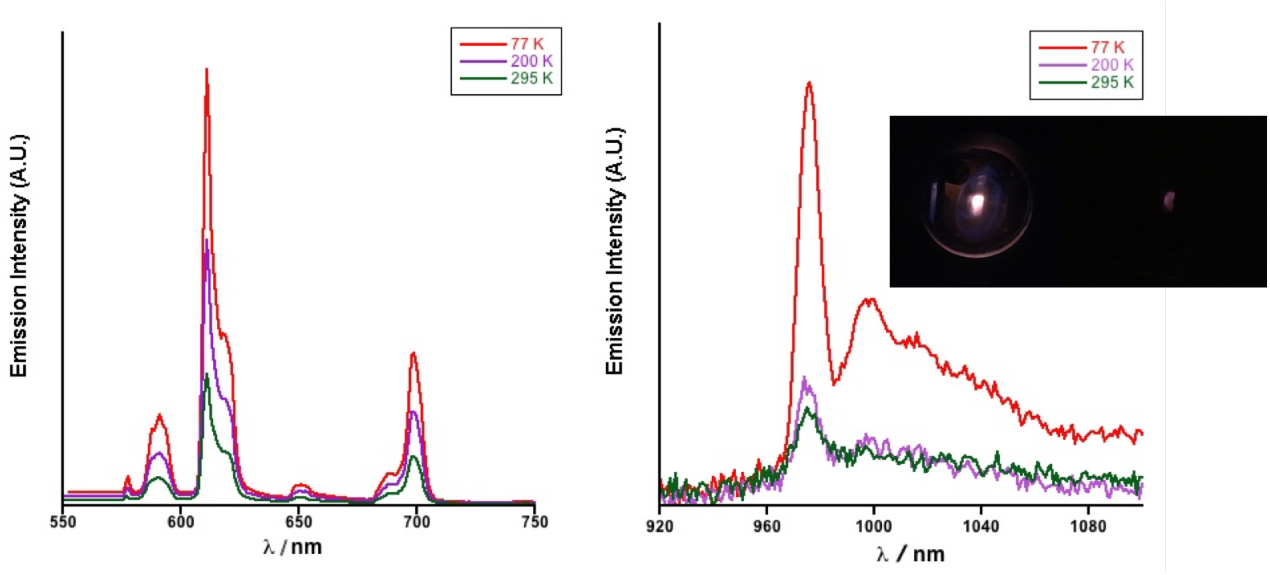

Figure 6.21. Emission spectra of [EuYb(bistpOp)$_3$] monitoring Eu^{3+} (left) and Yb^{3+} (right) emission under 394 nm excitation at 77, 200 and 295 K. Inset shows the luminescence output of the sample at 77 K and 295 K.

6.6 Conclusion

In summary, a series of neutral homodinuclear and two heterodinuclear lanthanide complexes based on a versatile H_2bistpOp were reported. The 3:2 stoichiometry of ligand to metal is proved by mass spectrometry, magnetic analysis and luminescence titration. Photophysical studies of the homodinuclear complexes demonstrate that H_2bistpOp ligand is able to sensitise visible emitting lanthanide ions with long lifetimes for [Tb_2(bistpOp)$_3$] and [Eu_2(bistpOp)$_3$] complexes, while NIR emission of [Yb_2(bistpOp)$_3$] can be observed. In addition, the heterodinuclear assembly of

[DyEu(bistpOp)$_3$] and [EuYb(bistpOp)$_3$] complex in solution was investigated by luminescence titration. Significant energy transfer from Dy^{3+} to Eu^{3+} and Eu^{3+} to Yb^{3+} was observed with above 50% efficiency in solution.

6.7 References

1. (a) L. Armelao, S. Quici, F. Barigelletti, G. Accorsi, G. Bottaro, M. Cavazzini and E. Tondello, *Coord. Chem. Rev.*, 2010, **254**, 487-505; (b) J.-C. G. Bünzli, *Coord. Chem. Rev.*, 2015, **293-294**, 19-47; (c) H. Uh and S. Petoud, *C. R. Chim.*, 2010, **13**, 668-680; (d) G. Richards, J. Osterwyk, J. Flikkema, K. Cobb, M. Sullivan and S. Swavey, *Inorg. Chem. Commum.*, 2008, **11**, 1385-1387; (e) S. Swavey and R. Swavey, *Coord. Chem. Rev.*, 2009, **253**, 2627-2638; (f) F. Zhao, J. Li, X.-Z. Wang, S.-J. Zhao, Y. Yang and P.-Z. Ma, *Dyes Pigm.*, 2020, **183**, 108738.
2. (a) J.-H. Jia, Q.-W. Li, Y.-C. Chen, J.-L. Liu and M.-L. Tong, *Coord. Chem. Rev.*, 2019, **378**, 365-381; (b) A. M. Nonat and L. J. Charbonnière, *Coord. Chem. Rev.*, 2020, **409**, 213192.
3. A. P. Bassett, S. W. Magennis, P. B. Glover, D. J. Lewis, N. Spencer, S. Parsons, R. M. Williams, L. De Cola and Z. Pikramenou, *J. Am. Chem. Soc.*, 2004, **126**, 9413-9424.
4. (a) D. J. Lewis, P. B. Glover, M. C. Solomons and Z. Pikramenou, *J. Am. Chem. Soc.*, 2011, **133**, 1033-1043; (b) D. J. Lewis, F. Moretta and Z. Pikramenou, *Supramol. Chem.*, 2012, **24**, 135-142; (c) K. Yanagisawa, Y. Kitagawa, T. Nakanishi, T. Seki, K. Fushimi, H. Ito and Y. Hasegawa, *Chem. – Eur. J.*, 2018, **24**, 1956-1961; (d) P. Guerriero, S. Tamburini, P. A. Vigato and C. Benelli, *Inorg. Chim. Acta*, 1991, **189**, 19-27; (e) S. Tamburini, P. A. Vigato, M. Gatos, L. Bertolo and U. Casellato, *Inorg. Chim. Acta*, 2006, **359**, 183-196; (f) T. Gao, Y. Yang, W.-B. Sun, G.-M. Li, G.-F. Hou, P.-F. Yan, J.-T. Li and D.-D. Ding, *CrystEngComm*, 2013, **15**, 6213-6220; (g) R. Sato, K. Suzuki, M. Sugawa and N. Mizuno, *Chem. – Eur. J.*, 2013, **19**, 12982-12990; (h) N. Souri, P. Tian, C. Platas-Iglesias, K.-L. Wong, A. Nonat and L. J.

Charbonnière, *J. Am. Chem. Soc.*, 2017, **139**, 1456-1459; (i) A. Nonat, T. Liu, O. Jeannin, F. Camerel and L. J. Charbonnière, *Chem. – Eur. J.*, 2018, **24**, 3784-3792.

5. (a) M. S. Tremblay and D. Sames, *Chem. Commun.*, 2006, 4116-4118; (b) G. Canard, S. Koeller, G. Bernardinelli and C. Piguet, *J. Am. Chem. Soc.*, 2008, **130**, 1025-1040; (c) M. P. Placidi, A. J. L. Villaraza, L. S. Natrajan, D. Sykes, A. M. Kenwright and S. Faulkner, *J. Am. Chem. Soc.*, 2009, **131**, 9916-9917; (d) N. Andre, R. Scopelliti, G. Hopfgartner, C. Piguet and J.-C. G. Bunzli, *Chem. Commun.*, 2002, 214-215; (e) J. P. Costes and F. Nicodème, *Chem. – Eur. J.*, 2002, **8**, 3442-3447.
6. S. W. Magennis, S. Parsons and Z. Pikramenou, *Chem. – Eur. J.*, 2002, **8**, 5761-5771.
7. D. Davis, A. J. Carrod, Z. Guo, B. M. Kariuki, Y.-Z. Zhang and Z. Pikramenou, *Inorg. Chem.*, 2019, **58**, 13268-13275.
8. M. L. Nielsen, *Inorg. Chem.*, 1964, **3**, 1760-1767.
9. (a) G. Aromí, P. Gamez and J. Reedijk, *Coord. Chem. Rev.*, 2008, **252**, 964-989; (b) A. V. Pestov, L. A. Khamidullina, V. Y. Sosnovskikh, P. A. Slepukhin and I. S. Puzyrev, *Polyhedron*, 2016, **106**, 75-83.
10. D. Davis, *Design of shell-type ligands for luminescent lanthanide complexes*, Ph.D., University of Birmingham, 2010, http://etheses.bham.ac.uk/id/eprint/1742.
11. G. Sheldrick, *Acta Crys. A*, 2015, **71**, 3-8.
12. O. V. Dolomanov, L. J. Bourhis, R. J. Gildea, J. A. K. Howard and H. Puschmann, *J. Appl. Cryst.*, 2009, **42**, 339-341.
13. G. Sheldrick, *Acta Cryst. C*, 2015, **71**, 3-8.
14. N. F. Chilton, R. P. Anderson, L. D. Turner, A. Soncini and K. S. Murray, *J. Comput. Chem.*, 2013, **34**, 1164-1175.

15. (a) C. Wang, S.-Y. Lin, J. Wu, S.-W. Yuan and J. Tang, *Dalton Trans.*, 2015, **44**, 4648-4654; (b) A.-J. Zhang, Y.-W. Wang, W. Dou, M. Dong, Y.-L. Zhang, Y. Tang, W.-S. Liu and Y. Peng, *Dalton Trans.*, 2011, **40**, 2844-2851; (c) P. Comba, M. Großhauser, R. Klingeler, C. Koo, Y. Lan, D. Müller, J. Park, A. Powell, M. J. Riley and H. Wadepohl, *Inorg. Chem.*, 2015, **54**, 11247-11258; (d) X.-W. Liu, Z. Wu, J.-T. Chen, L. Li, P. Chen and W.-B. Sun, *Inorg. Chem. Front.*, 2020, **7**, 1229-1238.

16. S. I. Klink, L. Grave, D. N. Reinhoudt, F. C. J. M. van Veggel, M. H. V. Werts, F. A. J. Geurts and J. W. Hofstraat, *J. Chem. Phys.*, 2000, **104**, 5457-5468.

17. G. Stein and E. Würzberg, *J. Chem. Phys.*, 1975, **62**, 208-213.

18. T. B. Jensen, R. Scopelliti and J.-C. G. Bünzli, *Chem. – Eur. J.*, 2007, **13**, 8404-8410.

19. N. L. Allinger, *J. Am. Chem. Soc.*, 1977, **99**, 8127-8134.

20. C. Piguet, J. C. G. Buenzli, G. Bernardinelli, G. Hopfgartner and A. F. Williams, *J. Am. Chem. Soc.*, 1993, **115**, 8197-8206.

Chapter 7

A DTPA-bisamide Ligand with Terpyridyl Arms for Luminescent Lanthanide Complexes and Heterometallic 3d-4f Assemblies

7.1 Abstract

A novel DTPA-bisamide type ligand bearing terpyridine arms (**K_3L**) and the related lanthanide complexes **LnL** (Ln = Eu, Tb and Nd, **1**-**3**) were synthesised and characterised. Photophysical measurements exhibited strong visible emissions and long lifetimes for **1** and **2** as well as near-infrared emission of **3** based on sensitisation from terpyridyl unit. The outward terpyridine arms allow the binding of secondary transition metal ion, hence the heterometallic 3d-4f self-assembly of a macrocyclic **Eu_2Fe_2** compound was studied in solution condition.

7.2 Introduction

The exceptional photophysical properties of lanthanide complexes have attracted more attention and have been applied as luminescent probes for sensing, detection and imaging due to the wide-range emission spectra, long lifetimes and high quantum yields.[1] The proper organic chromophore to produce effective non-radiation energy transfer to lanthanide ions is key to the design. Particularly carboxylate-rich ligands such as diethylenetriaminepetaacetic acid (DTPA) bisamide derivatives are able to form stable lanthanide complexes with good aqueous solubility and dominant luminescent outputs. Meanwhile, incorporating different functional groups into the bisamide pendant arms allows the attachment to surfaces or nanoparticles for more exciting applications.[2]

A growing amount of interest is being focused on the supramolecular heterometallic assemblies based on lanthanide ions combining 4f or d-block metals. General synthetic strategies include either metal complex precursors for lanthanide ion complexation or free ligands for selective coordination with metal ions (**Figure 7.1**). These complexes usually accompany with intricate architectures and have shown interesting magnetic and optical properties. Particularly in the 3d-4f systems, by introducing additional spin for stronger magnetic interactions, the slow magnetic relaxation

phenomena have been observed across many combinations.[3] The most commonly used precursors are metallocyanide and Schiff-base complexes. A recent example of a Dy-Cu complex using a [15-MC_{Cu}-5] metallacrown ring holds the largest effective energy barrier of 625 cm^{-1} among any d-f SMMs.[4] Moreover, the d-block metal ions may act as effective sensitisers for enhanced lanthanide luminescence[5] or energy transfer. In the well-studied Ln-Cr helicate complexes, a series of segmental bidentate-tridentate ligands have been introduced for their capacities to simultaneously match the stereochemical satisfaction for lanthanide ions.[6] There are also examples of Gd-Fe and Gd-Ru complexes that show potential in increasing the relaxivity of magnetic resonance imaging.[7]

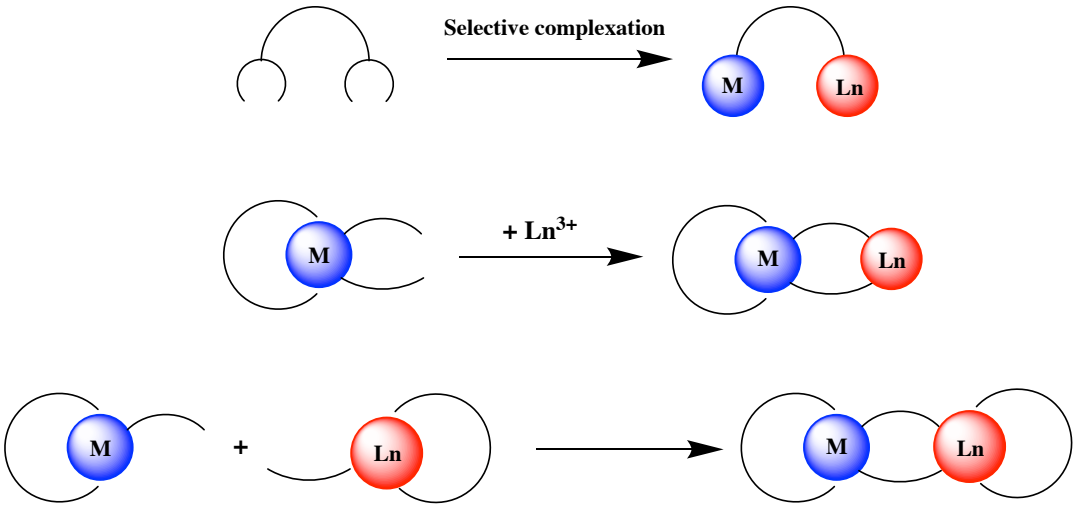

Figure 7.1. Different types of heterometallic assemblies for lanthanide-based complexes.

However, it is a challenge to achieve heteronuclear assembling with DTPA-bisamide type ligands due to the coordination preference of lanthanide ions. Our research group has reported a series of stable heterometallic complexes based on DTPA bisamide derivatives, including hairpin-shaped Ln-Pt_2 compounds for DNA photosensing and intercalative recognition in visible and near-infrared region[8] as well as heterodinuclear Eu-Tb and Eu-Nd macrocycles displaying dual-colour emission and energy transfer between lanthanide ions (**Figure 7.2**).[9]

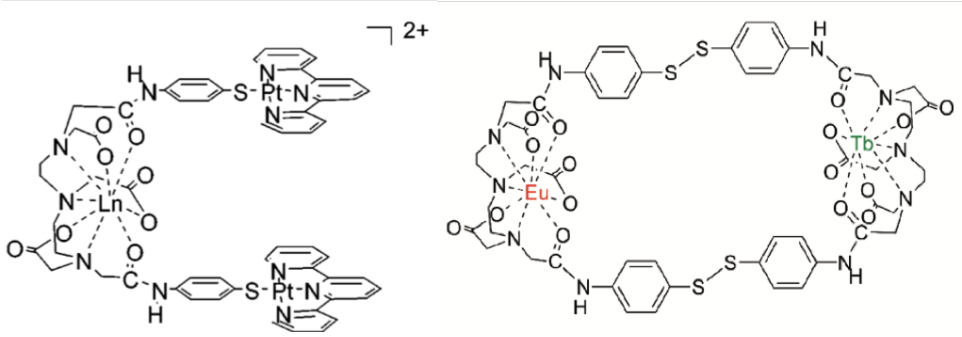

Figure 7.2. Examples of heterometallic assembly based on DTPA-bisamide derivatives.[8,9]

Terpyridine and its derivatives have been utilised in supramolecular assemblies due to their versatile coordination chemistry and high binding affinity towards metal ions.[10] The ligands and related metal complexes have shown great capability not only in optical or optical-electronic devices,[11] but also in catalysts for enhanced asymmetric organic synthesis[12] as well as molecular magnetism including spin crossover complexes with high transition temperatures and single-molecule magnets.[13] Herein we introduce a novel ligand combining DTPA bisamide and terpyridine arm (**K_3L**) for complexation and sensitisation of lanthanide ions and potential heterometallic assemblies (**Figure 7.3**). The combination of a secondary transition metal ion into a macrocyclic structure is also investigated in solution via titration method. During the course of our work, a derivative of DTPA with phenol-terpyridine has been reported and studied for its interactions with DNA for bioimaging and phototherapeutic applications.[14]

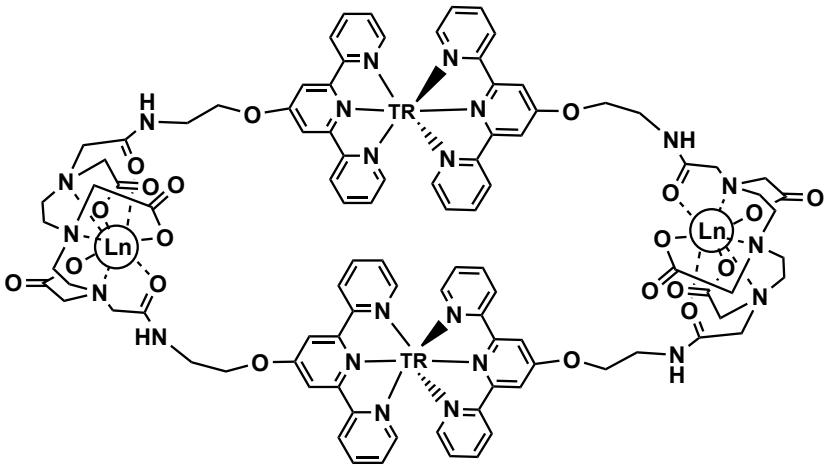

Figure 7.3. Desired macrocyclic complex using **K_3L** ligand for heterometallic assembly.

7.3 Experimental Section

7.3.1 General methods

All chemicals are commercially available from Acros and Sigma-Aldrich and used as received. Diethylenetriamine-N,N′,N″-triacetic-N,N″-dianhydride (DTPA bisanhydride) and 2-(2,2':6',2''-terpyridine-4'-yloxy)ethylamine (tpyEt) were synthesised according to literature methods and fully characterised.[9a, 15] Anhydrous pyridine was prepared by drying for 24 hours over 4 Å molecular sieves. HPLC grade solvents are used for photophysical measurements. ^{1}H and ^{13}C PENDANT NMR spectra were obtained using Bruker AV 300 and AVIII400 spectrometers. Electrospray mass spectra were recorded on a Micromass LC-TOF machine. Suitable crystals were selected for single crystal X-ray diffraction carried out on a Rigaku SuperNova, Dual, Cu at zero, Atlas diffractometer. The structure was solved with the ShelXT solution program using Intrinsic Phasing and refined with the ShelXL refinement package using Least Squares minimisation. Hydrogen atoms were added at the theoretical calculated positions. Disordered solvent molecules were squeezed in OLEX2 by solvent mask.

7.3.2 Photophysical measurements

UV-vis absorption spectra were recorded on Agilent Cary 60 spectrometer. Photophysical luminescence spectra were recorded on Edinburgh Instruments FLS 920/1000 steady-state and time-resolved spectrometer with F900 software and on a Photon Technology International spectrometer. The excitation and emission spectra are corrected for lamp/photomultiplier tube/instrument response. Time-resolved lifetime measurements were carried out by using a nanosecond flash lamp. Luminescent quantum yields were measured with an integrating sphere apparatus from Edinburgh Instruments with standard operations.

7.3.3 Synthesis

Synthesis of K_3L. To a suspension of DTPA bisanhydride (447.50 mg, 1.25 mmol) in 5 mL anhydrous pyridine under N_2, tpyEt (1299.29 mg, 4.4 mmol) was added. The mixture was stirred at room temperature for 24 h, then pyridine was removed under vacuum to form a white solid (or oil), which was then dissolved in 5 mL water and the pH was adjusted to 4 by dropwise addition of concentrated HCl. 50 mL MeCN were added and decanted three times to produce a white precipitate, then 50 mL MeCN and 30 mL chloroform was added to the mixture which was stirred at room temperature overnight. The crude product (**H_3L**) was collected by filtration and washed with MeCN, chloroform and diethyl ether. **H_3L** (275.34 mg) was dissolved in 4 mL water, the pH of which was adjusted to 7 by dropwise addition of an aqueous solution of KOH. After that 50 mL MeCN was added and decanted three times to precipitate the product, then 50 mL MeCN was added to the mixture and stirred at room temperature overnight. The solid was collected by filtration (130.20 mg). The final product was purified by alumina column chromatography using methanol as eluent to yield **K_3L** as a pale pink solid (58.25 mg, 45%).

^{1}H NMR (300 MHz, D_2O) δ ppm: 2.80 (s, 4H, CH_2), 2.90 (s, 4H, CH_2), 3.20 (s, 4H, CH_2), 3.23 (s, 2H, CH_2), 3.34 (s, 4H, CH_2), 3.62 (t, 4H, CH_2), 4.12 (t, 4H, CH_2), 7.25 (s, 4H, ArH), 7.39 (dd, J =

7.3, 4.9 Hz, 4H, ArH), 7.77 (td, *J* = 7.7, 1.7 Hz, 4H, ArH), 7.94 (d, *J* = 7.9 Hz, 4H, ArH), 8.44 (d, *J* = 5.2 Hz, 4H, ArH). ^{13}C NMR (75 MHz, D_2O) δ ppm: 38.26 (CH_2), 51.18 (CH_2), 52.42 (CH_2), 58.29 (CH_2), 58.67 (CH_2), 66.28 (CH_2), 108.34 (CH), 122.25 (CH), 124.49 (CH), 138.45 (CH), 148.18 (CH), 153.73 (C=O). HRMS (ESI^+) cal. for $K_3C_{48}H_{49}N_{11}O_{10}$: 1056.2575. Found 1056.2574. UV-vis (in methanol) λ in nm (log ε) 239 (4.0), 278 (3.9)

Synthesis of LnL. $LnCl_3 \cdot 6H_2O$ (Ln = Eu, Tb and Nd, 0.033 mmol) was added to an aqueous solution of **K_3L** (35.27 mg, 0.033 mmol) and stirred at room temperature for 1 h. 30 mL acetone was then added to the solution to precipitate the compound, which was filtered, washed with diethyl ether and dried under vacuum.

EuL (1): Yield 24.7 mg (68% based on ligand). MS (TOF ES^+) m/z: 1092.28 $\{M + H\}^+$. HRMS (ESI^+) calc. for $EuC_{48}H_{49}N_{11}O_{10}$: 1092.2871. Found: 1092.2879. UV-vis (in methanol) λ_{max} in nm (log ε): 244 (4.2), 278 (4.1), 320 (3.2).

TbL (2): Yield 23.2 mg (60% based on ligand). MS (TOF ES^+) m/z: 1098.29 $\{M + H\}^+$. HRMS (ESI^+) calc. for $TbC_{48}H_{49}N_{11}O_{10}$: 1098.2912. Found: 1098.2925. UV-vis (in methanol) λ_{max} in nm (log ε): 245 (4.1), 278 (4.0), 320 (3.4)

NdL (3): Yield 25.2 mg (69% based on ligand). MS (TOF ES^+) m/z: 1083.28 $\{M + H\}^+$. HRMS (ESI^+) calc. for $NdC_{48}H_{49}N_{11}O_{10}$: 1083.2759. Found: 1083.2770. UV-vis (in methanol) λ_{max} in nm (log ε): 245 (4.1), 278 (4.0), 320 (3.4)

Synthesis of $[Fe(tpyEt)_2](ClO_4)_2$ (4). To a 5 mL methanol solution of tpyEt (30.45 mg, 0.10 mmol), $Fe(ClO_4)_2 \cdot 6H_2O$ (14.97 mg, 0.05 mmol) in 5 mL acetonitrile was added. The mixture was stirred at room temperature for two hours, then filtered. Suitable crystals for single crystal X-ray diffraction were obtained within one week by slow evaporation of the solvent. Yield: 14.2 mg (33% based on ligand). HRMS (ESI^+) calc. for $C_{34}H_{32}N_8O_2Fe^{2+}$: 320.0993 $\{M\}^{2+}$. Found: 320.0992.

7.4 Results and discussion

7.4.1 Synthesis of ligand and lanthanide complexes

The ligand was synthesised from the acylation of tpyEt with DTPA-bisanhydride in pyridine at room temperature similar to the previously reported derivatives (**Figure 7.4**). The acidic work-up did not give good purity of the product so the potassium salt of the ligand was obtained by addition of KOH and purified by column chromatography. The ligand was characterised by NMR and mass spectrometry methods. The ^{1}H NMR spectrum (**Figure 7.5**) of the ligand in D_2O displays the features of the appended terpyridine in the aromatic region as well as the usual features of the DTPA-bisamide molecule, with an observed 2H singlet/4H singlet/4H singlet/4H triplet/4H triplet motif, as seen for reported DTPA-bisamide derivatives.[9a, 16] The molecular weight of the ligand was confirmed by electrospray mass spectrometry where the monoprotonated ligand is observed at m/z 1056.2, doublet and triplet charged at 528.6 and 352.8. Further mass determination using the same ionisation technique came within 1 ppm of the theoretical value.

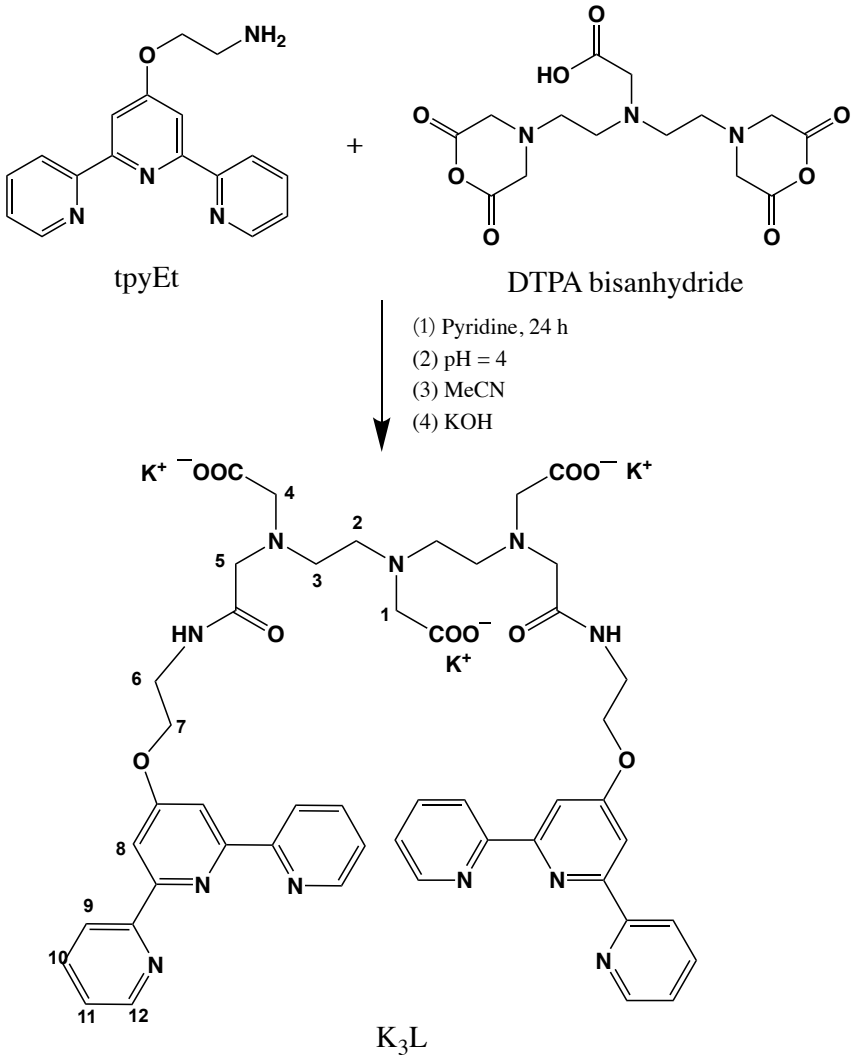

Figure 7.4. Synthetic route of **K_3L** with numbering scheme of H atoms.

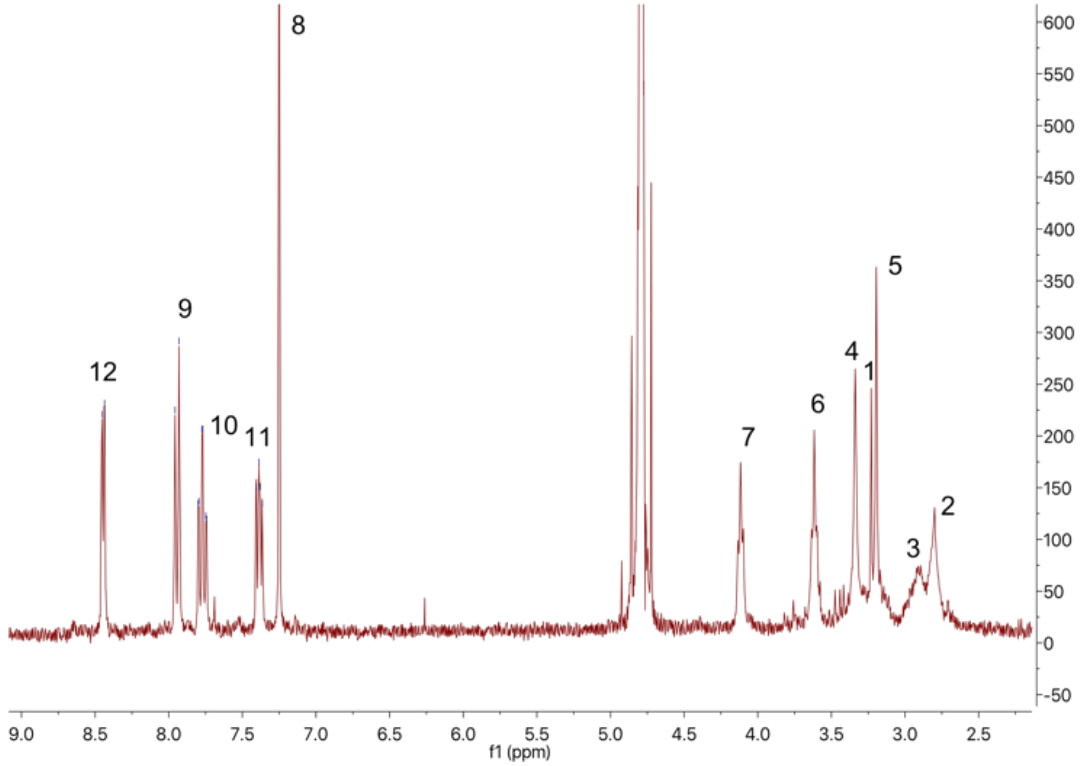

Figure 7.5. ^{1}H NMR spectrum of **K_3L** in D_2O with numbering scheme of the H atoms.

Reaction of $LnCl_3 \cdot 6H_2O$ with **K_3L** in water in a 1:1 ratio gave the according **LnL** complexes (**Figure 7.6**). Considering the coordination preference in aqueous solution, the lanthanide ions should be strongly bound to the aminocarboxylate site.[17] The complexation was supported by mass spectra of all complexes where the correct *m*/*z* isotopes were observed, corresponding to the 1:1 stoichiometry of lanthanide to ligand. It should be mentioned that luminescence titration could not be performed in methanol or water to further confirm the stoichiometry due to the possible coordination of terpyridine to lanthanide ion in solution.

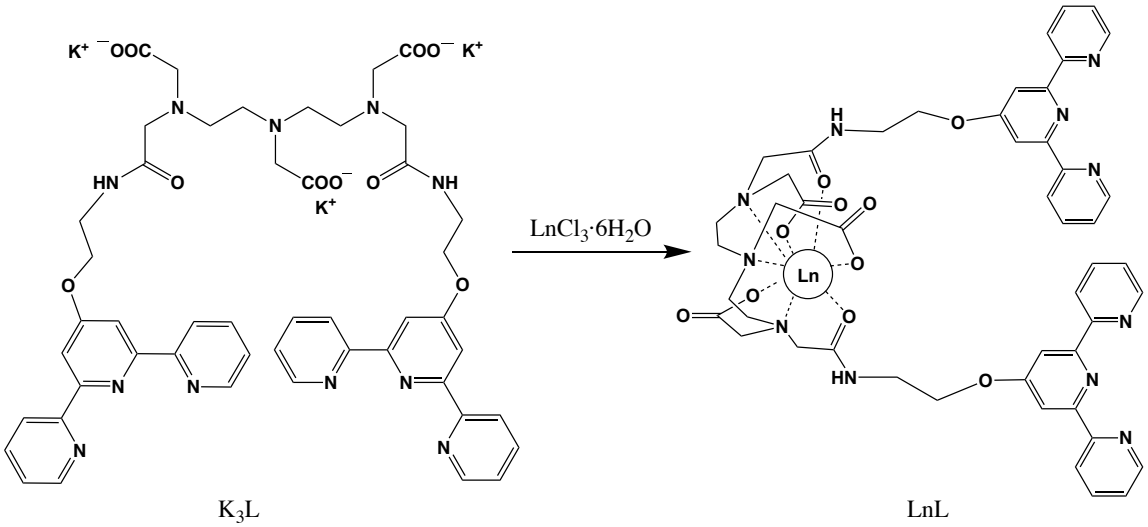

Figure 7.6. Synthetic scheme of **LnL**.

7.4.2 Photophysical studies

The UV-vis spectrum of **K_3L** in methanol shows two intense absorption bands at 240 nm and 278 nm which can be attributed to π-π* transition of aromatic rings of terpyridine (**Figure 7.7**). An additional small shoulder around 320 nm was observed which may be attributed to n-π* transition. Upon 320 nm excitation, **K_3L** displayed typical terpyridine emission centred at 355 nm (**Figure 7.8**).[18]

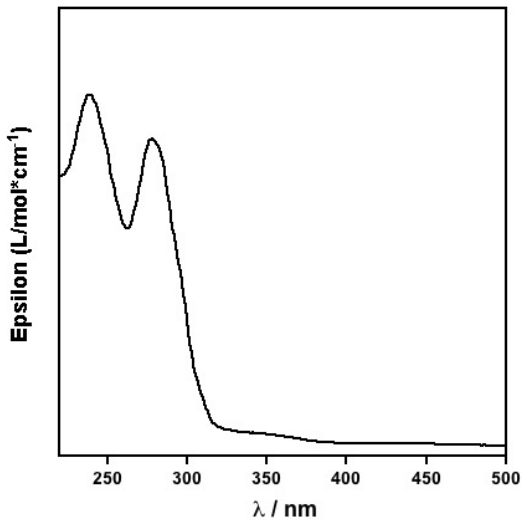

Figure 7.7. UV-vis spectrum of **K_3L** in methanol.

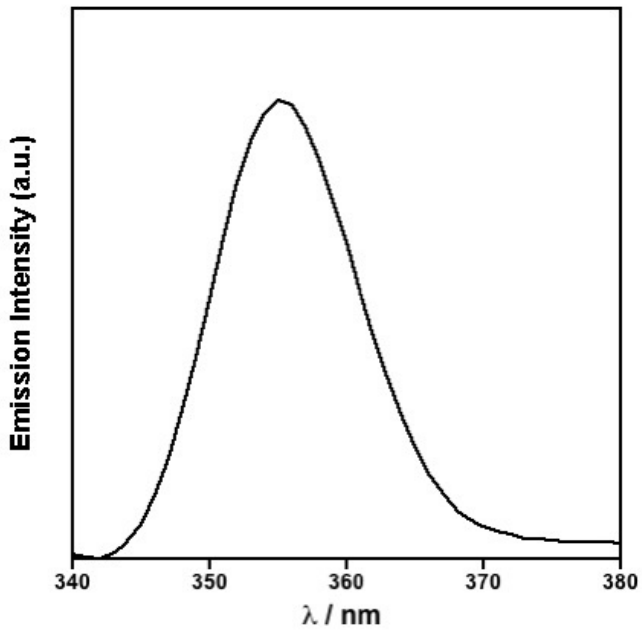

Figure 7.8. Emission spectra of **K_3L** in methanol (0.1 mM) under 320 nm excitation (corrected by PMT response).

The absorption spectra of **1** display bands centred at 243 and 278 nm which are similar to **K_3L** and tpyEt ligands (**Figure 7.9**). The broad peak at 320 nm can be attributed to n-π* transition. Considering the forbidden f-f transition of lanthanide ions and charge-transfer bands involving lanthanide orbits are not generally observable, these bands are attributed to the ligand-centred transitions. In addition, the absorption band at 278 nm attributed to π-π* transition did not show significant shift compared to terpy-coordinated lanthanide complexes,[19] indicating the lanthanide ion in **LnL** is not coordinated to the terpy.

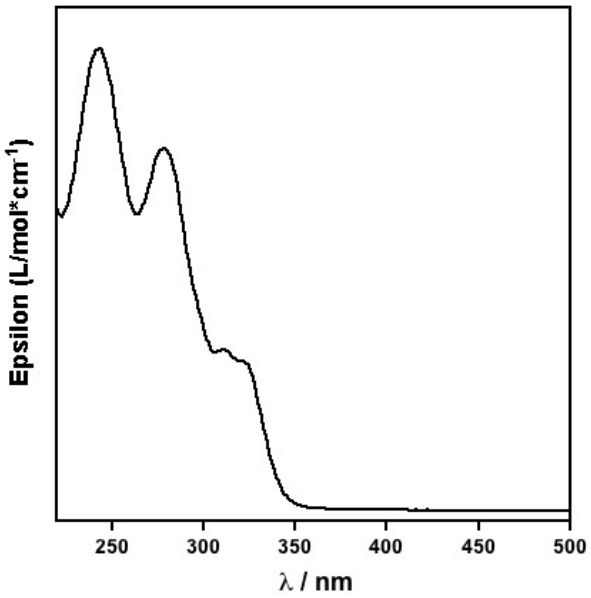

Figure 7.9. UV-vis spectrum of **1** in methanol.

The excitation spectrum for **1** and **2** monitored at the hypersensitive emission shows broad bands in the range of 270 to 340 nm (**Figure 7.10**), indicating the effective energy transfer from the ligand to lanthanide centre.

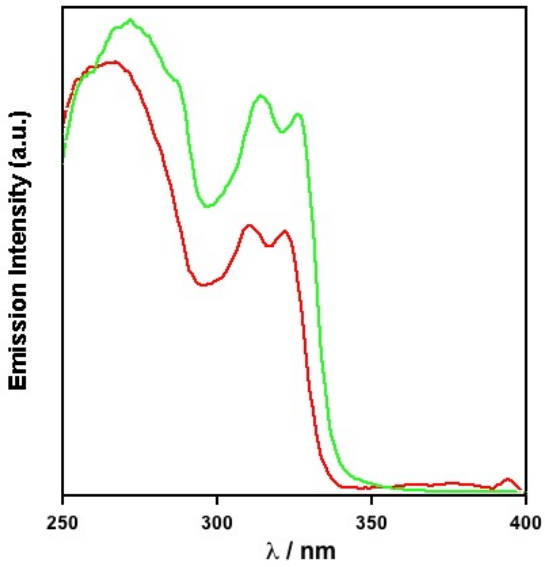

Figure 7.10. Excitation spectrum of **1** (red, λ_{em} = 616 nm) and **2** (green, λ_{em} = 545 nm) in MeOH.

Excitation of the complexes at ligand-centre bands results in characteristic lanthanide emission in methanol solution (**Figure 7.11**). Red emission of Eu^{3+} at 580, 594, 615, 650 and 694 nm was observed for **1** which are assigned to the $^5D_0 \rightarrow {}^7F_J$ transitions (J = 0, 1, 2, 3, 4). For **2**, the observed bands at 488, 545, 585, 622, 651 and 684 nm are attributed to the $^5D_4 \rightarrow {}^7F_J$ (J = 6, 5, 4, 3, 2, 1, and 0) transitions of Tb^{3+}. For the near-infrared emitted complexes, only **3** displays weak emission in degassed d^4-methanol solution (**Figure 7.12**), three bands at 890, 1062 and 1340 nm are attributed to transitions of $^4F_{3/2} \rightarrow {}^4I_J$ (J = 9/2, 11/2, and 13/2), respectively. However, the signals of the excitation spectrum for **3** are too weak to collect.

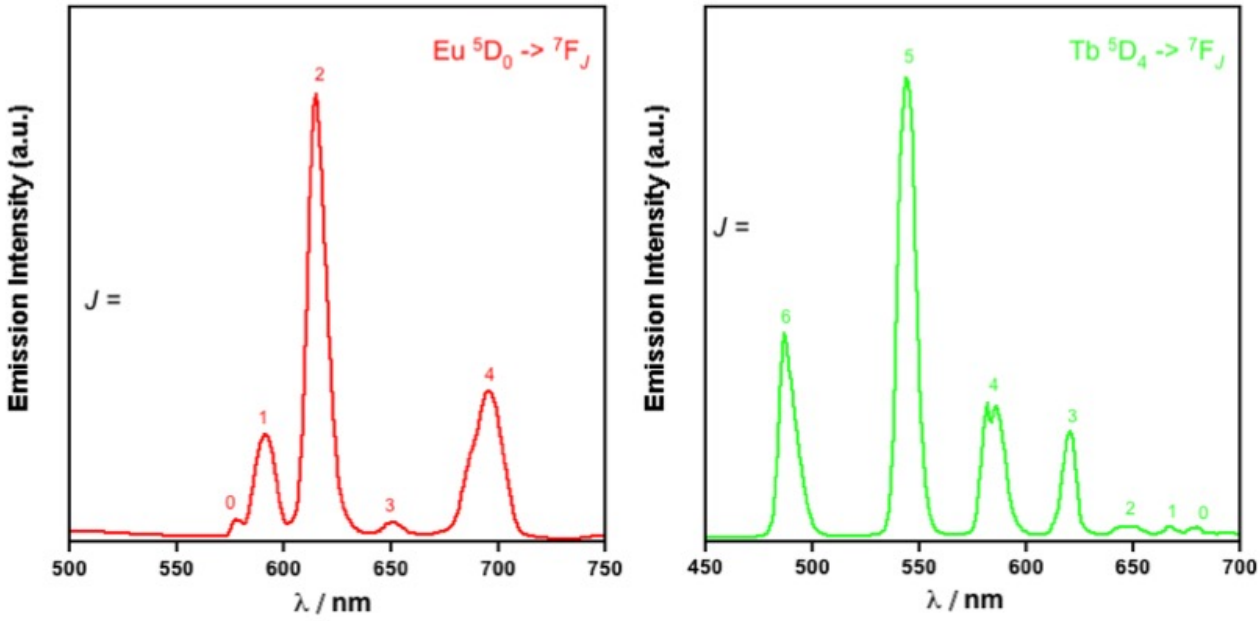

Figure 7.11. Emission spectra of **1** (0.02 mM, left) and **2** (0.02 mM, right) in methanol (λ_{exc} = 320 nm, corrected by PMT response).

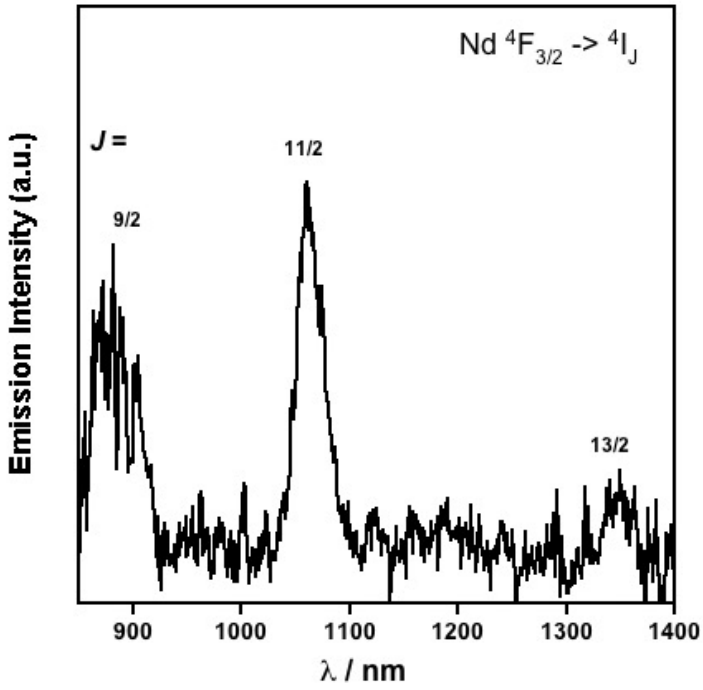

Figure 7.12. Emission spectrum of **3** in degassed d^4-methanol (λ_{exc} = 320 nm, 0.02 mM, corrected by NIR-PMT response).

The photophysical processes were further evaluated by luminescence lifetime and quantum yield measurements monitored at the hypersensitive emission of **1** and **2** in methanol. The lifetime data were fitted to be monoexponential decay curves, indicating the presence of only one discrete Ln^{3+} ion in solution. The results are summarised in **Table 7.1**. The two visible-emitted complexes show long luminescence lifetimes that are close to those observed in DTPA-bis(amidothiophenyl) based complexes[16] and are comparable to those using DTPA-cs124 and DTPA-bisamide with bipyridine tail ligands in aqueous media.[20] The quantum yields are measured to be 1.5% and 18.5% for **1** and **2**, respectively. The long lifetimes for the visible-emitted complexes are also comparable to the complexes with DTPA-phenol-terpy ligand, however, the quantum yields are relatively smaller, which may be due to a relatively larger separation between lanthanide and terpy chromophore.

Table 7.1. Luminescence lifetimes of **1** and **2** in methanol monitoring the hypersensitive transitions under 320 nm excitation.

	τ_L / ms	Φ / %
1	0.9	1.5
2	1.9	18.5

The photophysical measurements have indicated that the terpy unit of the **K_3L** ligand is an effective remote sensitiser for visible lanthanide luminescence. A simplified energy diagram adapting the triplet state energy of terpy ligand from previously reported literature[21] is shown in **Figure 7.13**. The energy gap between the T_1 state (~ 23000 cm^{-1}) and the emissive state of Tb^{3+} ($^5D_4$, ~ 20400 cm^{-1}) and Eu^{3+} ($^5D_0$, ~ 17500 cm^{-1}) are 2600 cm^{-1} and 5500 cm^{-1}, respectively, demonstrating the efficient energy transfer from the ligand to lanthanide ions. Yet it will be more accurate to determine the triplet state energy of **K_3L** by measuring **GdL** emission at 77 K.

Unfortunately, the weak emission of **3** prevented us from measuring the lifetime or the quantum yield. This is not unexpected because the triplet state energy level of terpy may be too high to provide an efficient energy transfer to Nd for NIR luminescence. Meanwhile, Nd^{3+} ion is sensitive to C-H, N-H or O-H vibrational oscillator, which is able to significantly quench the lanthanide luminescence.

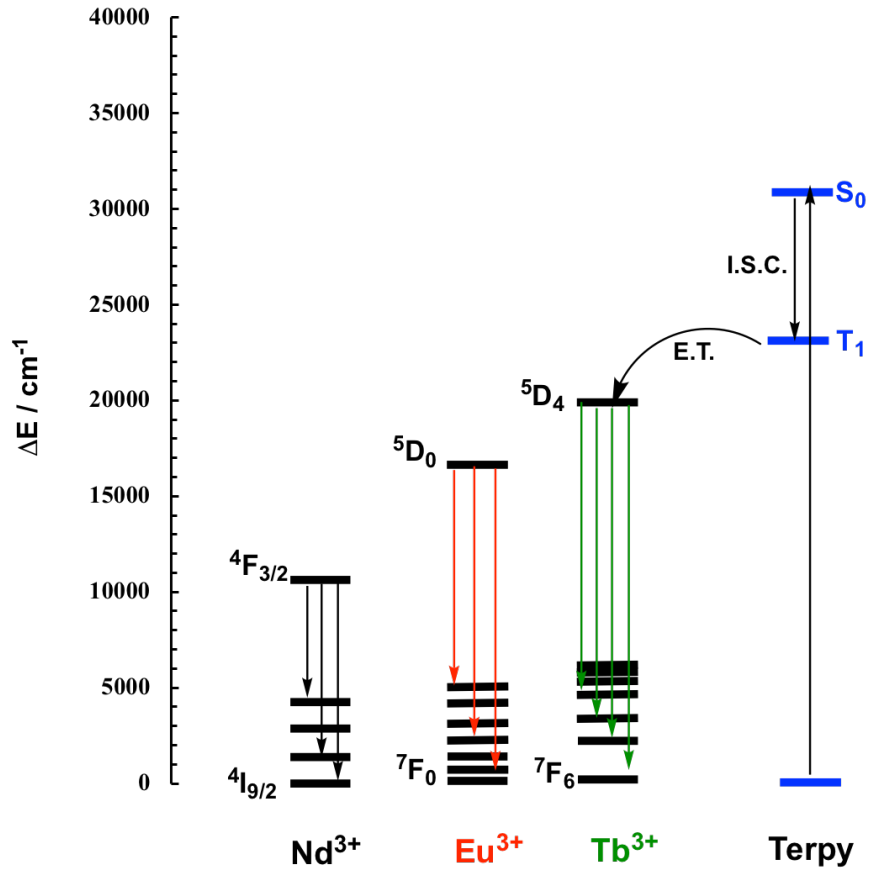

Figure 7.13. Simplified energy diagram of terpy ligand and lanthanide ions.

7.4.3. Mononuclear Fe(II) complex

Prior to investigating the heterometallic assembly, we first manage to synthesise the mononuclear compound $[Fe(tpyEt)_2](ClO_4)_2$ (**4**) as a reference. The structure was determined by SCXRD method (**Table 7.2** and **Table 7.3**). The Fe^{2+} ion is located in a distorted octahedral geometry (**Figure 7.14**). Similar to other Fe^{2+}-terpy complexes, the average Fe-N bond length is in a range of 1.88-1.98 Å at 100 K, indicating the presence of low-spin Fe^{2+}. The UV-vis spectrum in solution is similar in form to $Fe(terpyOH)_2^{2+}$ derivatives[13a] showing a broad absorption centred at 555 nm which is assigned as characteristic MLCT transition (**Figure 7.15**).

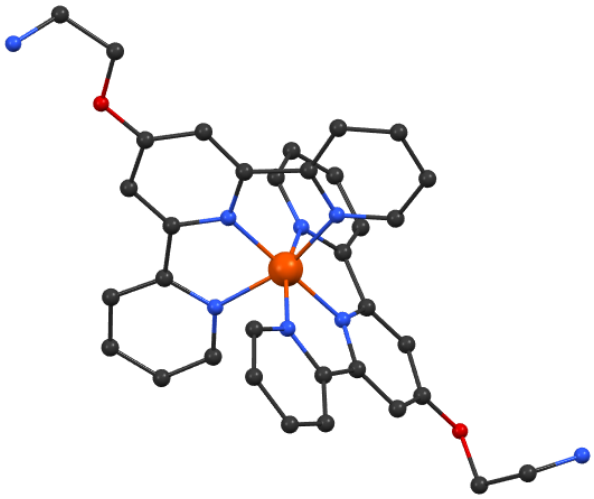

Figure 7.14. Crystal structure of **4**. Hydrogen atoms, counter ions and solvent molecules are omitted for clarity.

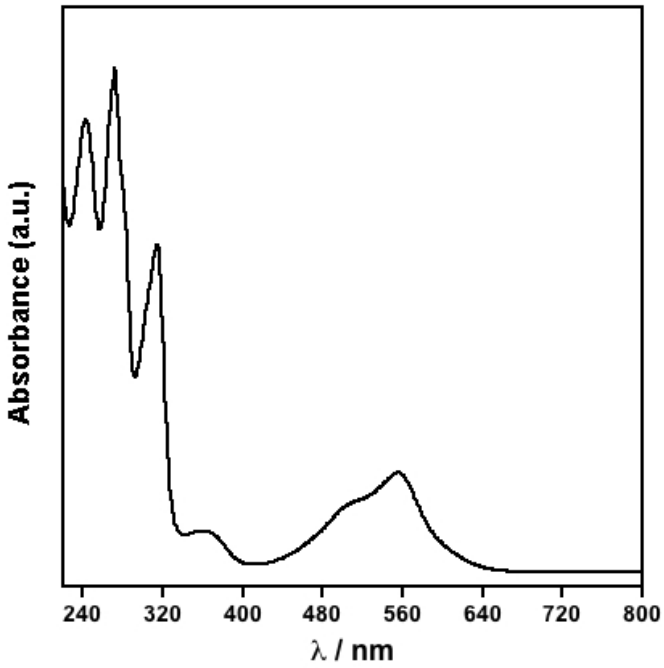

Figure 7.15. UV-vis spectrum of **4** in methanol.

Table 7.2. Crystallographic data for **4**.

Empirical formula	$C_{36}H_{35}Cl_3FeN_9O_{14}$
Formula weight	979.93
Temperature/K	100
Crystal system	triclinic
Space group	P-1
a/Å	8.8485(4)
b/Å	13.5295(5)
c/Å	18.4763(5)
α/°	98.829(2)
β/°	91.571(3)
γ/°	102.121(3)
Volume/Å^3	2132.89(14)
Z	2
ρ_{calc}g/cm^3	1.526
μ/mm^{-1}	5.232
F(000)	1006.0
Crystal size/mm^3	0.1 × 0.08 × 0.05
Radiation	CuKα (λ = 1.54184)
2Θ range for data collection/°	7.662 to 150.12
Index ranges	-10 ≤ h ≤ 7, -16 ≤ k ≤ 16, -22 ≤ l ≤ 22
Reflections collected	15069
Independent reflections	8455 [R_{int} = 0.0362, R_{sigma} = 0.0523]
Data/restraints/parameters	8455/0/625
Goodness-of-fit on F^2	1.062
Final R indexes [I>=2σ (I)]	R_1 = 0.0713, wR_2 = 0.1875
Final R indexes [all data]	R_1 = 0.0812, wR_2 = 0.1988

Table 7.3. Selected bond lengths [Å] and angles [deg] of **4**.

Fe1-N1	1.978(3)	Fe1-N5	1.978(3)
Fe1-N2	1.880(3)	Fe1-N6	1.880(3)
Fe1-N3	1.962(3)	Fe1-N7	1.976(3)
N6-Fe1-N5	80.68(13)	N2-Fe1-N1	81.03(13)
N6-Fe1-N2	178.52(13)	N2-Fe1-N3	80.87(14)
N6-Fe1-N7	81.20(13)	N7-Fe1-N5	161.85(13)
N6-Fe1-N1	97.58(13)	N7-Fe1-N1	91.51(12)
N6-Fe1-N3	100.51(14)	N3-Fe1-N5	92.46(13)
N2-Fe1-N5	99.84(13)	N3-Fe1-N7	89.85(13)
N2-Fe1-N7	98.30(13)	N3-Fe1-N1	161.86(14)
N5-Fe1-N1	91.86(13)		

7.4.4 Heterometallic 3d-4f solution self-assembly

The terpyridine arm of **K_3L** creates great ability to bind a secondary metal ion in the so-called molecular robot systems. A recent research on an Eu-cyclen complex demonstrates the multiplex recognition of Fe^{2+} with UV-vis, Zn^{2+} using photoluminescence and Mn^{2+} using MRI methods.[22] In our case we explored the assembly and photophysical property of heterometallic 3d-4f assembly in solution. The in situ formation of a heteronuclear Eu-Fe complex was performed by titrating $Fe(ClO_4)_2 \cdot 6H_2O$ into **1** in methanol solution, monitoring by UV-vis spectra. With the addition of Fe^{2+} ion, a clear colour change from colourless to purple can be directly observed. Meanwhile a broad absorption centred at 556 nm was detected, which is assigned to the characteristic MLCT transition of Fe^{2+}-terpy complexes, indicating the binding of Fe^{2+} to terpyridine arm of **1** (**Figure 7.16**). The

320 nm peak in the UV region also gradually increase with the addition of Fe^{2+}, which can be attributed to the change of electronic structure or the enhancement of the rigidity of terpy upon coordination.[22] After reaching 1:1 ratio of Fe^{2+} to Eu^{3+}, no significant increase of the MLCT absorbance was observed. A plot of integration of MLCT absorption vs. equivalents of Fe^{2+} ion shows a plateau at one equivalent of Fe^{2+} per Eu^{3+} in solution and no more increase after this point, indicating the Fe^{2+} ions are completely coordinated with the terpy arms.

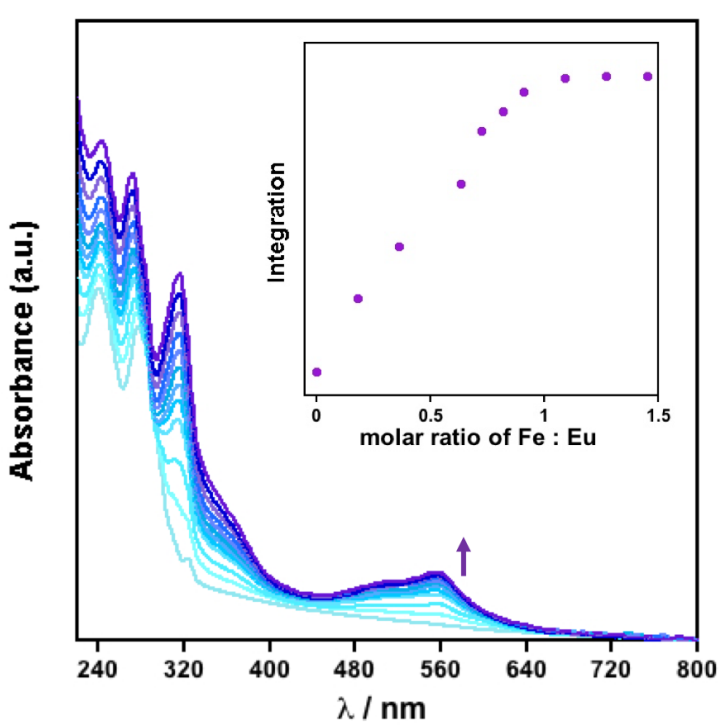

Figure 7.16. UV-vis titration of Fe^{2+} (2 mM) into **1** (0.044 mM) in methanol showing the formation of macrocyclic Eu_2Fe_2 compound. Inset shows the integration of MLCT area versus molar ratio of Fe^{2+} : Eu^{3+}.

Further analysis of the heterometallic assembly was by electrospray mass spectrometry. The mass spectrum of the resulting solution shows a most intense peak at 573.14 m/z value which is characteristic of a 4+ cation due to the pattern. This corresponded to the formula of $C_{96}H_{98}N_{22}O_{20}Eu_2Fe_2^{4+}$, which further supports the macrocyclic **Eu_2Fe_2** cationic compound formation in solution (**Figure 7.17**). The theoretical isotope pattern agrees with the experimental results. The additional peak at 797.83 is assigned to $C_{96}H_{98}N_{22}O_{20}Eu_2Fe_2(ClO_4)^{3+}$ conformation which is the related species of **$Eu_2Fe_2^{4+}$**.

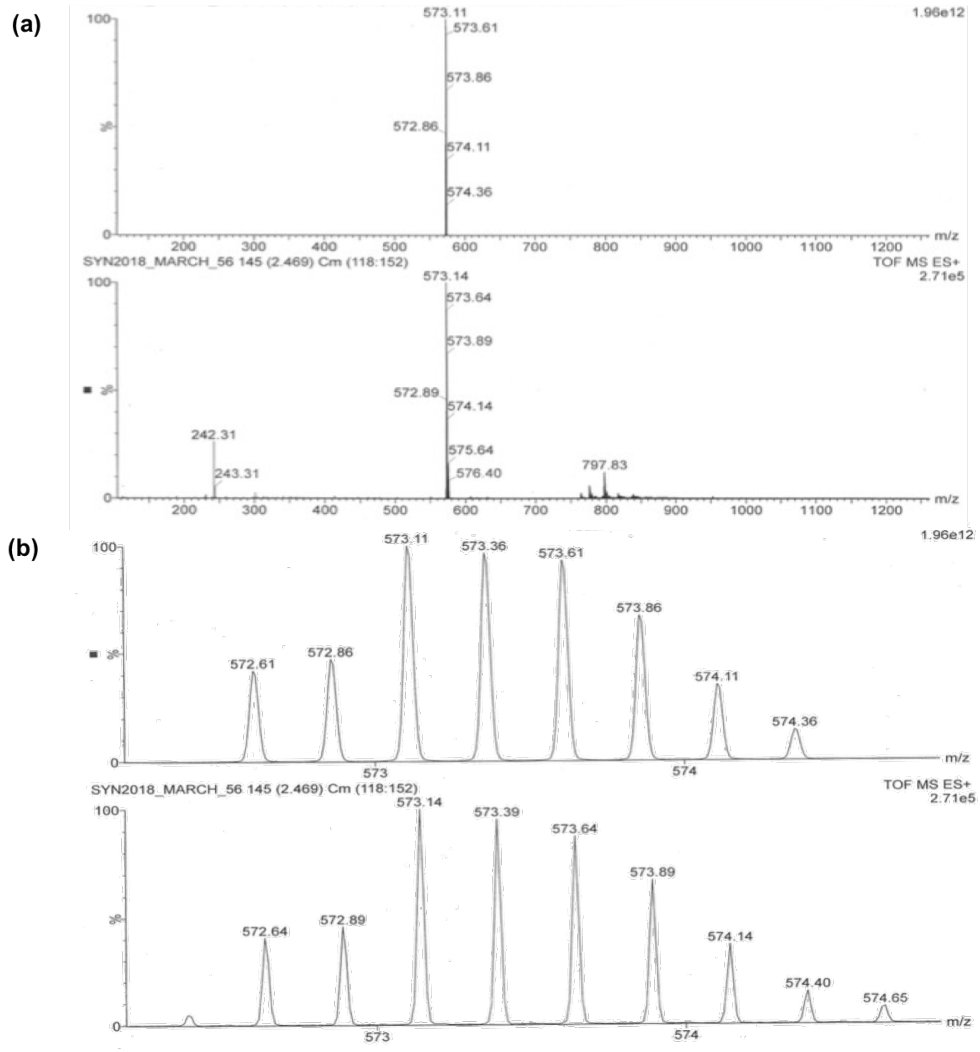

Figure 7.17. ESI(+) mass spectra of (a) full-range and (b) enlargement of the middle m/z isotope showing the formation of **$Eu_2Fe_2^{4+}$** after titration in solution. Simulated and experimental patterns are shown in the top and bottom of (a) and (b), respectively.

Luminescent investigation of the resulting $\mathbf{Eu_2Fe_2^{4+}}$ solution was carried out after titration in comparison to a isoabsorptive solution of **1** at 320 nm. Under 320 nm excitation, $\mathbf{Eu_2Fe_2^{4+}}$ shows characteristic Eu^{3+} emission peaks at 594, 615 and 694 nm (**Figure 7.18**), with a significant decrease of the intensity by 40% than the mononuclear complex **1**. The excitation spectrum of $\mathbf{Eu_2Fe_2^{4+}}$ showed broad peaks at 260 nm and 321 nm.

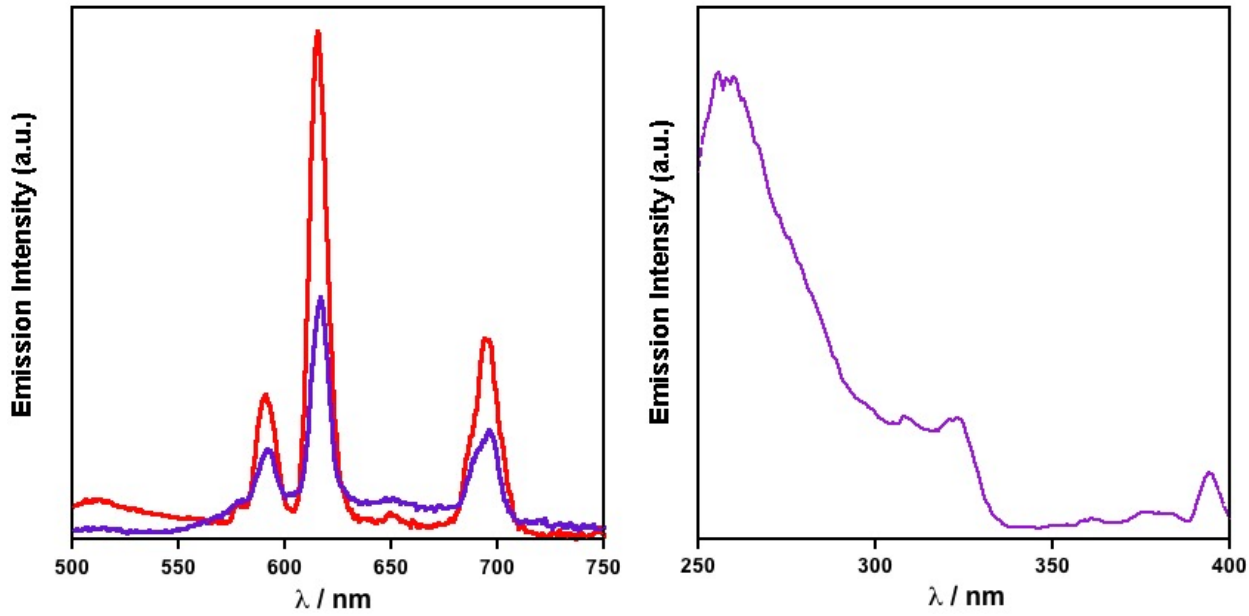

Figure 7.18. Emission (left) and excitation (right) spectra $\mathbf{Eu_2Fe_2^{4+}}$ (purple) after titration (λ_{exc} = 320 nm, corrected by PMT response) overlaid with **1** (red) emission**.** The emission spectra were recorded of isoabsorptive solution at 320 nm.

The luminescence lifetime of $\mathbf{Eu_2Fe_2^{4+}}$ (monitoring Eu^{3+} at 616 nm) is also significantly smaller than the mononuclear species, giving the longest component of 0.5 ms (94.8%) along with a short component of 0.03 ms (5.2%). The lifetime of the major component shows a 44% decrease compared to **1**. Such a significant luminescence quenching is probably due to a possible energy transfer from Eu^{3+} to Fe^{2+} that has been found in similar Eu-Fe complexes.[23] Generally the low-spin Fe(II) will quench the luminescence by an efficient $Eu^{3+} \rightarrow {}_{LS}Fe^{2+}$ energy transfer from the intense MLCT

absorption (**Figure 7.19**), while the higher MLCT energy in high-spin Fe(II) may lead to Eu^{3+} luminescence.[24] In our case, the observation of Eu^{3+} emission can be possibly due to the large separation between Eu and Fe, although the Fe(II) ions are in the low-spin state at room temperature for most of the Fe(II)-terpy systems.

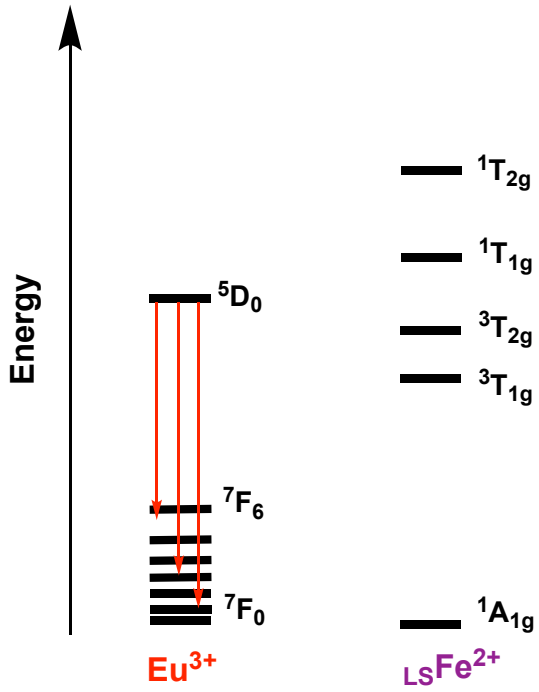

Figure 7.19. Simplified energy diagram showing 3d state of Fe^{2+} and 4f state of Eu^{3+}.

The isolation of the target macrocyclic complexes was not that successful because of the large cationic system which will generally require proper counter anions. However, this observation indicates the additional binding ability arising from terpyridine arms provides potential applications in paramagnetic transition metal ion detection, which can be also extended to other lanthanide complexes. A recently successful combination of slow magnetic relaxation and spin crossover in a heterometallic grid complex Dy_2Fe_2 compound[25] provides novel duel functions in such series of complexes.

7.5 Conclusion

A novel DTPA-bisamide derivative bearing terpyridine arm (**K_3L**) was successfully synthesised and assemble with lanthanide ions (Ln = Eu, Tb and Nd, **1**-**3**). The visible-emitted complexes **1** and **2** displayed characteristic emissions lanthanide with long lifetimes, while near-infrared emission was observed for **3**. The 3d-4f heterometallic assembly in solution resulted in a tetranuclear macrocyclic complex **$Eu_2Fe_2^{4+}$**, which is supported by mass spectrometry. The photophysical studies of **$Eu_2Fe_2^{4+}$** showed a significant quenching on Eu^{3+} luminescence. The successful heterometallic assembly provides potential application for ion detection or coating with different surfaces. Future work will be focused on evaluating the triplet state energy of the ligand and the energy transfer pathways, as well as the assembly with other transition metal ions or lanthanide ions and isolation of the heterometallic complexes to study their solid state luminescent and magnetic properties.

7.6 References

1. (a) L. Armelao, S. Quici, F. Barigelletti, G. Accorsi, G. Bottaro, M. Cavazzini and E. Tondello, *Coord. Chem. Rev.*, 2010, **254**, 487-505; (b) J.-C. G. Bünzli, *Eur. J. Inorg. Chem.*, 2017, **2017**, 5058-5063; (c) D. Parker, *Coord. Chem. Rev.*, 2000, **205**, 109-130.
2. (a) D. J. Lewis, T. M. Day, J. V. MacPherson and Z. Pikramenou, *Chem. Commun.*, 2006, 1433-1435; (b) L. L. Ruston, G. M. Robertson and Z. Pikramenou, *Chem. Asian. J.*, 2010, **5**, 571-580; (c) A. Davies, D. J. Lewis, S. P. Watson, S. G. Thomas and Z. Pikramenou, *Proc. Natl. Acad. Sci.*, 2012, **109**, 1862; (d) S. L. C. Pinho, H. Faneca, C. F. G. C. Geraldes, M.-H. Delville, L. D. Carlos and J. Rocha, *Biomaterials*, 2012, **33**, 925-935; (e) D. J. Lewis and Z. Pikramenou, *Coord. Chem. Rev.*, 2014, **273-274**, 213-225.

3. (a) M. Andruh, J.-P. Costes, C. Diaz and S. Gao, *Inorg. Chem.*, 2009, **48**, 3342-3359; (b) L. Rosado Piquer and E. C. Sañudo, *Dalton Trans.*, 2015, **44**, 8771-8780.

4. J. Wang, Q.-W. Li, S.-G. Wu, Y.-C. Chen, R.-C. Wan, G.-Z. Huang, Y. Liu, J.-L. Liu, D. Reta, M. J. Giansiracusa, Z.-X. Wang, N. F. Chilton and M.-L. Tong, *Angew. Chem. Int. Ed.*, 2021, **60**, 5299-5306.

5. (a) C. Y. Chow, S. V. Eliseeva, E. R. Trivedi, T. N. Nguyen, J. W. Kampf, S. Petoud and V. L. Pecoraro, *J. Am. Chem. Soc.*, 2016, **138**, 5100-5109; (b) I. Martinić, S. V. Eliseeva, T. N. Nguyen, V. L. Pecoraro and S. Petoud, *J. Am. Chem. Soc.*, 2017, **139**, 8388-8391.

6. (a) P. A. Brayshaw, J.-C. G. Buenzli, P. Froidevaux, J. M. Harrowfield, Y. Kim and A. N. Sobolev, *Inorg. Chem.*, 1995, **34**, 2068-2076; (b) S. Decurtins, M. Gross, H. W. Schmalle and S. Ferlay, *Inorg. Chem.*, 1998, **37**, 2443-2449; (c) Y. Shen, T. Riedener and K. L. Bray, *Phys. Rev. B*, 2000, **61**, 11460-11471; (d) J. C. Lutter, S. V. Eliseeva, J. W. Kampf, S. Petoud and V. L. Pecoraro, *Chem. Eur. J.*, 2018, **24**, 10773-10783.

7. (a) S. Aime, M. Botta, M. Fasano and E. Terreno, *Spectrochim. Acta, Part A*, 1993, **49**, 1315-1322; (b) T. N. Parac-Vogt, K. Kimpe and K. Binnemans, *J. Alloys. Compd.*, 2004, **374**, 325-329; (c) J. B. Livramento, É. Tóth, A. Sour, A. Borel, A. E. Merbach and R. Ruloff, *Angew. Chem. Int. Ed.*, 2005, **44**, 1480-1484; (d) J. B. Livramento, A. Sour, A. Borel, A. E. Merbach and É. Tóth, *Chem. Eur. J.*, 2006, **12**, 989-1003; (e) G. Dehaen, P. Verwilst, S. V. Eliseeva, S. Laurent, L. Vander Elst, R. N. Muller, W. M. De Borggraeve, K. Binnemans and T. N. Parac-Vogt, *Inorg. Chem.*, 2011, **50**, 10005-10014.

8. (a) L. Scarpantonio, S. A. Cotton, E. Del Giorgio, M. McCallum, M. J. Hannon and Z. Pikramenou, *J. Inorg. Biochem.*, 2020, **209**, 111119; (b) P. B. Glover, P. R. Ashton, L. J. Childs, A. Rodger, M. Kercher, R. M. Williams, L. De Cola and Z. Pikramenou, *J. Am. Chem. Soc.*, 2003, **125**, 9918-9919.

9. (a) D. J. Lewis, P. B. Glover, M. C. Solomons and Z. Pikramenou, *J. Am. Chem. Soc.*, 2011, **133**, 1033-1043; (b) D. J. Lewis, F. Moretta and Z. Pikramenou, *Supramol. Chem.*, 2012, **24**, 135-142.

10. (a) Ulrich S. Schubert, Andreas Winter and G. R. Newkome, *Terpyridine-Based Materials: For Catalytic, Optoelectronic and Life Science Applications*, Wiley, 2011; (b) L. Wang, B. Song, S. Khalife, Y. Li, L.-J. Ming, S. Bai, Y. Xu, H. Yu, M. Wang, H. Wang and X. Li, *J. Am. Chem. Soc.*, 2020, **142**, 1811-1821.

11. (a) R. F. Ziessel, G. Ulrich, L. Charbonnière, D. Imbert, R. Scopelliti and J.-C. G. Bünzli, *Chem. Eur. J.*, 2006, **12**, 5060-5067; (b) R. Sakamoto, S. Katagiri, H. Maeda and H. Nishihara, *Coord. Chem. Rev.*, 2013, **257**, 1493-1506.

12. (a) C. Wei, Y. He, X. Shi and Z. Song, *Coord. Chem. Rev.*, 2019, **385**, 1-19; (b) A. Winter and U. S. Schubert, *ChemCatChem*, 2020, **12**, 2890-2941.

13. (a) L. J. Kershaw Cook, F. Tuna and M. A. Halcrow, *Dalton Trans.*, 2013, **42**, 2254-2265; (b) M. Nakaya, W. Kosaka, H. Miyasaka, Y. Komatsumaru, S. Kawaguchi, K. Sugimoto, Y. Zhang, M. Nakamura, L. F. Lindoy and S. Hayami, *Angew. Chem. Int. Ed.*, 2020, **59**, 10658-10665.

14. S. Dasari, S. Singh, Z. Abbas, S. Sivakumar and A. K. Patra, *Spectrochim. Acta, Part A*, 2021, **256**, 119709.

15. G. Maayan, B. Yoo and K. Kirshenbaum, *Tetrahedron Lett.*, 2008, **49**, 335-338.

16. D. J. Lewis, F. Moretta, A. T. Holloway and Z. Pikramenou, *Dalton Trans.*, 2012, **41**, 13138-13146.

17. T. F. Gritmon, M. P. Goedken and G. R. Choppin, *J. Inorg. Nucl. Chem.*, 1977, **39**, 2021-2023.

18. D. W. Fink and W. E. Ohnesorge, *J. Phys. Chem.*, 1970, **74**, 72-77.

19. H. Zhang, X. Hua, X. Tuo and X. Wang, *J. Rare Earth*, 2012, **30**, 705-708.

20. J. M. Couchet, J. Azéma, C. Galaup and C. Picard, *J. Lumin.*, 2011, **131**, 2735-2745.

21. (a) H.-R. Mürner, E. Chassat, R. P. Thummel and J.-C. G. Bünzli, *J. Chem. Soc., Dalton Trans.*, 2000, 2809-2816; (b) V. Bekiari and P. Lianos, *Langmuir*, 2006, **22**, 8602-8606.

22. H. Chen, J. Cao, P. Zhou, X. Li, Y. Xie, W. Liu and Y. Tang, *Biosens. Bioelectron.*, 2018, **122**, 1-7.

23. T. Lathion, A. Fürstenberg, C. Besnard, A. Hauser, A. Bousseksou and C. Piguet, *Inorg. Chem.*, 2020, **59**, 1091-1103.

24. (a) C. Edder, C. Piguet, J.-C. G. Bünzli and G. Hopfgartner, *J. Chem. Soc., Dalton Trans.*, 1997, 4657-4664; (b) C. Edder, C. Piguet, G. Bernardinelli, J. Mareda, C. G. Bochet, J.-C. G. Bünzli and G. Hopfgartner, *Inorg. Chem.*, 2000, **39**, 5059-5073.

25. Y. Zhang, Q. Yang, J. Lu, M. Guo, X.-L. Li and J. Tang, *Inorg. Chem. Front.*, 2021, **8**, 1779-1787.

Chapter 8 Conclusions and outlooks

The primary aim of this thesis is to design and synthesise multinuclear transition metal and lanthanide based coordination complexes via supramolecular self-assembly processes to investigate their magnetic and luminescent properties. A series of compounds has been successfully synthesised and characterised by single crystal X-ray diffraction, powder X-ray diffraction, NMR, UV-vis, IR and mass spectrometry. A variety of techniques are used to analyse the properties including cyclic voltammetry, PPMS and SQUID magnetometry, Mössbauer spectroscopy and time-resolved luminescent spectroscopy.

8.1 Conclusions

In ***Chapter 2***, two tetranuclear Co^{II} complexes based on 3,6-substituded pyridazine ligands (pzdz and pydz) and azido-bridge are prepared. Typical ferromagnetic couplings are found and both complexes exhibits typical field-induced single-molecule magnetic behaviours with an effective energy barrier of 36 K and 56 K, respectively. Two isostructural Fe^{II}-grids are also synthesised in ***Chapter 3*** where the one with pzdz ligand exhibits overall antiferromagnetic interactions and the other one shows a remarkable spin crossover behaviour with $T_{1/2}$ = 230 K as well as LIESST effect, which is first discovered among the azido bridged complexes. In addition, the synergy between spin crossover and luminescence is investigated via variable-temperature emission spectra. These results have clearly demonstrated the substitution effect in making spin-crossover complexes.

In order to enhance the magnetic interactions, tetrazine radical bpztz is introduced in Co^{II}-grid complexes in ***Chapter 4***. Strong antiferromagnetic interaction with a constant of -64.7 cm^{-1} between Co^{II} and radical is observed as expected. Meanwhile, metamagnetism is observed due to the strong

intermolecular interaction. The SMM performance is also better than the neutral pyridazine bridged analogue.

Interestingly, another redox-active tetrazine ligand bptz is employed in ***Chapter 5***. In addition to a Co^{II} grid complex showing antiferromagnetic coupling and SMM at zero field, two mixed-valence Co grids are also obtained: $[Co^{2.5}{}_4]$ with positive charge delocalisation bearing tetrazine radicals and $[Co^{II}{}_2Co^{III}{}_2]$ with hydrogenated tetrazine bridge. Typical SMM under zero field is observed for the former complex, however the slow magnetic relaxation is switched off for the latter. This result indicates the magnetic properties can be easily tuned by the redox-active tetrazine ligand and the oxidation state of metal ions.

On the other hand, dinuclear lanthanide complexes bearing a diimidophosphonate ligand bistpOp are successfully obtained in ***Chapter 6***. Photophysical measurements demonstrate efficient sensitising of visible-emitted lanthanide complexes with long lifetimes for Tb^{3+} and Eu^{3+}. Static magnetic measurement shows the lanthanide ions are antiferromagnetically coupled. The heterodinuclear assembly are performed by luminescence titration where significant energy transfer from Dy^{3+} to Eu^{3+} and Eu^{3+} to Yb^{3+} are observed with the efficiency above 50%.

Moreover, in ***Chapter 7*** a novel DTPA bisamide derivative with terpyridine pendant arms has been synthesised and characterised. Photophysical studies of the related Tb^{3+} and Eu^{3+} complexes show characteristic emission with relatively long lifetimes. The hetero 3d-4f assembly of macrocyclic $Eu_2Fe_2{}^{4+}$ complex can be obtained via UV-vis titration and the formation of the target complex is also evidenced by mass spec.

To sum up, with the established theories and developed methods in coordination-driven self-assembly of luminescent complexes and molecular magnets, this thesis has provided programmable strategies for making heterometallic lanthanide-based complexes via *in situ* formation, and [2 × 2] grid complexes using radical or non-radical ligands with azido bridges. These could benefit not only

tuning magnetic interactions with better SMM performance, but also opening synergy between magnetic properties with luminescent centres.

8.2 Outlooks

While the limited Ph.D. length and the separation between two institutions only allow the completion of the above projects, some more have been inspired and proved feasible.

$[M_4(bpztz)_4(N_3)_4]$ complexes involving bpztz radical and other transition metal ions (M = Fe, Mn and Ni) have been synthesised and characterised to be isostructural to the Co analogue (**Figure 8.1**). Preliminary magnetic measurement of Ni_4 shows strong ferromagnetic interactions between Ni and tetrazine radicals with $J = 103$ cm^{-1}. However the data of Fe_4 and Mn_4 require further stimulation and theoretical investigation due to the large spin ground state and complicated magnetic interactions.

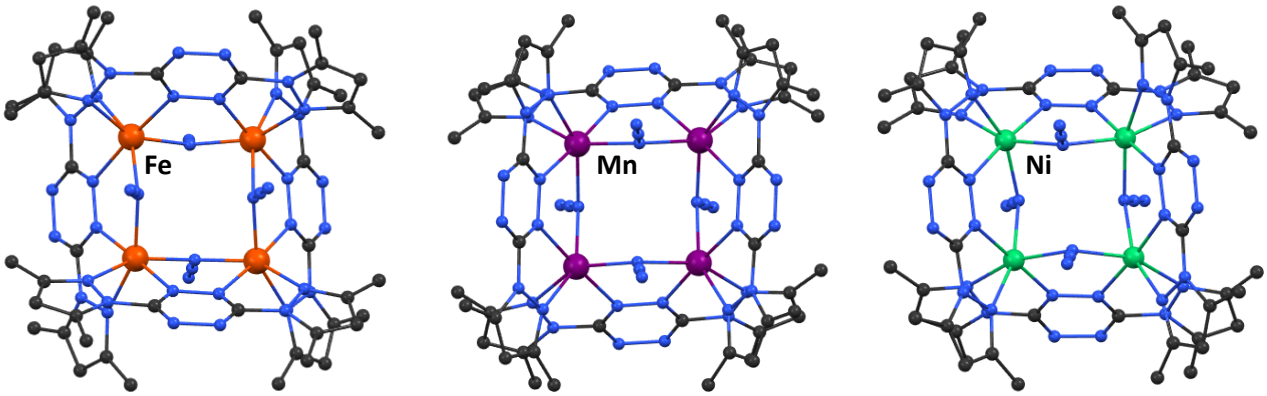

Figure 8.1. Crystal structures of $M_4(bpztz)_4(N_3)_4$ complexes. Hydrogen atoms are omitted for clarity.

With the successful assembly of 3d-4f macrocyclic complex using DTPA-terpy ligand, it can be also extended to other combinations. For instance, DyFe, DyCo or TbFe, TbCo combining different magnetic properties, GdFe or GdMn for magnetic resonance imaging and possible heterodinuclear lanthanides for dual emission. However, the isolation and crystallisation of the target complex are

still great challenges. In addition, the triplet state energy of the ligand should be evaluated by Gd^{3+} complex to better understand the sensitisation process and the possible energy transfer mechanism.

Appendices

Accession codes for published crystal structures

The following CCDC codes contain the supplementary crystallographic data for this thesis. These data can be obtained free of charge via www.ccdc.cam.ac.uk/data_request/cif, or by emailing data_request@ccdc.cam.ac.uk, or by contacting The Cambridge Crystallographic Data Centre, 12 Union Road, Cambridge CB2 1EZ, UK; fax: +44 1223 336033.

Chapter 2: 1945133 and 1945134.

Chapter 3: 2015661, 2015655, 2078512, 2015657 and 2015660.

Chapter 4: 1958192 and 1958193

Fitting models and equations for ac susceptibility data

Cole-Cole plot and Debye model

Cole-Cole plot is an effective way to investigate the relaxation dynamics of a SMM, which can be used to quantify the relaxation time and the width of its contribution. The plot is obtained by plotting in-phase ac magnetic susceptibility as x axis and out-of-phase ac magnetic susceptibility as y axis. In general, a semicircle of the plot indicates a single relaxation process.

The Cole-Cole-plot is then fitted by a generalised Debye model (eq. A1)

$$\chi(\omega) = \chi_S + \frac{\chi_T - \chi_S}{1 + (i\omega\tau)^{1-\alpha}} \qquad \text{(eq. A1)}$$

where χ_T, χ_S and ω is the isothermal susceptibility, adiabatic susceptibility and the angular ac frequency, respectively. The fitting gives α as Cole-Cole parameter ($0 < \alpha < 1$) and τ as Cole-Cole relaxation time.

All fittings of Cole-Cole plot in this thesis were performed via CC-FIT programme by Dr Nicholas F. Chilton.

Extraction of energy barrier

The effective energy barrier U_{eff} was calculated by the Arrhenius law $\tau = \tau_0 \exp(U_{eff}/k_B T)$. It can be determined in two ways by linear fitting of:

(1) A plot of $\ln\tau$ vs. $1/T$ (τ is the relaxation time from Cole-Cole fitting and T is the temperature) from frequency-dependent ac magnetic susceptibility measurement;

(2) A plot of $1/T_p$ vs. $\ln(2\pi v)$ from temperature-dependent ac magnetic susceptibility measurement (T_p is the peak temperature at each frequency and v is the frequency).

The slope of the plot represents the U_{eff} and τ_0 gives the information about the rate of the spin transition, which must be in a range of 10^{-6} to 10^{-12} to be considered as an SMM.

Additional figures and tables for each chapter

Chapter 2

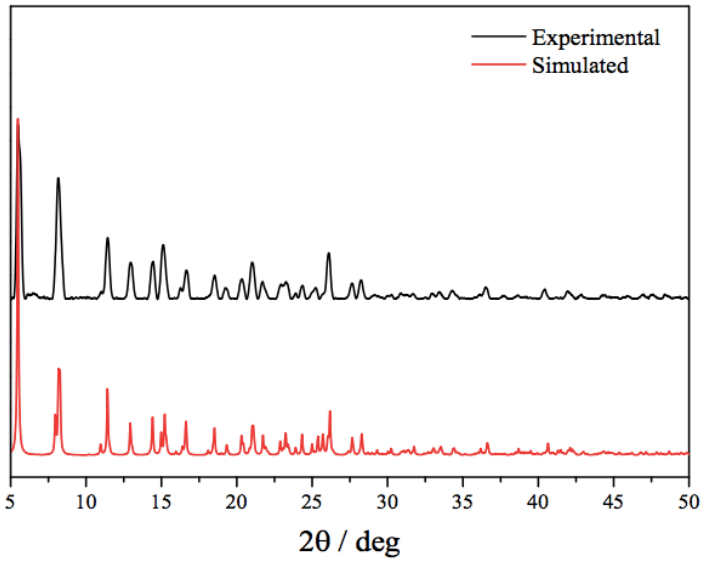

Figure A1. Powder X-ray diffraction pattern and the simulation from the single crystal data of **2**.

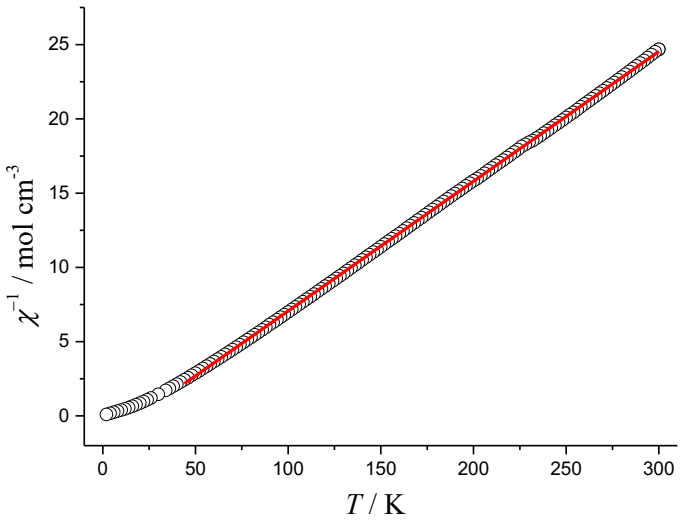

Figure A2. Temperature dependent χ^{-1} plots for **1** measured at 1000 Oe dc field. The red line represents the Curie-Weiss fit to the data.

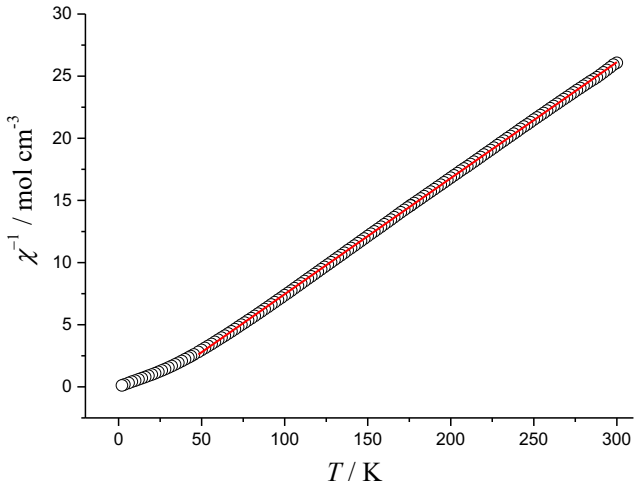

Figure A3. Temperature dependent χ^{-1} plots for **2** measured at 1000 Oe dc field. The red line represents the Curie-Weiss fit to the data.

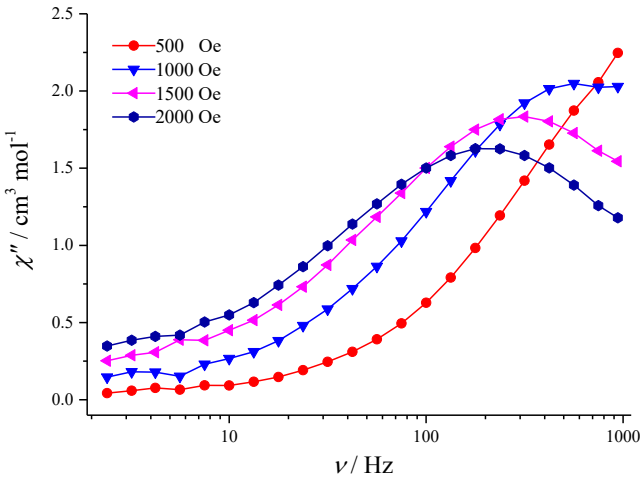

Figure A4. Frequency dependence of the out-of-phase (χ'') ac susceptibility for **1** as a function of applied field at 3 K. The lines are guides to the eye.

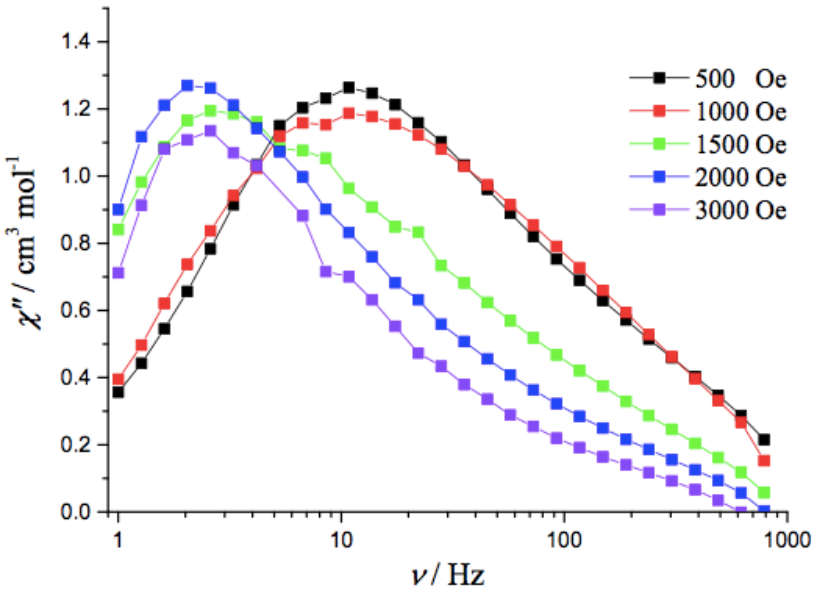

Figure A5. Frequency dependence of the out-of-phase (χ'') ac susceptibility for **2** as a function of applied field at 3 K. The lines are guides to the eye.

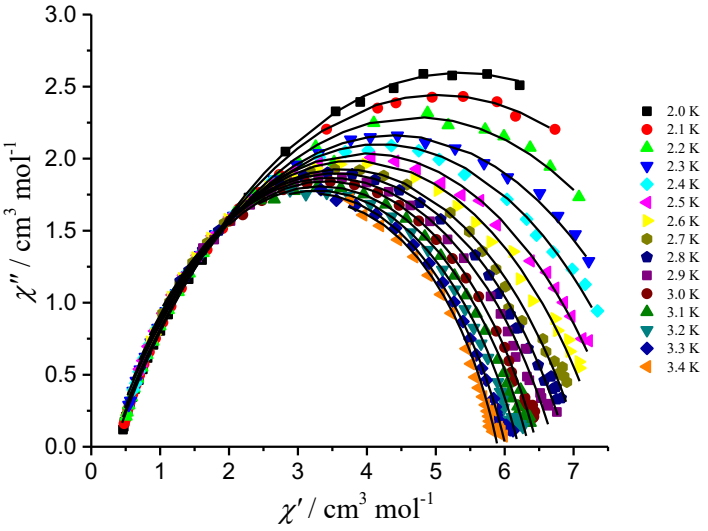

Figure A6. Cole-Cole plots of **1** under1500 Oe dc field. The lines represent the fit to the data.

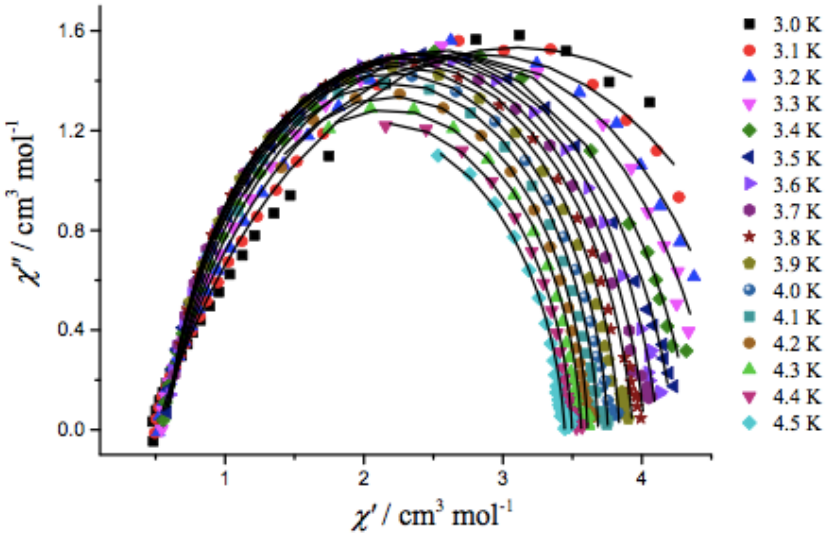

Figure A7. Cole-Cole plots of **2** under 1000 Oe dc field. The lines represent the fit to the data.

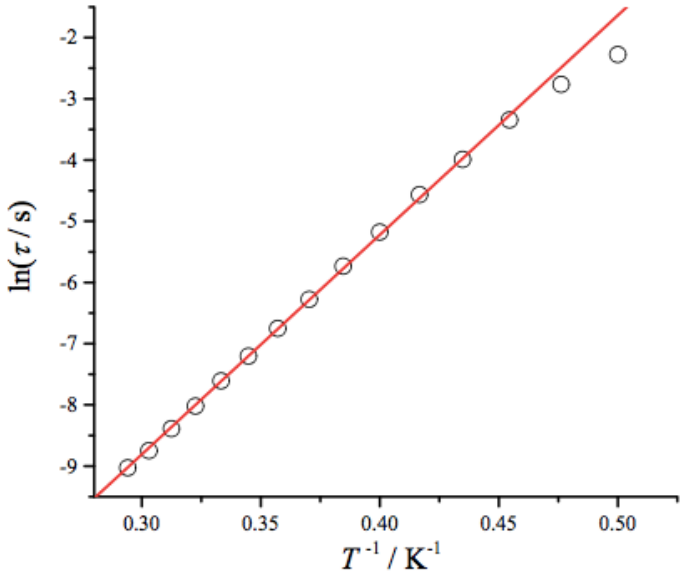

Figure A8. Temperature dependence of the relaxation time for **1** under 1500 Oe dc field. The line represents the fit by Arrhenius Law. The estimated energy barrier is 36 K (25 cm^{-1}) with a preexponential factor (τ_0) of 3.2×10^{-9} s.

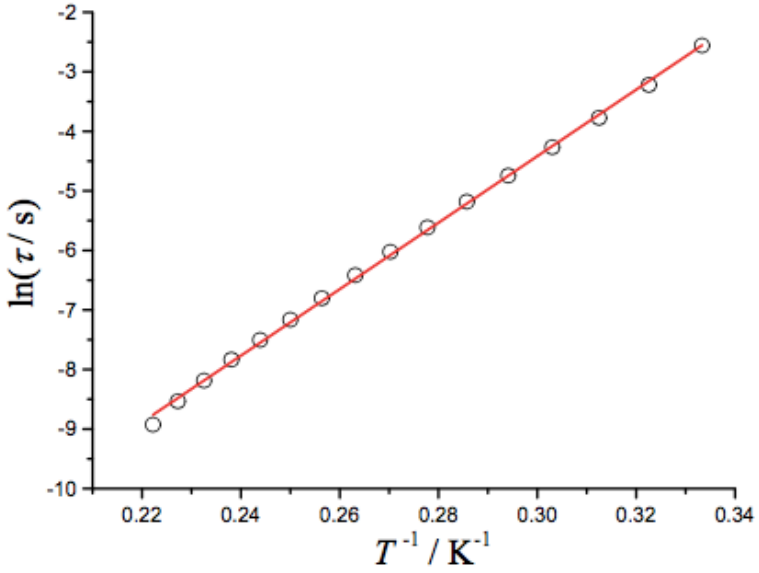

Figure A9. Temperature dependence of the relaxation time for **2** under 1500 Oe dc field. The line represents the fit by Arrhenius Law. The estimated energy barrier is 56 K (39 cm^{-1}) with a preexponential factor (τ_0) of 6.4×10^{-10} s.

Table A1. Parameters fitted by a generalised Debye model for **1** at 1500 Oe dc field.

T / K	τ / s	α
2.0	1.02×10^{-1}	0.39
2.1	6.29×10^{-2}	0.39
2.2	3.52×10^{-2}	0.39
2.3	1.85×10^{-2}	0.38
2.4	1.04×10^{-2}	0.37
2.5	5.65×10^{-3}	0.36
2.6	3.23×10^{-3}	0.35
2.7	1.88×10^{-3}	0.35
2.8	1.17×10^{-3}	0.34
2.9	7.43×10^{-4}	0.33
3.0	4.96×10^{-4}	0.31
3.1	3.29×10^{-4}	0.31
3.2	2.27×10^{-4}	0.30
3.3	1.59×10^{-4}	0.28
3.4	1.25×10^{-4}	0.26

Table A2. Parameters fitted by a generalised Debye model for **2** at 2000 Oe dc field.

T / K	τ / s	α
3.0	7.73×10^{-2}	0.32
3.1	3.99×10^{-2}	0.26
3.2	2.29×10^{-2}	0.21
3.3	1.40×10^{-2}	0.16
3.4	8.70×10^{-3}	0.14
3.5	5.62×10^{-3}	0.12
3.6	3.64×10^{-3}	0.10
3.7	2.42×10^{-3}	0.09
3.8	1.63×10^{-3}	0.08
3.9	1.11×10^{-3}	0.06
4.0	7.74×10^{-4}	0.05
4.1	5.50×10^{-4}	0.04
4.2	3.96×10^{-4}	0.03
4.3	2.78×10^{-4}	0.05
4.4	1.97×10^{-4}	0.06
4.5	1.33×10^{-4}	0.07

Chapter 3

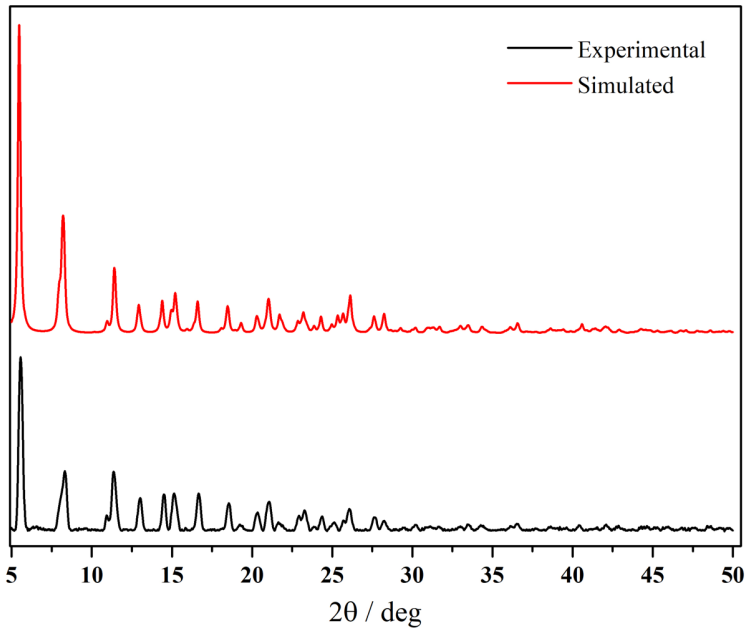

Figure A10. Powder X-ray diffraction pattern and the simulation from crystallographic data of **2** at 300 K.

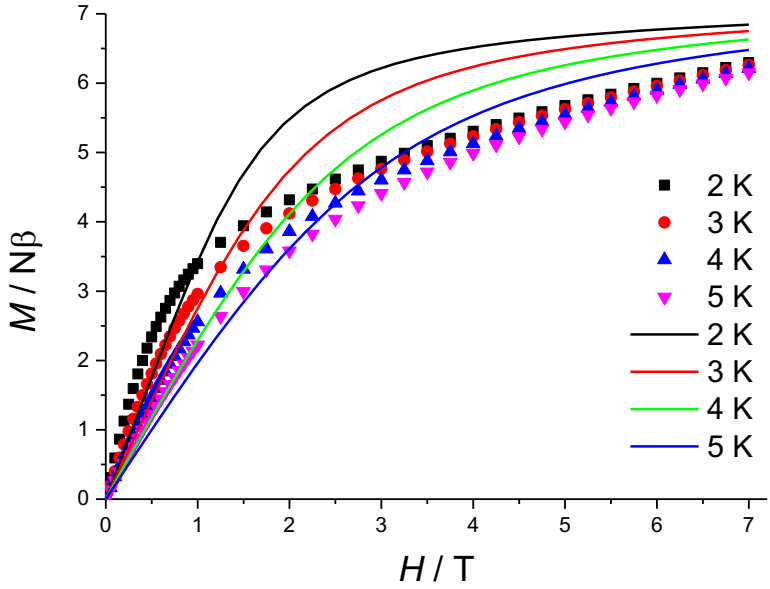

Figure A11. *M* vs *H* data for **1** at 2-5 K. The solid lines represent the simulations using the spin Hamiltonian parameters from the χT fit.

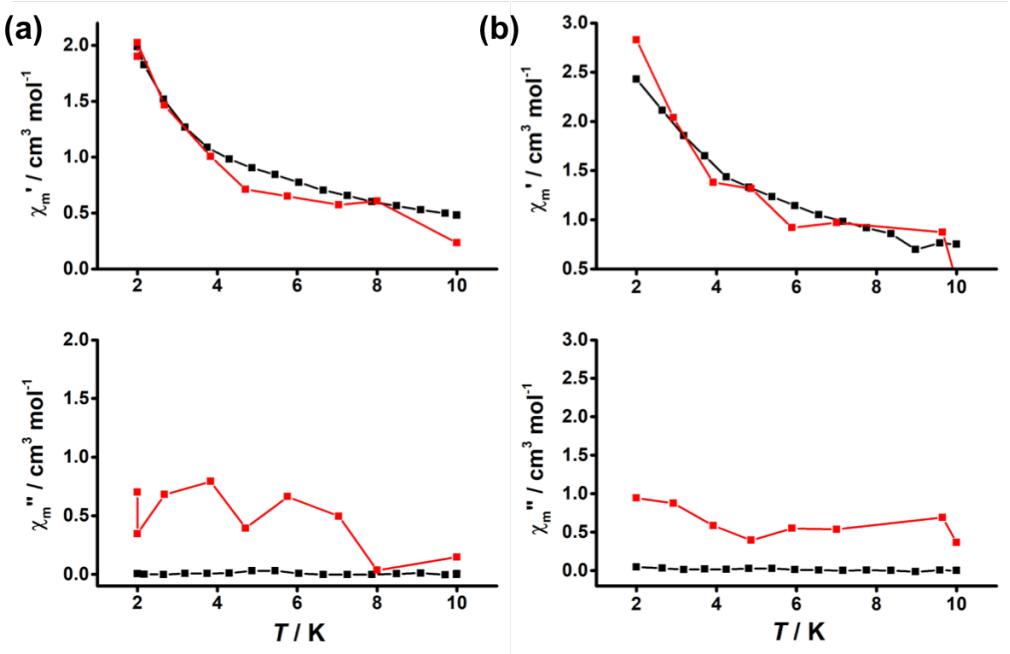

Figure A12. AC magnetic susceptibility measurement of **1** under zero (a) and 1000 Oe (b) applied dc field.

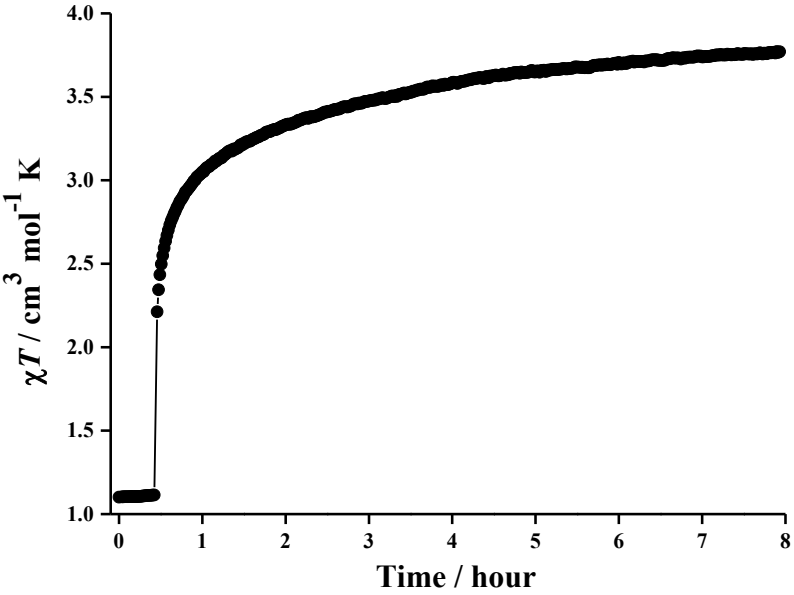

Figure A13. Time evolution of the χT products of **2** at 10 kOe under light irradiation (808 nm, 10 mW) at 10 K.

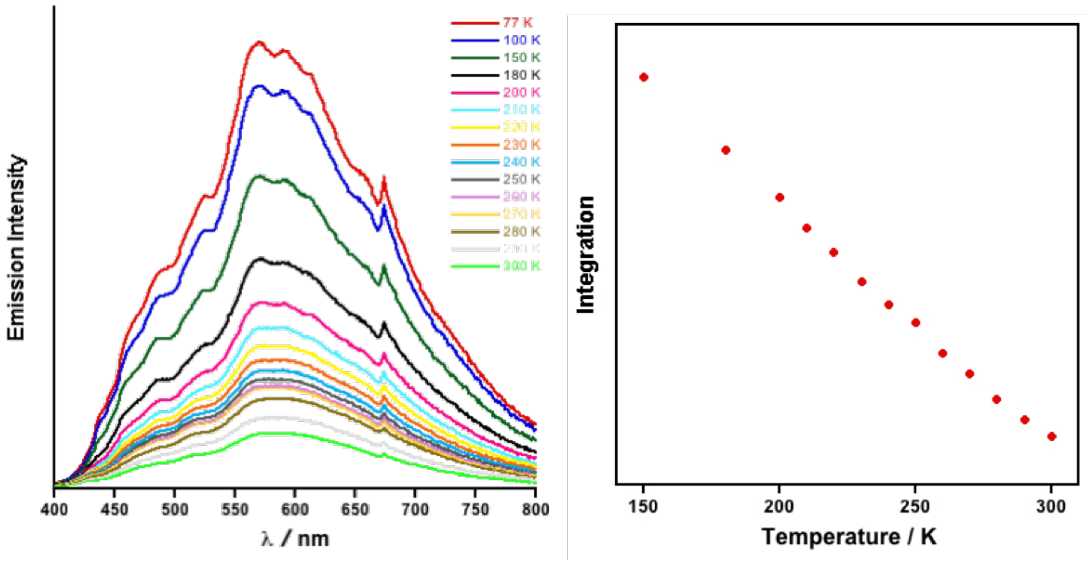

Figure A14. (left) Variable-temperature emission spectra of pydz ligand in solid state under 300 nm excitation, which cannot be directly compared to the emission of Fe_4 complex due to possible different packing or other solid state effect. (right) Integration of emission intensity of the emission spectra showing a linear decreasing luminescence signal under increasing temperatures.

Chapter 4

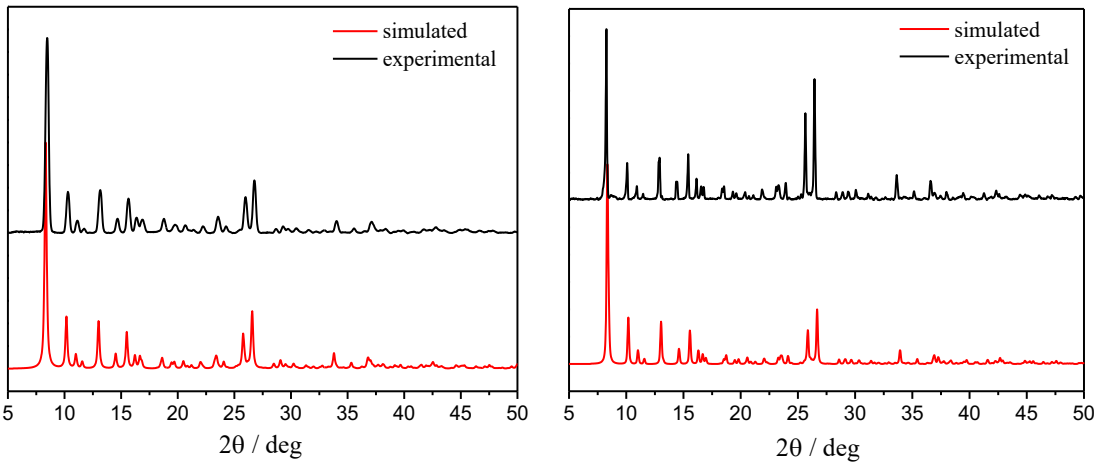

Figure A15. Powder X-ray diffraction pattern and the simulation from the single crystal data of **1** (left) and **2** (right).

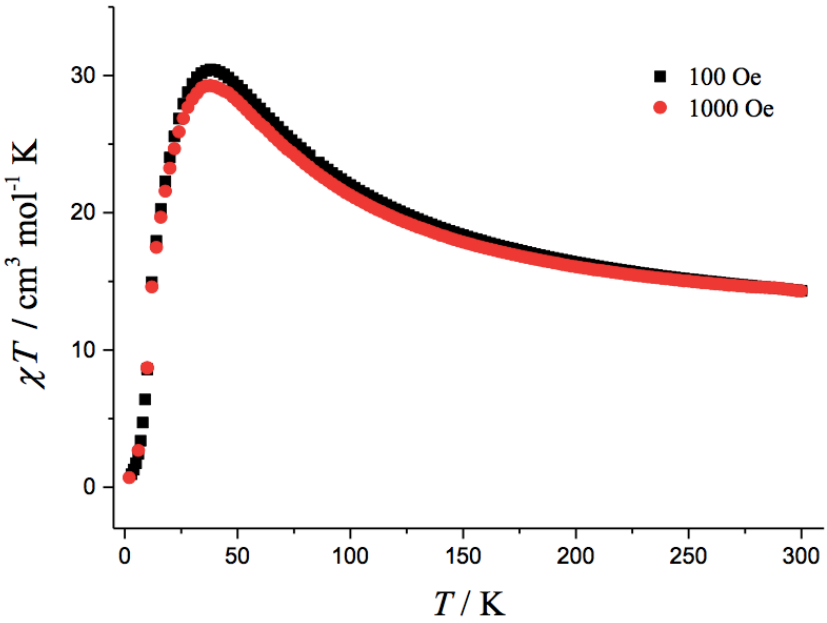

Figure A16. Variable-temperature magnetic susceptibility data for **2** under 100 Oe and 1 kOe dc fields.

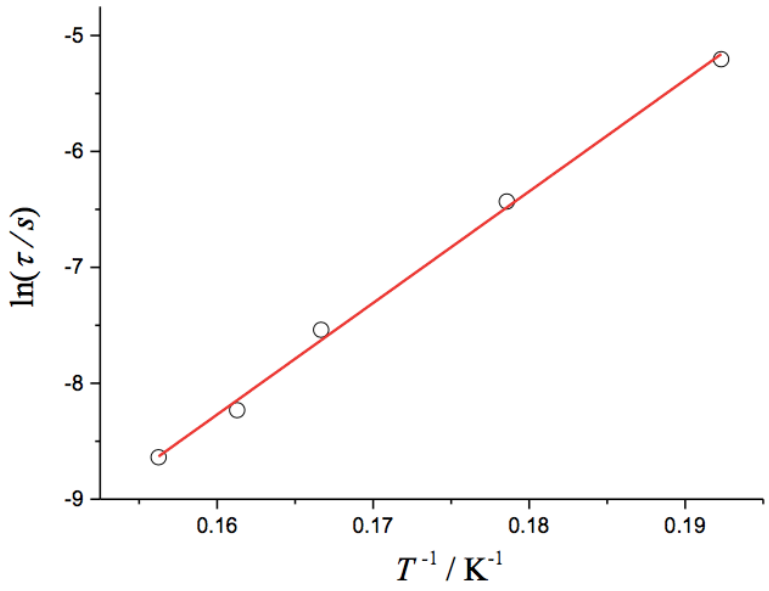

Figure A17. Arrhenius plots of **2** at zero dc field. The solid line represents the fit to the data. The estimated energy barrier is 96 K (67 cm^{-1}) with a preexponential factor (τ_0) of 5.2×10^{-10} s.

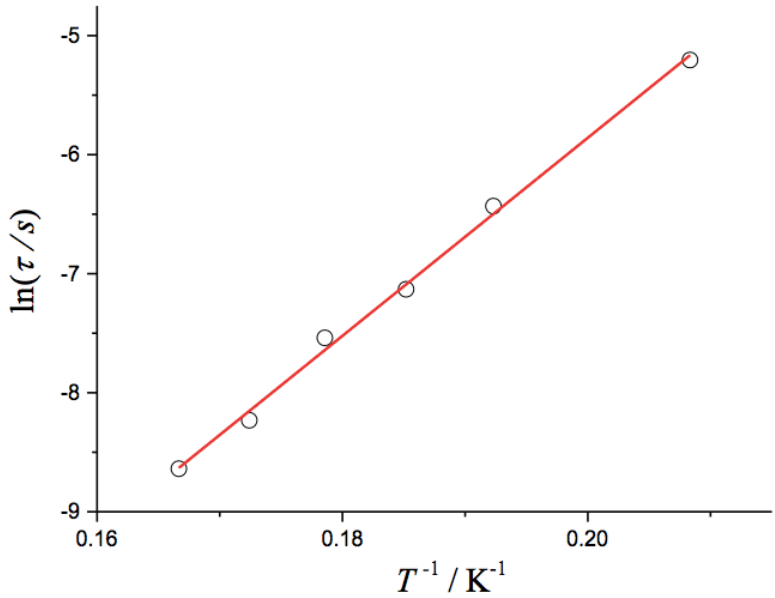

Figure A18. Arrhenius plots of **2** at 30 kOe applied dc field. The solid line represents the fit to the data. The estimated energy barrier is 83 K (58 cm^{-1}) with a preexponential factor (τ_0) of 1.7×10^{-10} s.

Table A3. Temperature dependence of the relaxation time for **2** obtained from χ'' vs T plots under zero and 30 kOe dc fields.

	Zero Field		30 kOe Field
T / K	τ / s	T / K	τ / s
5.2	5.49×10^{-3}	4.8	5.49×10^{-3}
5.6	1.61×10^{-4}	5.2	1.61×10^{-3}
6	5.32×10^{-4}	5.4	8.00×10^{-4}
6.2	2.66×10^{-4}	5.6	5.32×10^{-4}
6.4	1.77×10^{-4}	5.8	2.66×10^{-4}
		6	1.77×10^{-4}

Chapter 5

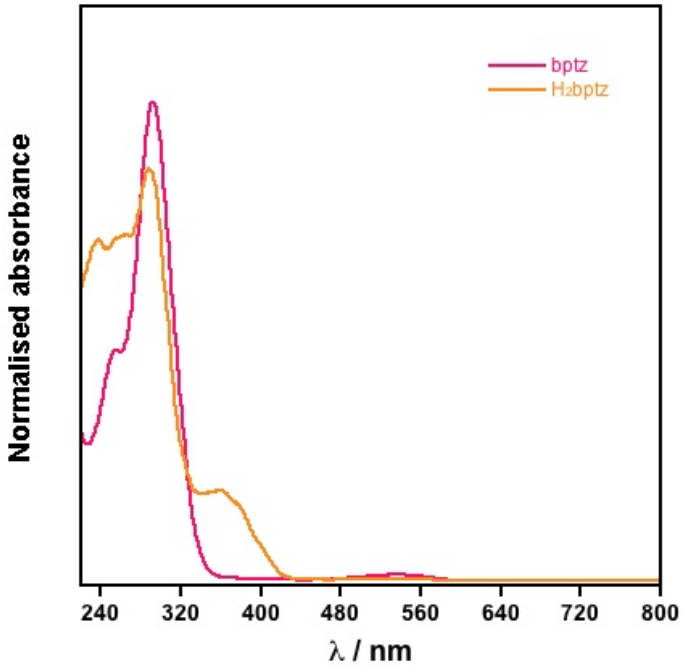

Figure A19. UV-vis spectra of bptz (red) and H_2bptz (orange) in acetonitrile solution at room temperature.

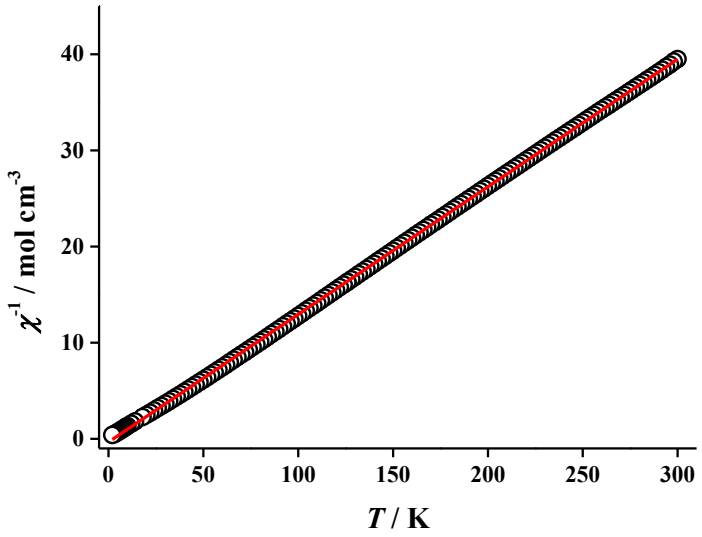

Figure A20. Curie-Weiss fitting of magnetic susceptibility data of **2**. The fitted Weiss constant is +2.5 K.

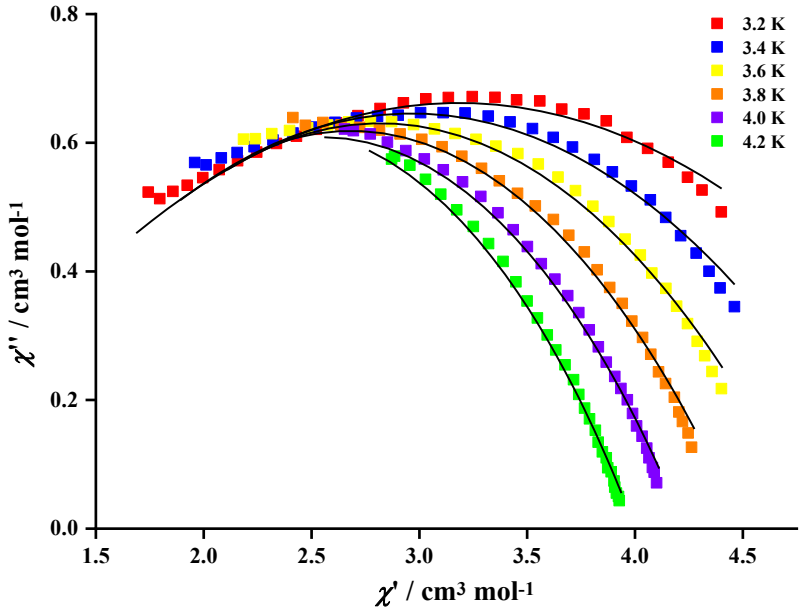

Figure A21. Cole-Cole plots for **1** under zero field from 1-1000 Hz frequency range. The solid line represents the fitting of the data.

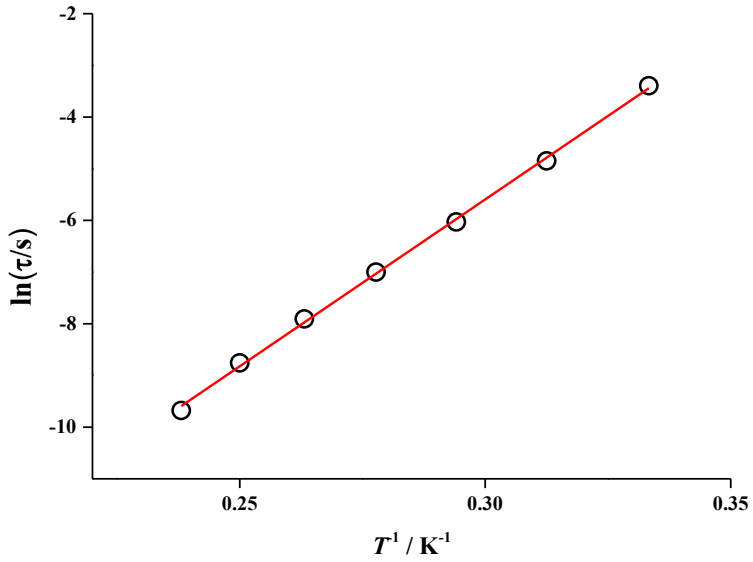

Figure A22. Arrhenius plots of **1** at zero applied dc field. The solid line represents the fit to the data. The estimated energy barrier is 65 K (45 cm^{-1}) with a preexponential factor (τ_0) of 1.43×10^{-11} s.

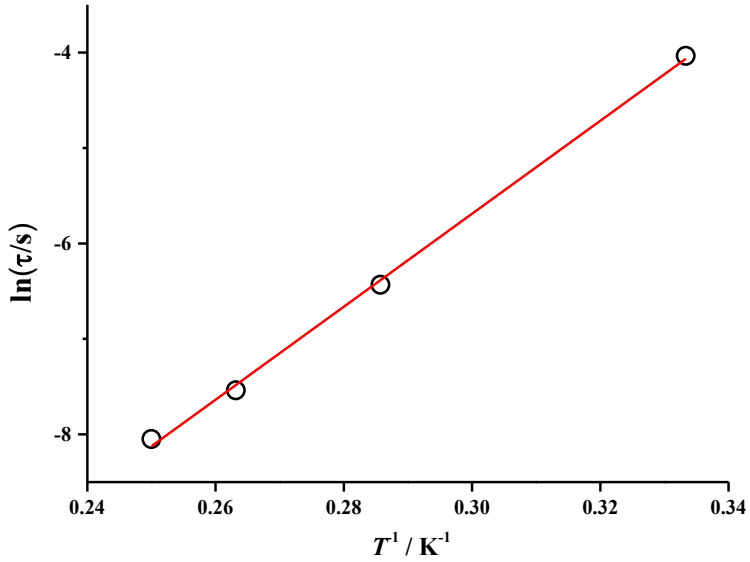

Figure A23. Arrhenius plots of **2** at zero applied dc field. The solid line represents the fit to the data. The estimated energy barrier is 49 K (34 cm^{-1}) with a preexponential factor (τ_0) of 1.5×10^{-9} s.

Chapter 6

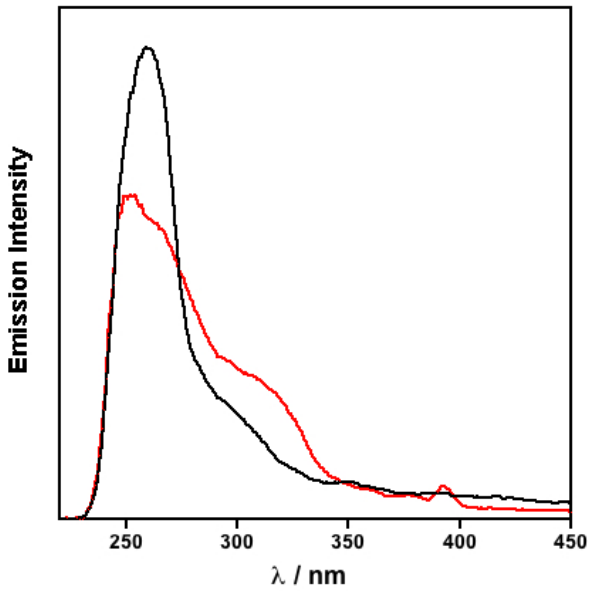

Figure A24. Excitation spectra of [DyEubistpOp$_3$] in dry MeCN solution by monitoring Dy^{3+} at 574 nm (black) and Eu^{3+} at 616 nm (red).

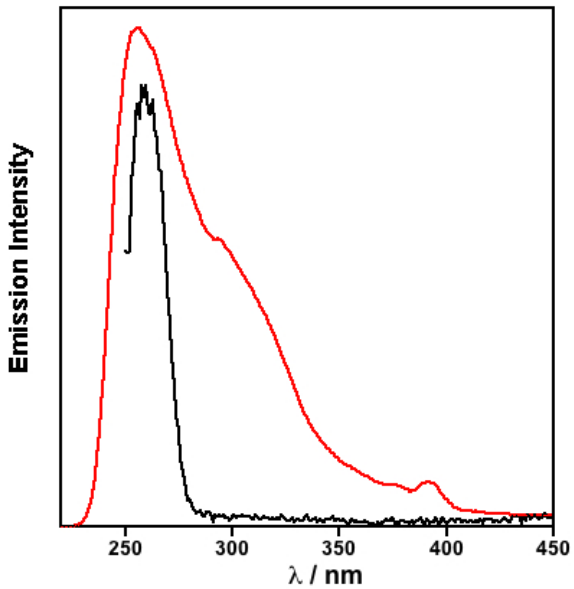

Figure A25. Excitation spectra of [EuYbbistpOp$_3$] in dry MeCN solution by monitoring Eu^{3+} at 616 nm (red) and Yb^{3+} at 975 nm (black).

Chapter 7

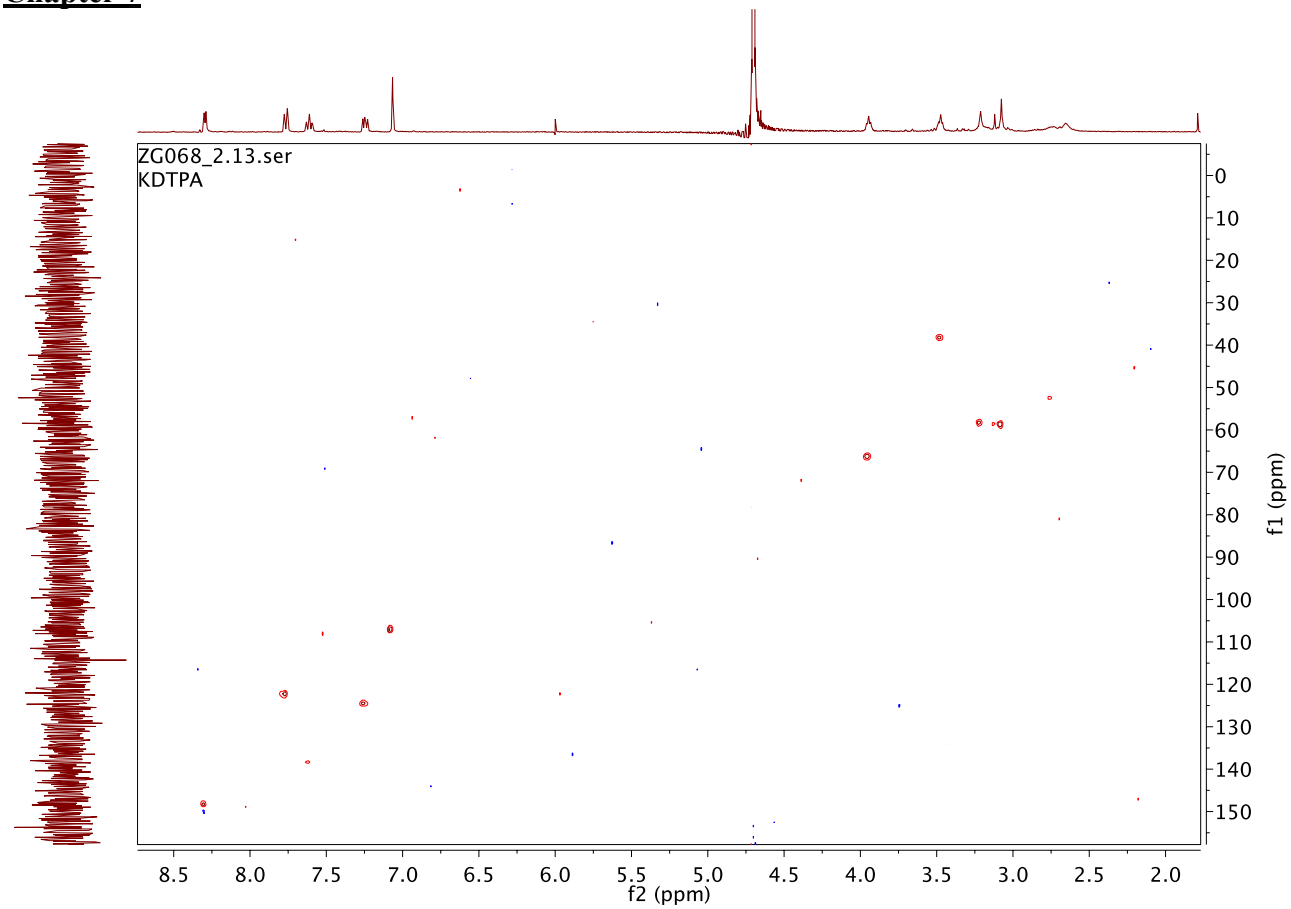

Figure A26. HSQC spectra of K_3L in D_2O.

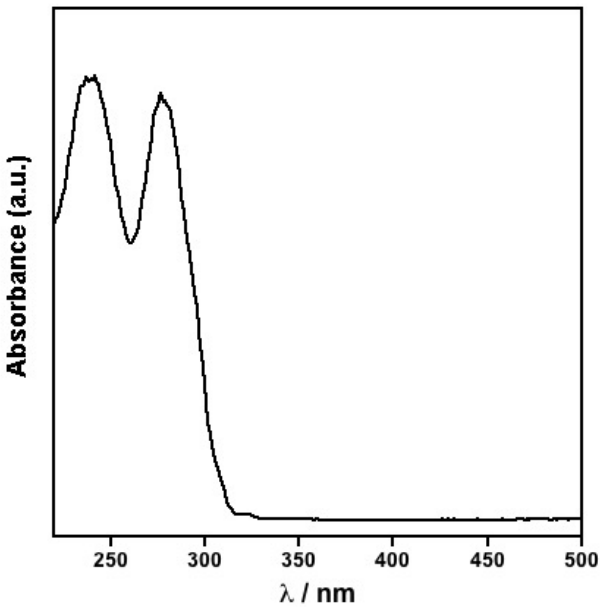

Figure A27. Absorption spectra of tpyEt in methanol solution.